Doctoral Thesis

High-Quality Single Crystal Growth and Novel Electronic States in the Quantum Critical Region of Rare Earth and Uranium Compounds

by

Yusuke Hirose

Department of Physics
Graduate School of Science
Osaka University

July , 2012

Doctoral Thesis

High-Quality Single Crystal Growth and Novel Electronic States in the Quantum Critical Region of Rare Earth and Uranium Compounds

by

Yusuke Hirose

Department of Physics
Graduate School of Science
Osaka University

July , 2012

Abstract

Rare earth and uranium compounds exhibit various kinds of electronic states such as magnetic and charge orderings, heavy fermions, and unconventional superconductivity, which are the result of the competitive phenomena between the RKKY interaction and the Kondo effect. In the present study, we succeeded in growing high-quality La, Ce, Yb, and U compounds, and clarified the novel electronic states in the quantum critical region where the Néel temperature becomes zero. Antiferromagnets of $CePtSi_2$, $CeRhGe_2$, and $CeIrGe_3$ are found to be changed into heavy fermion superconductors by applying pressure. The upper critical field H_{c2} of $CeIrGe_3$ for the magnetic field along the [001] direction is extremely large, reflecting the antisymmetric spin-orbit interaction based on the non-centrosymmetric tetragonal crystal structure along the [001] direction. In $LaNiC_2$ with the similar non-centrosymmetric orthorhombic crystal structure, we succeeded in growing single crystals and clarified that the Fermi surface is split into two kinds of Fermi surfaces, and superconductivity is of the BCS-type, although this compound has been studied experimentally and theoretically from a viewpoint of the triplet pairing state based on the non-centrosymmetric structure. We also clarified the electronic instability associated with the metamagnetic behavior or an abrupt nonlinear increase of magnetization in heavy fermion compounds such as $CeCu_6$, YbT_2Zn_{20}(T : Co, Rh, Ir), and UT_2Zn_{20}(T : Co, Ir). The metamagnetic behavior was observed at the metamagnetic field H_m below the characteristic temperature $T_{\chi max}$, where the magnetic susceptibility becomes maximum : $T_{\chi max} = 7.4$ K and $H_m = 97$ kOe in $YbIr_2Zn_{20}$, $T_{\chi max} = 5.3$ K and $H_m = 64$ kOe in $YbRh_2Zn_{20}$, and $T_{\chi max} = 0.32$ K and $H_m = 6$ kOe in $YbCo_2Zn_{20}$, together with $T_{\chi max} = 8.5$ K and $H_m = 80$ kOe in UCo_2Zn_{20}. From the present data and the previous data in several Ce, Yb, and U compounds, a simple relation between H_m and $T_{\chi max}$ was determined : $H_m(\mathrm{kOe}) = 15T_{\chi max}(\mathrm{K})$, namely $\mu_B H_m = k_B T_{\chi max}$. This reveals an important relation in f-electron systems, where the electronic state of f electrons is changed from localized to itinerant below $T_{\chi max}$, and from itinerant to localized above H_m. Furthermore we synthesized new compounds such as $CeRhGe_2$ and $YbPd_5Al_2$, together with the first single crystal sample of $YbGa_4$.

Contents

1 Introduction

The f electrons of rare earth and uranium compounds exhibit a variety of characteristic phenomena including spin and valence fluctuations, spin and charge orderings, heavy fermions and anisotropic superconductivity.[1)] In these compounds, the Ruderman-Kittel-Kasuya-Yosida (RKKY) interaction and the Kondo effect compete with each other. The RKKY interaction enhances the long-range magnetic ordering, where the f electrons with the magnetic moments are treated as localized electrons and the indirect f-f interaction is mediated by the spin polarization of the conduction electrons. The intensity of the RKKY interaction is proportional to the square of the magnetic exchange interaction between the localized f electrons and conduction electrons. On the other hand, the Kondo effect quenches the magnetic moments of the localized f electrons by the spin polarization of the conduction electrons, producing the singlet state with the binding energy $k_{\rm B}T_{\rm K}$, where $T_{\rm K}$ is called the Kondo temperature, which leads to the heavy fermion state with an extremely large effective mass at temperatures lower than $T_{\rm K}$. The $T_{\rm K}$ value depends exponentially on the magnetic exchange interaction.

The competition between the RKKY interaction and the Kondo effect was discussed by Doniach.[2)] Most of the cerium (Ce), ytterbium (Yb), and uranium (U) compounds order antiferromagnetically with the Néel temperature $T_{\rm N}$, because the RKKY interaction overcomes the Kondo effect at low temperatures. Some Ce, Yb, and U compounds such as $CeCu_6$, $CeRu_2Si_2$, $YbCu_2Si_2$, and UPt_3, however, exhibit no long-range magnetic ordering.[1,3)] The magnetic susceptibility of these compounds increases with decreasing temperature, following the Curie-Weiss law at high temperatures, with a maximum at a characteristic temperature $T_{\chi{\rm max}}$. Below $T_{\chi{\rm max}}$, the magnetic susceptibility becomes almost temperature-independent, and the f electron system is changed into a new electronic state, called the heavy fermion state. Here, $T_{\chi{\rm max}}$ approximately corresponds to the Kondo temperature. The f-localized electronic state is thus changed into an f-derived band with a flat energy vs momentum dispersion, possessing an extremely large effective mass.

Below $T_{\chi{\rm max}}$, the magnetization in the heavy fermion compounds indicates a metamagnetic behavior or an abrupt nonlinear increase in magnitude at the magnetic field $H_{\rm m}$. This is also a crossover behavior from the f-itinerant electronic state to the f-localized character.

The present strongly correlated electrons follow the Fermi liquid nature. The low-temperature electrical resistivity ρ varies as $\rho = \rho_0 + AT^2$, where ρ_0 is the residual resistivity. The coefficient $\sqrt{A}$ is two to three orders of magnitude larger than that in the usual s and p electron systems. $\sqrt{A}$ correlates with an enhanced Pauli susceptibility $\chi(T \to 0) \simeq \chi_0$ and with a large electronic specific heat coefficient $C/T(T \to 0) \simeq \gamma$.

Interestingly, some heavy fermion compounds show unconventional (anisotropic) superconductivity. The most important finding in the well-known heavy fermion superconductors such as $CeCu_2Si_2$[4)], UPt_3[5)], and UPd_2Al_3[6)] is that superconductivity is realized in the magnetically ordered state or the antiferromagnetic (ferromagnetic) fluctuations. It is theoretically difficult for the phonon-mediated attractive interaction to overcome

the strong repulsive interaction among the f electrons. To avoid a large overlap of the wave functions of the paired particles, the heavy fermion system preferentially chooses an anisotropic channel, such as a d-wave spin singlet state or a p-wave spin triplet state to form Cooper pairs.

Recently, it has been widely recognized that the electronic states in the Ce, Yb, and U compounds can be tuned by pressure. When pressure P is applied to a Ce-based antiferromagnet, the Néel temperature T_N reaches zero at the critical pressure P_c, following the Doniach phase diagram : $T_N \to 0$ for $P \to P_c$. The electronic state at P_c corresponds to the quantum critical point. Heavy fermion superconductivity mentioned above and the non-Fermi liquid nature are often observed in this critical pressure region or in the vicinity of the quantum critical point. Moreover, superconductivity in the non-centrosymmetric structure has been reported in $CePt_3Si$[7], $CeRhSi_3$[8,9], and $CeIrSi_3$[10–12]. The existence of inversion symmetry in the crystal structure is believed to be an important factor for the formation of Cooper pairs, particular for the spin-triplet configuration. Theoretically, the admixture of spin-singlet and spin-triplet Cooper pairs is realized in the non-centrosymmetric superconductor.

In the present thesis, we studies the La, Ce, Yb, and U compounds from the following three viewpoints :

1) pressure-induced superconductivity including superconductivity in the non-centrosymmetric crystal structure

2) metamagnetic behavior and electronic instability

3) searching for new Ce and Yb compounds.

We will explain relevant physics in the f-electron system in Chap.2, motivation of the present study in Chap.3, single crystal growth and measuring system including pulse magnetic field and high pressure in Chap.4, experimental results and discussion in Chap.5, and conclude the present experimental results in Chap.6.

2 Review of Relevant Physics in f-Electron Systems

2.1 CEF effect and the RKKY interaction

The $4f$ electrons in the Ce atom are pushed deeply into the interior of the closed $5s$ and $5p$ shells because of the strong centrifugal potential $\ell(\ell+1)/r^2$, where $\ell = 3$ holds for the f electrons. This is a reason why the $4f$ electrons possess an atomic-like character in the crystal.[13] On the other hand, the tail of their wave function spreads to the outside of the closed $5s$ and $5p$ shells, which is highly influenced by the potential energy, the relativistic effect and the distance between the Ce atoms. This results in the hybridization of the $4f$ electrons with the conduction electrons. These cause various phenomena such as magnetic ordering, quadrupolar ordering, valence fluctuations, Kondo lattice, heavy fermions, Kondo insulators and unconventional superconductivity.

The Coulomb repulsive force of the $4f$ electron at the same atomic site, U, is so strong, e.g., $U \simeq 5\,\mathrm{eV}$ in the Ce compounds (see Fig. 2.1), that occupancy of the same site by two $4f$ electrons is usually prohibited. In the Ce compounds, the tail of the $4f$ partial density of states extends to the Fermi level even at room temperature, and thus the $4f$ level approaches the Fermi level in energy and the $4f$ electron hybridizes strongly with the conduction electrons. This $4f$-hybridization coupling constant is denoted by V_{cf}. When U is strong and V_{cf} is ignored, the freedom of the charge in the $4f$ electron is suppressed, while the freedom of the spin is retained, representing the $4f$-localized state. Naturally, the degree of localization depends on the level of the $4f$ electron, E_f, where larger E_f helps to increase the localization.

In the localized $4f$-electronic scheme, the $4f$ ground multiplets, which obey the Hund rule in the LS-multiplets, split into the J-multiplets $J = 7/2$ and $J = 5/2$ in Ce^{3+} by the spin-orbit interaction. Moreover, the J-multiplets split into the $4f$ levels based on

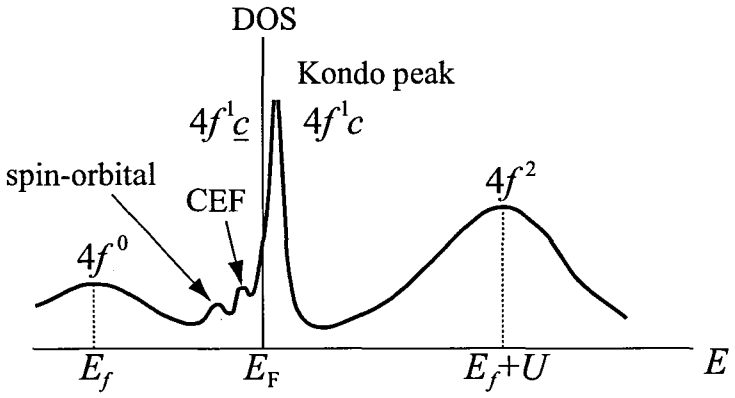

Fig. 2.1 Density of states (DOS) of the $4f$ electron in the Ce compound (Ce^{3+}), cited from ref. 14.

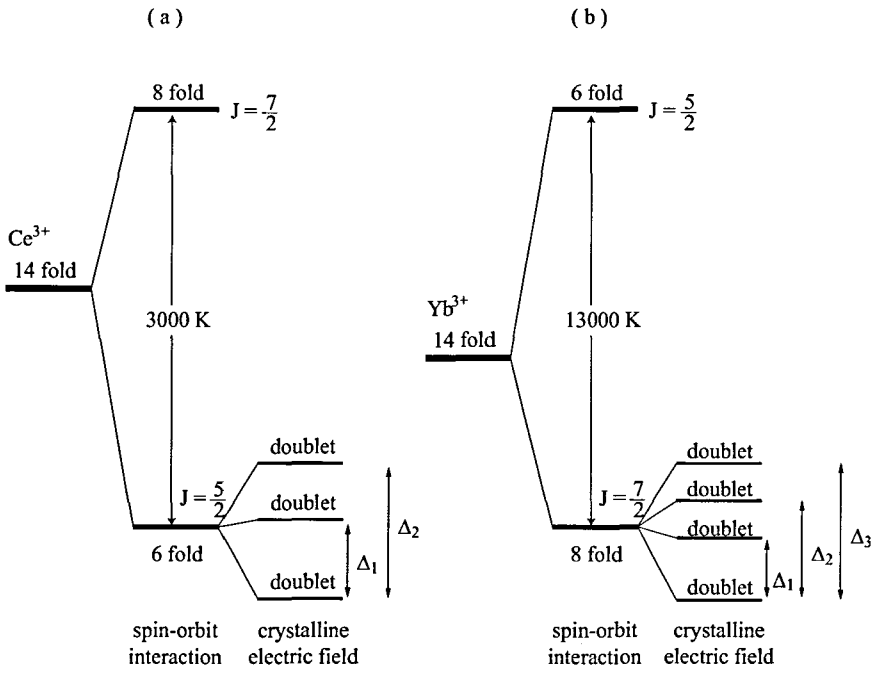

Fig. 2.2 Level scheme of the $4f$ electrons for (a) Ce^{3+} and (b) Yb^{3+} in the non-cubic crystal.

the crystalline electric field (CEF), as shown in Figs. 2.2 for (a) Ce^{3+} and (b) Yb^{3+} in the non-cubic crystal. It is noted that the $J = 7/2$ multiplet becomes the ground state in the spin-orbit interaction of Yb^{3+}, and eight fold $4f$-levels split into four doublets in the non-cubic CEF scheme. The CEF effect is as follows.

The electronic state of the point rare earth electron is influenced from the electric field of the surrounding negative ions. It is called the crystalline electric field (CEF) effect. The electrostatic potential can be expressed as follows:

$$\phi(\boldsymbol{r}) = \sum_i \frac{q_i}{|\boldsymbol{r} - \boldsymbol{R}_i|}, \tag{2.1}$$

where $\boldsymbol{r}$ is the position vector of the $4f$ electron in Ce^{3+}, q_i is the charge of the six-coordinated negative ion and $\boldsymbol{R}_i$ is the position vector of the corresponding ion.

For example, we consider the next case: the negative ion with the charge q is located at $(a,0,0)$, $(-a,0,0)$, $(0,a,0)$, $(0,-a,0)$, $(0,0,a)$ and $(0,0,-a)$, as shown in Fig. 2.3. We express eq. (2.1) by the Taylor expansion, and get the following equation:

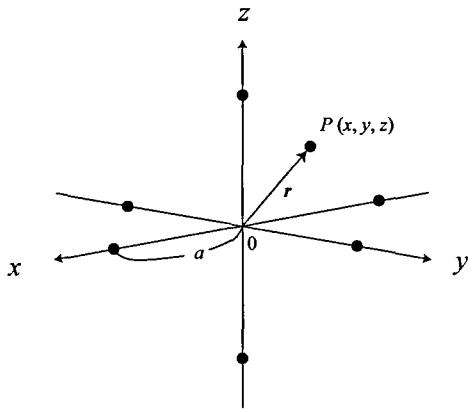

Fig. 2.3 Six-coordinated negative ions and the $4f$ electron at the point P.

$$\begin{aligned}\phi(x,\,y,\,z) \;\simeq\; & \frac{6q}{a} + D_4\left\{\left(x^4+y^4+z^4\right) - \frac{3}{5}r^4\right\} \\ & + D_6\left\{\left(x^6+y^6+z^6\right) + \frac{15}{4}\left(x^2y^4+x^2z^4+y^2x^4+y^2z^4+z^2x^4\right.\right. \\ & \left.\left. + z^2y^4\right) - \frac{15}{14}r^6\right\}, \end{aligned} \tag{2.2}$$

where $D_4 = 35q/4a^5$ and $D_6 = -21q/2a^7$.

Considering the charge distribution of the f electron, $\rho(r)$, the static potential energy is expressed as follows:

$$\int \rho(r)\phi(r)d^3r, \tag{2.3}$$

where $\phi(r)$ can be expanded by the multiplet term of the coordination x, y, z, and eq. (2.3) is expressed by the multiplet term of the coordination which is equivalent to the multiplet of the angular momentum operator based on the Wigner-Eckart's theorem in quantum mechanics. For example,

$$\begin{aligned}\int (3z^2-r^2)\rho(r)d^3r \;&=\; \alpha_J\left\langle r^2\right\rangle\left\{3J_z^2 - J\left(J+1\right)\right\} \\ &=\; \alpha_J\left\langle r^2\right\rangle O_2^0. \end{aligned} \tag{2.4}$$

We can represent the following CEF Hamiltonian corresponding to eqs. (2.2) and (2.3) by the Wigner-Eckart's theorem as follows:

$$\mathcal{H}_{\mathrm{CEF}} = B_4^0 \left(O_4^0 + 5O_4^4\right) + B_6^0 \left(O_6^0 - 21O_6^4\right). \tag{2.5}$$

Here we ignored the first term of eq. (2.2), because it have no coordination. $\mathcal{H}_{\mathrm{CEF}}$ is called the crystalline electric field Hamiltonian and the operator O_n^m: O_4^0, O_4^4, O_6^0, O_6^4 and so on, called Stevens operators. These operators are expressed by the matrix representation by Hutchings.[15,16)]

Next, we consider the case, where Ce^{3+} is influenced by the cubic crystalline electric field: $L = 3$, $S = 1/2$, $J = 5/2$ and $M = \frac{5}{2}, \frac{3}{2}, \frac{1}{2}, -\frac{1}{2}, -\frac{3}{2}, -\frac{5}{2}$. Therefore, the multiplet with the $J = 5/2$ case (six fold degenerate of $2J + 1 = 6$) splits by the CEF effect. For $J = 5/2$, $O_6^0 = O_6^4 = 0$, and O_4^0 and O_4^4 can be expressed as follows:

$$O_4^0 = 35J_z^4 - 30J(J+1)J_z^2 + 25J_z^2 - 6J(J+1) + 3J^2(J+1)^2 \tag{2.6}$$

$$O_4^4 = \frac{1}{2}(J_+^4 + J_-^4) \tag{2.7}$$

where $J_\pm = J_x \pm iJ_y$. The operator O_n^m can be expressed by (6×6)-matrix. Therefore, the CEF Hamiltonian of the cubic Ce^{3+} is expressed as follows:

$$\mathcal{H}_{\mathrm{CEF}} = \begin{array}{c} \\ \left\langle \frac{5}{2} \right| \\ \left\langle \frac{3}{2} \right| \\ \left\langle \frac{1}{2} \right| \\ \left\langle -\frac{1}{2} \right| \\ \left\langle -\frac{3}{2} \right| \\ \left\langle -\frac{5}{2} \right| \end{array} \begin{array}{c} \begin{array}{cccccc} \left|\frac{5}{2}\right\rangle & \left|\frac{3}{2}\right\rangle & \left|\frac{1}{2}\right\rangle & \left|-\frac{1}{2}\right\rangle & \left|-\frac{3}{2}\right\rangle & \left|-\frac{5}{2}\right\rangle \end{array} \\ \begin{pmatrix} 60B_4^0 & 0 & 0 & 0 & 60\sqrt{5}B_4^0 & 0 \\ 0 & -180B_4^0 & 0 & 0 & 0 & 60\sqrt{5}B_4^0 \\ 0 & 0 & 120B_4^0 & 0 & 0 & 0 \\ 0 & 0 & 0 & 120B_4^0 & 0 & 0 \\ 60\sqrt{5}B_4^0 & 0 & 0 & 0 & -180B_4^0 & 0 \\ 0 & 60\sqrt{5}B_4^0 & 0 & 0 & 0 & 60B_4^0 \end{pmatrix} \end{array}. \tag{2.8}$$

Next we represent the energy level state $|i\rangle$ and its energy scheme E_i as follows:

$$\mathcal{H}_{\mathrm{CEF}}|i\rangle = E_i|i\rangle. \tag{2.9}$$

Following wave functions and energies are obtained:

$$\left.\begin{aligned} |\Gamma_7^\alpha\rangle &= \tfrac{1}{\sqrt{6}}\left|\tfrac{5}{2}\right\rangle - \sqrt{\tfrac{5}{6}}\left|-\tfrac{3}{2}\right\rangle \\ |\Gamma_7^\beta\rangle &= \tfrac{1}{\sqrt{6}}\left|-\tfrac{5}{2}\right\rangle - \sqrt{\tfrac{5}{6}}\left|\tfrac{3}{2}\right\rangle \end{aligned}\right\} E_{\Gamma_7} = -240B_4^0 \tag{2.10}$$

$$\left.\begin{aligned} |\Gamma_8^\nu\rangle &= \sqrt{\tfrac{5}{6}}\left|\tfrac{5}{2}\right\rangle + \tfrac{1}{\sqrt{6}}\left|-\tfrac{3}{2}\right\rangle \\ |\Gamma_8^\kappa\rangle &= \sqrt{\tfrac{5}{6}}\left|-\tfrac{5}{2}\right\rangle + \tfrac{1}{\sqrt{6}}\left|\tfrac{3}{2}\right\rangle \\ |\Gamma_8^\lambda\rangle &= \left|\tfrac{1}{2}\right\rangle \\ |\Gamma_8^\mu\rangle &= \left|-\tfrac{1}{2}\right\rangle \end{aligned}\right\} E_{\Gamma_8} = 120B_4^0 \tag{2.11}$$

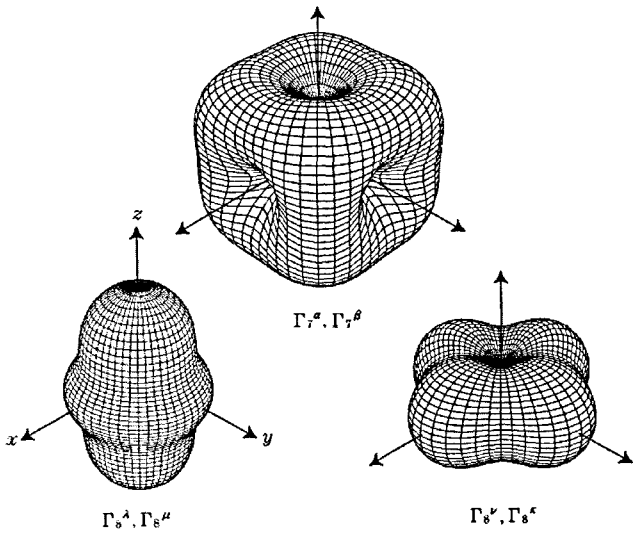

Fig. 2.4 Space charge distribution of Γ_7 and Γ_8 states, cited from ref. 14.

The energy state $-240B_4^0$ is named Γ_7 and the energy state $120B_4^0$ is Γ_8. We show in Fig. 2.4 the space charge distribution of Γ_7 and Γ_8 states. The quartet Γ_8 wave function expands along the x, y, z directions. On the other hand, the doublet Γ_7 expands along the $\langle 111 \rangle$ direction so as to avoid these axes. If the negative ions approach to the cerium ion along the principal axes, the Coulomb energy of the $4f$ electron is preferable to the Γ_7 ground state, compared with the Γ_8 ground state, indicating that the Γ_8 state becomes an excited state.

In general, the CEF Hamiltonian can be expressed as follows:

$$\mathcal{H}_{\mathrm{CEF}} = \sum_{n,m} B_n^m O_n^m. \tag{2.12}$$

If the number of the f electron is odd, namely, J has the half-integer for Ce^{3+}, Nd^{3+}, Sm^{3+}, Dy^{3+}, Er^{3+} and Yb^{3+}, the $4f$ energy level always possesses the doublet. This is called Kramers theorem, and this doublet is called the Kramers doublet. Kramers degeneration is based on the time reversal symmetry, and the doublet ground state always holds even if the crystal structure is changed into the low symmetry. Namely, its magnetic properties are different whether the number of the f electron is odd or even. When the magnetic field is applied to the system, all the degenerated $4f$ states, including the Kramers doublet, split into singlets. In the present thesis, Ce- and Yb- based compounds are studied mainly. The corresponding CEF scheme has been already shown in Fig. 2.2. U-based compounds are also studied. $5f^2$ or $5f^3$ configurations are treated in the CEF scheme, although it is difficult to determine the CEF scheme in the uranium compounds because the effective magnetic moments of $5f^2$ and $5f^3$ are 3.58 and 3.62 μ_{B}/U, respectively, revealing almost the same value, and $5f$ electrons become itinerant

at low temperatures.[17)]

We can obtain the mangetic moment of the f electron by measuring the magnetic susceptibility or magnetization under magnetic field H, considering the Zeeman energy term, as follows:

$$\mathcal{H} = \mathcal{H}_{\mathrm{CEF}} - g_J \mu_{\mathrm{B}} H J_z \qquad (\boldsymbol{H}//z)\,. \tag{2.13}$$

Here $|i\rangle$ is the state of the $4f$ energy level i, E_i is the eigenvalue, and μ_i is the magnetic moment of the energy level. The energy level is influenced by the other energy levels. We represent this energy state as $|i\rangle$ and $E_i\,(H)$. Namely, we calculate the energy state under magnetic field, $|i\rangle$ and $E_i(H)$, by diagonalizing the matrix of the Hamiltonian eq. (2.8). We calculate the magnetization and the magnetic susceptibility by $|i\rangle$ and $E_i(H)$. Here, the Helmholtz free energy F can be expressed by the partial function Z as follows:

$$F = -k_{\mathrm{B}} T \ln Z, \tag{2.14}$$

$$Z = \sum_i e^{-\frac{E_i(H)}{k_{\mathrm{B}}T}}. \tag{2.15}$$

The magnetization M is expressed as the differential of F by magnetic field:

$$\begin{aligned} M &= -\frac{\partial F}{\partial H} \\ &= \frac{\sum_i \mu_{z_i} e^{-E_i(H)/k_{\mathrm{B}}T}}{\sum_i e^{-E_i(H)/k_{\mathrm{B}}T}} \\ &\equiv \langle \mu_{z_i} \rangle\,, \end{aligned} \tag{2.16}$$

where μ_{z_i} is the magnetic moment of the state $|i\rangle$.

$$\begin{aligned} \mu_{z_i} &= -\frac{\partial E_i\,(H)}{\partial H} \\ &= g_J \mu_{\mathrm{B}} \langle i | J_z | i \rangle. \end{aligned} \tag{2.17}$$

Namely, the magnetization M corresponds to the average $\langle \mu_{z_i} \rangle$ of the magnetic moment μ_{z_i}.

The magnetic susceptibility χ is the differential of magnetization $\partial M/\partial H (H \to 0)$:

$$\chi = \frac{1}{k_{\mathrm{B}}T} \left(\left\langle \left(\frac{\partial E_i(H)}{\partial H} \right)^2 \right\rangle - \left\langle \frac{\partial E_i(H)}{\partial H} \right\rangle^2 \right) - \left\langle \frac{\partial^2 E_i(H)}{\partial H^2} \right\rangle. \tag{2.18}$$

In case of the calculation of the magnetic susceptibility, we can treat the Zeeman energy $-g_J\mu_B H J_z$ as the perturbation. The energy $E_i(H)$ by the second perturbation can be expressed as follows:

$$E_i(H) = E_i - g_J\mu_B H\langle i|J_z|i\rangle + (g_J\mu_B)^2 H^2 \sum_{j(\neq i)} \frac{|\langle j|J_z|i\rangle|^2}{E_j - E_i}. \tag{2.19}$$

By using eq. (2.19), eq. (2.18) is obtained as

$$\chi = \frac{(g_J\mu_B)^2 \sum_i e^{-E_i/k_BT}\left(|\langle i|J_z|i\rangle|^2 + 2k_BT\sum_{j(\neq i)}\frac{|\langle j|J_z|i\rangle|^2}{E_j - E_i}\right)}{k_BT\sum_i e^{-E_i/k_BT}}. \tag{2.20a}$$

Eq. (2.20a) is the general expression of the magnetic susceptibility under consideration of CEF, but another expression is often used:

$$\chi = \frac{(g_J\mu_B)^2}{\sum_i e^{-E_i/k_BT}}\left(\frac{\sum_i |\langle i|J_z|i\rangle|^2 e^{-E_i/k_BT}}{k_BT} + \sum_i\sum_{j(\neq i)}|\langle j|J_z|i\rangle|^2\frac{e^{-E_i/k_BT} - e^{-E_j/k_BT}}{E_j - E_i}\right). \tag{2.20b}$$

The first term is the Curie term which can be determined from the diagonal terms of the matrix J_z, and the second term is related to the non-diagonal terms. Namely, it is the Van-Vleck term, which is related to the transition between the states. It is known from eqs. (2.20) that the magnetic susceptibility can be determined from the state of the f electron without magnetic field.

Next, we calculate J_z for the cubic Ce^{3+}. The J_z matrix can be expressed as follows:

$$J_z = \begin{array}{c} \\ \langle\Gamma_7^\alpha| \\ \langle\Gamma_7^\beta| \\ \langle\Gamma_8^\nu| \\ \langle\Gamma_8^\kappa| \\ \langle\Gamma_8^\lambda| \\ \langle\Gamma_8^\mu| \end{array} \begin{array}{c} \begin{array}{cccccc} |\Gamma_7^\alpha\rangle & |\Gamma_7^\beta\rangle & |\Gamma_8^\nu\rangle & |\Gamma_8^\kappa\rangle & |\Gamma_8^\lambda\rangle & |\Gamma_8^\mu\rangle \end{array} \\ \begin{pmatrix} -\frac{5}{6} & 0 & \frac{2\sqrt{5}}{3} & 0 & 0 & 0 \\ 0 & \frac{5}{6} & 0 & -\frac{2\sqrt{5}}{3} & 0 & 0 \\ \frac{2\sqrt{5}}{3} & 0 & \frac{11}{6} & 0 & 0 & 0 \\ 0 & -\frac{2\sqrt{5}}{3} & 0 & -\frac{11}{6} & 0 & 0 \\ 0 & 0 & 0 & 0 & \frac{1}{2} & 0 \\ 0 & 0 & 0 & 0 & 0 & -\frac{1}{2} \end{pmatrix} \end{array}. \tag{2.21}$$

We obtain the magnetic moment as $-5/7\,\mu_B$ for $|\Gamma_7^\alpha\rangle$ and $+5/7\,\mu_B$ for $|\Gamma_7^\beta\rangle$ from $g_J = 6/7$. The summation over the two degenerated states of the Γ_7 state is zero. The magnetic

moments for $|\Gamma_8^\nu\rangle$, $|\Gamma_8^\kappa\rangle$, $|\Gamma_8^\lambda\rangle$ and $|\Gamma_8^\mu\rangle$ are $11/7\,\mu_B$, $-11/7\,\mu_B$, $3/7\,\mu_B$ and $-3/7\,\mu_B$, respectively. Eq. (2.20b) can be expressed as follows (Γ_7 is the ground state, Γ_8 is the excited state and $E_{\Gamma_8} - E_{\Gamma_7} = \Delta$):

$$\chi_z = \frac{(g_J\mu_B)^2}{1+2e^{-\Delta/k_BT}} \left\{ \frac{\frac{25}{36} + \frac{65}{18}e^{-\Delta/k_BT}}{k_BT} + \frac{40\left(1-e^{-\Delta/k_BT}\right)}{9\Delta} \right\}. \tag{2.22}$$

Figures 2.5(a) and (b) show the temperature dependence of the inverse magnetic susceptibility and magnetization, respectively, on the basis of eqs. (2.16), (2.20) and (2.21), for three cases: no CEF, Γ_7 ground state and Γ_8 ground state with the splitting energy $\Delta = 200\,\mathrm{K}$ between Γ_7 and Γ_8. If there is no CEF, $\Delta \to 0$ and $\chi_z = \frac{35}{4}(g_J\mu_B)^2/3k_BT$. The case of $\Delta \to 0$ is equivalent to the expression $k_BT \gg \Delta$ and to the Curie law which ignores CEF. When Γ_7 is the ground state, the magnetization approaches the magnetic moment of $0.7 - 0.8\,\mu_B$. On the other hand, when Γ_8 is the ground state, the magnetization becomes $1.7 - 1.8\,\mu_B$. If the Zeeman energy due to the magnetic field is larger than the CEF splitting energy, the magnetization becomes the saturated magnetic moment g_JJ.

The $4f$-localized situation is applied to most of the lanthanide compounds in which Ruderman-Kittel-Kasuya-Yosida (RKKY) interaction plays a predominant role in magnetism.[18-20] The mutual magnetic interaction between the $4f$ electrons occupying different atomic sites cannot be of a direct type such as $3d$ metal magnetism, but should be indirect one, which occurs only through the conduction electrons.

In the RKKY interaction, a localized spin $\boldsymbol{S}_i$ of the $4f$ electron interacts with a conduction electron with spin $\boldsymbol{s}$, which leads to a spin polarization of the conduction electron. This polarization interacts with another neighboring spin $\boldsymbol{S}_j$ and therefore

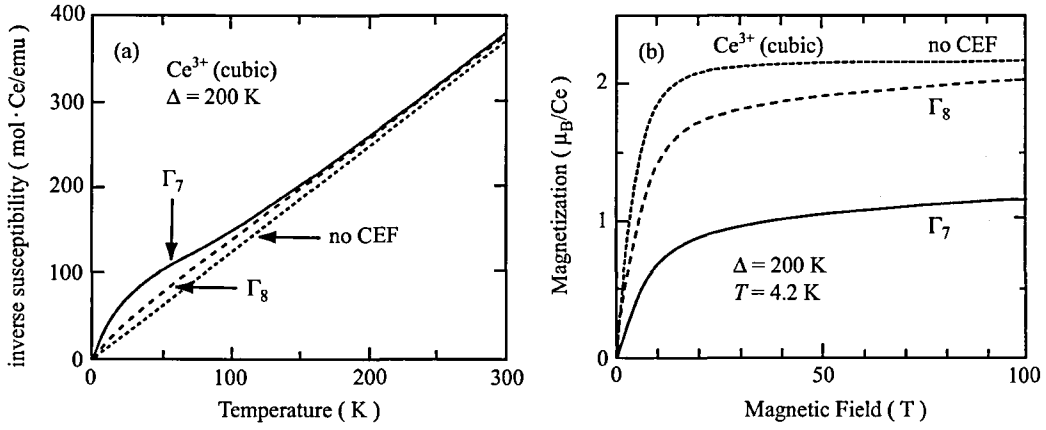

Fig. 2.5 (a) Inverse magnetic susceptibility and (b) magnetization for $\Delta = 200\,\mathrm{K}$ in cubic Ce^{3+}, cited from ref. 14.

creates an indirect interaction between the spins $\boldsymbol{S}_i$ and $\boldsymbol{S}_j$. This indirect interaction extends to the far distance and damps with a sinusoidal $2k_{\mathrm{F}}$ oscillation (named the Friedel oscillation), where k_{F} is half of the caliper dimension of the Fermi surface. When the total spin angular momentum of $4f$ electrons increases in such a way that the lanthanide element changes from Ce to Gd or reversely from Yb to Gd in the compound, the magnetic moment becomes larger and the RKKY interaction stronger, leading to the magnetic ordering. The ordering temperature roughly follows the de Gennes relation, $(g_J-1)^2J(J+1)$ if the overall CEF splitting energy is small compared with the strength of the magnetic exchange interaction. Here g_J is the Landé g-factor and J is the total angular momentum.

2.2 Kondo effect and heavy fermions

Contrary to what happens at a large U, higher V_{cf} tends to enhance the hybridization of the $4f$ electron with conduction electrons, thus accelerating the delocalization of the $4f$ electron. The delocalization of the $4f$ electron tends to make the $4f$ band wide. When $E_f > V_{cf}$, the $4f$ electron is still better localized and the Kondo regime is expected in the Ce compounds.

The study of Kondo effect began when a low-temperature resistivity minimum was found for non-magnetic metals with ppm-order magnetic impurities. Kondo showed theoretically that the electrical resistivity increases logarithmically at low temperatures, namely, $\rho(T) \sim \ln T$, as a result of the spin-flip scattering of the conduction electrons by the localized magnetic moments of impurities.[21] In the $3d$-based dilute alloys, the magnetic impurity Kondo effect can be observed only in the case of very low concentration $3d$ magnetic impurities. This is because the degeneracy of the localized spins is very important for the Kondo effect. When the concentration of $3d$ magnetic impurities is increased, the $3d$ elements would come near each other and thus the overlapping or interaction between $3d$ shells would occur, which would lift the degeneracy of the impurity spin and suppress the Kondo spin-flip process.

Since the observation of the $\rho(T) \sim \ln T$ dependence in $CeAl_3$ by Buschow *et al.*[22], many rare earth compounds, in particular, Ce compounds were found to show the anomalous behavior similar to the impurity Kondo effect. In these compounds, the $4f$ ions have very high concentration and can even form the crystalline lattice with the anions and thus it cannot be considered as the impurities. From the appearance of a Kondo-like behavior, this phenomenon is called the dense Kondo effect.

The property of the dense Kondo effect at high temperatures is the same as that of the dilute Kondo system, but at low temperatures it is quite different in behavior. For instance, we show in Fig. 2.6 the temperature dependence of the electrical resistivity in $Ce_xLa_{1-x}Cu_6$.[23] This resistivity increases logarithmically with decreasing the temperature for all range of concentration. The Kondo effect occurs independently at each Ce site, because the slope of the logarithmically curve is almost proportional to the concentration of Ce. In $CeCu_6$ ($x = 1$), the behavior is, however, very different from the dilute Kondo impurity system. The resistivity increases with decreasing the temperature, forms

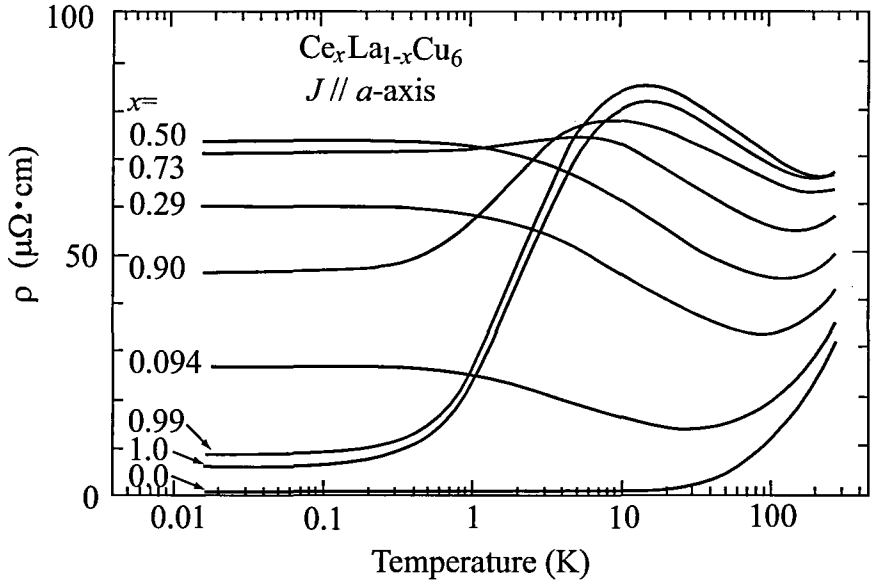

Fig. 2.6 Temperature dependence of the electrical resistivity in $Ce_xLa_{1-x}Cu_6$, cited from ref. 23.

a maximum around 15 K and decreases rapidly at lower temperatures, following the Fermi liquid nature of $\rho = \rho_0 + AT^2$. This behavior is in contrast to the dilute system ($x = 0.094$) characterized by a resistivity minimum, -ln$T$ dependence, and finally the constant residual resistivity called the unitary limit.

The many-body Kondo bound state is now understood as follows: For the simplest case of no orbital degeneracy, the localized spin $\boldsymbol{S}(\uparrow)$ is coupled antiferromagnetically with the conduction electrons $\boldsymbol{s}(\downarrow)$. Consequently the singlet state $\{\boldsymbol{S}(\uparrow)\cdot\boldsymbol{s}(\downarrow)\pm\boldsymbol{S}(\downarrow)\cdot\boldsymbol{s}(\uparrow)\}$ is formed with the binding energy k_BT_K. Here the Kondo temperature T_K is the single energy scale. In other words, disappearance of the localized moment is thought to be due to the formation of a spin-compensating cloud of the conduction electrons around the impurity moment.

The Kondo temperature in the Ce compounds is large compared with the magnetic ordering temperature based on the RKKY interaction. For example, the Ce ion is trivalent ($J = \frac{5}{2}$) and the $4f$ energy level splits into the three doublets by the crystalline electric field, namely possessing the splitting energy of Δ_1 and Δ_2, as shown in Fig. 2.2(a).

The Kondo temperature is given as follows[24]:

$$T_K^h = D\exp\left\{-\frac{1}{3|J_{cf}|D(E_F)}\right\} \qquad \text{when } T > \Delta_1, \Delta_2, \tag{2.23}$$

and

$$T_{\mathrm{K}} = \frac{D^2}{\Delta_1 \Delta_2} D \exp\left\{-\frac{1}{|J_{cf}| D(E_{\mathrm{F}})}\right\} \quad \text{when } T < \Delta_1, \Delta_2. \tag{2.24}$$

Here D, $|J_{cf}|$ and $D(E_{\mathrm{F}})$ are the band width, exchange energy and the density of states at the Fermi energy E_{F}, respectively. If we assume $T_{\mathrm{K}} \simeq 5\,\mathrm{K}$ for $D = 10^4\,\mathrm{K}$, $\Delta_1 = 100\,\mathrm{K}$ and $\Delta_2 = 200\,\mathrm{K}$, the value of $T_{\mathrm{K}}^{\mathrm{h}} \simeq 50\,\mathrm{K}$ is obtained, which is compared with the $S = \frac{1}{2}$-Kondo temperature of $10^{-3}\,\mathrm{K}$ defined as $T_{\mathrm{K}}^0 = D\exp\{-1/|J_{cf}|D(E_{\mathrm{F}})\}$. These large values of the Kondo temperature shown in eqs. (2.23) and (2.24) are due to the orbital degeneracy of the $4f$ levels. Therefore, even at low temperatures the Kondo temperature is not T_{K}^0 but T_{K} shown in eq. (2.24).

On the other hand, the magnetic ordering temperature is about 5 K in the Ce compounds, which can be simply estimated from the de Gennes relation of $(g_J - 1)^2 J(J+1)$ under the consideration of the Curie temperature of about 300 K in Gd. Therefore, it depends on the compound whether magnetic ordering occurs at low temperatures or not.

The ground state properties of the dense Kondo system are interesting in magnetism, which are highly different from the dilute Kondo system. In the cerium intermetallic compounds such as $CeCu_6$, cerium ions are periodically aligned whose ground state cannot be a scattering state but becomes a coherent Kondo lattice state.

The effective mass m^* of the conduction electron in the Kondo lattice of $CeCu_6$ is extremely large, compared with the mass of the free electron. It is reflected in the electronic specific heat coefficient γ and magnetic susceptibility $\chi(0)$, which can be expressed as

$$\gamma = \frac{2\pi^2 {k_{\mathrm{B}}}^2}{3} D(E_{\mathrm{F}}) \tag{2.25a}$$

$$= \frac{{k_{\mathrm{B}}}^2 k_{\mathrm{F}}}{3\hbar^2} m^* \qquad \text{(free electron model)}, \tag{2.25b}$$

and

$$\chi(0) = 2{\mu_{\mathrm{B}}}^2 D(E_{\mathrm{F}}) \tag{2.26a}$$

$$= {\mu_{\mathrm{B}}}^2 \frac{k_{\mathrm{F}}}{\pi^2 \hbar^2} m^* \quad \text{(free electron model)}. \tag{2.26b}$$

where k_{F} is Fermi wave number. These parameters are proportional to the effective mass.

The electrical resistivity ρ decreases steeply with decreasing the temperature, following a Fermi liquid behavior as $\rho \sim AT^2$ with a large value of the coefficient A[24]. The $\sqrt{A}$ value is proportional to the effective mass of the conduction electrons m^* and thus inversely proportional to the Kondo temperature. Correspondingly, the electronic specific heat coefficient γ roughly follows the simple relation $\gamma \sim 10^4/T_{\mathrm{K}}\,(\mathrm{mJ/K^2 \cdot mol})$ because the Kramers doublet of the $4f$ levels is changed into the γ value in the Ce compounds:

$$R\ln 2 = \int_0^{T_K} \frac{C}{T} dT, \tag{2.27}$$

$$C = \gamma T, \tag{2.28}$$

thus

$$\gamma = \frac{R\ln 2}{T_K} = \frac{5.8 \times 10^3}{T_K} \ (\mathrm{mJ/K^2 \cdot mol}). \tag{2.29}$$

It reaches 1600 $\mathrm{mJ/K^2 \cdot mol}$ for $CeCu_6$ [25] because of a small Kondo temperature of 4 - 5 K. The conduction electrons possess the large effective masses and thus move slowly in the crystal. Actually in $CeRu_2Si_2$, an extremely heavy electron of $120\,m_0$ was detected from the de Haas-van Alphen (dHvA) effect measurements [26,27].

Therefore, the Kondo lattice system is called a heavy fermion or heavy electron system. It is noticed that the Ce-based Kondo lattice compound with magnetic ordering also possesses the large γ value even if the RKKY interaction overcomes the Kondo effect at low temperatures. For example, the γ value of CeB_6 is 260 $\mathrm{mJ/K^2 \cdot mol}$ [28], which is roughly one hundred times as large as that of LaB_6, 2.6 $\mathrm{mJ/K^2 \cdot mol}$ [29]. This means that the Kondo effect at high temperatures influences the electronic state, although the $4f$ electron is localized and orders antiferromagnetically.

A significant correlation factor is thought to be the ratio of the measured magnetic susceptibility $\chi(0)$ to the observed γ value:

$$R_W \equiv \left(\frac{\pi^2 {k_B}^2}{\gamma}\right)\left\{\frac{\chi(0)}{{\mu_B}^2 {g_J}^2 J(J+1)}\right\}. \tag{2.30}$$

This ratio R_W is called Wilson-Sommerfeld ratio. Stewart [30] evaluated R_W for the heavy fermion system, as shown in Fig. 2.7. In the f electron system, R_W is not 1 but roughly 2. Kadowaki and Woods stressed the importance of a universal relationship between A and γ, as shown in Fig. 2.8.[31] They noted that the ratio A/γ has a common value of 1.0×10^{-5} $\mu\Omega \cdot \mathrm{cm \cdot K^2 \cdot mol^2/mJ^2}$. In Fig. 2.8, another line shown by a broken line is presented.[32] The Kadowaki-Woods relation is most likely applied to the doublet ground state in the CEF scheme, or the $S = 1/2$ case. In the other words, this relation is applied to the case that the f-electron with the doublet ground state becomes itinerant. The conduction electrons based on eq. (2.24), for example, is applied to the Kadowaki-Woods relation. On the other hand, a dotted line is applied to the conduction electrons based on eq. (2.23), for example, in the Ce case.

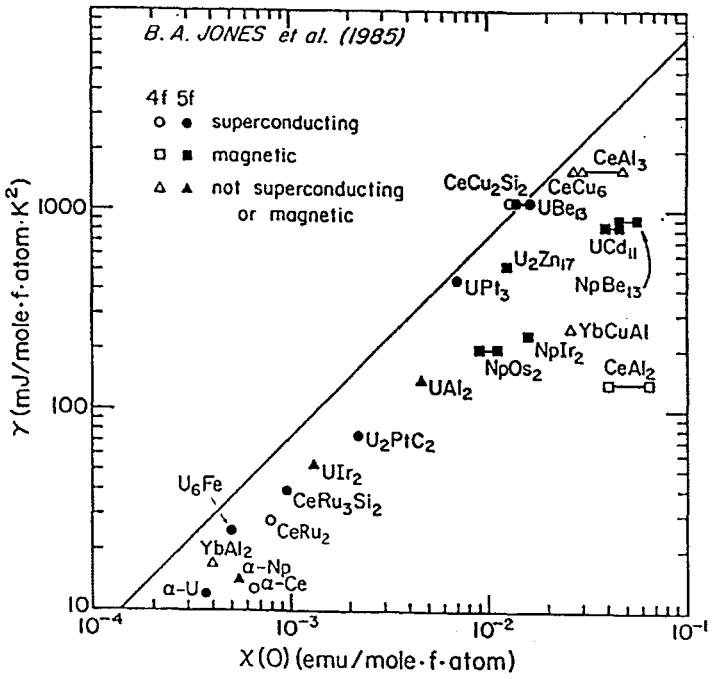

Fig. 2.7 Specific heat coefficient γ versus the susceptibility $\chi(0)$ for some heavy fermion systems. The values are extrapolated to zero by a variety of methods. Any free, non-interacting fermion gas would lie on the straight line, cited from ref. 33.

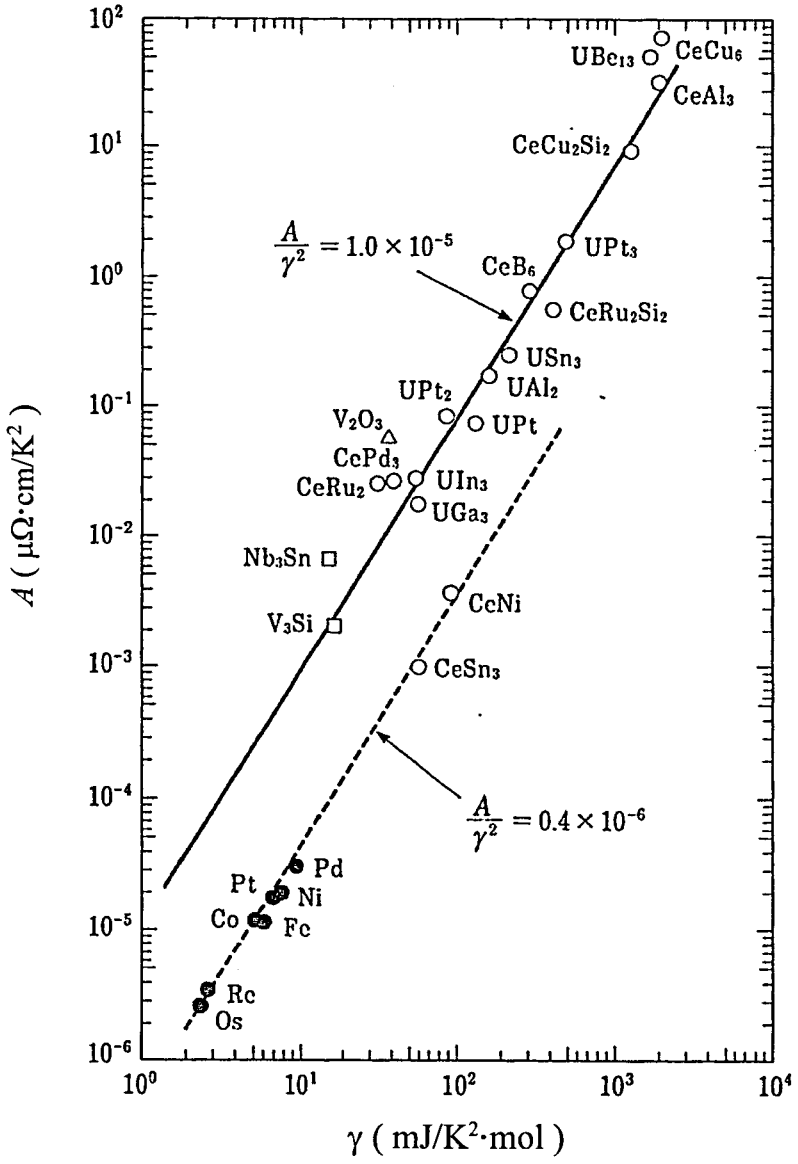

Fig. 2.8 A vs γ in the logarithmic scale, cited from refs. 31 and 32.

2.3 Competition between the RKKY interaction and the Kondo effect

The electronic state in the cerium compound can be qualitatively understood by the competition between the Kondo screening and the tendency towards magnetic ordering via RKKY-type indirect exchange mechanism. The Kondo temperature T_{K} depends exponentially on $|J_{\mathrm{cf}}|$ as follows:

$$T_{\mathrm{K}} \propto e^{-\frac{1}{D(\epsilon_{\mathrm{F}})|J_{\mathrm{cf}}|}}. \tag{2.31}$$

The magnitude of an indirect RKKY interaction can be characterized by the ordering temperature T_{RKKY} as follows:

$$T_{\mathrm{RKKY}} \propto |J_{\mathrm{cf}}|^2 D(E_{\mathrm{F}}), \tag{2.32}$$

where

$$J_{\mathrm{cf}} \simeq \frac{{V_{\mathrm{cf}}}^2}{E_{\mathrm{F}} - E_{\mathrm{f}}}. \tag{2.33}$$

Actually the magnitude of this interaction is also dominated by the de Gennes factor, and eq. (2.32) is given by the product with $(g_J - 1)^2 J(J+1)$. This leads to the phase diagram for a Kondo lattice, originally derived by Doniach[2]. Figure 2.9 is well known as the Doniach phase diagram. If $|J_{\mathrm{cf}}|D(E_{\mathrm{F}})$ is small, the compound becomes an antiferromagnet with a large magnetic moment, while with increasing $|J_{\mathrm{cf}}|D(E_{\mathrm{F}})$, both the magnetic moment and the ordering temperature tend to zero. The critical point where T_{N} becomes zero is called a **quantum critical point** (QCP). Above the quantum critical point, Kondo lattice paramagnetism is realized and consequently the f-atom valency becomes unstable, leading to the heavy fermion system. Here, the heavy fermion system is based on the Landau's Fermi liquid, where the interacting electron system or the heavy electron system is related to the non-interacting one by the scaling law without a phase transition. The characteristic features are $\rho = \rho_0 + AT^2$, $C/T(T \to 0) = \gamma$ and $\chi(T \to 0) = \chi(0)$ at low temperatures: $\sqrt{A} \sim \gamma \sim \chi(0)$.

Nearby the quantum critical point, the cerium compounds with an extraordinary wide variety of possible ground states are found. These include Kondo lattice compounds with magnetic ordering ($CeIn_3$, $CeAl_2$, CeB_6), small-moment antiferromagnets ($CePd_2Si_2$, $CeAl_3$), an anisotropic superconductor ($CeCu_2Si_2$), no magnetically ordered Kondo lattice compounds or the heavy fermion compounds ($CeCu_6$, $CeRu_2Si_2$) and valence fluctuation compounds (CeNi, $CeRh_2$, $CeRu_2$, $CeSn_3$). Significant differences are small between the heavy fermion compounds ($CeCu_6$, $CeRu_2Si_2$) and valence fluctuation compounds (CeNi, $CeRh_2$, $CeRu_2$, $CeSn_3$), mainly depending on the magnitude of the Kondo temperature. It is, however, noted that a heavy fermion compound $CeCu_6$ is changed into the valence

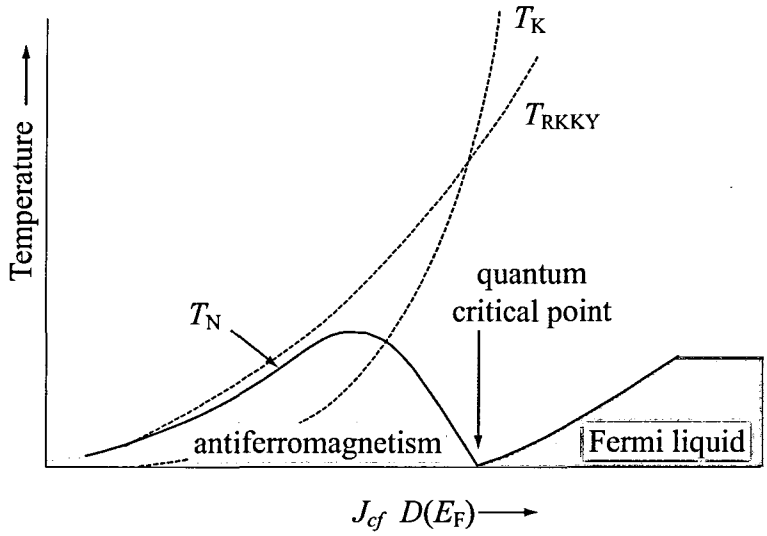

Fig. 2.9 Doniach phase diagram cited from ref. 34.

fluctuation compound by applying pressure. There might occur an electronic instability in magnetic fields at a crossover region from the heavy fermion state to the valence fluctuation state. This is studied later in $CeCu_6$ under pressure.

We note the non-magnetic cerium compounds at low temperatures. In $CeCu_6$ and $CeRu_2Si_2$ with a small Kondo temperature, there exist no magnetic ordering but exist antiferromagnetic correlations between the Ce sites[35], showing the metamagnetic behavior in the magnetic field: $H_m = 20\,\mathrm{kOe}$ in $CeCu_6$[36] and 80 kOe in $CeRu_2Si_2$ as shown later.[37] The results of dHvA experiments[27,38,39] and the band calculations[40] in $CeRu_2Si_2$ show that $4f$ electrons are itinerant. Namely, the $4f$ electrons in the cerium compounds such as $CeSn_3$ with a large Kondo temperature, which belong to the valence-fluctuation regime, are also itinerant in the ground state and contribute directly to the formation of the Fermi surface.[41,42]

Furthermore, we pay attention to the non-magnetic Ce compounds to clarify the magnitude of Kondo temperature reflected in the magnetic susceptibility. Figure 2.10 shows the temperature dependence of the magnetic susceptibility in some cerium compounds without magnetic ordering: $CeCu_6$ ($T_K \simeq 5\,\mathrm{K}$), $CeRu_2Si_2$ (20 K), CeNi (150 K) and $CeSn_3$ (200 K).[1] The magnetic susceptibility in these compounds follows the Curie-Weiss law at higher temperatures, possessing the magnetic moment near Ce^{3+} of $2.54\,\mu_B$, while it becomes approximately temperature-independent with decreasing the temperature, namely showing a broad maximum and then forming enhanced Pauli paramagnetism. The temperature $T_{\chi max}$ indicating the broad peak of the susceptibility almost corresponds to the characteristic temperature T_K.

Experimentally, pressure corresponds to $|J_{cf}|D(\epsilon_F))$. For example, the Néel temperature T_N in an antiferromagnet decreases with increasing pressure, and becomes zero:

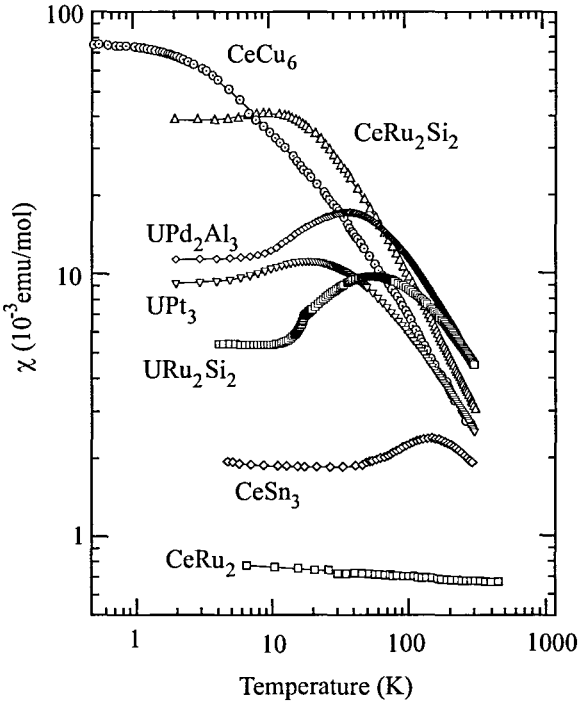

Fig. 2.10 Temperature dependence of the magnetic susceptibility for typical Ce and U compounds, cited from ref. 1.

$T_N \to 0$ for $P \to P_c$. The electronic state thus can be tuned by pressure. Namely, the antiferromagnet is changed into the non-magnetic compound. Around the quantum critical point, the heavy fermion state is realized as mentioned above, together with the non-Fermi liquid nature and appearance of superconductivity.

The non-Fermi liquid behavior around the quantum critical point is one of the recent topics in the f electron system. In the non-Fermi liquid system the following relations are characterized:

$$\rho \sim T^n \quad \text{with } n < 2, \tag{2.34}$$

$$C/T \sim -\log T. \tag{2.35}$$

The typical non-Fermi liquid nature and appearance of superconductivity were observed in $CeCu_2Ge_2$ under pressure.[43] $CeCu_2Ge_2$ is an antiferromagnet with $T_N = 4\,K$, but superconductivity is realized under pressure as in a heavy fermion superconductor $CeCu_2Si_2$. Figure 2.11 shows the low-temperature resistivity of $CeCu_2Ge_2$ for $9.7 < P < 18.6\,GPa$. At 15.6 GPa, the electrical resistivity decreases linearly with decreasing temperature: $\rho \sim T^n\,(n = 1)$, and becomes zero below the superconducting transition temperature $T_{sc} = 1.8\,K$.

Finally we note how the electronic state changes as a function of the distance between neighboring two f electrons. This is based on a so-called Hill plot[44] and the

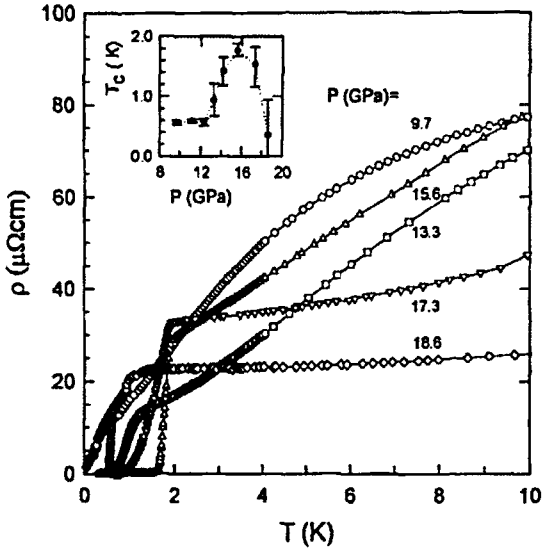

Fig. 2.11 Low-temperature resistivity under various pressure in $CeCu_2Ge_2$, cited from ref. 43.

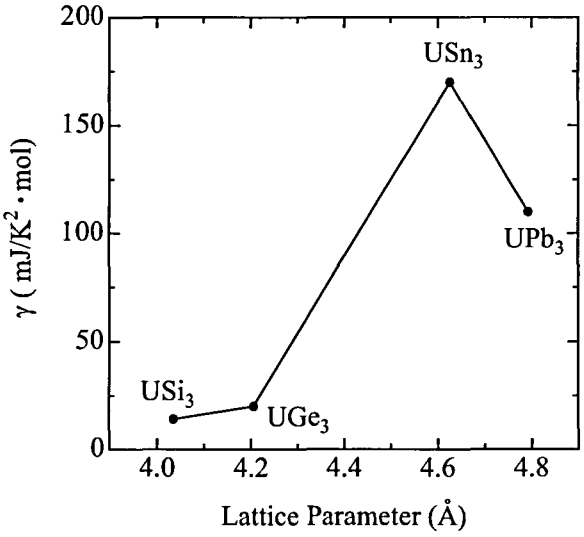

Fig. 2.12 γ vs the lattice constant in UX_3, cited from ref. 1.

Doniach phase diagram. Figure 2.12 shows the relation of the electronic specific heat coefficient γ vs the lattice constant in UX_3.[1)] The uranium compounds UX_3 with the cubic $AuCu_3$-type crystal structure, where X is a group IVb (X: Si, Ge, Sn and Pb) element of the periodic table, show various magnetic properties: Pauli paramagnetism in USi_3 and UGe_3, spin fluctuation in USn_3, and antiferromagnetism in UPb_3. The variety in the magnetic properties is closely related to the lattice constant or the distance between

the U atoms, d_{U-U}. This is reflected in the electronic specific heat coefficient γ, which varies from 14 mJ/K^2·mol in USi_3 to 170 mJ/K^2·mol in USn_3, as shown in Fig. 2.12. When the antiferromagnetic order occurs at $T_N = 30$ K in UPb_3, the γ value is reduced to 110 mJ/K^2·mol. The γ value in the UX_3 (IVb) series thus depends on the lattice constant, d_{U-U}. We can be deduced from Fig. 2.12 that as d_{U-U} becomes shorter, the wave function of $5f$ electrons is overlapped, enhancing Pauli itinerancy, while with increasing d_{U-U}, forming a heavy fermion state, as shown in USn_3, and finally the $5f$-electronic state exhibits magnetic ordering. The typical heavy fermion state most likely exists in an electronic state between USn_3 and UPb_3.

Another example is the $CeTX_3$ (T : Co, Rh, Ir, X : Si, Ge) case. The Néel temperature T_N and the γ value for $CeTSi_3$ and $CeTGe_3$ with the non-centrosymmetric tetragonal crystal structure shown in Figs. 2.13 as a function of the average lattice constant $\sqrt[3]{a^2c}$. Note that the lattice constant decreases from left to right. The observed relation of T_N vs $\sqrt[3]{a^2c}$ in Fig. 2.13(a) corresponds to the Doniach phase diagram, including a competition between the RKKY interaction and the Kondo screening effect. In fact, an antiferromagnetic state is changed into the heavy fermion superconducting state under pressures of 25 GPa in $CeIrGe_3$, 6.5 GPa in $CeCoGe_3$, and 2.5 GPa in $CeRhSi_3$ and $CeIrSi_3$. Superconductivity in $CeIrSi_3$ will be shown later.

One of the characteristic properties of heavy fermion compounds is a metamagnetic behavior or an abrupt nonlinear increase in magnetization at a magnetic field H_m at temperatures below $T_{\chi max}$. Figure 2.14 shows typical magnetization curves for $CeRu_2Si_2$[37] and UPt_3[48]. Metamagnetic behavior appears at $H_m = 77$ kOe in $CeRu_2Si_2$ and at $H_m = 200$ kOe in UPt_3. Note that the metamagnetic behavior is of the Ising type in $CeRu_2Si_2$, which occurs for the magnetic field along the tetragonal [001] direction (c-axis). On the other hand, it is of the xy-type in UPt_3, which occurs for the magnetic field in the basal plane, namely perpendicular to the hexagonal [0001] direction (c-axis). The magnetic field dependence of specific heat in these compounds has a maximum at H_m. For $H > H_m$, the cyclotron effective mass m_c^*, which is determined from the temperature dependence of de Haas- van Alphen (dHvA) oscillation, decreases with an increase in magnetic field. The mass reduction at magnetic fields above H_m is a characteristic feature of heavy fermion compounds.

There exist, however, controversial proposals on the basis of the experimental results for these metamagnetic behaviors, for example in $CeRu_2Si_2$.[27,37,39,49–54] From the magnetization measurement in $CeRu_2Si_2$, the metamagnetism is not of the first-order phase transition, suggesting that the itinerant nature of f electrons is preserved in the magnetized state at $H \gg H_m$.[53] On the other hand, Fermi surfaces of $CeRu_2Si_2$ at $H > H_m$ can be explained very well by the $4f$-localized band model, whereas Fermi surfaces below H_m are well explained by the $4f$-itinerant band model, as mentioned above.[27] The itinerant electron metamagnetism in heavy fermion systems has not yet been settled experimentally, but plausible explanations have been given theoretically.[55–60]

The metamagnetic transition is one of the important characteristics in the heavy fermion compounds. It is also due to the hybridization effect between the conduction electrons and almost localized f-electrons, as mentioned above. As a consequence, the

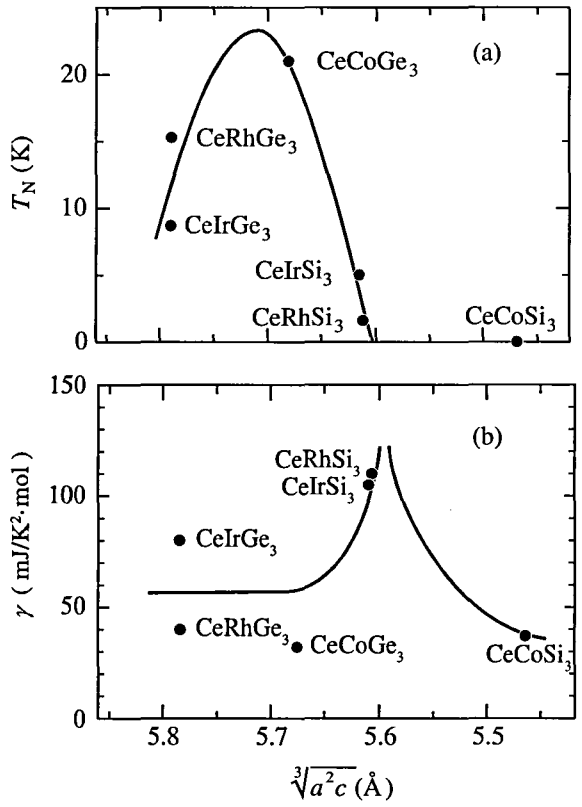

Fig. 2.13 (a) $\sqrt[3]{a^2c}$ dependence of T_N and (b) the γ value in $CeTSi_3$ and $CeTGe_3$ (T: Co, Rh, Ir), cited from refs. 11,12, and 45–47.

almost localized f-electrons become itinerant with decreasing temperature through the many-body Kondo effect. The crossover from localized to itinerant occurs at a characteristic temperature $T_{\chi max}$, where the magnetic susceptibility has a maximum, as mentioned above. $T_{\chi max}$ corresponds approximately to the Kondo temperature T_K, which is about 20 K in $CeRu_2Si_2$, for example. At temperatures lower than $T_{\chi max}$, the metamagnetic transition occurs at a magnetic field H_m such that $k_B T_{\chi max} = g_{eff}\mu_B H_m$. Figure 2.15 shows the relation of H_m vs $T_{\chi max}$ in cerium and uranium compounds.[1)]

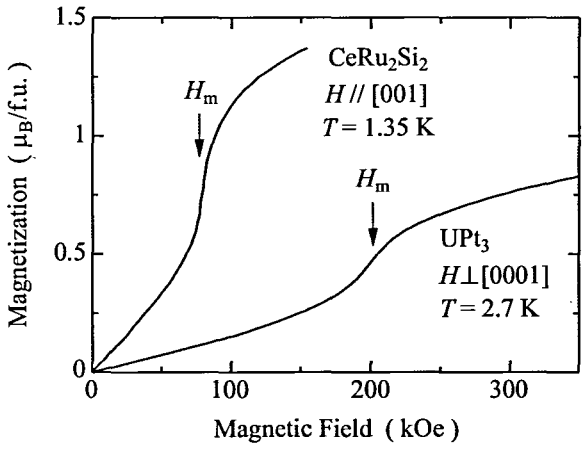

Fig. 2.14 Magnetization curves in typical heavy fermion compounds $CeRu_2Si_2$ and UPt_3, cited from refs. 37 and 48

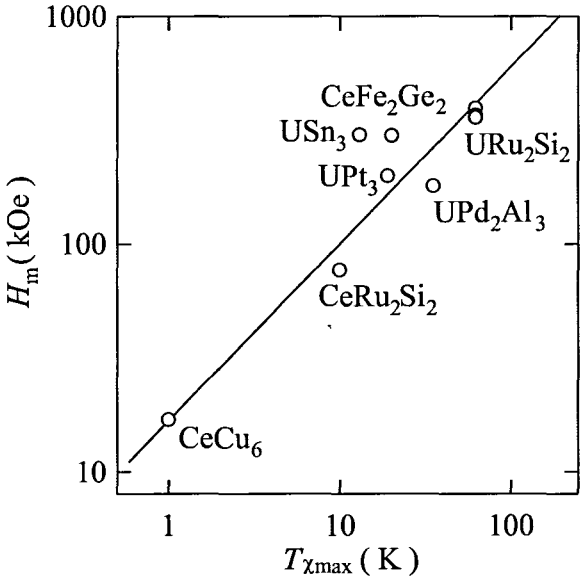

Fig. 2.15 H_m vs $T_{\chi max}$ in heavy fermions of cerium and uranium compounds, cited from ref. 1.

2.4 Fermi surface properties

Fermi surface studies are very important because the ground-state properties of the electronic state are clarified.[13] As mentioned in Sec. 2.2, the ground state of the Ce compounds is mainly determined by the competition between the RKKY interaction and the Kondo effect (see Fig. 2.9). When T_{RKKY} overcomes T_{K}, the ground state is the magnetic ordered one, and $4f$ electron is regarded as localized. On the other hand, when the Kondo effect is dominant, the ground state is the non-magnetic one, and the $4f$ electrons become itinerant.

In the $4f$-localized system, the Fermi surface is similar to that of corresponding La compound, but the presence of $4f$ electrons alters the Fermi surface through the $4f$-electron contribution to the crystal potential and through the introduction of new Brillouin zone boundaries and magnetic energy gaps which occur when $4f$-electron moments order. The latter effect may be approximated by a band-folding procedure where the paramagnetic Fermi surface is folded into a smaller Brillouin zone based on the magnetic unit cell, because the magnetic unit cell is larger than the chemical one. If the magnetic energy gaps associated with the magnetic structure are small enough, conduction electrons undergoing cyclotron motion in the presence of magnetic field can tunnel through these gaps and circulate the orbit on the paramagnetic Fermi surface. If this magnetic breakthrough (breakdown) effect occurs, the paramagnetic Fermi surface might be observed in the de Haas-van Alphen (dHvA) effect even in the presence of magnetic ordering.

For Kondo lattice compounds with magnetic ordering, the Kondo effect is expected to have minor influence on the topology of the Fermi surface, representing that the Fermi surfaces of the Ce compounds are roughly similar to those of the corresponding La compounds, but are altered by the magnetic Brillouin zone boundaries mentioned above. Nevertheless, the effective masses of the conduction carriers are extremely large compared with those of La compounds, as noted in the case of CeB_6. In this system, a small amount of $4f$ electron most likely contributes to make a sharp density of states at the Fermi energy. Thus, the energy band becomes flat around the Fermi energy, which brings about the large effective mass.

In some cerium compounds such as $CeCu_6$, $CeRu_2Si_2$, CeNi and $CeSn_3$, the magnetic susceptibility follows the Curie-Weiss law with a moment of Ce^{3+}, $2.54\,\mu_{\mathrm{B}}/\mathrm{Ce}$, has a maximum at a characteristic temperature $T_{\chi\mathrm{max}}$, and becomes constant at lower temperatures (see Fig. 2.10). This characteristic temperature $T_{\chi\mathrm{max}}$ corresponds to the Kondo temperature T_{K} as mentioned in Sec. 2.2. A characteristic peak in the susceptibility is a crossover from the localized $4f$ electron to the itinerant one. The Fermi surface below $T_{\chi\mathrm{max}}$ is thus highly different from that of the corresponding La compound. The cyclotron mass is also extremely large, reflecting a large γ-value of $\gamma \simeq 10^4/T_{\mathrm{K}}\,(\mathrm{mJ/K^2{\cdot}mol})$ based on eq. (2.29). The cerium compounds are thus classified as either the localized electron system or the itinerant electron system.

The electronic states in Ce, Yb and U compounds can be tuned by applying pressure P and/or magnetic field H. The Néel temperature in the Ce compounds becomes a guiding

parameter to tune the electronic state under pressure. The quantum critical point is therefore defined as the electronic state at which the Néel temperature becomes zero at the critical pressure P_c: $T_N \to 0$ at $P \to P_c$. We clarified the Fermi surface properties as a function of pressure, especially at P_c, for three typical antiferromagnets of $CeRh_2Si_2$, $CeIn_3$ and $CeRhIn_5$[12]. The following are the experimental results of $CeRhIn_5$.

The dHvA results for an antiferromagnet $CeRhIn_5$ were studied under pressure in comparison with those of a non-$4f$ reference compound $LaRhIn_5$ and a heavy fermion superconductor $CeCoIn_5$ without magnetic ordering[61–64]. With increasing pressure P, the Néel temperature $T_N = 3.8$ K in $CeRhIn_5$ increases, has a maximum around 1 GPa, and decreases with further increasing pressure, as shown in Fig. 2.16(a). The critical pressure P_c is 2.0 GPa, while a smooth extrapolation indicates $T_N \to 0$ at a pressure of 2.3 - 2.5 GPa. $CeRhIn_5$ reveals superconductivity over a wide pressure region from 1.6 to 5.2 GPa. Its transition temperature T_{sc} has a maximum around 2.3 - 2.5 GPa, with $T_{sc} = 2.2$ K. From the NQR and specific heat experiments[64-67], together with the dHvA experiment[61] shown below, the critical pressure is P_c $(H = 0) \simeq 2.0$ GPa at zero field, whereas P_c $(H \neq 0) = 2.4$ - 2.5 GPa in magnetic fields, as shown in Fig. 2.16(b).

To elucidate a change of the Fermi surface properties under pressure, the pressure dependences of the dHvA frequency and the cyclotron mass were studied, as shown in Figs. 2.16(d) and 2.16(g)[61]. The dHvA frequencies for the main dHvA branches named β_2, α_1, and $\alpha_{2,3}$ are approximately unchanged up to about 2.3 GPa.[61] These branches, however, disappear completely at $P_c(H \neq 0) \simeq 2.4$ GPa. New branch α_3 appears abruptly at 2.4 GPa, together with appearance of branches α_1 and α_2 at higher pressures.

The detected dHvA branches of $CeRhIn_5$ at ambient pressure and below 2.3 GPa, as shown in Fig. 2.16(d), are well explained by the experimental dHvA branches in a non-$4f$ reference compound $LaRhIn_5$ and the result of energy band calculations for $LaRhIn_5$, as shown in Figs. 2.16(c) and 2.16(f)[62]. The corresponding topologies of the main Fermi surfaces in $CeRhIn_5$ are nearly cylindrical and are found to be approximately the same as those in $LaRhIn_5$, indicating that the $4f$ electron in $CeRhIn_5$ is localized and does not contribute to the volume of the Fermi surfaces.

Above $P_c(H \neq 0) \simeq 2.4$ GPa, the detected dHvA frequencies change abruptly in magnitude, but correspond to those in $CeCoIn_5$, as shown in Fig. 2.16(e). The main Fermi surfaces in $CeCoIn_5$, as shown in Fig. 2.16(h), are also nearly cylindrical. The topologies of two kinds of cylindrical electron Fermi surfaces in $CeCoIn_5$ are similar to those in $LaRhIn_5$($CeRhIn_5$), but the Fermi surfaces of $CeCoIn_5$ are larger than those of $LaRhIn_5$ in volume. The detected dHvA branches in $CeCoIn_5$ are consistent with the $4f$-itinerant band model[63]. This is because one $4f$ electron in each Ce site in $CeCoIn_5$ becomes a valence electron and contributes to the conduction electrons. The contribution of the $4f$ electron to the density of states at the Fermi energy is about 70%. The corresponding cyclotron masses of 5-87 m_0 in $CeCoIn_5$ are extremely large.

As shown in Fig. 2.16(g), the cyclotron masses of the main branches β_2 and $\alpha_{2,3}$ increase rapidly above 1.6 GPa, where superconductivity sets in: 5.5 m_0 at ambient pressure, 20 m_0 at 1.6 GPa, and 60 m_0 at 2.2 GPa for branch β_2. On the other hand, the cyclotron mass of the new branch α_3, which was observed above 2.4 GPa, decreases slightly with

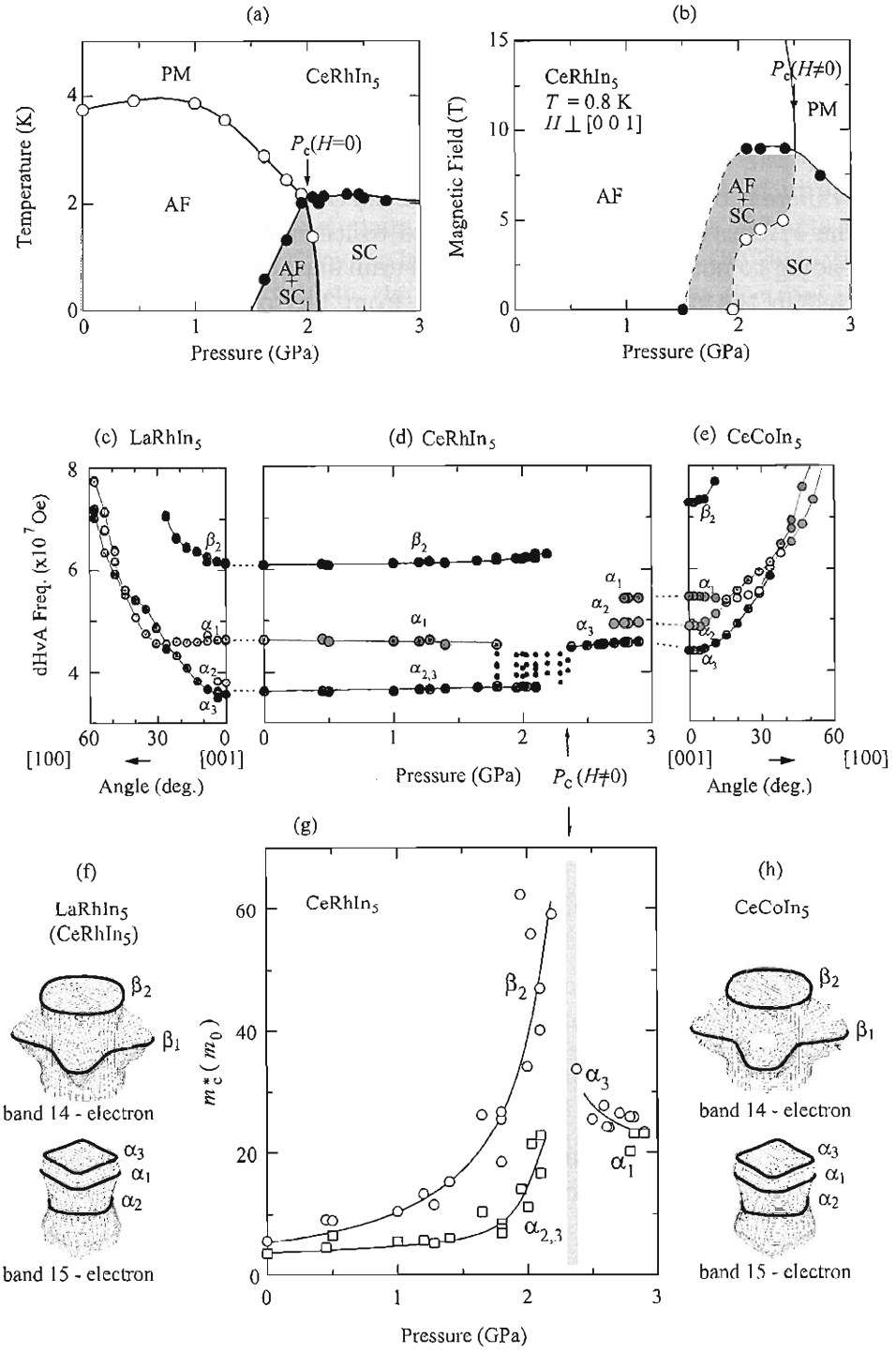

Fig. 2.16 (a) Pressure vs temperature phase diagram, and (b) pressure vs magnetic field phase diagram for $H \perp [001]$ in $CeRhIn_5$, (c) angular dependence of the dHvA frequency in $LaRhIn_5$, (d) pressure dependence of the dHvA frequency for $H \parallel [001]$ in $CeRhIn_5$, and (e) angular dependence of the dHvA frequency in $CeCoIn_5$, (f) Fermi surfaces of $LaRhIn_5$, (g) pressure dependence of the cyclotron mass m_c^* for $H \parallel [001]$ in $CeRhIn_5$, and (h) Fermi surfaces of $CeCoIn_5$, cited from refs. 61–66.

increasing pressure: about $30\,m_0$ at 2.4 GPa and $24\,m_0$ at 2.9 GPa. Branch β_2 was, however, not detected above 2.4 GPa. This is mainly due to a large cyclotron effective mass close to $100\,m_0$.

From these experimental results, the critical pressure under magnetic fields is determined as $P_c(H \neq 0) \simeq 2.4$ GPa. The corresponding topology of the Fermi surface is, thus, found to be different between $P < P_c(H \neq 0)$ ($\simeq 2.4$ GPa) and $P > P_c(H \neq 0)$. A marked change in the $4f$-electron nature from localized to itinerant is realized at $P_c(H \neq 0)$ ($\simeq$ 2.4 GPa), leading to noticeable changes in the Fermi surfaces. Superconductivity is, however, observed in the pressure region ranging from 1.6 to 5.2 GPa. It is important to emphasize that the cyclotron masses are extremely large in this pressure region, forming a heavy fermion state. The similar first-order phase transition was studied from a viewpoint of Fermi surface properties for $CeRh_2Si_2$ and $CeIn_3$[12,68–70].

2.5 Superconductivity

The microscopic theory of superconductivity, which was provided by Bardeen, Cooper and Schrieffer in 1957, is based on a following idea.[71] When an attractive interaction between fermions is present, the stable ground state is no longer the degenerated Fermi gas but becomes a coherent state in which the electrons are combined into pairs of spin-singlet with zero total momentum (Cooper pairs). A conduction electron attracts the positive ion and distorts the lattice by moving in the lattice, and then the distortion attracts another conduction electron. Namely, the interaction between two electrons mediated by the phonon forms the Cooper pair of the electrons. Since an excited energy of BCS type superconductor has an isotropic superconducting gap Δ, namely the superconducting energy gap is opened over the entire of the Fermi surface, the temperature dependence of physical quantities obeys the exponential law theoretically ($T^{-3/2}e^{-\Delta/k_{\rm B}T}$).

It is difficult to express superconductivity for the compounds which have heavy quasi-particles located adjacent to the quantum critical point by the attraction mediated the phonon because of strongly Coulomb repulsion. It have been found the heavy fermion superconductor located adjacent to the quantum critical point. This superconductor does not obeys the exponential law of the temperature but obey the power law. We explain the present unconventional (anisotropic) superconductivity.

Anisotropic superconductivity

Heavy fermion superconductors are, however, well known to show the power law in physical properties such as the electronic specific heat $C_{\rm e}$ and the nuclear spin-lattice relaxation rate $1/T_1$, not indicating an exponential dependence predicted by the BCS theory, namely :

$$C_{\rm e} = \begin{cases} T^3 & \text{(axialtype, pointnode)} \\ T^2 & \text{(polartype, linenode)} \\ T & \text{(gapless)} \end{cases} \tag{2.36}$$

$$\frac{1}{T_1} = \begin{cases} T^5 & \text{(axialtype, pointnode)} \\ T^3 & \text{(polartype, linenode)} \\ T & \text{(gapless)} \end{cases} \tag{2.37}$$

This indicates the existence of an anisotropic gap, namely existence of a node in the energy gap. When we compare the phonon-mediated attractive interaction based on the BCS theory to the strong repulsive interaction among the f electrons, it is theoretically difficult for the former interaction to overcome the latter one. To avoid a large overlap of the wave functions of the paired particles, the heavy electron system would rather choose an anisotropic channel, like a p-wave spin triplet or a d-wave spin singlet state, to form Cooper pairs.

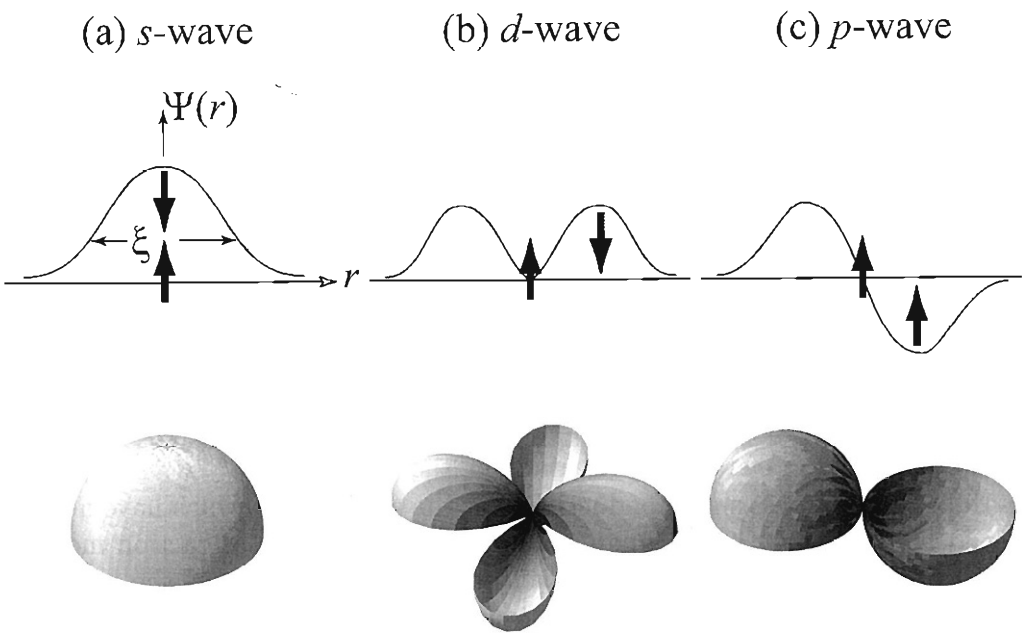

Fig. 2.17 Schematic view of the superconducting parameter with the s-, d- and p-wave pairing, cited from ref. 14.

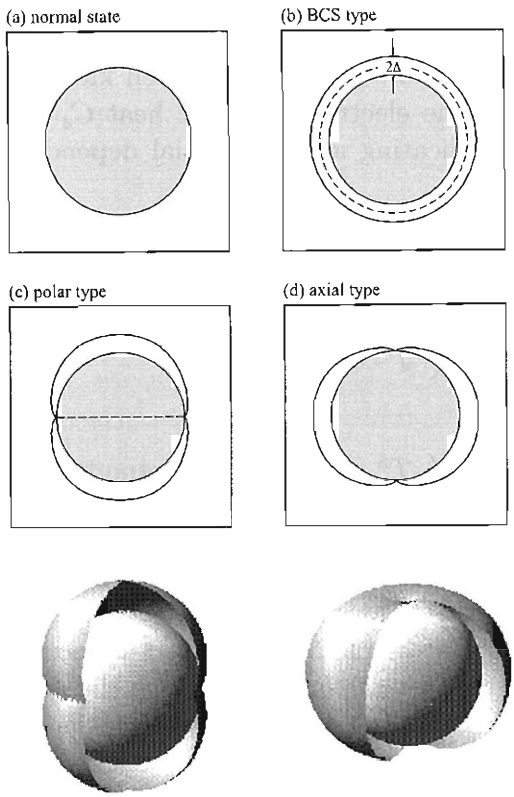

Fig. 2.18 Schematic picture of the gap structures: (a) normal state, (b) BCS-type superconductor, which has an isotropic gap, (c) polar type and (d) axial type, cited from ref. 14.

Figure 2.17 shows a schematic view of the superconducting parameter with the s-, d- and p-wave pairing. The order parameter $\Psi(\boldsymbol{r})$ with the even parity (s- and d-wave) is symmetric with respect to $\boldsymbol{r}$, where one electron with the up-spin state of the Cooper pair is simply considered to be located at the center of $\Psi(\boldsymbol{r})$, $\boldsymbol{r} = 0$, and the other electron with the down-spin state is located at $\boldsymbol{r}$. The width of $\Psi(\boldsymbol{r})$ with respect to $\boldsymbol{r}$ is called the coherence length ξ. For example, UPd_2Al_3 is consider to be a d-wave superconductor from the NMR Knight shift experiment,[72] which corresponds to the case (b) in Fig. 2.17. On the other hand, $\Psi(\boldsymbol{r})$ with odd parity (p-wave) is not symmetric with respect to $\boldsymbol{r}$, where the parallel spin state is shown in Fig. 2.17(c). From the NMR Knight shift experiment, UPt_3 is considered to possess odd parity in symmetry.[73]

For an anisotropic state, there are three kinds of gap structures, as shown in Fig. 2.18. First one indicates the superconducting gap, which is the same as the s-wave and is isotropic. This is called the Balian-Werthamer (BW) state. Second one shows a line node in the equator on the Fermi surface. This structure is called the polar type, as shown in Fig. 2.18(c). Third one has a point node in the pole on the Fermi surface. This condition has the Anderson-Brinkman-Morel (ABM) state. This is called the axial type, as shown in Fig. 2.18(d).

Pressure-induced superconductivity

The study of unconventional superconductivity is still active in condensed matter physics, ever since the discovery of the first heavy fermion superconductor, $CeCu_2Si_2$.[4] Recently, some Ce-based heavy fermion compounds were found to exhibit superconducting under pressure, as shown in Fig. 2.19 for $CeIn_3$.[74] In these compounds, superconductivity appears around the quantum critical point. The similar pressure-induced superconductivity was also reported for the other Ce-based compounds such as $CeCu_2Ge_2$[75] and $CeRh_2Si_2$.[76,77] In these compounds, the attractive force between quasiparticles are possible to be magnetically mediated, not to be phonon-mediated.

$CeCu_2Si_2$ is a superconductor with the transition temperature $T_{sc} = 0.7\,\mathrm{K}$ at ambient pressure. When pressure is applied, T_{sc} initially remains close to its ambient pressure value but shows a sudden increase of $T_{sc} = 2\,\mathrm{K}$ at about 3 GPa.[79] This strange superconducting phase was also observed in a pressure-induced superconductor $CeCu_2Ge_2$.[75] According to the report by Holmes *et al.*,[78] these anomalies can be linked with an abrupt change of the Ce valence, and suggested a second quantum critical point at a pressure P_v, where critical valence fluctuations provide the superconducting pairing mechanism, which is compared with superconducting pair mechanism based on spin fluctuations at ambient pressure in $CeCu_2Si_2$ or at 10 GPa in $CeCu_2Ge_2$, as shown in Fig. 2.20. Figure 2.20 shows the temperature-pressure phase diagram for $CeCu_2Si_2$ and $CeCu_2Ge_2$ showing the two critical pressures P_c and P_v.

Superconductivity in the non-centrosymmetric crystal structure

Recently, it has been reported that $CePt_3Si$ is the first heavy fermion superconductor lacking a center of inversion symmetry in the tetragonal structure, where the

upper critical field $H_{c2} = 50\,\mathrm{kOe}$ exceeds the Pauli paramagnetic limiting field $H_p = 10\,\mathrm{kOe}$,[7] and the spin relaxation rate of ^{195}Pt-NMR indicated a clear peak structure just below the superconducting transition temperature $T_{sc} = 0.75\,\mathrm{K}$.[80] Subsequently, Akazawa *et al.* found pressure-induced superconductivity in a ferromagnet UIr with the monoclinic structure,[81,82] which also lacks inversion symmetry in the crystal structure. In addition, Kimura *et al.* reported pressure-induced superconductivity in an antiferromagnet $CeRhSi_3$, which crystallizes in the tetragonal crystal structure without inversion symmetry.[8,9,47] Moreover, similar superconducting properties are observed in $CeIrSi_3$[10–12] and $CeCoGe_3$.[83]

The experimental technique of NQR/NMR has proved to be a useful tool to determine the symmetry of the superconducting condensate. For example, UPt_3 was shown to be the first case of odd-parity (p- or f-wave type) superconductivity,[73] while even-parity (d-wave type) superconductivity is realized in UPd_2Al_3.[72] For the study of these superconductors, it was assumed that the crystal structure has an inversion center, which makes it possible to consider separately the even (spin-singlet) and odd (spin-triplet) components of the superconducting order parameter. When inversion symmetry is absent in the crystal structure, such classification for superconductivity is no longer possible. The order parameter contains not only a spin-singlet part, but also an admixture of a spin-triplet state.[84]

In this section, the characteristic features of superconductivity, which is realized in

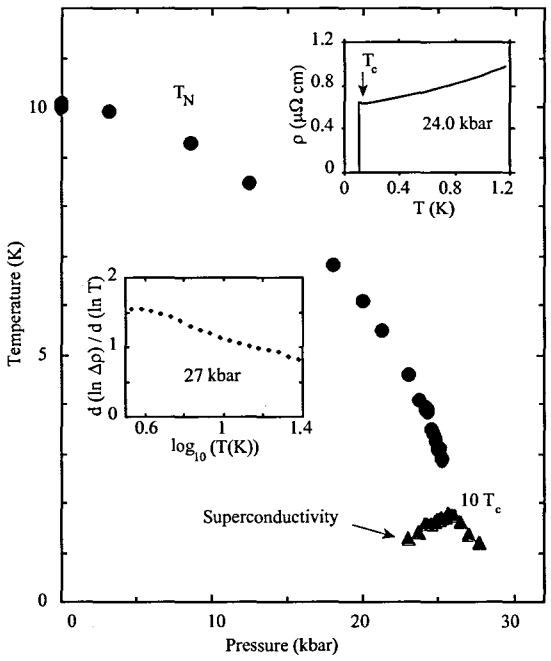

Fig. 2.19 Pressure phase diagram in $CeIn_3$. Superconductivity is observed below T_{sc} in a narrow window where the Néel temperature T_N tends to zero, cited from ref. 74.

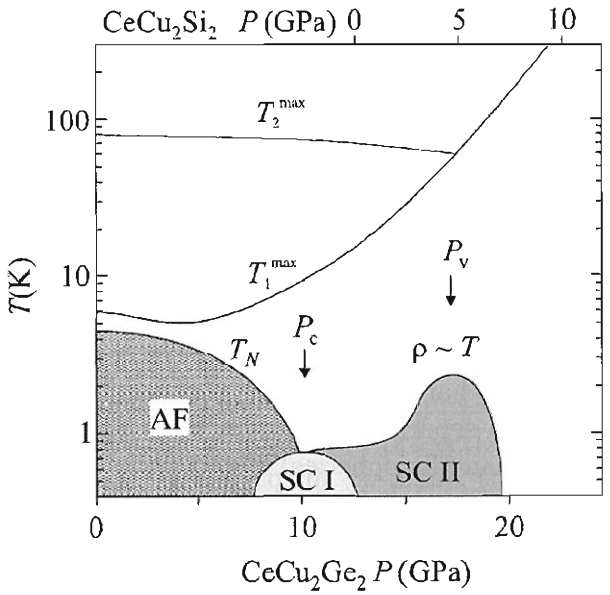

Fig. 2.20 Schematic temperature-pressure phase diagram of $CeCu_2Si_2$ and $CeCu_2Ge_2$. Superconductivity is observed in a wide window, cited from ref. 78.

a non-centrosymmetric crystal, are explained on the basis of the recently reported theoretical studies. When the crystal structure lacks inversion symmetry, the Fermi surface splits into two Fermi surfaces due to the Rashba-type antisymmetric spin-orbit interaction.[85] Here, the effect of spin-splitting of the Fermi surface via the antisymmetric spin-orbit interaction is discussed from the viewpoint of the conduction electrons in the non-centrosymmetric tetragonal crystal structure. The spin-orbit interaction for the conduction electrons can be calculated by considering the following effective single-band Hamiltonian with the Rashba-type spin-orbit interaction:[85]

$$\mathcal{H} = \frac{\boldsymbol{p}^2}{2m^*} + \alpha(\boldsymbol{p} \times \boldsymbol{n}) \cdot \boldsymbol{\sigma}, \tag{2.38}$$

where α denotes the strength of the spin-orbit coupling, $\boldsymbol{p}$ is a momentum of conduction electrons, $\boldsymbol{n}$ is a unit vector taken to be parallel to the z-axis or the c-axis (the [001] direction), $\boldsymbol{\sigma}$ is the Pauli matrices, and the m^* is the effective mass. The term $\alpha(\boldsymbol{p} \times \boldsymbol{n}) \cdot \boldsymbol{\sigma}$ is explained as follows. The non-uniform lattice potential $V(\boldsymbol{r})$ in the tetragonal crystal structure induces the electric field $(-\nabla V(\boldsymbol{r}))$ along the [001] direction. The effective magnetic field, which approximately corresponds to $\boldsymbol{p} \times \nabla V$, namely $\alpha(\boldsymbol{p} \times \boldsymbol{n})$ in eq. (2.38) is brought about for moving conduction electrons with the momentum $\boldsymbol{p}$ in this electric field. The term $\alpha\ (\boldsymbol{p} \times \boldsymbol{n}) \cdot \boldsymbol{\sigma}$ is regarded as a Zeeman energy arising from the magnetic interaction between this effective magnetic field and spins of the conduction electrons.

By diagonalizing this Hamiltonian, the following two energies, which correspond to

two separated energy bands, are obtained:

$$\epsilon_{p\pm} = \frac{p^2}{2m^*} \mp \alpha p_\perp, \tag{2.39}$$

where $p_\perp = \sqrt{p_x^2 + p_y^2}$ is the component of the moment $\boldsymbol{p}$ normal to $\boldsymbol{n}$. A simple example of the Fermi surface splitting due to the Rashba-type spin-orbit interaction with ∇V parallel to the z-axis is shown in Fig. 2.21. Note that in Fig. 2.21 the spin quantization axis is chosen along $\boldsymbol{p} \times \boldsymbol{n}$. The degenerate spherical Fermi surface splits into two sheets, namely up-spin and down-spin bands, except for high-symmetry line $\boldsymbol{p} \parallel z$, as shown in Fig. 2.21(a). One of the two separated Fermi surfaces has a smaller volume and the other has a larger volume than the spherical Fermi surface, as shown in Fig. 2.21(b). Arrows indicate spins on the Fermi surfaces for the up-spin and down-spin bands. An important point is that a conduction electron with a momentum $\boldsymbol{p}$ and an up-spin state and another conduction electron with a momentum $-\boldsymbol{p}$ and an up-spin state belong to two different Fermi surfaces, which are separated by $2|\alpha p_\perp|$. A simple p-wave pairing is thus prohibited because $|\alpha p_\perp|$ is about 10 - 1000 K, shown later experimentally, which is much larger than the superconducting energy gap of a few Kelvin. On one of the spin-orbit split Fermi surfaces, namely the (+)-band in Fig. 2.21, the Cooper pair between electrons with momentum p, spin $\uparrow$ and momentum $-p$, spin $\downarrow$ is formed. This state, denoted as $|p,\uparrow\rangle|-p,\downarrow\rangle$, is *not* a spin singlet state, because the counterpart of this state $|p',\downarrow\rangle|-p',\uparrow\rangle$ is formed on another Fermi surface and thus the superposition between these two states is not possible.[86] Actually, the pairing state $|p,\uparrow\rangle|-p,\downarrow\rangle$ and $|p,\downarrow\rangle|-p,\uparrow\rangle$ are the admixture of spin singlet and triplet states, as easily verified by

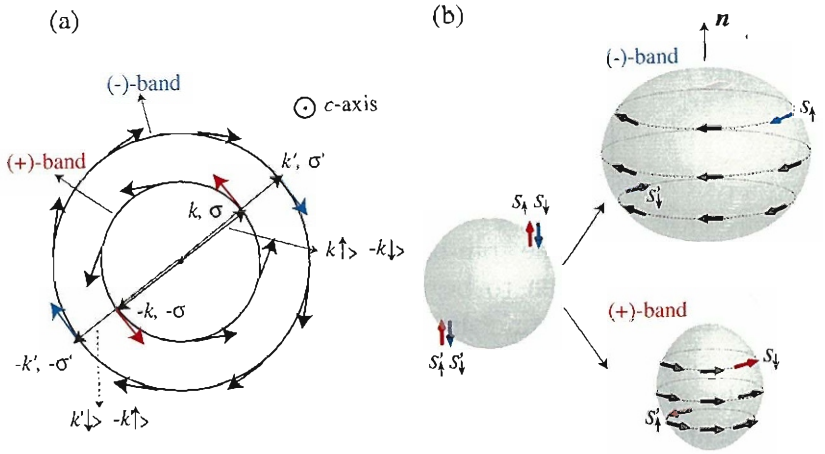

Fig. 2.21 Two separated (a) energy bands and (b) Fermi surfaces in the non-centrosymmetric crystal structure, cited from ref. 87.

$$|\boldsymbol{p},\uparrow\rangle|-\boldsymbol{p},\downarrow\rangle = \frac{1}{2}(|\boldsymbol{p},\uparrow\rangle|-\boldsymbol{p},\downarrow\rangle - |\boldsymbol{p},\downarrow\rangle|-\boldsymbol{p},\uparrow\rangle) \quad \text{(singlet)}$$
$$+\frac{1}{2}(|\boldsymbol{p},\uparrow\rangle|-\boldsymbol{p},\downarrow\rangle + |\boldsymbol{p},\downarrow\rangle|-\boldsymbol{p},\uparrow\rangle) \quad \text{(triplet)}$$

$$|\boldsymbol{p}',\downarrow\rangle|-\boldsymbol{p}',\uparrow\rangle = \frac{1}{2}(|\boldsymbol{p},\uparrow\rangle|-\boldsymbol{p},\downarrow\rangle - |\boldsymbol{p},\downarrow\rangle|-\boldsymbol{p},\uparrow\rangle) \quad \text{(singlet)}$$
$$+\frac{1}{2}(|\boldsymbol{p},\uparrow\rangle|-\boldsymbol{p},\downarrow\rangle + |\boldsymbol{p},\downarrow\rangle|-\boldsymbol{p},\uparrow\rangle) \quad \text{(triplet)}$$

The first and second terms of the right-hand side express a spin singlet state and a spin triplet state, respectively, with the in-plane spin projection S_{inplane} equal to 0. Since we take the spin quantization axis parallel to the xy-plane, this triplet state corresponds to the $S_z = \pm 1$ state for the spin quantization axis along the z-direction. This means that the $\boldsymbol{d}$-vector of the triplet component is parallel to the plane. The above explanation is also applicable to general cases with more complicated form of ∇V. This unique superconducting state exhibits various interesting electromagnetic properties as extensively argued by many authors.[84,86,88–100] Frigeri *et al.* also proposed the possible existence of spin-triplet pairing state in the non-centrosymmetric crystal, where the inversion symmetry breaking in the presence of a spin-orbit interaction was introduced on the basis of the Rashba model.[99,100] It was clarified that, in contrast to a common belief, the spin-triplet pairing state is not entirely excluded in such systems. The favorable pairing state for the triplet state is of the p-wave type. The $\boldsymbol{d}$ vector, which is characteristic of the spin-triplet superconductivity, is parallel to $\boldsymbol{p}_\perp$: $\boldsymbol{d}(\boldsymbol{k}) = \Delta(\hat{\boldsymbol{x}}k_y - \hat{\boldsymbol{y}}k_x)$, and the order parameter becomes a admixture of spin-singlet and spin-triplet components.

Next we show a theoretically suggested superconducting gap for the non-centrosymmetric superconductor with the Rashba-type spin-orbit coupling. Here we consider a two-component order parameter with spin-singlet and spin-triplet components as follows:

$$\Delta(\boldsymbol{k}) = \{\Psi(\boldsymbol{k})\sigma_0 + \boldsymbol{d}(\boldsymbol{k})\cdot\boldsymbol{\sigma}\}\cdot i\sigma_y, \tag{2.40}$$

where $\Psi(\boldsymbol{k})$ is the spin-singlet component, $\boldsymbol{d}(\boldsymbol{k}) = \Delta(-k_x,k_y,0)$ is the d-vector which characterizes a spin-triplet component, $\boldsymbol{\sigma}$ is the Pauli matrices and σ_0 is the unit matrix. The theoretical calculation by Hayashi *et al.*[95,96] has shown that the superconducting energy gap is different on the separated two Fermi surfaces and is expresses by

$$\Delta(\theta) = |\Psi \pm \Delta\sin\theta|. \tag{2.41}$$

Figure 2.22 shows the schematic structures of the superconducting energy gap on the separated Fermi surfaces. Here, the superconducting energy gap on the S_+-Fermi surface has the shape of s-wave (the equivalent gap) + p-wave (the axial type) and is nodeless. On the other hand, line nodes appear in the superconducting energy gap on the S_--Fermi surface, leading to the low-temperature power law behavior of $1/T_1$[80] and the specific heat divided by temperature C/T in $CePt_3Si$.[101]

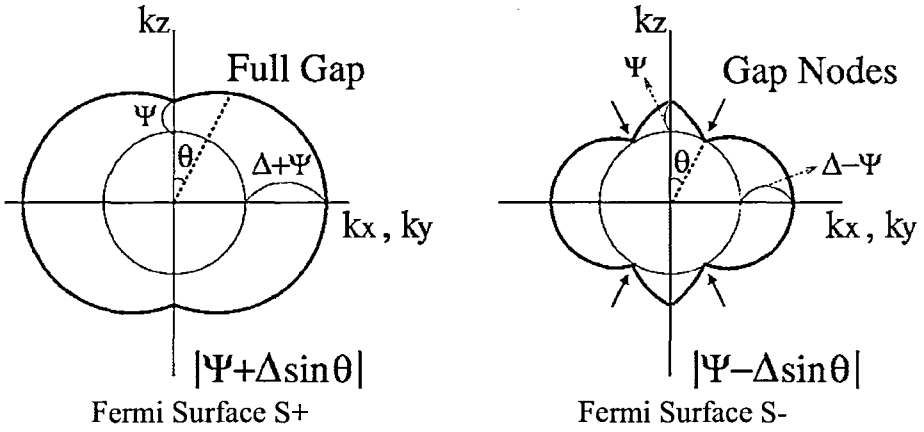

Fig. 2.22 Gap structures on the Fermi surface, cited from refs. 95 and 96.

Next we discuss the effect of the magnetic field on the superconducting state. Principally, there are two mechanisms, by which a magnetic field interacts with the electrons in the superconducting state. Both mechanisms are pair breaking and lead to the destruction of the superconducting state at a critical magnetic field, H_{c2}. These mechanisms are as follows.

Orbital pair breaking

This is due to an interaction of the magnetic field with the orbital motion of the electrons and described by the term $(e/m)(\boldsymbol{p} \cdot \boldsymbol{A})$, where $\boldsymbol{A}$ is the vector potential. This term corresponds to the Lorentz force. This is theoretically discussed by Werthamer, Helfand, and Hohenberg (so-called WHH)[102], shown later.

Pauli limiting

This comes from an interaction with the spins of electrons and is described by $g_J \mu_B \boldsymbol{S} \cdot \boldsymbol{H}$. This is discussed theoretically by Clogston shown later.[103]

Orbital pair breaking takes place in all the superconducting states, both conventional and unconventional ones. For small magnetic fields, this is the only important pair breaking mechanism due to the external field. Therefore, it determines the initial slope of H_{c2} at T_{sc}. The critical field determined only by orbital pair breaking is defined as orbital critical field H^*_{c2}, in the absence of any other pair breaking effect. The upper critical field at $T = 0\,\mathrm{K}$ varies between $H^*_{c2} = -0.693\,(\mathrm{d}H^*_{c2}/\mathrm{d}T) \cdot T_{sc}$ for a conventional superconductor in the dirty limit and $H^*_{c2} = -0.850\,(\mathrm{d}H^*_{c2}/\mathrm{d}T) \cdot T_{sc}$ for a polar triplet state. Because of the similarity of the upper critical fields, one can hardly make any statements about the order parameter for a superconductor just based on an analysis of

H_{c2}^{*}. The discussion of the critical field is, therefore, concentrated on the second pair breaking mechanism, Pauli limiting.

The influence of the magnetic field on the spins of the electrons in the superconducting states has first been reported by Clogston[103] and by Chandrasekhar.[104] The physical reason for this mechanism is that, in a conventional superconductor, the Cooper pairs have a total spin $S = 0$. Therefore, the spin susceptibility is $\chi_s = 0$ (s-wave state). For this reason, the normal state becomes energetically more favorable for the system when the magnetic energy $\frac{1}{2}\chi_n H^2$ of the normal state reaches the condensation energy $\frac{H_c^2}{8\pi}$ of the superconductor. In a BCS superconductor, this gives rise to an upper limit of $H_{c2}(0)$. This field is called Pauli limiting field and expressed as $H_p = 1.857 \times 10^4 T_{sc}$ (Oe). Pauli limiting occurs also in all other superconducting states, in which χ_s is reduced compared with the susceptibility of the normal state χ_n. When the spin susceptibility of the superconducting state χ_s has a substantial value compared with χ_n, the superconducting condensation energy can be expressed by

$$\frac{1}{2}(\chi_n - \chi_s)H_p^2 = \frac{1}{8\pi}H_c^2. \tag{2.42}$$

By using the equations $\chi_n = 2\mu_B^2 D(\epsilon_F)$ and the relation of BCS theory: $\frac{H_c^2}{8\pi} = \frac{1}{2}D(\epsilon_F)\Delta_0^2$, the Pauli limiting field will be expresses as:

$$H_p = \frac{\Delta_0}{\sqrt{2}\sqrt{1 - \chi_s^s(T)/\chi_n^s}\mu_B}. \tag{2.43}$$

In conventional superconductors ($s = 0$ and $\ell = 0$), as in all the unconventional singlet superconductors ($s = 0$, $\ell = 0, 2, 4, \cdots$), the spin susceptibility in the superconducting state $\chi_s = 0$. Therefore, the Pauli limiting is maximum. On the other hand, in some simple triplet state ($s = 1$, $\ell = 1, 3, \cdots$), the z-component of the Cooper pair spins can only be $s_z = \pm 1$. As long as the spin part of the order parameter can rotate freely with respect to orbital part, $\chi_s = \chi_n$ for these equal spin pairing state. In this case, the Pauli limiting does not occur. The order parameter of the equal spin pairing states has an intrinsic anisotropy. An intermediate case between the singlet and the equal spin pairing states has been taken by the Balian-Werthamer (BW) state.[105] It exhibits $\chi_s = \frac{2}{3}\chi_n$ and therefore, shows reduced Pauli limiting.

Next we discuss the spin susceptibility in the non-centrosymmetric superconductor with antisymmetric spin-orbit interaction. Frigeri *et al.* proposed that the Van Vleck term of spin susceptibility χ_s^s in the system without inversion symmetry has a finite value by the strong spin-orbit interaction.[106] Namely, the paramagnetic effect decreases in the spin singlet state.

The spin susceptibility for the singlet s-wave gap function is shown in Fig. 2.23.[106] The left panel shows the temperature dependence of the spin susceptibility for the field along the c-axis ($\chi_{\parallel} = \chi_c$). The middle panel shows the spin susceptibility for the field in the ab-plane ($\chi_{\perp} = \chi_a = \chi_b$) as a function of the temperature for three different values of the spin-orbit coupling α. The susceptibility increases with the spin-orbit coupling

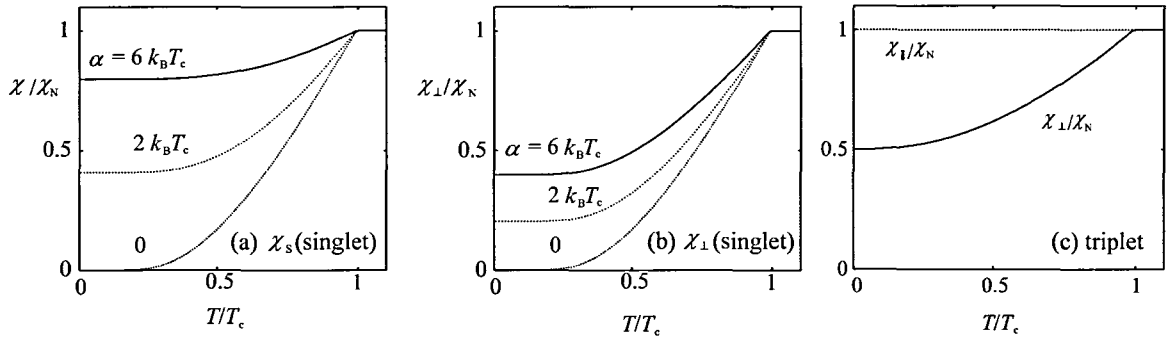

Fig. 2.23 (a), (b) Spin susceptibility in the case of singlet s-wave gap function for $\boldsymbol{g}_{\boldsymbol{k}} \propto (-k_y, k_x, 0)$ ($CePt_3Si$). The spin susceptibility in the ab-plane $\chi_\perp$ and along the c-axis $\chi_\parallel$ as a function of T for three different values of the antisymmetric spin-orbit coupling α. The susceptibility in the superconducting state ($T/T_c < 1$) increases with the spin-orbit coupling strength. The susceptibility is more strongly suppressed in the ab-plane than along the c-axis. At $T = 0$ we have $\chi^s_\perp = \chi^s_\parallel/2$ and (c) Spin susceptibility for a spin-triplet p-wave gap function $\boldsymbol{d}(\boldsymbol{k}) \parallel \boldsymbol{g}_{\boldsymbol{k}} \propto (-k_y, k_x, 0)$ ($CePt_3Si$). The susceptibility is in this case independent of the spin-orbit coupling α. In the superconducting state, the susceptibility in the ab-plane coincides with that of the normal state, cited from ref. 106.

strength. When α becomes very large, the resulting susceptibility looks very similar to that obtained for the triplet p-wave gap function, as shown in the right panel of Fig. 2.23. For the spin-triplet phase, we chose the pairing state $\boldsymbol{d}(\boldsymbol{k}) = \Delta(\hat{\boldsymbol{x}}k_y - \hat{\boldsymbol{y}}k_x)$. Therefore, for the superconducting state in the non-centrosymmetric crystal structure, the similar properties of the spin susceptibilities make it difficult to distinguish between a spin-triplet and spin-singlet order parameter through NMR measurements in the strong spin-orbit coupling limit.

Figure 2.24(a) shows the pressure dependence of the Néel temperature T_N, the superconducting transition temperature T_{sc}, and the upper critical field at 0 K, $H_{c2}(0)$ for $H \parallel [001]$ in $CeIrSi_3$[87,107]. The critical pressure, where the Néel temperature becomes zero, is estimated to be $P_c = 2.25$ GPa. The superconducting transition temperature becomes maximum at about 2.6 GPa, as shown in Fig. 2.24(a). Simultaneously, the jump of the specific heat at T_{sc} in Fig. 2.24(b) becomes extremely large at 2.58 GPa: $\Delta C_{ac}/C_{ac}(T_{sc}) = 5.8$, indicating a strong-coupling superconductor. The upper critical field $H_{c2}(0)$ for $H \parallel [001]$ becomes maximum at $P_c^* = 2.63$ GPa, as shown in Fig. 2.25.

The upper critical field deviates substantially between $H \parallel [001]$ and [110] as shown in Fig. 2.25.[87] The superconducting properties become highly anisotropic: $-dH_{c2}/dT = 170$ kOe/K at $T_{sc} = 1.56$ K, and $H_{c2}(0) \simeq 450$ kOe for $H \parallel [001]$, and $-dH_{c2}/dT = 145$ kOe/K at $T_{sc} = 1.59$ K, and $H_{c2}(0) = 95$ kOe for $H \parallel [110]$ at 2.65 GPa. The upper critical field H_{c2} for $H \parallel [1\,1\,0]$ shows a strong sign of Pauli paramagnetic suppression with decreasing temperature because the orbital limiting field $H_{orb}(= -0.73(dH_{c2}/dT)T_{sc})$ is estimated to be 170 kOe[102], which is larger than $H_{c2}(0) = 95$ kOe for $H \parallel [110]$. On

the other hand, the upper critical field $H \parallel [001]$ is not destroyed by spin polarization based on Zeeman coupling but possesses an upturn curvature below 1 K, as shown later in Fig. 2.25, reflecting a strong-coupling nature of superconductivity. This is because all the spins of conduction electrons are perpendicular to the magnetic field direction of $H \parallel [001]$, as shown in Fig. 2.21(b), revealing that the spin susceptibility for $H \parallel [001]$ is unchanged below T_{sc} in this non-centrosymmetric crystal structure and then the Pauli paramagnetic suppression of H_{c2} is not realized for $H \parallel [001]$. Moreover, the electronic state at P_c^* is found to correspond to an antiferromagnetic quantum critical point from the result of the ^{29}Si-NMR experiment[108].

Furthermore, the low-temperature electrical resistivity under pressures ranging from ambient pressure to 3.00 GPa in magnetic fields, together with the specific heat was precisely measured. From these pressure experiments, the magnetic field vs temperature phase diagram under pressures up to 3.00 GPa was constructed[109], as shown in Fig. 2.26. The present precise experimental results reveal that the antiferromagnetic phase is robust in magnetic fields. In other words, superconductivity in magnetic fields is realized in the antiferromagnetic state. It is also suggested that the H_{c2} value for $H \parallel [001]$ becomes maximum when the antiferromagnetic phase disappears completely in magnetic fields. This pressure corresponds to $P_c^* \simeq 2.63$ GPa, as shown in Figs. 2.26(j) , 2.26(k), and 2.25 where $H_{c2}(0)$ becomes approximately 450 kOe. It is concluded that the magnetic quantum phase transition thus occurs in $CeIrSi_3$ at $P_c^* \simeq 2.63$ GPa, coinciding with a huge H_{c2} value of $H_{c2}(0) \simeq 450$ kOe for $H \parallel [001]$ for a low $T_{sc} = 1.6$ K value. A similar result is also obtained for $CeRhSi_3$[8,9].

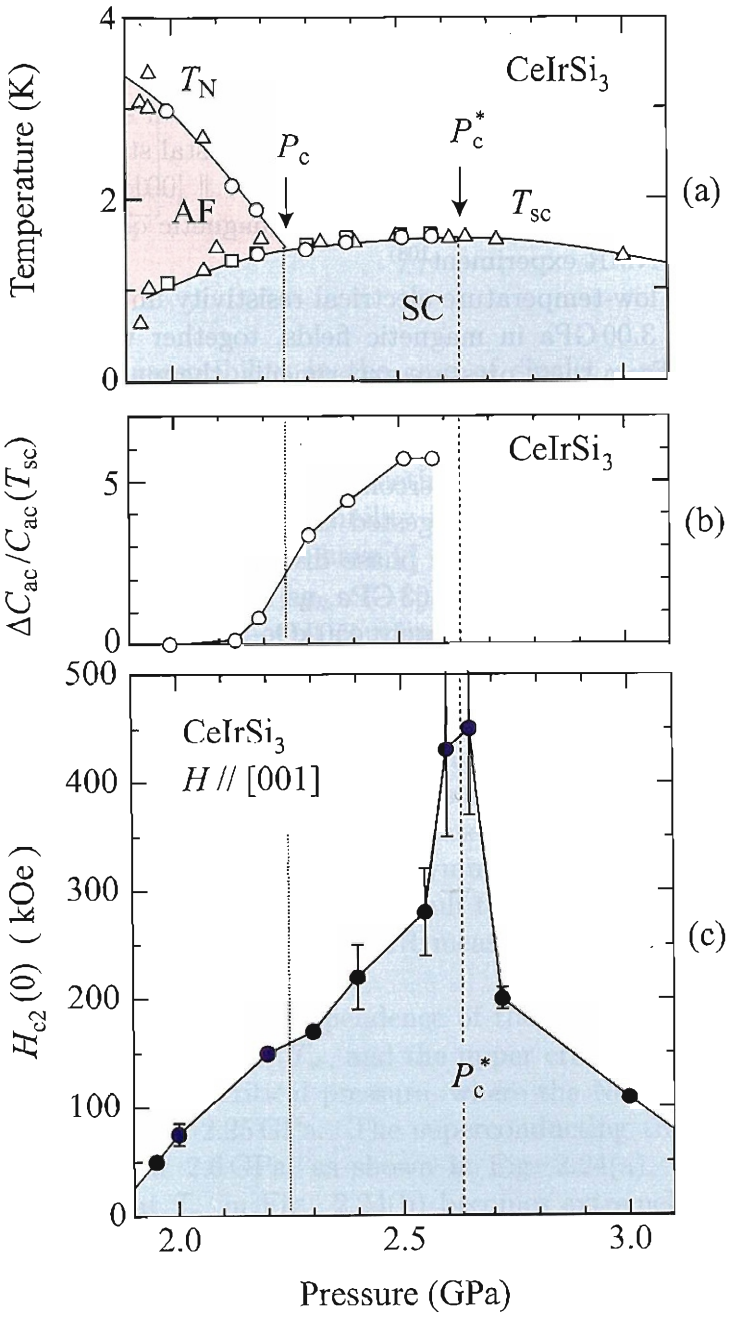

Fig. 2.24 Pressure dependences of (a) the Néel temperature T_N and superconducting transition temperature T_C, (b) specific heat jump $\Delta C_{ac} = C_{ac}(T_C)$, and (c) the upper critical field $H_{c2}(0)$ for $H \parallel [001]$ in $CeIrSi_3$, cited from refs. 87 and 107.

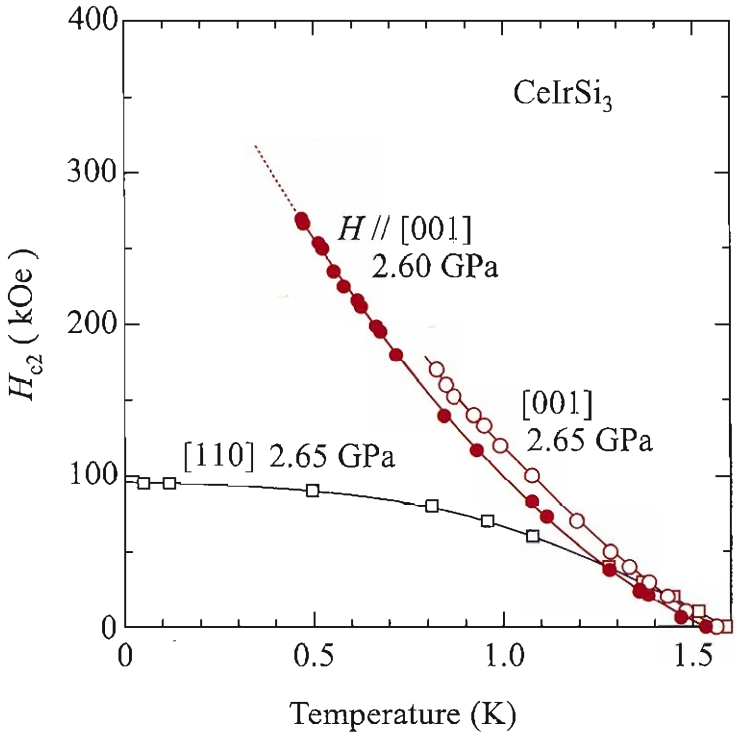

Fig. 2.25 Temperature dependence of upper critical field H_{c2} for magnetic field along [001] at 2.60 GPa, together with those at 2.65 GPa in $CeIrSi_3$, cited from ref. 87.

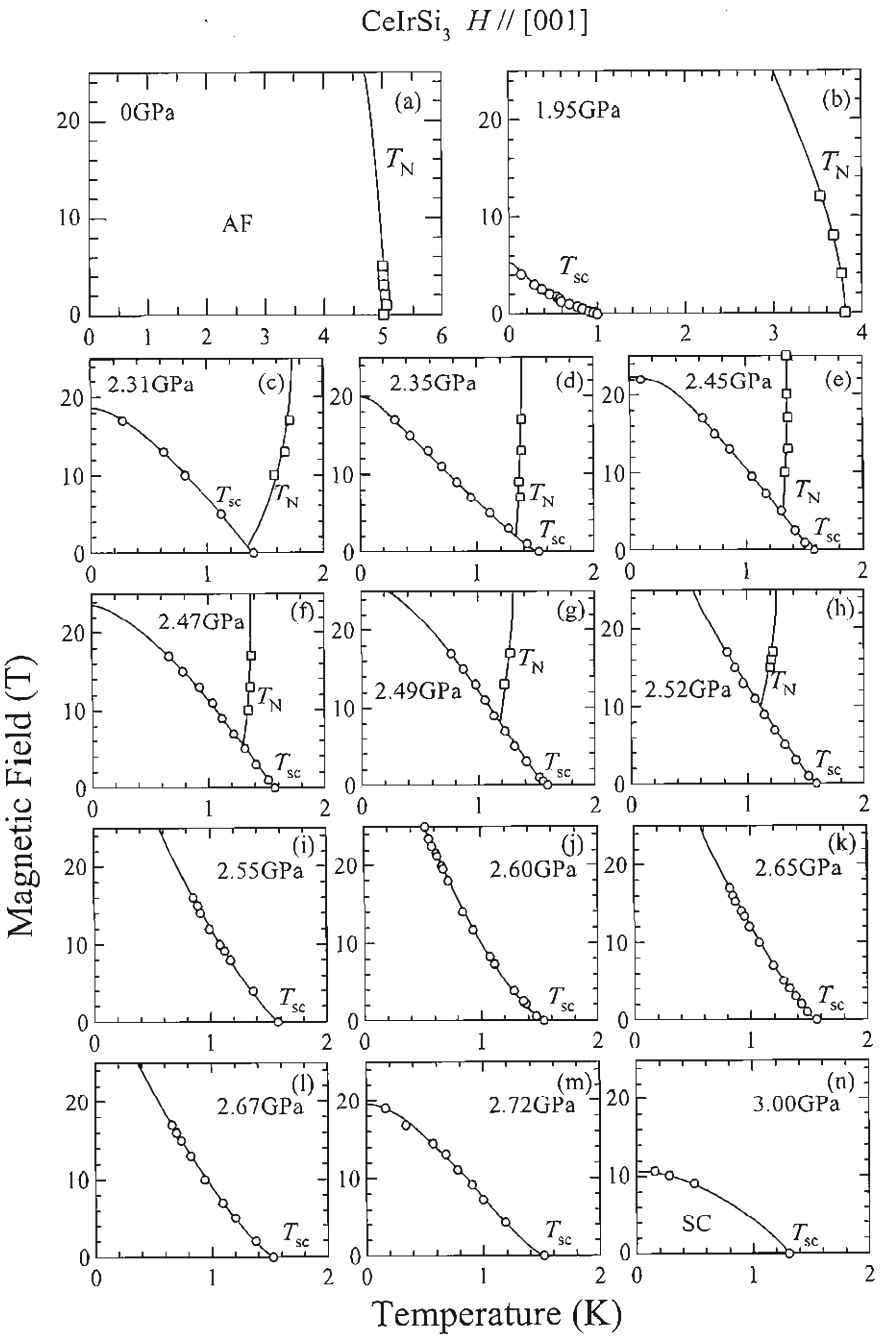

Fig. 2.26 Antiferromagnetic and superconducting phase diagram in magnetic fields along [001] under various pressures in $CeIrSi_3$, cited from ref. 109.

3 Motivation of the Present Study

Various kinds of rare earth and uranium compounds were studied in the present study, following the Doniach phase diagram. This is because the heavy fermions and unconventional superconductivity are realized in the quantum critical region of the Doniach phase diagram. Ce and Yb compounds were especially studied in the rare earth compounds.

In the usual Ce compounds, the magnetic ordering occurs on the basis of the RKKY interaction, as in an antiferromagnet $CeCu_2Ge_2$ with $T_N = 4.2$ K.[110] This is because the ground state is the Kramers doublet in the $4f$ -crystalline electric field (CEF) scheme. This is schematically shown by a dotted line in Fig. 3.1, following a Doniach phase diagram. On the other hand, the Néel temperature is close to zero in a heavy fermion superconductor $CeCu_2Si_2$, via the many-body Kondo effect.[4] This is because the ionic radius of Si is smaller than that of Ge. In fact, the antiferromagnetic state of $CeCu_2Ge_2$ is changed into a superconducting state by applying pressure: $T_N \rightarrow 0$ for $P \rightarrow P_c$ = 8 GPa in $CeCu_2Ge_2$.[4] In other words, typical heavy fermion compounds without magnetic ordering such as $CeCu_6$, $CeCu_2Si_2$ and $CeRu_2Si_2$ are changed into the nonmagnetic electronic state, following a solid line in Fig. 3.1, with decreasing temperature. $CeCu_2Ge_2$ follows a dotted line and orders antiferromagnetically, as mentioned above. In these compounds, the relative linear thermal expansion shrinks monotonically with decreasing temperature.

Yb compounds possess the similar Kramers doublet in the $4f$-CEF scheme and are expected to order magnetically at low temperatures. $YbCu_2Si_2$ with the tetragonal crystal

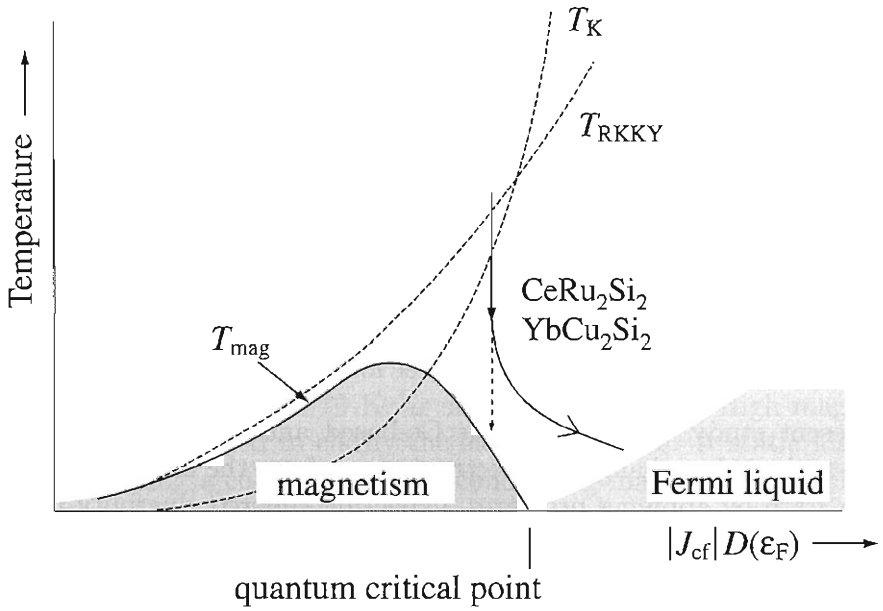

Fig. 3.1 Doniach phase diagram cited from ref. 2.

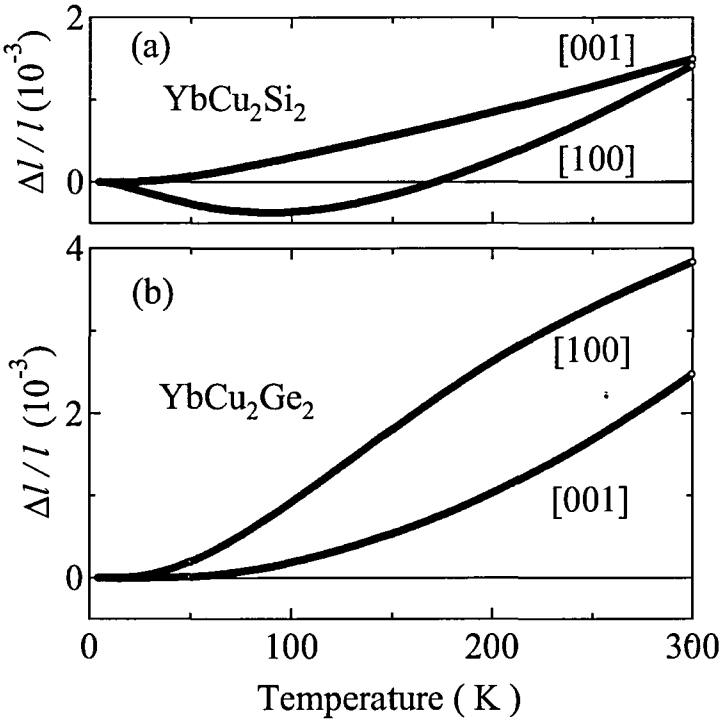

Fig. 3.2 Temperature dependence of thermal expansion for (a) $YbCu_2Si_2$ and (b) $YbCu_2Ge_2$, cited from ref. 3.

structure, however, do not order magnetically. The temperature dependence of the linear thermal expansion is characteristic.[3,111] The relative linear thermal expansion of a Pauli paramagnet $YbCu_2Ge_2$ shrinks monotonically with decreasing temperature, and becomes approximately zero at low temperatures as shown Fig. 3.2(b). This is a usual behavior, indicating an unchange of the electronic state as a function of temperature. On the other hand, there appears a negative thermal expansion in $YbCu_2Si_2$ below 90 K, as shown in Fig. 3.2(a), revealing that the electronic state changes from the trivalent state of the Yb ion to the $4f$-itinerant state with decreasing temperature. In other words, $YbCu_2Si_2$ should order antiferromagnetically if the $4f$ electrons are localized even at low temperatures.

In the present study, we searched for Ce-based antiferromagnets with small Néel temperatures and tried to change the electronic state from the antiferromagnetic state to non-magnetic state by applying pressures, expecting superconductivity in the quantum critical region ($T_N \rightarrow 0$). The Néel temperature or antiferromagnetic ordering will become a guide to reach the quantum critical point.

In the case of Yb-based compounds, we searched for Yb-based heavy fermions or non-magnetic but non-divalent Yb compounds. The non-magnetic electronic state of Yb compounds can be changed into the antiferromagnetic state by applying pressures,

expecting also superconductivity in the quantum critical region.

It is also noted that heavy fermion compounds reveal the metamagnetic behavior. Namely, an f-itinerant electronic state below the metamagnetic transition field H_m, as mentioned Sec. 2.3 (see Figs. 2.14 and 2.15), is changed into an electronic state with an f-localized character above H_m. The H_m value or metamagnetic behavior will also become a good guide to reach the quantum critical point in the Yb compounds.

In the previous studies, unconventional superconductivity or heavy fermion superconductivity were observed in many Ce-based compounds even at ambient pressure and under pressures, more than 10 in number. On the other hand, Yb-based heavy fermion superconductivity was observed only in β-$YbAlB_4$.[112] In the present study, we searched for new Yb-based heavy fermion superconductors. One guideline is to search for Yb-based compounds of which the corresponding Ce and actinide (U, Np, and Pu) compounds are superconductors. This is not easy because these exist the divalent electronic state in Yb compounds, such as $YbTIn_5$ (T : Co, Rh, Ir) and $YbCoGa_5$, where $CeTIn_5$ (T : Co, Rh, Ir), and $PuTGa_5$ (T : Co, Rh) are typical heavy fermion superconductors.[62,113–118] Following compounds are thus studied in the present thesis from a viewpoint of physics in heavy fermions :

1) pressure-induced superconductivity including non-centrosymmetric superconductivity in $CePtSi_2$, $CeRhGe_2$, $CeIrGe_3$, and $LaNiC_2$

2) metamagnetic behavior and electronic instability in $CeCu_6$, YbT_2Zn_{20}(T : Co, Rh, Ir) and UT_2Zn_{20}(T : Co, Ir)

3) searching for new Ce and Yb compounds of $YbPd_5Al_2$ and $YbGa_4$.

These compounds are shown in the following chapters.

Here we mention about the experimental conditions in the present study. The heavy fermion state can be usually realized below 1 K, and a much lower than temperature of 30 - 40 mK is needed to clarify the electronic state. In the antiferromagnetic Ce compounds, the Néel temperature is in the range from 1 to 10 K. The high magnetic fields of 100 - 500 kOe is necessary to reach the saturated magnetization of gJ. Anisotropy of magnetization at low temperatures, together with anisotropy of the magnetic susceptibility and the magnetic entropy, is needed to estimate the $4f$-CEF scheme. In the non-magnetic Ce compounds, the metamagnetic behavior is realized at about $H_m = 100$ kOe if the Kondo temperature or the $T_{\chi max}$ value is 10 K, as shown in Fig. 2.15. High magnetic fields of 100 - 500 kOe are thus needed to clarify the electronic states. A static high field of 170 kOe is attained by using a commercial superconducting magnet, and much higher fields up to 500 kOe are attained by a pulse-magnet in the present study.

Pressure is also a very useful technique to change the electronic state in the f-electron system. A pressure of 3 GPa is attained by the usual piston cylinder-type cell, 5 GPa by the Bridgman anvil cell, and 25 GPa by the diamond anvil pressure cell. It is desired that these three conditions of low temperatures, higher magnetic fields, and high pressures are combined and included in one experimental system.

The following experiments were mainly carried out under high-quality samples in the present study.

1) specific heat and de Haas-van Alphen effect at low temperatures down to 30 - 40 mK and high magentic fields up to 170 kOe

2) magnetic susceptibility and magnetization in the temperature range from 2 to 300 K and in magnetic fields up to 50 or 70 kOe(pulse-field magnetization measurements were done at 1.3 K and in high magnetic fields up to 500 kOe)

3) electrical resistivity at low temperatures down to 30 - 40 mK, in high magnetic fields up to 170 kOe and at high pressures up to 25 GPa.

It is finally stressed that high-quality samples are essentially important to clarify the electronic states in the f-electron systems. Three techniques of single-crystal growth were carried out in the present study :

1) flux method by using an alumina crucible even for the compounds with the high vapor pressure

2) Czochralski method in the rf furnace for compounds with a melting point less than 1500 °C and in the tetra-arc furnace for compounds with a high melting point up to 2500 °C

3) Bridgman method by using an Mo-crucible for the compounds with the high vapor pressure at high temperatures up to 1500 °C.

4 Experimental

4.1 Single crystal growth

In the present thesis, we grew single crystals of $CePtSi_2$, $CeRhGe_2$, $CeIrGe_3$, $LaNiC_2$, $CeCu_6$, YbT_2Zn_{20}(T : Co, Rh, Ir), UT_2Zn_{20}(T: Co, Ir), $YbPd_5Al_2$, and $YbGa_4$ by means of various methods such as flux, Czochralski and Bridgman methods. The flux method was applied to $CeIrGe_3$, YbT_2Zn_{20}(T : Co, Rh, Ir), and UT_2Zn_{20}(T: Co, Ir), the Czochralski method to $CePtSi_2$, $LaNiC_2$, and $CeCu_6$, and the Bridgman method to $CeRhGe_2$ and $YbPd_5Al_2$. It is noted that single crystals of $YbGa_4$ were obtained by annealing. The single crystal growth will be introduced in this chapter.

4.1.1 Flux method

The flux method is a kind of the single crystal growth method, which corresponds to a slow cooling process of the premelted components, taken in non-stoichiometric amounts. The advantages of this technique are shown below:[119,120]

(1) Single crystals can be grown often well below their melting points, and this often produces single crystals with fewer defects and much less thermal strain.

(2) Flux metals offer a clean environment for growth, since the flux getters impurities which do not subsequently appear in the crystal.

(3) There are no stoichiometric problems caused, for instance, by oxidation or evaporation of one of the components. Single crystal stoichiometry "control" itself.

(4) This technique can be applied to the compounds with high evaporation pressure, since the crucible is sealed in the ampule and the flux prevents evaporation.

(5) No special technique is required during the crystal growth, and it can be done with the simple and inexpensive equipment. This is a reason why the flux method is sometimes called "poor man's" technique.[119]

There are, to be sure, a number of disadvantages to the technique. The first and foremost is that it is no always an applicable method: an appropriate metal flux from which the desired compound will crystallize may not be found. In addition, difficulties are encountered with some flux choices, when the flux enters the crystal as an impurity. The excessive nucleation causes small crystals, which takes place either due to a too fast cooling rate, or supercooling of the melt by subsequent multiple nucleation and fast growth of large but imperfect crystals usually containing inclusions. The contamination from the crucible cannot be ignored, when reactions with materials occur at high temperatures. Finally, the ability to separate crystals from the flux at the end of growth needs special considerations.

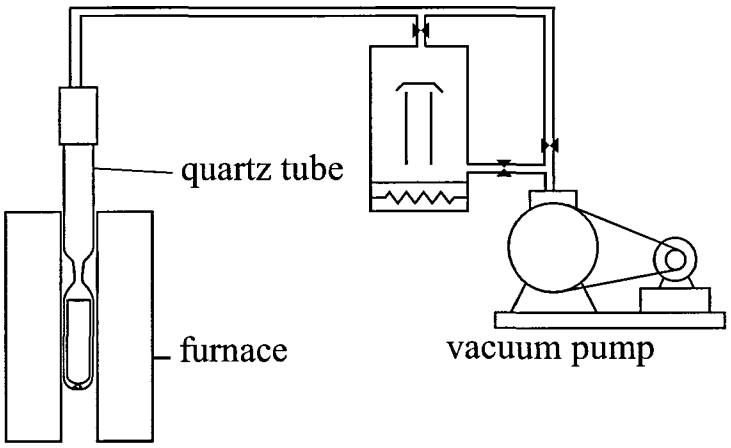

Fig. 4.1 Baking of an alumina crucible.

$CeIrGe_3$

To eliminate the possibility of having traces of Bi in the resulting crystals, as occurred in $CeCoGe_3$, the present single crystals of $CeIrGe_3$ were grown by the Sn-flux method and offstoichiometry.

Here, we describe the growing process in $CeIrGe_3$. At first, we prepared a polycrystalline ingot of $CeIrGe_2$ was prepared by arc-melting of high-pure metals of 4N(99.99 % pure)-Ce, 4N-Rh and 5N-Ge, and crashed it into tiny pieces with a hammer. The high-quality alumina crucible (Al_2O_3: 99.9 %) was used as a container with outer diameter of 15.5 mm^3, inner diameter of 11.5 mm^3 and length of 60 mm^3. Since the crucible usually contains impurities, the crucible was cleaned in alcohol and baked it up to 1000 ˚C under high-vacuum (less than 1×10^{-6} torr), as shown in Fig. 4.1. These polycrystalline samples, together with Sn-metal in the atomic ratio $CeIrGe_2$: Sn = 1 : 20, were put into the alumina crucible and sealed in a quartz ampule with 160 mmHg pressure of Ar-gas, which is adjusted to reach at 1 atm at the highest temperature.

Next the sealed ampule was set in an electric furnace, as shown in Fig. 4.2. A commercial box-type furnace was also used. The furnace possesses the temperature gradient naturally. As we know from our own experience, the better results are obtained when we put the ampule where the temperature is more homogeneous. Therefore, we placed the ampule at the highest- and the flat-temperature gradient position. Nevertheless, the temperature gradient is useful for growing some compounds. There are some reports of growing crystals by temperature gradient method (ex. GdB_6).[119)]

The furnace is controlled by the PID temperature controller with Pt-PtRh13% (type-R) thermocouple. Figure 4.3 shows the block diagram of the furnace control system. In this system, we obtained the temperature stability less than 0.1 °C.

The growth process of $CeIrGe_3$ is shown in Fig. 4.4. The crucible are heated up to 1000 °C which is the maximum temperature of the electric furnace. Then the temperature keeps for 2 days. The temperature was decreased down quickly to 800 °C, then slowly for

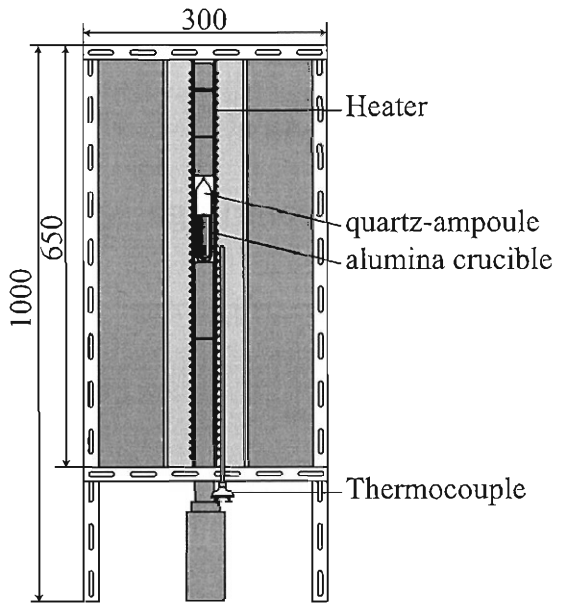

Fig. 4.2 Illustration of the electric furnace.

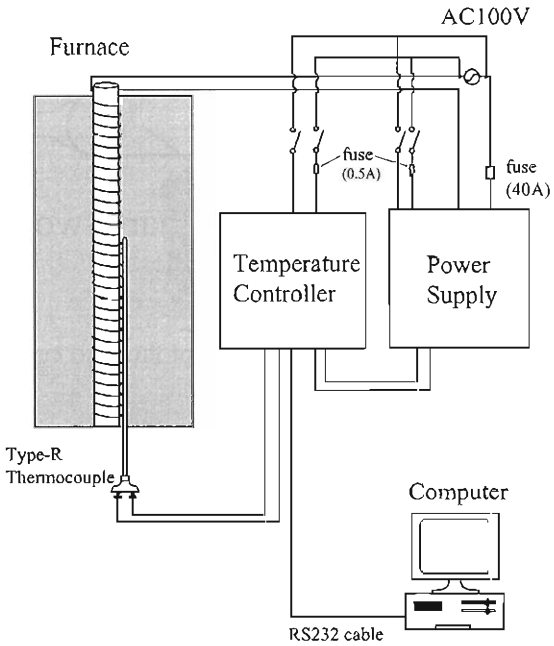

Fig. 4.3 Block diagram of the furnace control system.

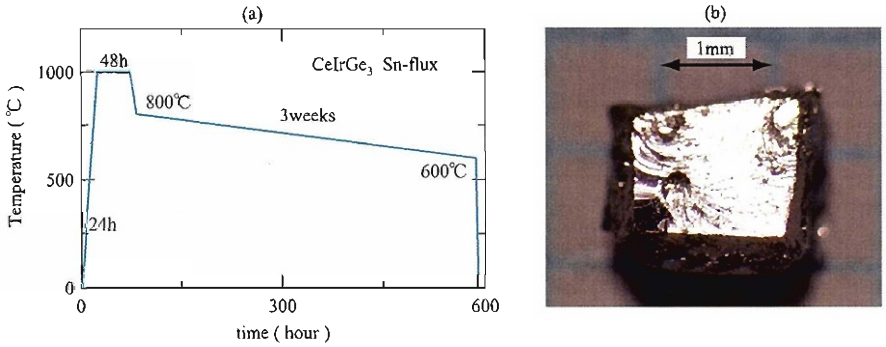

Fig. 4.4 Growing process in and photograph of $CeIrGe_3$.

3 weeks to 600 °C and furnace was turned switch off.

After taking out the ampule from the furnace, the ampule was opened and sealed it again in a pyrex ampule with a neck under high vacuum, as shown in Fig. 4.5. The ampule was heated up to 400 ℃, which is sufficiently higher than the melting point of Sn-metal (231.9 °C), in the muffle furnace. Next the ampule was taken out quickly from the furnace and was set into the centrifuge. Finally the flux was removed from the crystals by spinning the ampule in the centrifuge.

The photograph of single crystal of $CeIrGe_3$ is also shown in Fig. 4.4(b) in which the flat plane is perpendicular to the c-axis. We could get larger single crystals rather than

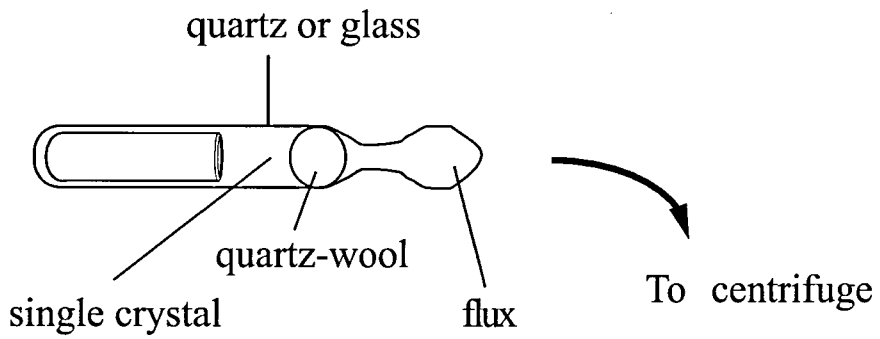

Fig. 4.5 Separation of flux and crystals by spinning the ampule in the centrifuge.

that grown by the Bi-flux method.

YbT_2Zn_{20}(T : Co, Rh, Ir) and UT_2Zn_{20}(T : Co, Ir)

In the same way, single crystals of YbT_2Zn_{20} and UT_2Zn_{20} were grown by the self-flux method, namely using Zn as a flux. Starting materials were 3N-Yb, Co, Rh, Ir, U and 4N-Zn. The composition ratio of starting materials show in Table. 4.I. The following Figures 4.6, 4.7, 4.8, and 4.9 show the time dependence of temperature during growth process and photographs of obtained single crystals of $YbIr_2Zn_{20}$, $YbRh_2Zn_{20}$, $YbCo_2Zn_{20}$, and UT_2Zn_{20}, respectively. Except for $YbRh_2Zn_{20}$, centrifugal separation was done at 470 - 540 °C, which is enough high to melt Zn(melting point : 420 °C). On the other hand, in $YbRh_2Zn_{20}$ case, we set a quartz ampule with neck in the furnace, kept the temperature which growing process finished, and directly removed the flux at 700 °C.

Obtained single crystal ingots are pyramidal in shape, as shown in Figs. 4.6 - 4.9, where flat planes correspond to the {111} planes, reflecting the diamond structure of Yb (U) atoms. Yb (U) and T atoms are surrounded by Zn atoms, forming a cubic cage-structure, as shown later.

Table 4.I The composition ratio of starting materials in growing single crystals of YbT_2Zn_{20} and UT_2Zn_{20}

$YbCo_2Zn_{20}$	Yb : Co : Zn	=	1 : 2 : 50
$YbRh_2Zn_{20}$	Yb : Rh : Zn	=	1 : 2 : 60
$YbIr_2Zn_{20}$	Yb : Ir : Zn	=	1 : 2 : 130
UCo_2Zn_{20}	U : Co : Zn	=	1 : 2 : 47
UIr_2Zn_{20}	U : Ir : Zn	=	1 : 2 : 130

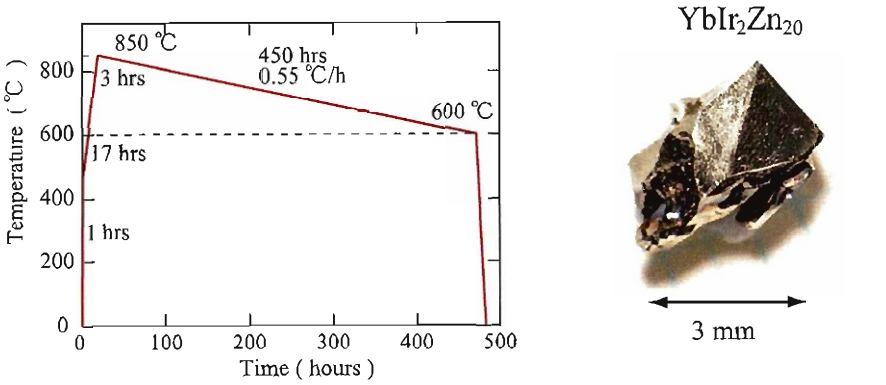

Fig. 4.6 Growing process and photograph of $YbIr_2Zn_{20}$.

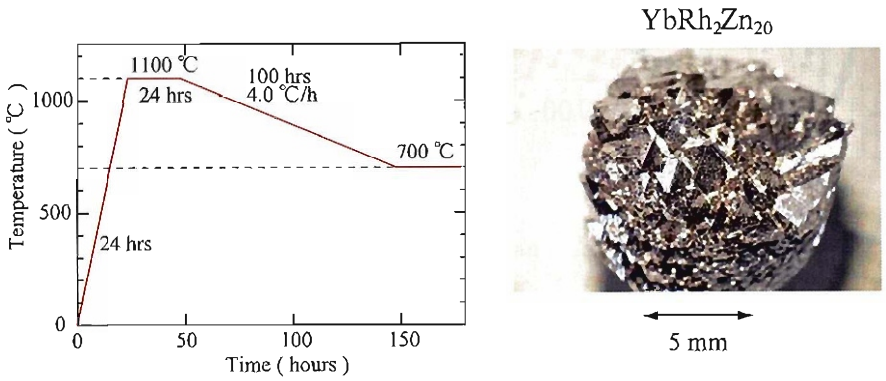

Fig. 4.7 Growing proccss and photograph of $YbRh_2Zn_{20}$.

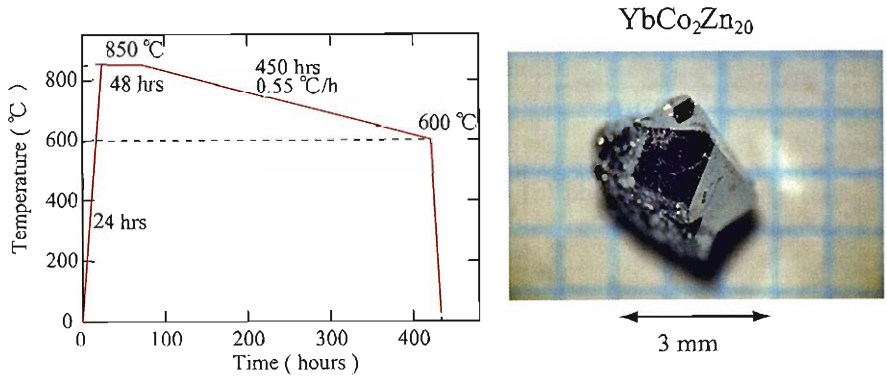

Fig. 4.8 Growing process and photograph of $YbCo_2Zn_{20}$.

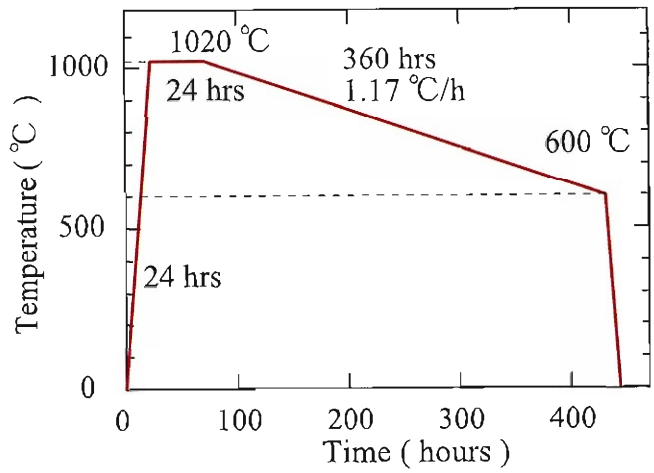

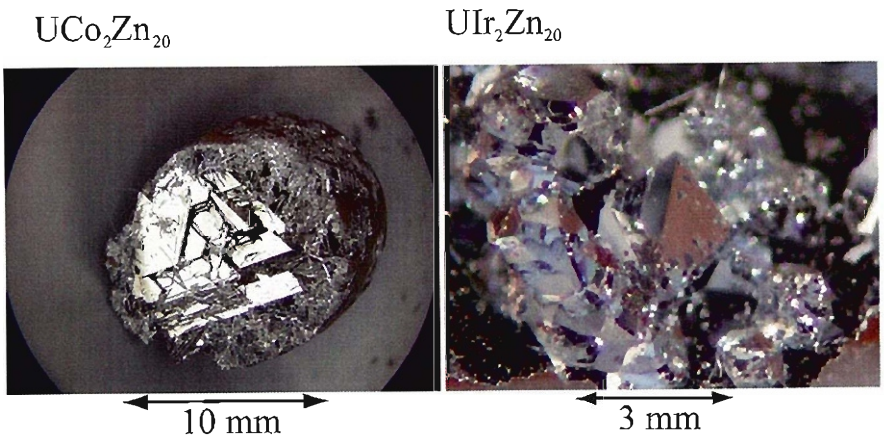

Fig. 4.9 Growing process and photograph of UT_2Zn_{20}(T : Co, Ir).

$YbGa_4$

A binary phase diagram is generally investigated and we can know how to grow the single crystal which we want to get. In the case of Yb - Ga, the binary phase diagram exists and is shown in Figs. 4.10(a) and 4.10(b). Following these phase diagrams, we tried to grow single crystals of $YbGa_4$ by the Ga-self flux method, but single crystals were not obtained. Therefore, stoichiometric Yb - Ga compounds of $YbGa_4$ were heated up to 900 °C, then quenched to 700 °C and annealed in a period of 8 days, as shown in Fig. 4.11(a). Small single crystals were obtained in many numbers, as shown in Fig. 4.11(b).

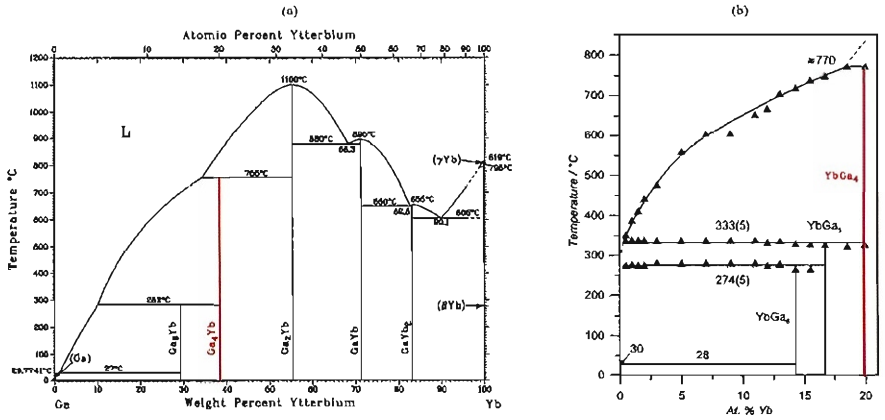

Fig. 4.10 The binary phase diagram of Yb and Ga cited from refs. 121, 122.

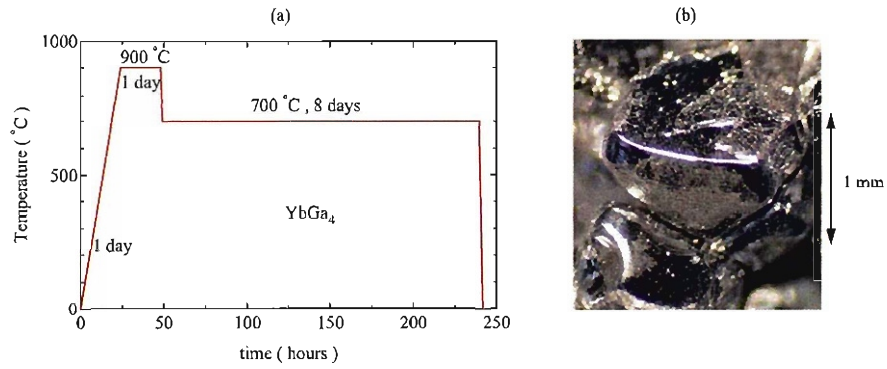

Fig. 4.11 (a) Growing process in and (b) photograph of $YbGa_4$.

4.1.2 Czochralski method

The schematic view of the arc-furnace is shown in Fig. 4.12. It has four tungsten torches to improve a stability of the temperature between the melted material and a water-cooled Cu hearth. Arc-melting has been done under high-quality argon gas atmosphere. The melting procedure was repeated several times to ensure the sample homogeneity.

This method is only applicable to the compounds with low-vapor pressure. When we pull up the crystal from a melt by using a seed, it is important to control the diameter of the crystal, a pulling speed and the power of torches. A typical necking diameter is about 1 mm, while a typical diameter of the ingot is 3-4 mm. The growth rate is 10-15 mm/h to avoid stacking faults in the sample. We usually keep this speed all over the time and do not rotate both the seed and hearth to avoid stacking faults in the sample.

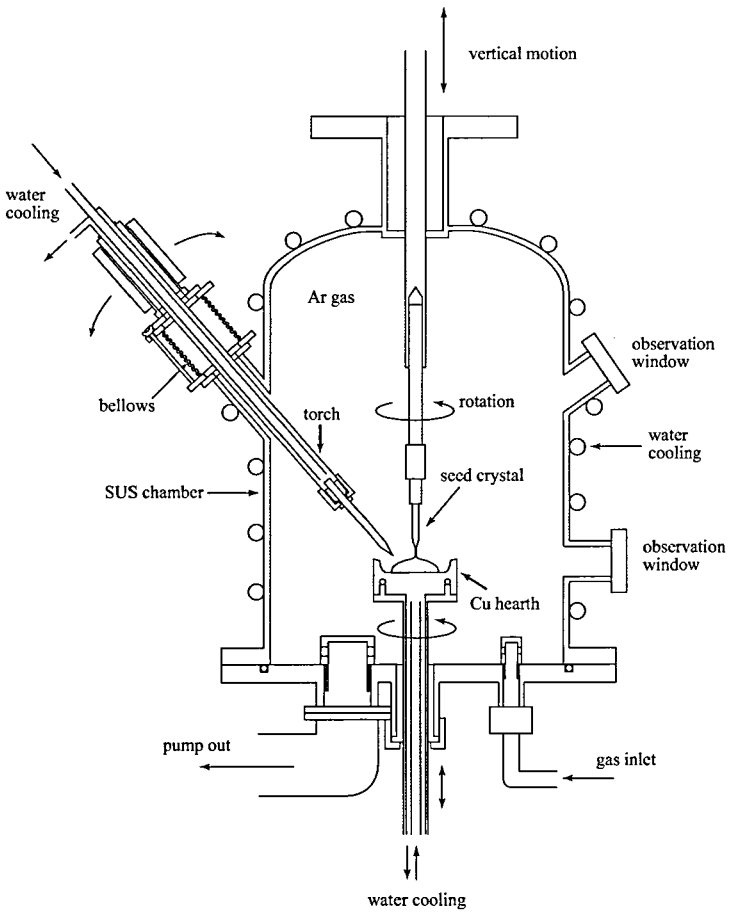

Fig. 4.12 Schematic view of the tetra-arc-furnace.

$CePtSi_2$

We grew a single crystal ingot of $CePtSi_2$ by the Czochralski method from an off-stoichiometric concentration of $CePt_{1.2}Si_{2.2}$, after the previous report[123]. Figure 4.13 shows a single crystal ingot of $CePtSi_2$ grown in a tetra-arc furnace.

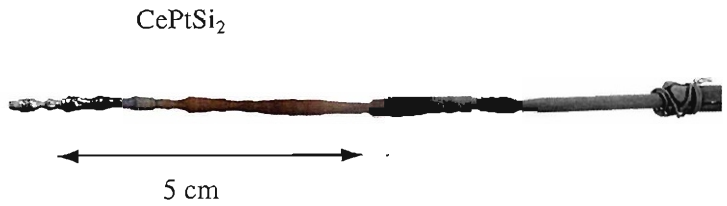

Fig. 4.13 Single crystal ingot of $CePtSi_2$ grown by the Czochralski method.

$LaNiC_2$

Starting materials were 99.9%-pure (3N-)La, 4N-Ni, and 4N-C, which were arc-melted, with a slightly off-stoichiometric composition of 1 : 1 : 2.00 - 2.08. We show in Fig. 4.14 an as-grown ingots with 2-3 mm in diameter and 50 mm in length.

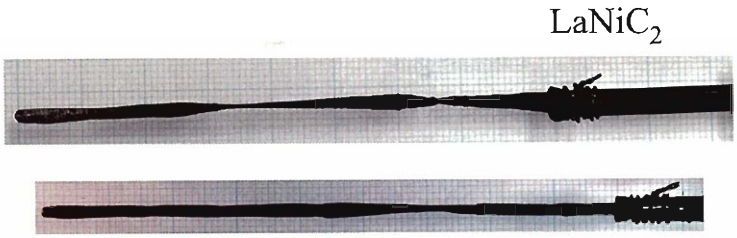

Fig. 4.14 Single crystal ingots of $LaNiC_2$ grown by the Czochralski method.

$CeCu_6$

Starting materials of $CeCu_6$ were 3N(99.9% pure)-Ce, 5N(99.999% pure)-Cu. The phase diagram of Ce-Cu alloys is shown in Fig. 4.15. $CeCu_6$ is a congruent-melting compound and the melting point is about 935 °C.

The single crystal of $CeCu_6$ was grown by the Czochralski method in an radio frequency (rf) furnace under He gas atmosphere. He gas was purified by a liquid nitrogen trap and the gas pressure was 4.0 kg/cm^2. Figure 4.16 shows the schematic view of the rf furnace. A tungsten crucible, which is supported by a tungsten bar standing on the stainless table, is heated by a rf-water-cooled working coil. These are surrounded with a quartz-glass thermal insulator wall. The tungsten crucible was heated up to the temperature slightly higher than the melting point. After melting of the starting materials, a seed crystal was inserted into the melt and then pulled out to grow a single crystal ingot. The pulled single crystal rod of $CeCu_6$ was about 90 mm in length.

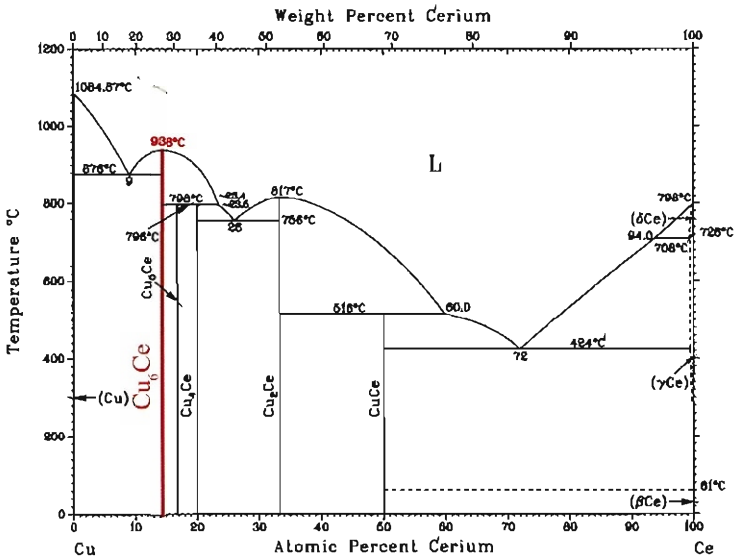

Fig. 4.15 Binary phase diagram of Ce-Cu alloys cited from 121.

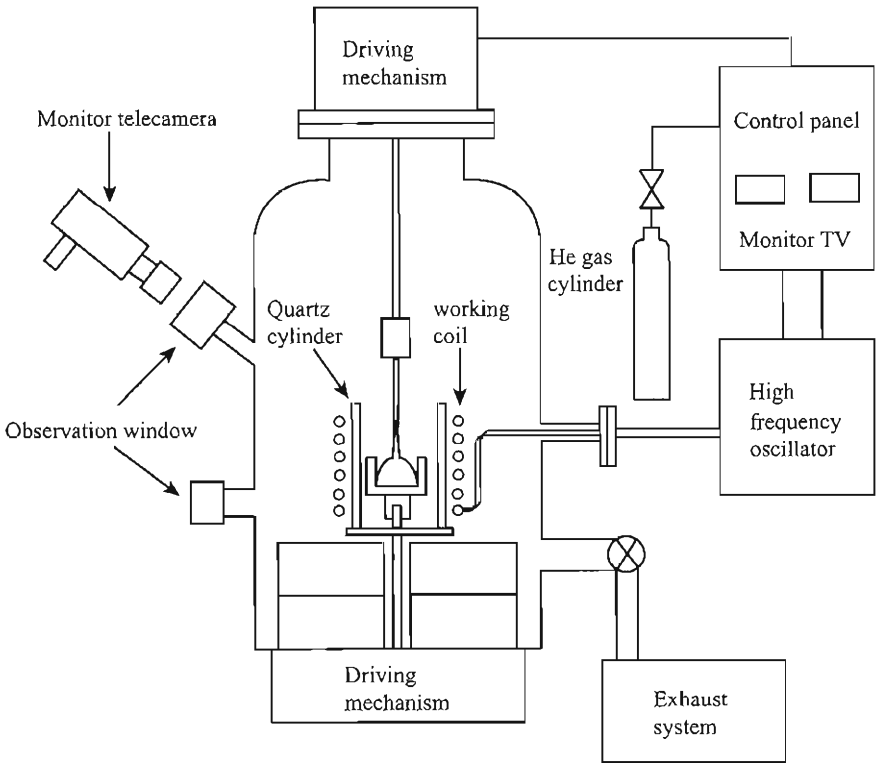

Fig. 4.16 Schematic view of the rf furnace.

4.1.3 Bridgman method

A single crystal was grown by the Bridgman method in both rf furnace and siliconit furnace. There are two kinds of crystal growth in the Bridgman method. One is based on a partial melting of the ingot. This was achieved by using the rf furnace. The carbon heater surrounded the crucible in which a compound is inserted. The single crystal was grown by moving the crucible away from the heater with a speed of 10 mm/hour.

The another type is, in principle, similar to the former but is to use a thermal gradient. This was done by using a siliconit furnace, which is one kind of the vertical electric furnace. A siliconit furnace can be heated up to high temperatures up to 1700 °C. Figure 4.17 shows a block diagram of the siliconit furnace. A molybdenum crucible was set up at a position with a slightly lower temperature compared to the center of the furnace with the highest temperature. The single crystal was grown by decreasing temperature of the furnace.

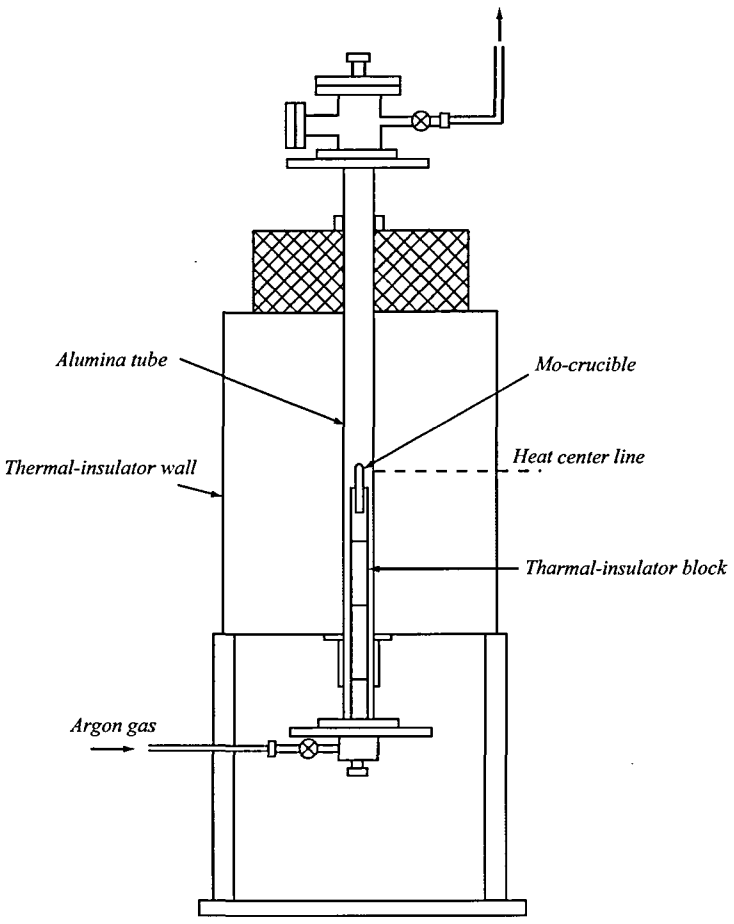

Fig. 4.17 Schematic view of the siliconit furnace.

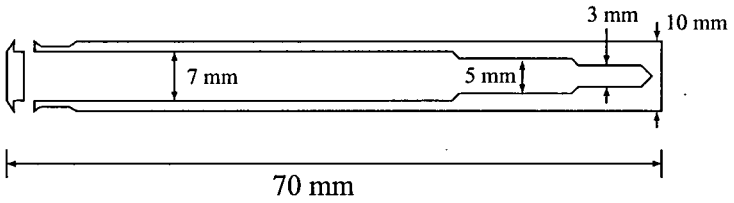

Fig. 4.18 Schematic view of the molybdenum crucible.

We can know the melting point of the compounds by changing the temperature and taking the crucible out from the furnace several times. The melting points was, for example, about 1300 °C in $CeRhGe_2$.

The single crystal sample was grown from the lowest part of the crucible. In order to gain a better single crystal sample, the end of crucible is requested to be narrow, which is similar to the necking in the Czochralski method. Figure 4.18 indicates the molybdenum crucible made by hands.

$CeRhGe_2$

We succeeded in growing single crystals of new compound $CeRhGe_2$ by the Bridgman method. A polycrystalline ingot was synthesized by arc-melting 3N- or 4N-Ce, 4N-Rh, and 5N-Ge in the stoichiometric proportion 1 : 1 : 2 under argon atmosphere, as shown in Fig. 4.19(a), of which surface plane is found to be the *b*-plane of $CeRhGe_2$ from Laue diffraction, as shown in Fig. 4.19(b). The polycrystal was crashed into small pieces and was encapsulated into a molybdenum crucible. Then, we set it in a siliconit furnace with the process shown in Fig. 4.20(a) and got a single crystal of $CeRhGe_2$ as shown in Fig. 4.20(b). The crystal plane was also found to be the *b*-plane from a X-ray Laue pattern.

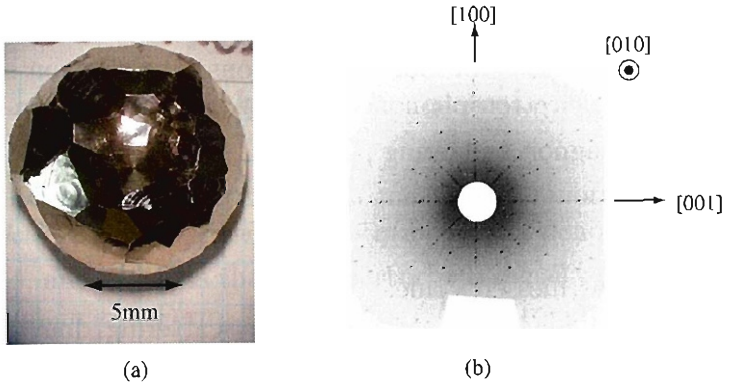

Fig. 4.19 (a) Polycrystalline arc-melted ingot of $CeRhGe_2$ and (b) Laue pattern of *b*-plane.

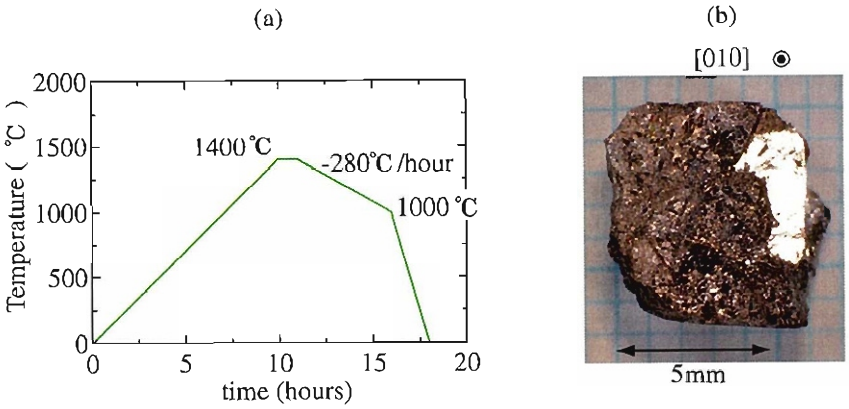

Fig. 4.20 (a) The growing process and (b) single crystal of $CeRhGe_2$.

4.2 Experimental methods

4.2.1 Electrical resistivity

Introduction to the electrical resistivity

An electrical resistivity consists of four contributions: the electron scattering due to impurities or defects ρ_0, the electron-phonon scattering ρ_{ph}, the electron-electron scattering $\rho_{\mathrm{e\text{-}e}}$ and the electron-magnon scattering ρ_{mag}:

$$\rho = \rho_0 + \rho_{\mathrm{ph}} + \rho_{\mathrm{e\text{-}e}} + \rho_{\mathrm{mag}}. \tag{4.1}$$

This relation is called a Matthiessen's rule.

The ρ_0-value, which originates from the electron scattering due to impurities and defects, is constant for a variation of the temperature. This value is important to know the quality of an obtained sample. If ρ_0 is large, the sample contains many impurities or defects. A quality of a sample can be estimated by determining a so-called residual resistivity ratio (RRR $= \rho_{\mathrm{RT}}/\rho_0$), where ρ_{RT} is the resistivity at room temperature. Of course, a large value of RRR indicates that the quality of the sample is good.

Let us introduce a scattering lifetime τ_0 and a mean free path l_0 from the resistivity. The residual resistivity ρ_0 can be written as

$$\rho_0 = \frac{m^*}{ne} \cdot \frac{1}{\tau_0}, \tag{4.2}$$

where n is a density of carrier and e is an electric charge. Then τ_0 and l_0 values are

$$\tau_0 = \frac{m^*}{ne\rho_0}, \tag{4.3}$$

$$l_0 = v_{\mathrm{F}}\tau_0 = \frac{\hbar k_{\mathrm{F}}}{ne\rho_0}. \tag{4.4}$$

The temperature dependence of ρ_{ph}, which originates from the electron scattering by phonon, changes monotonously. ρ_{ph} is proportional to T above the Debye temperature, while it is proportional to T^5 far below the Debye temperature, and ρ_{ph} will be zero at $T = 0$.

In the strongly correlated electron system, the contribution of $\rho_{\mathrm{e\text{-}e}}$ is dominant at low temperatures. Therefore, we can regard the total resistivity in non-magnetic compounds at low temperatures as follows:

$$\rho(T) = \rho_0 + \rho_{\mathrm{e\text{-}e}}(T), \tag{4.5}$$

$$= \rho_0 + AT^2, \tag{4.6}$$

where the coefficient $\sqrt{A}$ is proportional to the effective mass. Yamada and Yosida obtained the rigorous expression of $\rho_{\mathrm{e\text{-}e}}$ in the strongly correlated electron system on the

basis of the Fermi liquid theory.[24] According to their theory, $\rho_{\text{e-e}}$ is proportional to the imaginary part of the f electron self-energy $\Delta\boldsymbol{k}$, and $\Delta\boldsymbol{k}$ is written as

$$\rho_{\text{e-e}} \propto \Delta\boldsymbol{k} \simeq \frac{4}{3}(\pi T)^2 \sum_{\boldsymbol{k}',\boldsymbol{q}} \pi D^f_{\boldsymbol{k}-\boldsymbol{q}}(0)\, D^f_{\boldsymbol{k}'}(0)\, D^f_{\boldsymbol{k}'+\boldsymbol{q}}(0) \times \left\{ {\Gamma_{\uparrow\downarrow}}^2(\boldsymbol{k},\boldsymbol{k}';\boldsymbol{k}'+\boldsymbol{q},\boldsymbol{k}-\boldsymbol{q}) + \frac{1}{2}{\Gamma_{\uparrow\uparrow}}^{A^2}(\boldsymbol{k},\boldsymbol{k}';\boldsymbol{k}'+\boldsymbol{q},\boldsymbol{k}-\boldsymbol{q}) \right\}, \quad (4.7)$$

where $\Gamma_{\sigma\sigma}$ is the four-point vertex, which means the renormalized scattering interaction process of $\boldsymbol{k}(\sigma)\boldsymbol{k}'(\sigma) \rightarrow \boldsymbol{k}'+\boldsymbol{q}(\sigma)\boldsymbol{k}-\boldsymbol{q}(\sigma)$, $\Gamma^A_{\uparrow\uparrow}$ is denoted as $\Gamma_{\uparrow\uparrow}(\boldsymbol{k}_1,\boldsymbol{k}_2;\boldsymbol{k}_3,\boldsymbol{k}_4) - \Gamma_{\uparrow\uparrow}(\boldsymbol{k}_1,\boldsymbol{k}_2;\boldsymbol{k}_4,\boldsymbol{k}_3)$, and $D^f_{\boldsymbol{k}}(0)$ is the true (perturbed) density of states of f electrons with mutual interaction in the Fermi level. This $\Delta\boldsymbol{k}$ is proportional to the square of the enhancement factor and gives a large T^2-resistivity to the heavy fermion system.

In a magnetic compound, an additional contribution to the resistivity must be taken into consideration, namely ρ_{mag}. This contribution describes scattering processes of conduction electrons due to disorder in the arrangement of the magnetic moments. In general, above the ordering temperature T_{ord}, ρ_{mag} is given by

$$\rho_{\text{mag}} = \frac{3\pi N m^*}{2\hbar e^2 \varepsilon_{\text{F}}} |J_{\text{ex}}|^2 (g_{\text{J}}-1)^2 J(J+1), \quad (4.8)$$

where J_{ex} is the exchange integral for the direct interaction between the local moments and conduction electrons. When $T = T_{\text{ord}}$, ρ_{mag} shows a pronounced kink, and when $T < T_{\text{ord}}$, ρ_{mag} strongly decreases with decreasing temperature. The magnetic resistivities in the actinides, however, are ascribed to strong scattering of the conduction electrons by the spin fluctuations of $5f$ electrons. This contribution to the resistivity at low temperatures is given by the square of the temperature, namely $\rho_{\text{mag}} = A'T^2$. In the heavy fermion system, the coefficient A' is extremely large. Therefore, ρ_{mag} and $\rho_{\text{e-e}}$ are inseparable and ρ_{mag} can be considered to correspond to $\rho_{\text{e-e}}$. An analogous situation occurs to the specific heat. Namely, in the heavy fermion system, the magnetic specific heat C_{mag} is changed into a large electronic specific heat C_{e}, namely γT.

Experimental method of the resistivity measurement

We have done the resistivity measurement using a standard four-probe DC or AC current method. The sample was fixed on a plastic plate by an instant glue. The gold wire with 0.025 mm in diameter and silver paste were used to form contacts on the sample. The sample was mounted on a sample-holder and installed in a ^{4}He or ^{3}He cryostat. We measured the resistivity from 1.3 or 0.5 K (the lowest temperature 50 mK) to the room temperature. The thermometers are a Cernox resistor for all the temperature region or a combination between a RuO_2 resistor at lower temperatures (below 20 K) and a diode resistor at higher temperatures.

4.2.2 Specific heat

Introduction to the specific heat

At low temperatures, the specific heat is written as the sum of electronic, lattice, magnetic and nuclear contributions:

$$C = C_{\mathrm{e}} + C_{\mathrm{ph}} + C_{\mathrm{mag}} + C_{\mathrm{nuc}} \tag{4.9}$$

$$= \gamma T + \beta T^3 + C_{\mathrm{mag}} + \frac{A}{T^2}, \tag{4.10}$$

where A, γ and β are constants because of the characteristic properties of the material.

The electronic term C_{e} is linear in T and is dominant at sufficiently low temperatures. If we can neglect the magnetic and nuclear contributions, it is convenient to exhibit the experimental values of C as a plot of C/T versus T^2:

$$\frac{C}{T} = \gamma + \beta T^2. \tag{4.11}$$

Then we can estimate the electronic specific heat coefficient γ. Using the density of states $D(\varepsilon_{\mathrm{F}})$, the coefficient γ can be expressed as

$$\gamma = \frac{\pi^2}{3} {k_{\mathrm{B}}}^2 D(\varepsilon_{\mathrm{F}}), \tag{4.12}$$

where k_{B} is the Boltzmann constant. Since the density of states $D(\epsilon_{\mathrm{F}})$ based on the free electron model is proportional to the electron mass, the coefficient γ possesses an extremely large value in the heavy fermion system.

According to the Debye T^3 law, for $T \ll \Theta_{\mathrm{D}}$:

$$C_{\mathrm{ph}} \simeq \frac{12\pi^4 N k_{\mathrm{B}}}{5} \left(\frac{T}{\Theta_{\mathrm{D}}}\right)^3 \equiv \beta T^3, \tag{4.13}$$

where Θ_{D} is the Debye temperature and N is the number of atoms. For the actual lattices the temperatures at which the T^3 approximation holds are quite low. It may be necessary to be below $T = \Theta_{\mathrm{D}}/50$ to get a reasonably pure T^3 law.

If the f energy level splits due to the crystalline electric field (CEF) in the paramagnetic state, the inner energy per one magnetic ion is given by

$$E_{\mathrm{CEF}} = \langle E_i \rangle = \frac{\sum_i n_i E_i \exp(-E_i/k_{\mathrm{B}}T)}{\sum_i \exp(-E_i/k_{\mathrm{B}}T)}. \tag{4.14}$$

where E_i and n_i are the energy and the degenerate degree on the level i. Thus the magnetic contribution to the specific heat is given by

$$C_{\mathrm{Sch}} = \frac{\partial E_{\mathrm{CEF}}}{\partial T}. \tag{4.15}$$

This contribution C_{Sch} is called a Schottky term. Here, the magnetic entropy of the f electron S_{mag} is defined as

$$S_{\mathrm{mag}} = \int_0^T \frac{C_{\mathrm{Sch}}}{T}\,\mathrm{d}T. \tag{4.16}$$

The magnetic entropy is also described as

$$S = R \ln W, \tag{4.17}$$

where W is a state number at temperature T. Therefore we acquire information about the CEF level.

In the magnetic ordering state C_{mag} is:

$$C_{\mathrm{mag}} \propto T^{3/2} \quad \text{(ferromagnetic ordering)} \tag{4.18}$$

$$\propto T^3 \quad \text{(antiferromagnetic ordering).} \tag{4.19}$$

When the antiferromagnetic magnon is accompanied with the energy gap Δ_{m}, eq. (4.19) is modified to $C_{\mathrm{mag}} \propto T^3 \exp(-\Delta_{\mathrm{m}}/k_{\mathrm{B}}T)$.

Experimental method of the specific heat

The specific heat was measured by the quasi-adiabatic heat pulse method using dilution refrigerator, ^{3}He and ^{4}He cryostats at temperatures down to 0.1, 0.6 and 1.7 K, respectively. The sample was put on the Cu-addenda. The RuO_2 resister thermometer and two strain gage heaters were also put on the addenda. One of the strain gage heater generated constant heater to compensate heat leak via to the heat radiation and/or the thermal conduction by the wire which suspended the addenda.

We gave heat pulse to the sample and addenda due to the another heater. Then we measured the change of the temperature at addenda. The specific heat is deduced as follows:

$$C = \frac{\Delta Q}{\Delta T} = \frac{I \cdot V \cdot \Delta t}{\Delta T}. \tag{4.20}$$

Here, ΔQ is the amount of heat, I and V are the current and the voltage flowing to the heater, respectively, Δt is the duration of heating and ΔT is the change of temperature due to heating. Here, this C includes both of the specific heat of the sample and that of the addenda. The specific heat of the sample is thus derived by subtracting the specific heat of the addenda.

4.2.3 Magnetic susceptibility

Introduction to the magnetic susceptibility

At high temperatures, the $4f$ electron in most of the Ce compounds is localized. The crystalline electric field (CEF) theory is thus well applicable to the magnetic property of the Ce compounds. By using the CEF theory, the $4f$ energy level in the Ce compounds

with the non-cubic crystal structure splits into three doublets. Hamiltonian of this system is given by

$$H = H_{\mathrm{CEF}} + H_{\mathrm{Zeeman}}. \tag{4.21}$$

Here, H_{CEF} is expressed as

$$H_{\mathrm{CEF}} = B_2^0 O_2^0 + B_4^0 O_4^0 + B_4^4 O_4^4, \tag{4.22}$$

in the tetragonal symmetry and

$$H_{\mathrm{CEF}} = B_2^0 O_2^0 + B_2^2 O_2^2 + B_4^0 O_4^0 + B_4^2 O_4^2 + B_4^4 O_4^4, \tag{4.23}$$

in the orthorhombic symmetry, where B_l^m and O_l^m are the CEF parameters and the Stevens operators, respectively.[15,16] Due to the CEF effect, the sixfold degenerate $4f$-levels of the Ce ion are split into three doublets.

The CEF susceptibility is given by

$$\chi_{\mathrm{CEF}}^i = N(g_J\mu_{\mathrm{B}})^2 \frac{1}{Z}\left(\sum_{m\neq n} |\langle m|J_i|n\rangle|^2 \frac{1-e^{-\frac{\Delta_{m,n}}{k_{\mathrm{B}}T}}}{\Delta_{m,n}} e^{-\frac{E_n}{k_{\mathrm{B}}T}} + \frac{1}{k_{\mathrm{B}}T}\sum_n |\langle n|J_i|n\rangle|^2 e^{-\frac{E_n}{k_{\mathrm{B}}T}}\right) \tag{4.24}$$

and

$$Z = \sum_n e^{-\frac{E_n}{k_{\mathrm{B}}T}}, \tag{4.25}$$

where g_J is the Landé g-factor (6/7 for Ce^{3+}), J_i is the component of the angular momentum and $\Delta_{m,n} = E_n - E_m$. The magnetization can be also calculated by

$$M_i = g_J\mu_{\mathrm{B}} \sum_n |\langle n|J_i|n\rangle| \frac{e^{-\frac{E_n}{k_{\mathrm{B}}T}}}{Z}. \tag{4.26}$$

Thus, the CEF susceptibility is also given by

$$\chi_{\mathrm{CEF}} = \lim_{H\to 0} \frac{dM}{dH}. \tag{4.27}$$

The magnetic susceptibility including the molecular field contribution λ_i is given as follows:

$$\chi_i^{-1} = (\chi_{\mathrm{CEF}}^i)^{-1} - \lambda_i. \tag{4.28}$$

The eigenvalue E_n and eigenfunction $|n\rangle$ are determined by diagonalizing the total Hamiltonian

$$H = H_{\mathrm{CEF}} - g_J\mu_{\mathrm{B}} J_i(H_i + \lambda_i M_i), \tag{4.29}$$

where the second term is the Zeeman term and the third one is a contribution from the molecular field. The magnetic susceptibility was measured by a commercial SQUID magnet meter, produced by Quantum Design.

4.2.4 de Haas-van Alphen effect

Introduction to the de Haas-van Alphen effect

Under a high magnetic field, the orbital motion of the conduction electron is quantized and forms Landau levels[124]. Therefore various physical qualities show a periodic variation with H^{-1} since increasing the field strength H causes a sharp change in the free energy of the electron system when Landaus level crosses the Fermi energy. In a three-dimensional system this sharp structure is observed at extremal areas in $\boldsymbol{k}$-space, perpendicular to the field direction and enclosed by the Fermi energy because the density of state also becomes extremal. From the field and temperature dependence of various physical quantities, we can obtain the extremal area S, the cyclotron mass m_{c}^* and the scattering lifetime τ for this cyclotron orbit. The magnetization or the magnetic susceptibility is the most common one of these physical quantities, and its periodic character is called the de Haas-van Alphen (dHvA) effect. It provides one of the best tools for the investigation of Fermi surfaces of metals.

The theoretical expression for the oscillatory component of magnetization M_{osc} due to the conduction electrons was given by Lifshitz and Kosevich as follows:[125]

$$M_{\mathrm{osc}} = \sum_r \sum_i \frac{(-1)^r}{r^{3/2}} A_i \sin\left(\frac{2\pi r F_i}{H} + \beta_i\right), \tag{4.30a}$$

$$A_i \propto F H^{1/2} \left|\frac{\partial^2 S_i}{\partial k_{\mathrm{H}}{}^2}\right|^{-1/2} R_{\mathrm{T}} R_{\mathrm{D}} R_{\mathrm{S}}, \tag{4.30b}$$

$$R_{\mathrm{T}} = \frac{\alpha r m_{ci}^* T/H}{\sinh(\alpha r m_{ci}^* T/H)}, \tag{4.30c}$$

$$R_{\mathrm{D}} = \exp(-\alpha r m_{ci}^* T_{\mathrm{D}}/H), \tag{4.30d}$$

$$R_{\mathrm{S}} = \cos(\pi g_i r m_{ci}^*/2m_0), \tag{4.30e}$$

$$\alpha = \frac{2\pi^2 k_{\mathrm{B}}}{e\hbar}. \tag{4.30f}$$

Here the magnetization is periodic on $1/H$ and has a dHvA frequency F_i

$$\begin{aligned} F_i &= \frac{\hbar}{2\pi e} S_i \\ &= 1.05 \times 10^{-12}\ [\mathrm{T \cdot cm^2}] \cdot S_i \\ &= 1.05 \times 10^{-8}\ [\mathrm{Oe \cdot cm^2}] \cdot S_i \end{aligned} \tag{4.31}$$

which is directly proportional to the i-th extremal (maximum or minimum) cross-sectional area S_i $(i = 1, \ldots, n)$. The extremal area means a gray plane in Fig. 4.21, where there is one extremal area in a spherical Fermi surface. The factor R_{T} in the amplitude A_i is related to the thermal damping at a finite temperature T. The factor R_{D} is also related to the Landau level broadening $k_{\mathrm{B}}T_{\mathrm{D}}$. Here T_{D} is due to both the lifetime broadening and inhomogeneous broadening caused by impurities, crystalline imperfections or strains.

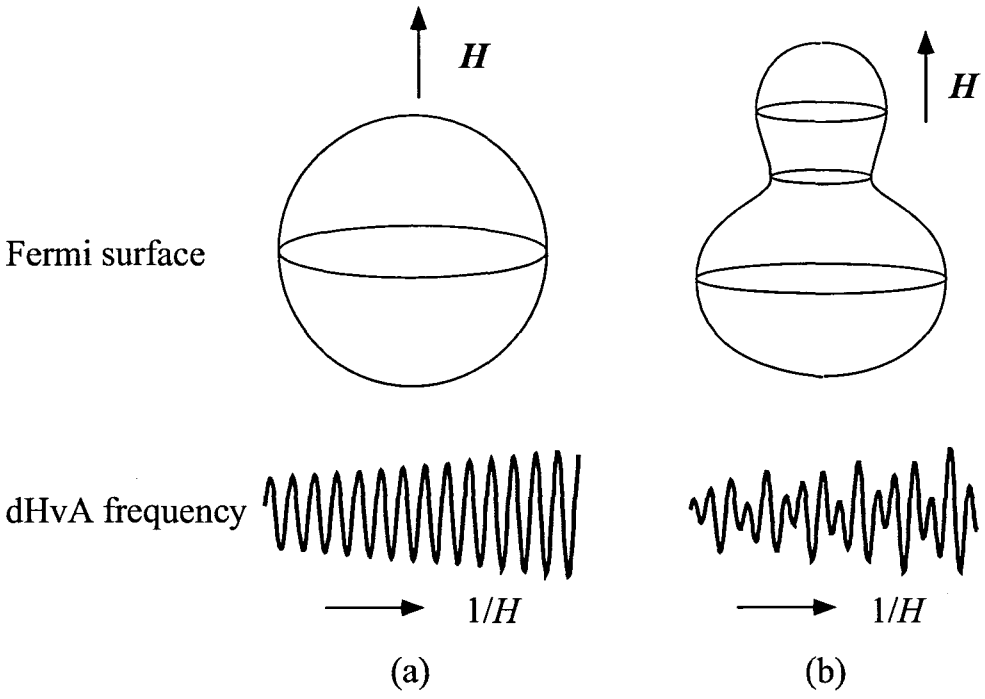

Fig. 4.21 Simulations of the cross-sectional area and its dHvA signal for a simple Fermi surface. There is one dHvA frequency in (a), while there are three different frequencies in (b).

The factor T_D is called the Dingle temperature and is given by

$$\begin{aligned} T_D &= \frac{\hbar}{2\pi k_B}\tau^{-1} \\ &= 1.22 \times 10^{-12}\ [\mathrm{K}\cdot\mathrm{sec}]\cdot\tau^{-1}. \end{aligned} \tag{4.32}$$

The factor R_S is called the spin factor and related to the difference of phase between the Landau levels due to the Zeeman splitting. When $g_i = 2$ (a free electron value) and $m_c^* = 0.5\ m_0$, this term becomes zero for $r = 1$. The fundamental oscillation vanishes for all the values of the field. This is called the zero spin splitting situation in which the up and down spin contributions to the oscillation are canceled out, and this can be useful for determining the value of g_i. Note that in this second harmonics for $r = 2$ the dHvA oscillation should show full amplitude. The quantity $|\partial^2 S/\partial {k_H}^2|^{-1/2}$ is called the curvature factor. The rapid change of cross-sectional area around the extremal area along the field direction diminishes the dHvA amplitude for this extremal area.

The detectable conditions of dHvA effect are as follows:

1) The distance between the Landau levels $\hbar\omega_c$ must be larger than the thermal broadening width $k_B T$: $\hbar\omega_c \gg k_B T$ (high fields, low temperatures).

2) At least one cyclotron motion must be performed during the scattering, namely $\omega_c\tau/2\pi > 1$ (high quality samples). In reality, however, it can be observed even if a cyclotron motion is about ten percent of one cycle, although the dHvA amplitude becomes extremely small.

3) The fluctuation of the static magnetic field must be smaller than the field interval of one cycle of the dHvA oscillation (homogeneity of the magnetic field).

Shape of the Fermi surface

The angular dependence of dHvA frequencies gives very important information about a shape of the Fermi surface. As a value of Fermi surface corresponds to a carrier number, we can obtain the carrier number of a metal directly.

We show the typical Fermi surfaces and their angular dependences of dHvA frequencies in Fig. 4.22. In a spherical Fermi surface, the dHvA frequency is constant for any field direction. On the other hand, in an cylindrical Fermi surface such as in Fig. 4.22(b),

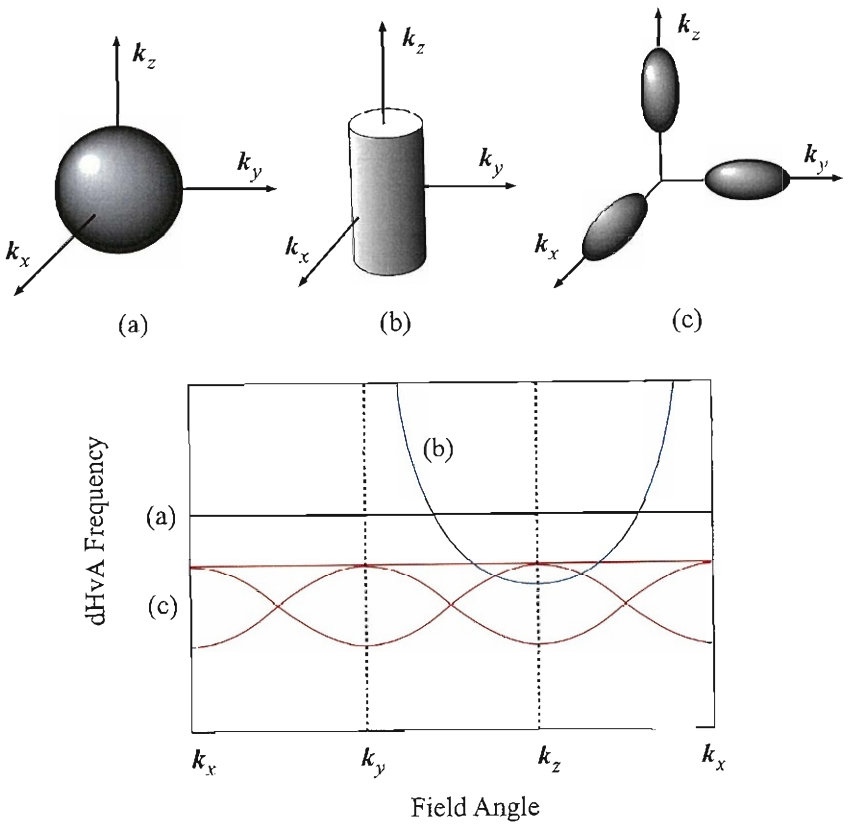

Fig. 4.22 Angular dependence of the dHvA frequency in three typical Fermi surfaces (a) sphere (black), (b) cylinder (blue), and (c) ellipsoid (red).

it takes a minimum value for the field along the z-axis. These relatively simple shape Fermi surfaces can be determined only by the experiment. However, information from an energy band calculation is needed to determine a complicated one.

Cyclotron effective mass

We can determine the cyclotron effective mass m^*_{ci} from the measuring a temperature dependence of a dHvA amplitude. Equation (4.30c) is transformed into

$$\log\left\{A_i\left[1-\exp\left(\frac{-2\alpha m^*_{ci}T}{H}\right)\right]/T\right\}=\frac{-\alpha m^*_{ci}}{H}T+\text{const.} \tag{4.33}$$

Therefore, from the slope of a plot of $\log\{A_i[1-\exp(-2\lambda m^*_{ci}T/H)]/T\}$ versus T at constant field H, the effective mass can be obtained.

Let us consider the relation between the cyclotron mass and the electrical specific heat γ. Using a density of states $D(E_\mathrm{F})$, γ is written as

$$\gamma=\frac{\pi^2}{3}{k_\mathrm{B}}^2D(E_\mathrm{F}). \tag{4.34}$$

In the spherical Fermi surface, using $E_\mathrm{F}=\hbar^2{k_\mathrm{F}}^2/2m^*_\mathrm{c}$ takes

$$\begin{aligned}\gamma&=\frac{\pi^2}{3}{k_\mathrm{B}}^2\frac{V}{2\pi^2}\left(\frac{2m^*_\mathrm{c}}{\hbar^2}\right)^{3/2}{E_\mathrm{F}}^{1/2}\\&=\frac{{k_\mathrm{B}}^2V}{3\hbar^2}m^*_\mathrm{c}k_\mathrm{F},\end{aligned} \tag{4.35}$$

where V is molar volume and $k_\mathrm{F}=(S_\mathrm{F}/\pi)^{1/2}$. We obtain from eq. (4.31)

$$\begin{aligned}\gamma&=\frac{{k_\mathrm{B}}^2m_0}{3\hbar^2}\left(\frac{2e}{\hbar}\right)^{1/2}V\frac{m^*_\mathrm{c}}{m_0}F^{1/2}\\&=2.87\times10^{-4}\,[(\mathrm{mJ/K^2\cdot mol})(\mathrm{mol/cm^3})\mathrm{T}^{-1/2}]\cdot V\frac{m^*_\mathrm{c}}{m_0}F^{1/2}\\&=2.87\times10^{-2}\,[(\mathrm{mJ/K^2\cdot mol})(\mathrm{mol/cm^3})\mathrm{Oe}^{-1/2}]\cdot V\frac{m^*_\mathrm{c}}{m_0}F^{1/2}.\end{aligned} \tag{4.36}$$

In the case of the cylindrical Fermi surface,

$$\begin{aligned}\gamma&=\frac{\pi^2}{3}{k_\mathrm{B}}^2\frac{V}{2\pi^2\hbar^2}m^*_\mathrm{c}k_z\\&=\frac{{k_\mathrm{B}}^2V}{6\hbar^2}m^*_\mathrm{c}k_z,\end{aligned} \tag{4.37}$$

where the Fermi wave number k_z is parallel to an axial direction of the cylinder. If we regard simply the Fermi surfaces as sphere, ellipse or cylinder approximately and then we can calculate them.

Dingle temperature

We can determine the Dingle temperature T_D from measuring a field dependence of a dHvA amplitude. Equations (4.30b)-(4.30d) yield

$$\log\left\{A_i H^{1/2}\left[1-\exp\left(\frac{-2\lambda m_{ci}^* T}{H}\right)\right]\right\} = -\lambda m_{ci}^*(T+T_D)\frac{1}{H} + \text{const.} \tag{4.38}$$

From the slope of a plot of $\log\{A_i H^{1/2}[1-\exp(-2\lambda m_{ci}^* T/H)]\}$ versus $1/H$ at constant T, the Dingle temperature can be obtained. Here, the cyclotron effective mass must have been already obtained.

We can estimate the mean free path l or the scattering life time τ from the Dingle temperature. The relation between an effective mass and lifetime takes the form

$$\hbar k_F = m^* v_F, \tag{4.39}$$

$$l = v_F \tau. \tag{4.40}$$

Then eq. (4.32) is transformed into

$$l = \frac{\hbar^2 k_F}{2\pi k_B m_c^* T_D}. \tag{4.41}$$

When the extremal area can be regarded as a circle approximately, using eq. (4.31), the mean free path is expressed as

$$\begin{aligned} l &= \frac{\hbar^2}{2\pi k_B m_0}\left(\frac{2e}{\hbar c}\right)^{1/2} F^{1/2}\left(\frac{m_c^*}{m_0}\right)^{-1} {T_D}^{-1} \\ &= 77.6\ [\text{Å}\cdot \text{T}^{-1/2}\cdot \text{K}]\cdot F^{1/2}\left(\frac{m_c^*}{m_0}\right)^{-1} {T_D}^{-1} \\ &= 77.6\times 10^2\ [\text{Å}\cdot \text{Oe}^{-1/2}\cdot \text{K}]\cdot F^{1/2}\left(\frac{m_c^*}{m_0}\right)^{-1} {T_D}^{-1}. \end{aligned} \tag{4.42}$$

Field modulation method with the pick-up coil dHvA system

Experiments of the dHvA effect were constructed by using the usual ac-susceptibility field modulation method. Now we give an outline of the field modulation method with pick-up coil dHvA system.

A small ac-field $h_0 \cos\omega t$ is varied on an external field H_0 ($H_0 \gg h_0$) in order to obtain the periodic variation of the magnetic moment M_{osc}. The sample is set up into a pair of balanced coils (pick up and compensation coils), as shown in Fig. 4.23. An induced emf (electromotive force) V_{osc} will be proportional to $\mathrm{d}M_{osc}/\mathrm{d}t$:

$$\begin{aligned} V_{osc} &= c\frac{\mathrm{d}M_{osc}}{\mathrm{d}t} \\ &= c\frac{\mathrm{d}M_{osc}}{\mathrm{d}H}\frac{\mathrm{d}H}{\mathrm{d}t} \\ &= -ch_0\omega\sin\omega t\sum_{k=1}^{\infty}\frac{h_0^k}{2^{k-1}(k-1)!}\left(\frac{\mathrm{d}^k M_{osc}}{\mathrm{d}H^k}\right)_{H_0}\sin k\omega t, \end{aligned} \tag{4.43}$$

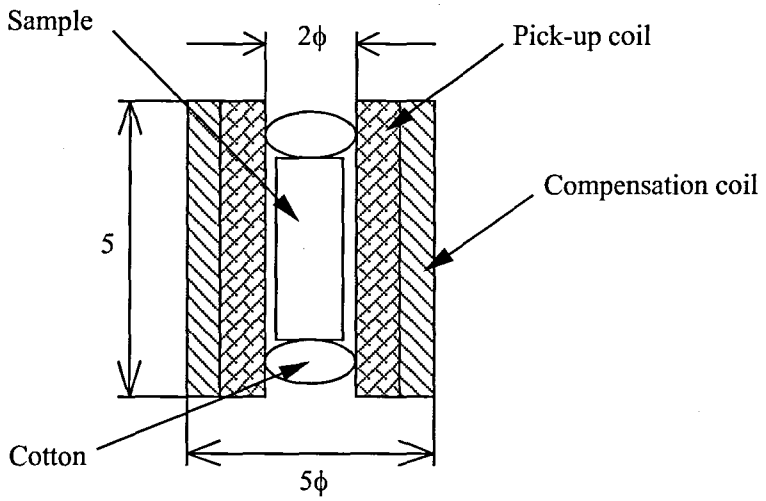

Fig. 4.23 Detecting coil and the sample location.

where c is constant which is fixed by the number of turns in the coil and so on, and the higher differential terms of the coefficient of $\sin k\omega t$ are neglected. Calculating the $\mathrm{d}^k M/\mathrm{d}H^k$, it becomes

$$V_{\mathrm{osc}} = -c\omega A \sum_{k=1}^{\infty} \frac{1}{2^{k-1}(k-1)!} \left(\frac{2\pi h_0}{\Delta H}\right)^k \sin\left(\frac{2\pi F}{H} + \beta - \frac{k\pi}{2}\right) \sin k\omega t. \tag{4.44}$$

Here, $\Delta H = H^2/F$. Considering ${h_0}^2 \ll {H_0}^2$, the time dependence of magnetization $M(t)$ is given by

$$M_{\mathrm{osc}}(t) = A\left[J_0(\lambda)\sin\left(\frac{2\pi F}{H_0} + \beta\right) + 2\sum_{k=1}^{\infty} kJ_k(\lambda)\cos k\omega t \sin\left(\frac{2\pi F}{H_0} + \beta - \frac{k\pi}{2}\right)\right], \tag{4.45}$$

where

$$\lambda = \frac{2\pi F h_0}{{H_0}^2}. \tag{4.46}$$

Here, J_k is k-th Bessel function. Figure 4.24 shows the Bessel function of the first kind for the various order k. Finally we can obtain the output emf as follows:

$$V_{\mathrm{osc}} = c\left(\frac{\mathrm{d}M}{\mathrm{d}t}\right) = -2c\omega A \sum_{k=1}^{\infty} kJ_k(\lambda)\sin\left(\frac{2\pi F}{H_0} + \beta - \frac{k\pi}{2}\right)\sin k\omega t. \tag{4.47}$$

The signal was detected at the second harmonic of the modulation frequency 2ω using a lock-in amplifier, since this condition may cut off the offset magnetization and then detect the component of the quantum oscillation only. Thus, eq. (4.47) becomes

$$V_{\mathrm{osc}} = -4c\omega A J_2(\lambda)\sin\left(\frac{2\pi F}{H_0} + \beta\right)\sin 2\omega t. \tag{4.48}$$

Here, we summarize eq. (4.48) as follow:

$$
\begin{aligned}
V_{\rm osc} &= A\left|\frac{\partial^2 S_{\rm F}(k_z)}{\partial k_z^2}\right|^{-1/2} R_{\rm T}R_{\rm D}R_{\rm S}\sin\left(\frac{2\pi F}{H}+\beta\right), && (4.49)\\
A &\propto \omega J_2(x)H^{1/2}, && (4.50)\\
R_{\rm T} &= \frac{2\alpha m_{\rm c}^* T/H}{\sinh(2\alpha m_{\rm c}^* T/H)},\\
R_{\rm D} &= \exp(-\alpha m_{\rm c}^* T_{\rm D}/H),\\
R_{\rm S} &= \cos(\pi m_{\rm c}^* g/2m_0),\\
\alpha &= 2\pi^2 c k_{\rm B}/e\hbar.\\
x &= \frac{2\pi F h}{H^2}.
\end{aligned}
$$

A in eq. (4.50) is the factor depending on the detecting method. We usually choose the modulation field h_0 to make the value of $J_2(\lambda)$ maximum, namely $\lambda = 3.14$. A modulation frequency of 11 Hz is also used in the dHvA experiment. Figure 4.25 shows a block diagram for the dHvA measurement in the present study.

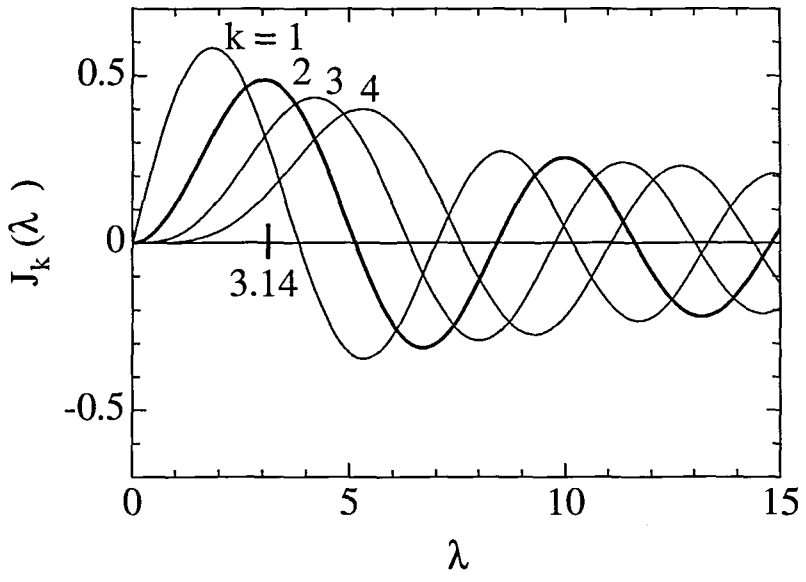

Fig. 4.24 Bessel function $J_k(\lambda)$ of the first kind.

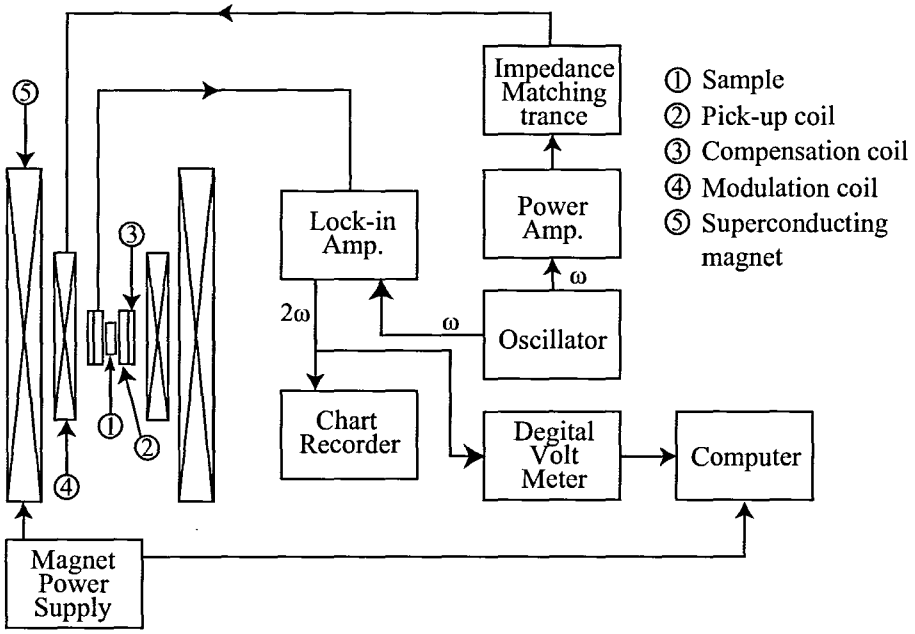

Fig. 4.25 Block diagram for the dHvA measurement.

Magnetization in high magnetic field

We measured the high field magnetization in at High-field Laboratory, Center for Quantum Science and Technology under Extreme Conditions, Osaka University (KYOKUGEN). Figure 4.26 shows the block diagram of magnetization measurement. At first, the huge condenser bank is electrically charged. When we turn on the switch of circuit, the charge flows through the magnet coil and generate high magnetic field in the coil. The long-pulse magnet that we used for this research can generates the magnetic field up to 550 kOe. The pulse width is 50 msec. We used the uniaxial coil in order to compensate a background flux change due to a transient field, as shown in Fig. 4.27. The turn number of outer B coil is half of A, and B is twice the area of A. Ideally, we can compensete perfectly by A and B coils. However this is ideal, and in fact the background signals are not zero, containing linear and nonlinear components of the dH/dt. The linear component can be minimized by tuning a bridge balance circuit connected with a compensation C coil.

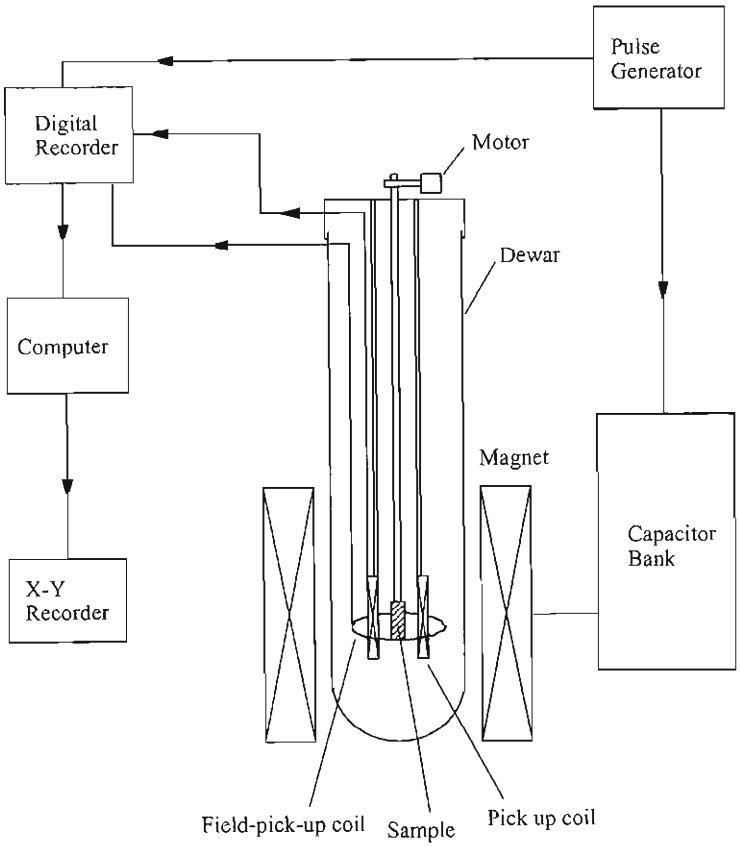

Fig. 4.26 Block diagram of measurement of magnetization with a pulse-field magnet.

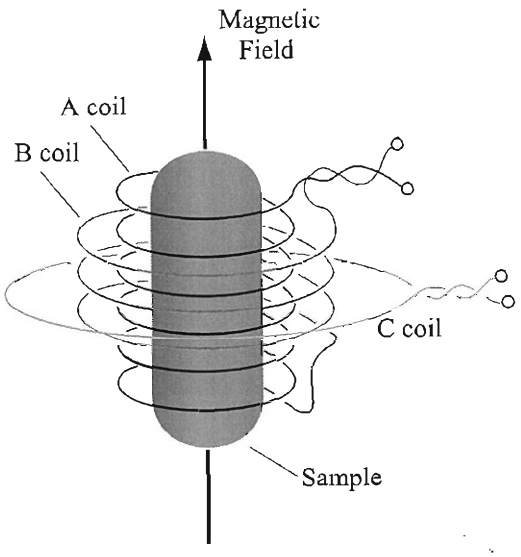

Fig. 4.27 Pick-up coil for high-magnetic field experiment.

4.2.5 High-pressure technique

Piston cylinder cell

A cross-sectional view of the clamped type piston-cylinder cell used for the electrical resistivity measurement is shown in Figs. 4.28(a) and 4.28(b). The cylinder body, clamping nuts, and obturator are made of a nonmagnetic MP35N (nickel-cobalt-chromium-molybdenum) alloy.[126] The inner piston is made of a non-magnetic tungsten carbide (WC). Samples were placed inside a Teflon cell with 4.2 mm in an inner diameter and 15 mm height. The relatively large sample chamber enabled us to put not only resistivity samples but also the pick-up coil for dHvA experiments. The electrical leads were introduced into the sample chamber through a hole of the obturator. The hole was sealed by epoxy resin (stycast 2850 FT). The sample chamber was also sealed by the Backup rings made of copper-beryllium (Cu-Be) alloy. 1 : 1 mixture of Daphne oil (7373) and petroleum ether were used as a pressure-transmitting medium. Pressure inside the cell at low temperatures was calibrated by the superconducting transition temperature of Sn.[127] High pressures up to 3 GPa are realized by this piston cylinder cell. Figure 4.28(c) shows the photograph of sample setting.

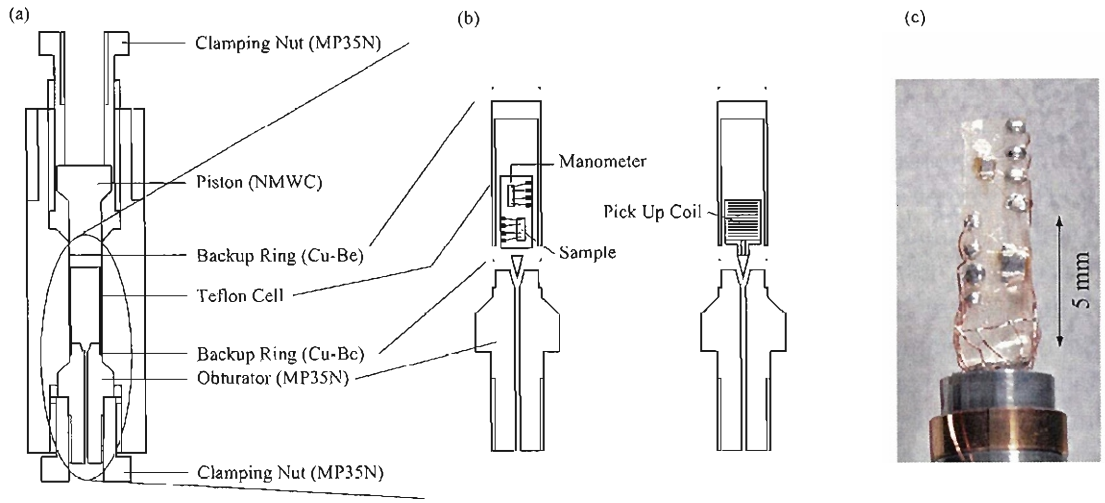

Fig. 4.28 (a) and (b) Cross-sectional views of the pressure cell, and (c) the picture of the sample setting.

Bridgman anvil cell

Figure 4.29 shows the schematic view of a Bridgman anvil type pressure cell. The Bridgman anvil cell consists of 2 opposed anvils face, together with a sample compressed in between. The cylinder body and clamping nuts are made of MP35N, and anvils are made of a non-magnetic WC. A Cu-Be pressure gasket (inner gasket) is supported by

the MP35N outer ring (gasket support) in order to tighten the inner gasket. The size of the anvil top and outer diameter of the inner gasket is 3 mm. The inner diameter and the thickness of the gasket is 1.8 mm and 0.5 mm, respectively. The photograph of a sample setting and schematic diagram are shown in Fig. 4.30. The electrical leads were introduced into the sample space through a hole of the WC anvil. Daphne oil (7373) was used as a pressure-transmitting medium. Pressure inside the cell at low temperatures was calibrated by the superconducting transition temperature of Pb.[127] High pressures up to 6 GPa are realized by using the Bridgman anvil cell.

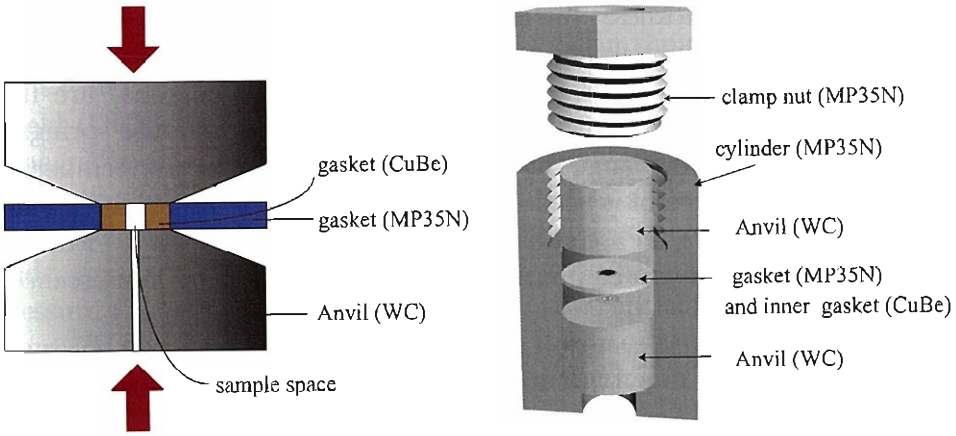

Fig. 4.29 Schematic view of a Bridgman anvil cell.

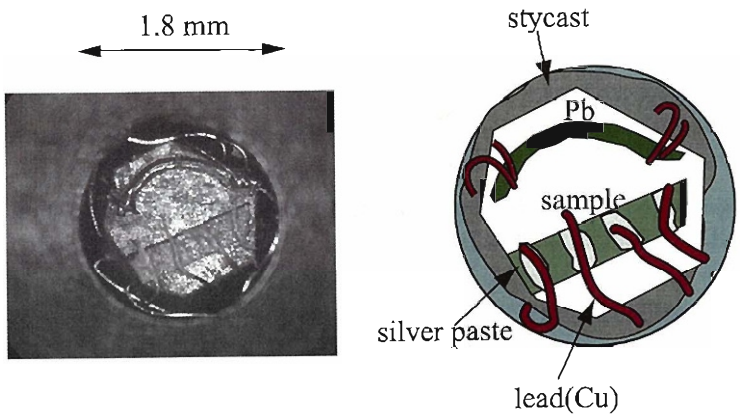

Fig. 4.30 Top view of the sample setting on the WC anvil.

Diamond anvil cell

The main concept of the diamond anvil cell is similar to that of the above mentioned Bridgman anvil-type pressure cell. A pair of diamonds is used instead of the non-magnetic WC as anvils. Figure 4.31 is a schematic view of the diamond anvil cell used in the present study. Most of parts, including bolts and clamping nuts, are made of Cu-Be. Gasket made of stainless steel (SUS304) is covered with an insulation layer of sintered Al_2O_3. The inner diameter of the gasket hole and the thickness of the gasket is about 0.35 - 0.45 mm depending on the culet size of a diamond anvil and about 0.1 mm, respectively. Due to the small sample space, the typical sample size for the pressure cell is about 0.15 mm $\times$ 0.08 mm $\times$ 0.03 mm (thickness), as shown in Fig. 4.31(c). The four point contacts are made by means of the spot welding using the gold wire of 10 microns in diameter. The electrical leads (Au or Pt foil with the thickness of 10 microns) are introduced through the surface of the gasket with the insulation layer. Several disc springs are used in order to reduce a pressure change due to thermal shrinkage at low temperatures. In the present experiment, Glycerol is used as a pressure-transmitting medium which shows better hydrostaticity above 5 GPa compared with Daphne oil (7373).[128] Pressure inside the cell at low temperatures was calibrated by the shift of the ruby fluorescence.[129,130]

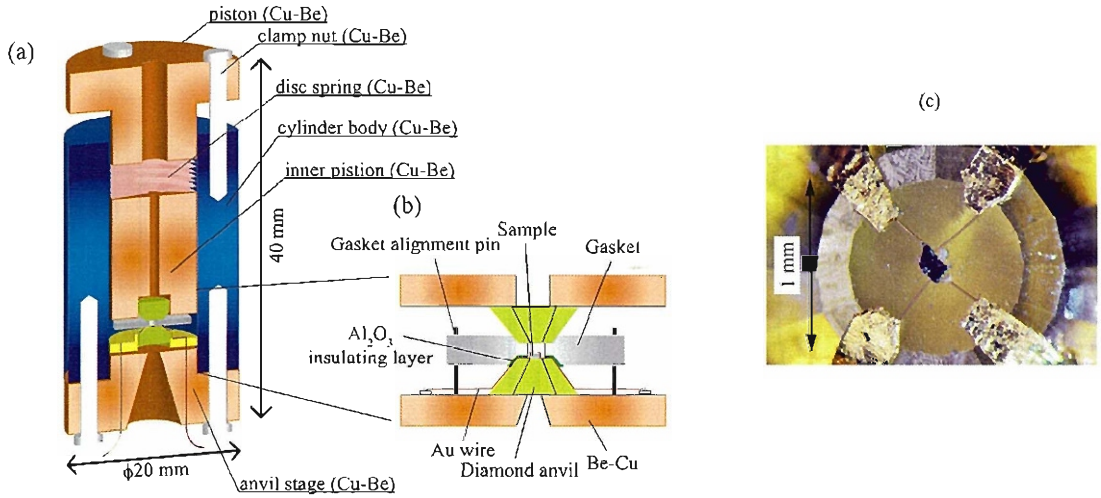

Fig. 4.31 (a) and (b) Schematic views of Diamond anvil cell, and (c) the picture of sample on the diamond anvil cell.

5 Experimental Results, Analyses, and Discussion

5.1 $CePtSi_2$ and $CeRhGe_2$

Introduction

Many interesting phenomena are observed in the ternary intermetallic compounds CeT_nX_m (T: transition metal, X: Si, Ge). For example, $CeCu_2Si_2$ with the tetragonal structure is a prototype heavy fermion superconductor with a d-wave character.[4,131] $YbCu_2Si_2$ is a valence fluctuating compound with $T_K \simeq 80$ K, and a relatively large cyclotron mass of 30 m_0 (m_0 : rest mass of an electron) was detected in the de Haas-van Alphen (dHvA) experiment.[3] In the recent systematic study of RCu_2Si_2 (R: rare earth)[132], the crystalline electric field (CEF) scheme was estimated from the specific heat, magnetic susceptibility, and magnetization, and the magnetic exchange interaction as well as the quadrupole interaction was clarified especially in $PrCu_2Si_2$. $CeTX_3$ (T: Co, Rh, Ir, X: Si, Ge) compounds are also characterized as non-centrosymmetric superconductors.[8,87,133–136] These compounds, except $CeCoSi_3$, order antiferromagnetically and become superconductive under pressure ($T_N \to 0$ for $P \to P_c$), where P_c is a critical pressure at which the Néel temperature T_N becomes zero. For example, T_N becomes zero at $P_c = 2.2$ GPa in $CeIrSi_3$ with $T_N = 5.0$ K, and $CeIrSi_3$ becomes superconductive in a wide pressure region from 1.9 to 3.5 GPa, with a maximum superconducting transition temperature $T_{sc} \simeq 1.6$ K. A huge upper critical field $H_{c2}(0) \simeq 450$ kOe has been observed for the magnetic field along the tetragonal [001] direction, which is a combined phenomenon between the electronic instability and non-centrosymmetric nature of superconductivity.

CeT_2X_2 and $CeTX_3$ mentioned above are three dimensional in the electronic states. On the other hand, $CeTX_2$ is expected to become quasi-two dimensional according to the recent report on the Ce $4d$-$4f$ resonant angle-resolved photoemission spectroscopy (ARPES) for $CeCoGe_{1.2}Si_{0.8}$.[137] The energy band calculations reveal four kinds of Fermi surfaces. Among them, band 28 and band 29 Fermi surfaces are nearly cylindrical along the b-axis ([010] direction), as observed in the ARPES experiment.

$CeTX_2$ compounds crystallize in the orthorhombic $CeNiSi_2$-type (Cmcm) structure, as shown in Fig. 5.1. The structural parameters are $a = 4.29$ Å, $b = 16.79$ Å, and $c = 4.24$ Å in $CePtSi_2$, for example.[138,139] The crystal structure consists of layers perpendicular to the [010] direction (b-axis) with the sequence of X-Ce-T-X-T-Ce-X-X-Ce-T-X-T-Ce-X. The shortest inter-Ce spacing amounts to 4.17 Å, whereas the shortest Ce-Pt and Ce-Si distances are 3.28 and 3.20 Å, respectively, in $CePtSi_2$. The primitive cell of the present crystal structure possesses two molecules of $CeTX_2$, revealing that $CeTX_2$ is a compensated metal with equal volumes of electron and hole Fermi surfaces. The Brillouin zone thus becomes flat along the b-axis, reflecting the large b-value of the lattice constant. This might favor the nearly cylindrical Fermi surfaces along the b-axis.

Very recently superconductivity was observed in $CePtSi_2$ by measuring the electrical resistivity and ac-susceptibility for a polycrystalline sample under pressure. A sharp resistivity drop due to superconductivity was observed at the superconducting transition tem-

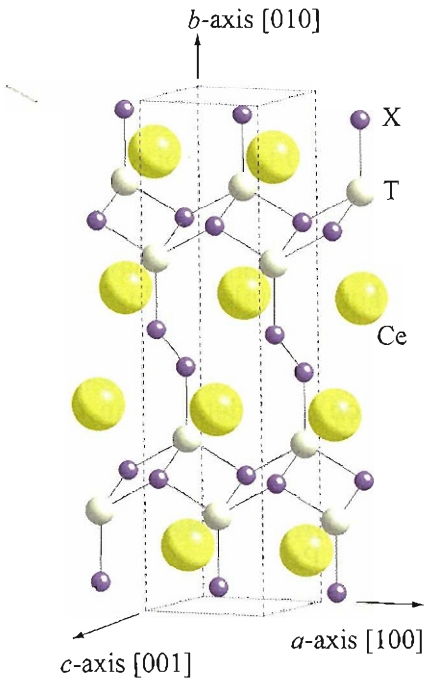

Fig. 5.1 Crystal structure of $CeTX_2$ with the $CeNiSi_2$-type orthorhombic crystal structure.

perature $T_{sc} = 0.14$ K, although zero-resistivity was not attained in this experiment.[140]

In the present study, we grew a single crystal of $CePtSi_2$ to clarify the superconducting property. Furthermore, we synthesized $CeTX_2$ compounds and found that $CeRhGe_2$ also crystallizes in the $CeNiSi_2$-type orthorhombic structure. The magnetic and superconducting properties of $CeRhGe_2$ were studied.

Experimental procedure

$CeTSi_2$ (T: transition metal) compounds are known to crystallize in the $CeNiSi_2$-type orthorhombic structure (Cmcm) for T = Co, Rh, Ir, Ni, and Pt, and the other compounds belong to another crystal structure.[141] On the other hand, $CeTGe_2$ compounds crystallize in the $CeNiSi_2$-type structure only for T = Fe, Co, and Ni.[142,143]

First we investigated $CeTGe_2$ by arc-melting 3N (99.9% pure)-Ce, 3N- or 4N-T, and 5N-Ge materials. It was found that arc-melted ingots of $CeCoGe_2$ and $CeNiGe_2$, together with $CeRhGe_2$, reveal several flat planes, as shown in Fig. 4.19(a) for $CeRhGe_2$, as described in Chap.3. From this procedure, $CeRhGe_2$ was found to crystallize in the $CeNiSi_2$-type orthorhombic structure. In fact, we verified the stoichiometry of the crystal using an electron probe micro-analyzer. Furthermore, x-ray diffraction measurements were performed using a single crystal sample grown by the Bridgman method, where arc-melted $CeRhGe_2$ polycrystals were sealed in a Mo-crucible and were heated up to 1400

Table 5.I Lattice parameters and positions of atoms in $CeRhGe_2$.

$a = 4.333$ Å $b = 17.115$ Å $c = 4.319$ Å			
atom	position		
	x	y	z
Ce	0	0.108	0.25
Rh	0	0.319	0.25
Ge1	0	0.460	0.25
Ge2	0	0.750	0.25

°C in an electric furnace. A single crystal ingot with a flat b-plane, *i.e.*, the (010) plane, is shown in Fig. 4.20(a). The lattice parameters and site positions of the constitutional elements were determined from the X-ray diffraction measurements of the single crystal sample, as summarized in Table 5.I. Ternary Ce-Rh-Ge compounds were precisely investigated in the previous study,[144] as shown in Fig. 5.2, but the existence of $CeRhGe_2$ was not identified. $CeRhGe_2$ is thus a new compound.

We also grew a single crystal ingot of $CePtSi_2$ by the Czochralski method from an off-stoichiometric concentration of $CePt_{1.1}Si_{2.2}$, after the previous report[123], as described in Chap.4. Figure 4.13 shows a single crystal ingot of $CePtSi_2$ grown in a tetra-arc furnace. The direction of the single crystal sample was determined from the x-ray Laue pattern for $CeRhGe_2$ and $CePtSi_2$.

The electrical resistivity was measured by the conventional four-probe DC and/or AC method. The magnetic susceptibility and magnetization measurements were carried out using a commercial SQUID magnetometer. The high-field magnetization was measured by the standard pick up coil method using a long-pulse magnet with a pulse duration of 50 msec. The specific heat was measured by the quasi-adiabatic heat pulse method. The electrical resistivity was also measured under pressure using a piston cylinder cell, a Bridgman anvil cell with a mixture of Daphne 7373 and petroleum ether as a pressure transmitting medium, and a diamond anvil cell with glycerine as a pressure transmitting medium.

Experimental results and analyses

First we show the temperature dependence of the electrical resistivity for the current J along three principal directions in $CeRhGe_2$, as shown in Fig. 5.3(a). The resistivity for $J \| b$-axis is much larger than those for $J \| a$- and c-axes. The steep decrease in the resistivity at low temperatures is due to antiferromagnetic ordering with the Néel temperature $T_N = 7.6$ K, discussed later.

Similarly, we measured the electrical resistivity of $CePtSi_2$, as shown in Fig. 5.3(b), together with the previous resistivity data for $CeNiGe_2$[145] shown in Fig. 5.3(c). The

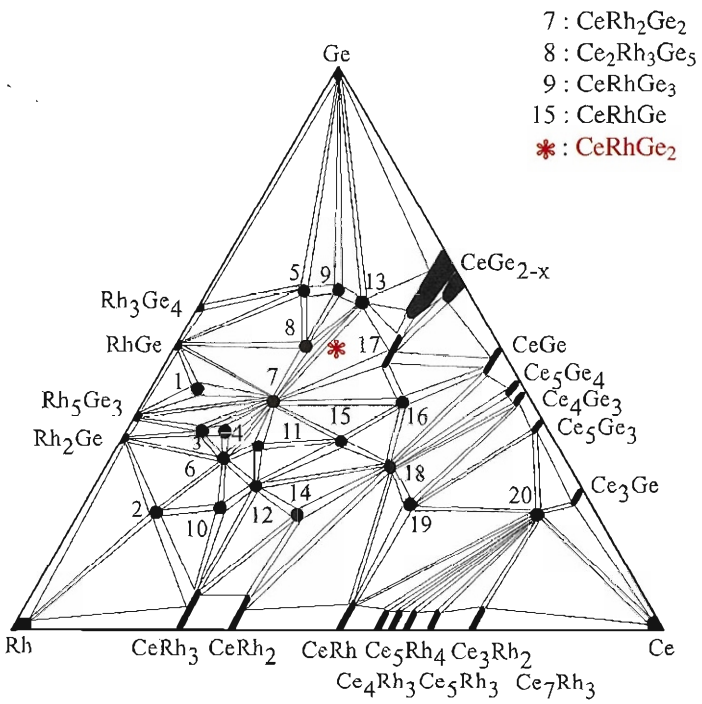

Fig. 5.2 Ternary Ce-Rh-Ge alloy phase diagram, where the existence of $CeRhGe_2$ was not identified in the previous diagram, cited from ref. 144. Among twenty Ce-Rh-Ge compounds, compounds 7, 8, 9, and 15 are shown, together with the new compound $CeRhGe_2$.

anisotropy of electrical resistivity between $J \| b$-axis and $J \perp b$-axis is distinguished in $CePtSi_2$ and $CeNiGe_2$. The corresponding Fermi surface is most likely nearly cylindrical along the b-axis, as mentioned above.

Figures 5.4(a)-5.4(c) show the temperature dependences of magnetic susceptibility, inverse susceptibility, and magnetization of $CeRhGe_2$, respectively. The magnetic susceptibility follows the Curie-Weiss law at high temperatures. The effective magnetic moment $\mu_{\rm eff}$ and paramagnetic Curie temperature $\theta_{\rm P}$ are $\mu_{\rm eff}$ = 2.41 $\mu_{\rm B}$/Ce and $\theta_{\rm P}$ = -26.3 K for $H \| a$-axis, $\mu_{\rm eff}$ = 2.39 $\mu_{\rm B}$/Ce and $\theta_{\rm P}$ = -69.9 K for $H \| b$-axis, and $\mu_{\rm eff}$ = 2.44 $\mu_{\rm B}$/Ce and $\theta_{\rm P}$ = 25.8 K for $H \| c$-axis, respectively. The effective Bohr magnetic moment is very close to the moment of a free Ce^{3+} ion, 2.54 $\mu_{\rm B}$.

The magnetic susceptibility for $H \| c$-axis in the inset of Fig. 5.4(a) decreases steeply below $T_{\rm N}$ = 7.6 K, indicating the antiferromagnetic ordering, while the susceptibility for $H \| a$- and b-axis increases slightly below $T_{\rm N}$ = 7.6 K. It is concluded that the antiferromagnetic easy-axis corresponds to the c-axis, while the a- and b-axes are hard axes.

Figure 5.4(c) shows the corresponding typical magnetization curves. It is clear that the c-axis is an easy-axis in the magnetization. The ordered moment is estimated to be 1.3 $\mu_{\rm B}$/Ce. Thin solid lines in Fig. 5.4 are the result of CEF calculations, which will be

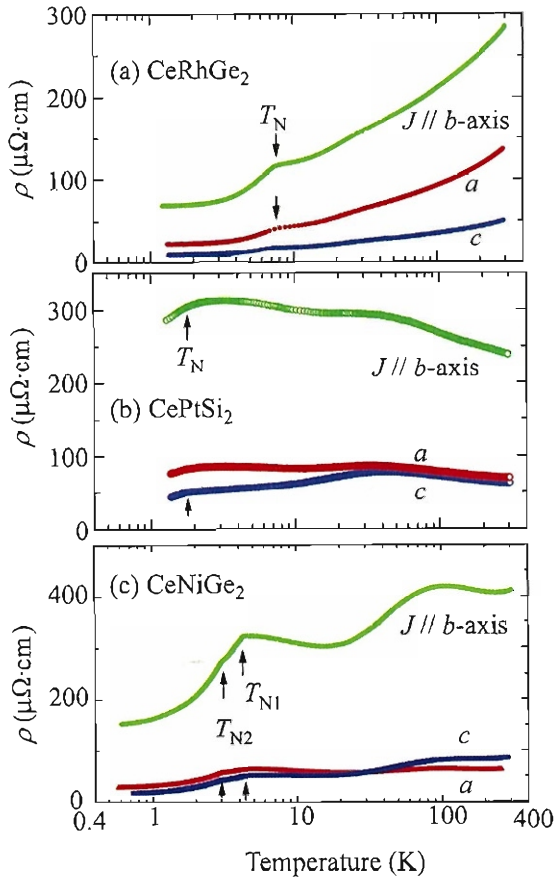

Fig. 5.3 Electrical resistivity for the current J along three principal directions in (a) $CeRhGe_2$, (b) $CePtSi_2$, and (c) $CeNiGe_2$ cited from ref. 145.

discussed later.

From the differential magnetization dM/dH curves and temperature dependences of magnetization at several magnetic fields, as shown in Figs. 5.5(a) and 5.5(b), respectively, we constructed the magnetic phase diagram, as shown in Fig. 5.6. This means that there exist three antiferromagnetic phases named AF1, AF2, and AF3.

Next we show in Figs. 5.7 and 5.8, the corresponding susceptibility, inverse magnetic susceptibility, and magnetization curves of $CePtSi_2$ and $CeNiGe_2$, respectively. The magnetic anisotropy is approximately the same in $CeRhGe_2$, $CePtSi_2$, and $CeNiGe_2$. Solid lines are the result of CEF calculations, discussed later.

We measured the low-temperature specific heat C in the form of C/T for $CeRhGe_2$ and $CePtSi_2$, as shown in Figs. 5.9(a) and 5.9(b), respectively. A λ-type antiferromagnetic transition was found at $T_N = 7.6$ K in $CeRhGe_2$. The inset shows the T^2-dependence of C/T. The electronic specific heat coefficient was obtained as $\gamma = 70$ mJ/(K^2·mol) for $CeRhGe_2$. The magnetic entropy obtained by integrating C/T as a function of temper-

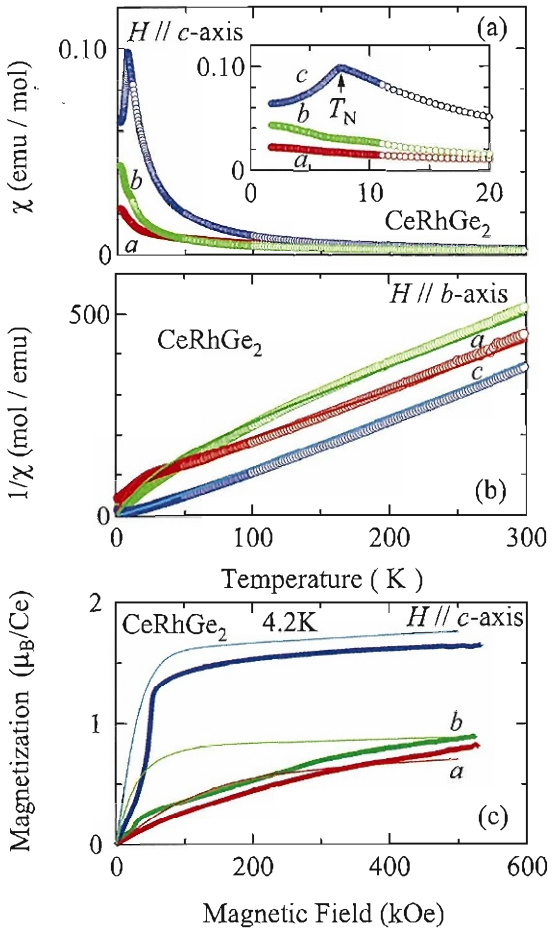

Fig. 5.4 (a) Temperature dependences of magnetic susceptibility and (b) inverse magnetic susceptibility, and (c) magnetization curves at 4.2 K for the magnetic field along three principal field directions in $CeRhGe_2$. Thin solid lines are the result of CEF calculations.

ature was roughly estimated to be $0.75R\ln 2$ at $T_N = 7.6$ K, indicating that the ground state is a doublet in the CEF scheme.

Similarly, we observed the antiferromagnetic ordering at $T_N = 1.9$ K and obtained a large γ value of 800 mJ/(K^2·mol) in $CePtSi_2$. The magnetic entropy was roughly estimated to be $0.35R\ln 2$ at $T_N = 1.9$ K. The small magnetic entropy is mainly due to the Kondo effect. The present result for $CePtSi_2$ is approximately the same as that in the previous report.[123)]

In order to clarify the magnetic structure of $CeRhGe_2$, powder and single crystal neutron diffraction experiments were carried out using the thermal triple-axis spectrometer PONTA (5G) installed at the research reactor JRR-3M in the Japan Atomic Energy Agency. The single crystals were crushed and carefully milled to a powder for the neutron

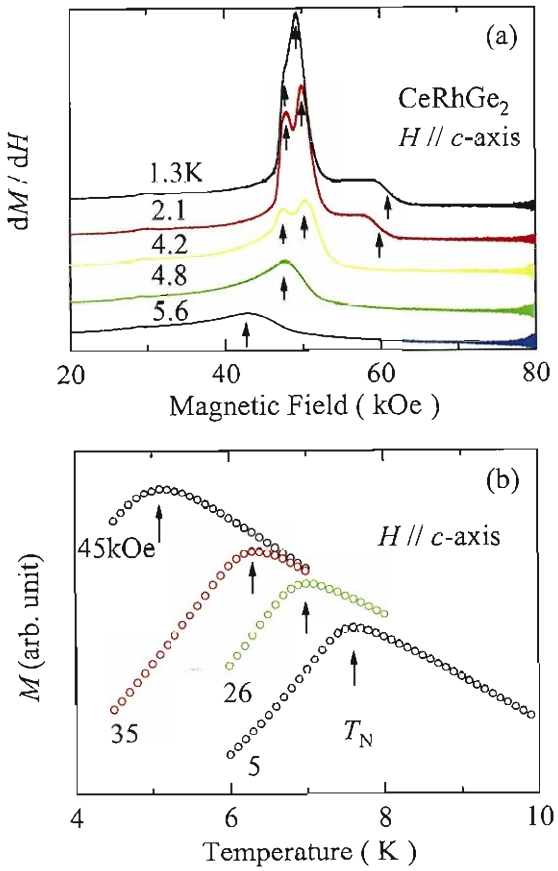

Fig. 5.5 (a) Magnetic field dependence of dM/dH curves at several temperatures, and (b) temperature dependence of magnetization in several magnetic fields for $H \| c$-axis in $CeRhGe_2$.

powder diffraction experiment. Elastic scattering was measured with neutrons of energy $E = 14.7$ meV monochromatized and analyzed with pyrolytic graphite crystals.

Figure 5.10 shows powder-diffraction patterns at 3.8 and 10 K. Around $2\theta = 16°$, the (020) nuclear reflection was observed at both temperatures. At 3.8 K, two other distinct peaks were observed around $2\theta = 18°$ and 21°, which correspond to reciprocal lattice vectors of $|Q| = 0.83$ and 0.97 $Å^{-1}$, respectively, as indicated by arrows. Since both peaks appear just below $T_N = 7.6$ K, they are attributed to the magnetic reflections due to the antiferromagnetic ordering. These Q values cannot be explained by a simple antiferromagnetic structure.

In order to determine the magnetic structure for $CeRhGe_2$, we searched for superlattice reflections on $(h\ k\ 0)$ and $(h\ 0\ l)$ planes using a single crystal. On the $(h\ k\ 0)$ plane, we carried out several line scans and also constant Q scans with $|Q| = 0.83$ and 0.97 $Å^{-1}$, but no indication of a superlattice reflection was observed. Then we continued to study superlattice reflections on $(h\ 0\ l)$ planes. After several attempts of line scans, we carried

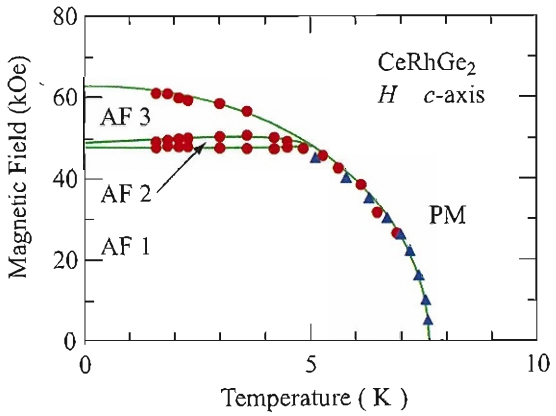

Fig. 5.6 Magnetic phase diagram for $H \| c$-axis in $CeRhGe_2$, where closed circles and triangles were obtained by the pulsed-field magnetization and SQUID magnetization measurements, respectively.

out a constant Q scan with $|Q| = 0.83$ Å^{-1} and observed a remarkable superlattice peak at (0.475 0 0.330).

Figure 5.11(a) shows the corresponding line scans around (0.475 0 0.330) at several temperatures below 8.1 K. Since the peak appeared below $T_N = 7.6$ K, it is attributed to a magnetic origin, implying an incommensurate antiferromagnetic structure. We measured the temperature dependence of the integrated intensity of the magnetic reflection at (0.475 0 0.330), as shown in Fig. 5.11(b). The antiferromagnetic peak intensity increases below $T_N = 7.6$ K, indicating a clear temperature dependence associated with the antiferromagnetic ordering.

We also searched for antiferromagnetic peaks with a symmetric position of (k_1 0 k_2): $k_1 = 0.475$ and $k_2 = 0.330$ such as (2-k_1 0 k_2), (k_1 0 2-k_2) and so forth. The detected antiferromagnetic peak positions (shown by crosses) and their intensities, together with the nuclear peak positions (closed circles) are summarized in Fig. 5.12(a). The integrated intensity of the magnetic scattering for a non-polarized neutron beam is given as follows:

$$I_{mag} = Ap^2 \mid F_M(Q) \mid^2 L(\theta)(\sin^2\alpha), \tag{5.1}$$

and

$$p = \frac{\gamma e^2}{2m_e c^2} = 0.2696 \times 10^{-12}(\text{cm}), \tag{5.2}$$

where A, $L(\theta)$, sin α, and $F_M(Q)$ are the scale factor, Lorenz factor, angle factor, and magnetic structure factor, respectively. Neutrons have a magnetic scattering length for the projection of the magnetic moment onto the plane perpendicular to the scattering vector Q, and thus, the intensity is proportional to $\sin^2\alpha$, which is called as angle factor.

In order to confirm the direction of the magnetic moment, the integrated intensities of the observed magnetic peaks were measured and plotted as a function of $\sin^2\alpha$, where α is

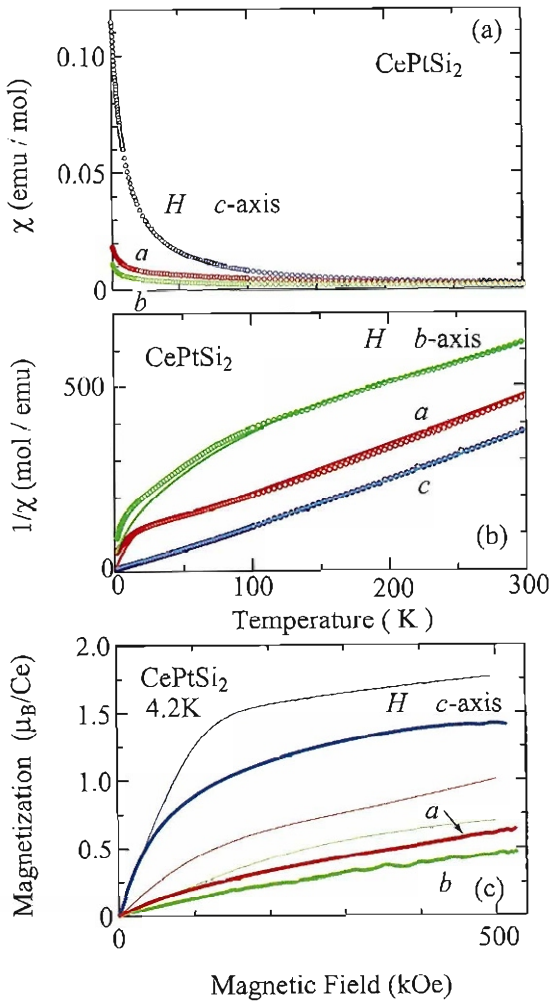

Fig. 5.7 Temperature dependences of (a) magnetic susceptibility and (b) inverse magnetic susceptibility, and (c) magnetization curves at 4.2 K for the magnetic field along three principal directions in $CePtSi_2$. Thin solid lines are the result of CEF calculations.

the angle between the scattering vector Q and the c^*-axis. As shown in Fig. 5.12(b), the normalized integrated intensity exhibits a linear relation with respect to $\sin^2\alpha$. Therefore, the direction of the magnetic moment is parallel to the c-axis, which is consistent with the results of magnetic susceptibility and magnetization curves.

In order to find the other antiferromagnetic reflections observed in the powder neutron diffraction measurement, we carried out another constant Q scan with $|Q| = 0.97$ Å^{-1}, but no peak was observed on the $(h\ 0\ l)$ plane. Therefore we searched for the second magnetic reflection in three dimensional reciprocal space. In order to make the survey more efficient, we estimated the magnetic peak position in connection with the first magnetic peak at $(k_1\ 0\ k_2)$ and $|Q| = 0.97$ Å^{-1}. An expected antiferromagnetic peak is at

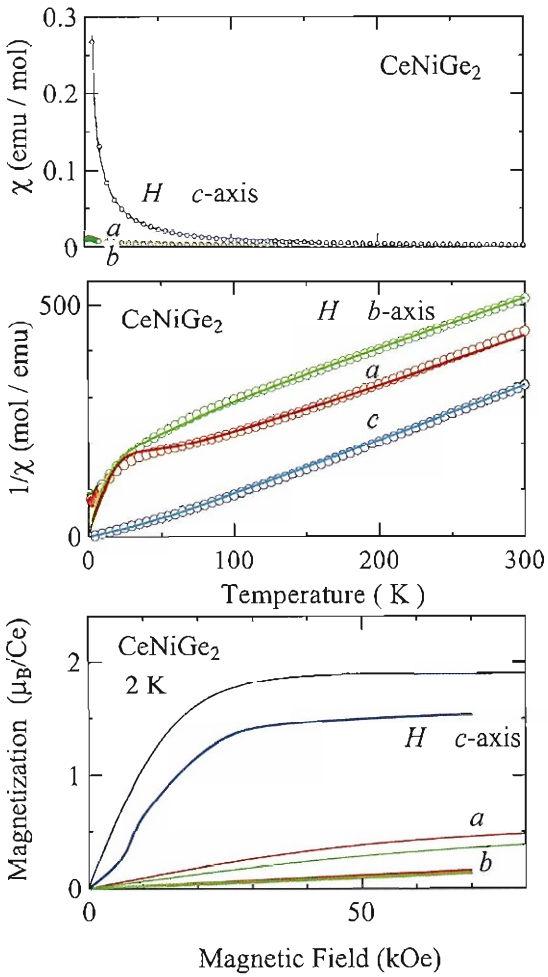

Fig. 5.8 Temperature dependences of (a) magnetic susceptibility and (b) inverse magnetic susceptibility, and (c) magnetization curves at 2 K for the magnetic field along three principal directions in $CeNiGe_2$. Thin solid lines are the result of CEF calculations.

(1-k_1 1 k_2). It should be noted that this experiment was performed in another triple axis spectrometer (AKANE) installed in the guide hall in JRR-3M with the neutron energy of 19.47 meV (λ = 2.05 Å). Figure 5.13 shows the line scans at (0.525 1 0.330) at 4.35 and 10.3 K, which are below and above T_N = 7.6 K, respectively. It is noteworthy that we found the second magnetic reflection at (0.525 1 0.330) = (1-k_1 1 k_2).

On the basis of these experimental results, we illustrated one of possible magnetic structures of $CeRhGe_2$ in Fig. 5.14. In this crystal structure, cerium atoms occupy the 4*c* site of the *Cmcm* space group. In this case, following three antiferromagnetic models are plausible for the magnetic structure of $CeTX_2$[146] according to the Bertaut method based on the irreducible representation theory:[147] (i) A-type : (+) S_1 and S_4, (-) S_2 and

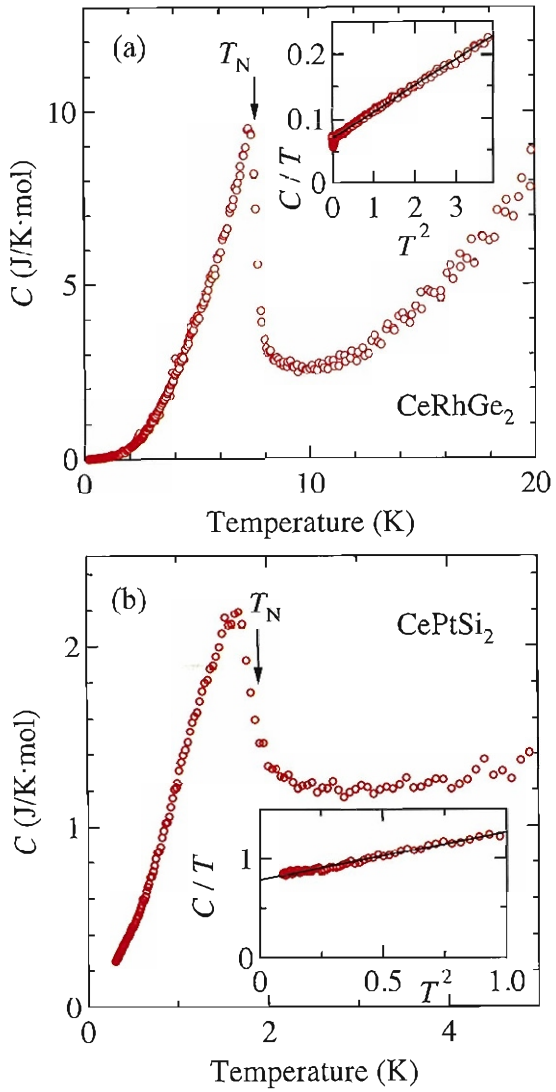

Fig. 5.9 Low-temperature specific heat in (a) $CeRhGe_2$ and (b) $CePtSi_2$. Insets show C/T as a function of T^2.

S_3, (ii) C-type : (+) S_1 and S_2, (-) S_3 and S_4, and (iii) G-type : (+) S_1 and S_3, (-) S_2 and S_4, where (+) and (-) correspond to the spin orientation of the magnetic ions at the S_1 (0, y, 1/4), S_2 (0, -y, 3/4), S_3 (1/2, 1/2+y, 1/4), and S_4 (1/2, 1/2-y, 3/4) sites. Among them, the model (ii) C-type magnetic structure is most likely applicable to $CeRhGe_2$, as in the case of $CeCu_{0.86}Ge_2$.[146] Since the magnetic structure is incommensurate, the entire magnetic structure is not shown in Fig. 5.14.

First we confirmed whether or not superconductivity is truly realized in $CePtSi_2$ by measuring the electrical resistivity under pressure. This was necessary because the

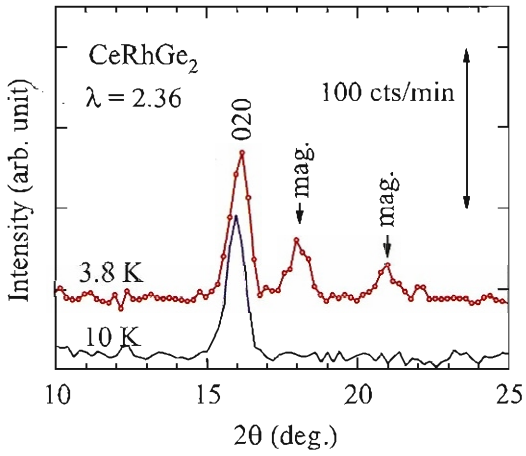

Fig. 5.10 Neutron powder diffraction patterns at 3.8 and 10 K for $CeRhGe_2$.

zero-resistivity was not attained in the previous report.[140] This often occurs in pressure-induced superconductivity, mainly due to sample quality, a very narrow superconducting region in the pressure phase diagram and inhomogeneous pressures. In the previous experiment using a piston cylinder cell in $CeRh_2Si_2$, zero-resistivity was obtained in a very narrow pressure region from 1.03 to 1.08 GPa, although the resistivity drop due to superconductivity was obtained from 0.97 to 1.20 GPa.[69]

Under the consideration of a narrow superconducting pressure region in $CePtSi_2$, we carried out the resistivity measurement under pressure, as shown in Fig. 5.15. The temperature dependences of overall resistivity is approximately the same at different pressures. The resistivity peak at 30 K shifts to a higher temperature of 40−50 K under pressures of 1.22−1.69 GPa, as shown in Fig. 5.15(a). Zero-resistivity due to superconductivity is obtained in a narrow pressure region centered around 1.5 GPa, namely, from 1.3 to 1.8 GPa, as shown in Fig. 5.15(b). At 1.51 GPa, the onset of superconductivity occurs at 0.18 K and zero-resistivity is obtained below $T_{sc} = 0.16$ K. Figure 5.16 shows the pressure dependences of the Néel temperature T_N, cited from ref. 140, and the superconducting transition temperature T_{sc} obtained in the present experiment.

We measured the electrical resistivity by applying magnetic fields, as shown in Fig. 5.17. The experiments were carried out for three different samples. Zero-resistivity was not found at the same temperature, although the onset of superconductivity was realized at almost the same temperature. The superconducting transition temperature shifts to a lower temperature with increasing the magnetic field.

Figure 5.18 shows the upper critical field H_{c2} for three principal directions, which is defined as the zero-resistivity even under magnetic field. The slope of H_{c2} at T_{sc}, $-dH_{c2}/dT$, and $H_{c2}(0)$ are approximately obtained as $-dH_{c2}/dT = 350$ kOe/K at $T_{sc} = 0.14$ K, and $H_{c2}(0) = 11$ kOe for $H \| a$-axis, $-dH_{c2}/dT = 240$ kOe/K at $T_{sc} = 0.16$ K, and $H_{c2}(0) = 22$ kOe for $H \| b$-axis, and $-dH_{c2}/dT = 89$ kOe/K at $T_{sc} = 0.15$ K, and $H_{c2}(0) = 3$ kOe for $H \| c$-axis, respectively. The upper critical field is highly anisotropic,

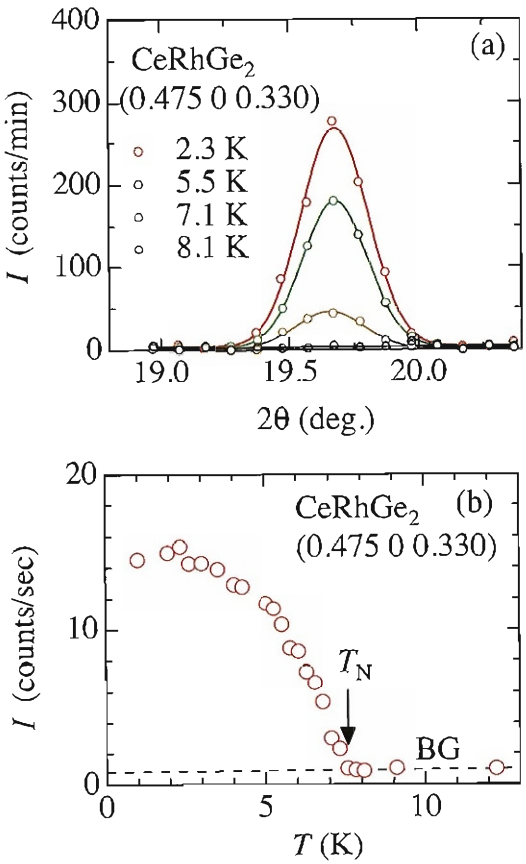

Fig. 5.11 (a) Line scan around (0.475 0 0.330) at several temperatures and (b) temperature dependence of the integrated intensity of the magnetic reflection in $CeRhGe_2$.

which will be discussed in the next section.

Next we carried out similar pressure experiments for $CeRhGe_2$ using the piston cylinder and Bridgman anvil type pressure cells, revealing that higher pressure are needed in order to suppress the antiferromagnetism of $CeRhGe_2$. Furthermore, we studied the effect of pressure on the electronic state of this compound using the diamond anvil cell. Figure 5.19 shows the temperature dependence of the electrical resistivity under high pressures up to 7.1 GPa.

With increasing pressure, the Néel temperature $T_N = 7.6$ K increases slightly up to about 3.5 GPa, then decreases steeply, and almost becomes zero around 7 GPa. At 7.1 GPa, the electrical resistivity exhibits a sudden drop below $T_{sc} = 0.45$ K. This is most likely due to the superconducting transition. The corresponding pressure phase diagram is shown in Fig. 5.20. The critical pressure P_c is estimated to be about 7 GPa.

Finally we note the pressure experiments for $CeNiGe_2$ with a Néel temperature $T_{N1} = 3.9$ K and another magnetic transition temperature $T_{N2} = 3.2$ K. The electrical resistivity

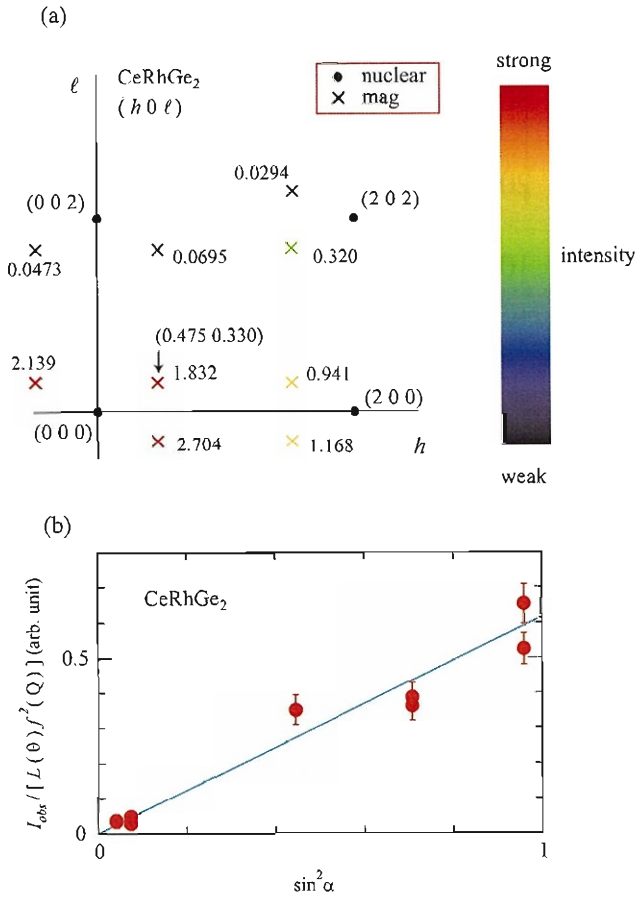

Fig. 5.12 (a) Observed nuclear (closed circles) and magnetic (crosses) reflections on the (h 0 l) space in CeRhGe$_2$. The integrated intensity for each reflection is shown following the color chart. (b) Normalized integrated intensity with respect to the angle factor sin$^2\alpha$.

and ac-specific heat were measured up to 2 GPa, indicating that the Néel temperature decreases monotonically down to 1.35 K at 1.9 GPa.[148] The critical pressure was roughly estimated to be P_c = 3.5 GPa. Another experiment, however, indicated saturated behavior of T_N in the pressure region from 0.5 to 2 GPa, suggesting a large P_c value.[149]

Discussion

On the basis of the above experimental results of magnetic susceptibility and magnetization, we constructed the CEF scheme for CeTX$_2$. We performed the CEF analyses based on these data. The CEF Hamiltonian for the orthorhombic site symmetry is given by

$$\mathcal{H}_{CEF} = B_2^0 O_2^0 + B_4^0 O_4^0 + B_4^4 O_4^4 + B_6^0 O_6^0 + B_6^4 O_6^4, \tag{5.3}$$

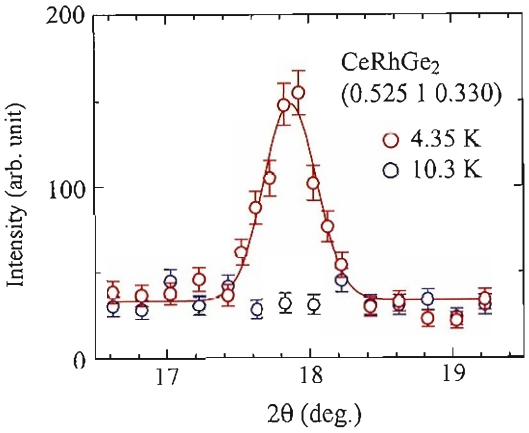

Fig. 5.13 $\theta - 2\theta$ scan at (0.525 1 0.330) for another magnetic reflection measured at 4.35 ($< T_{\mathrm{N}} = 7.6$ K) and 10.3 K ($> T_{\mathrm{N}}$) in $CeRhGe_2$.

where B_l^m are the CEF parameters and O_l^m are the Stevens operators.[15,16] The magnetic susceptibility based on the CEF model, χ^i_{CEF} ($i = x, y, z$), is given by

$$\chi^i_{\mathrm{CEF}} = N\frac{(g_J\mu_{\mathrm{B}})^2}{Z}\left(\frac{\sum_n |\langle n|J_i|n\rangle|^2}{k_{\mathrm{B}}T}e^{-\frac{E_n}{k_{\mathrm{B}}T}} + \sum_{n\neq m}|\langle m|J_i|n\rangle|^2\frac{e^{-\frac{E_n}{k_{\mathrm{B}}T}} - e^{-\frac{E_m}{k_{\mathrm{B}}T}}}{E_m - E_n}\right), \tag{5.4}$$

and

$$Z = \sum_n e^{-\frac{E_n}{k_{\mathrm{B}}T}}, \tag{5.5}$$

where g_J is the Landé g-factor and J_i is the component of angular momentum. The magnetic susceptibility χ_i, including the molecular field contribution λ_i and a temperature-independent susceptibility χ^i_0, is given as follows:

$$\chi_i = \frac{1}{\frac{1}{\chi^i_{\mathrm{CEF}}} - \lambda_i} + \chi^i_0. \tag{5.6}$$

We also calculated the magnetization using the following formula:

$$M_i = -\sum_n \frac{g_J\mu_{\mathrm{B}}\langle n|J_i|n\rangle}{Z}e^{-\frac{E_n}{k_{\mathrm{B}}T}}, \tag{5.7}$$

where the eigenvalue E_n and the eigenfunction $|n\rangle$ are determined by diagonalizing the total Hamiltonian:

$$\mathcal{H} = \mathcal{H}_{\mathrm{CEF}} - g_J\mu_{\mathrm{B}}J_i(H + \lambda_i M_i), \tag{5.8}$$

where $\mathcal{H}_{\mathrm{CEF}}$ is given by eq. (5.3), the second term is the Zeeman term and the third one is the molecular field.

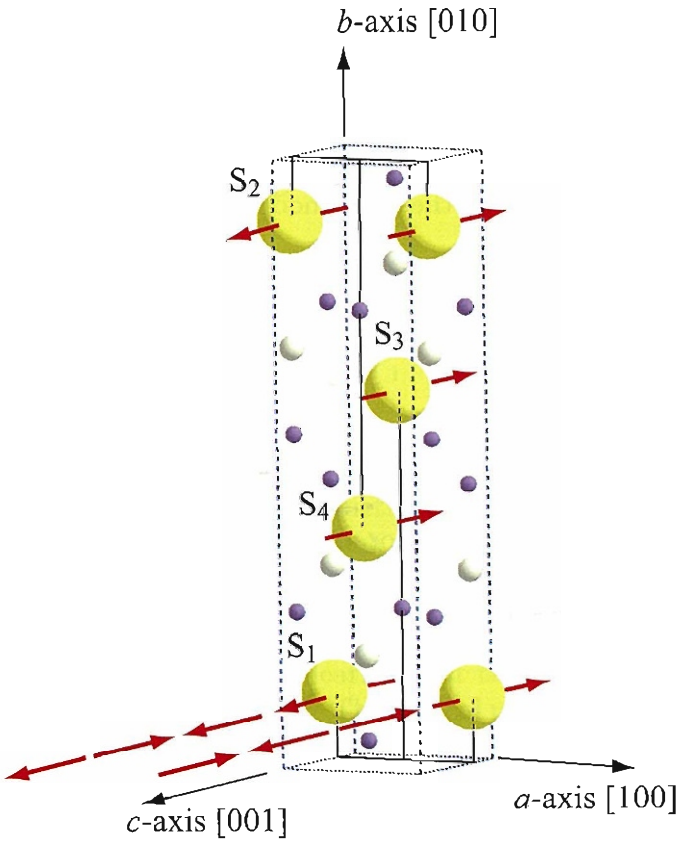

Fig. 5.14 Possible magnetic structure model of $CeRhGe_2$.

Thin solid lines for the inverse magnetic susceptibility in Figs. 5.4(b), 5.7(b), and 5.8(b), and the magnetization in Figs. 5.4(c), 5.7(c), and 5.8(c) are the results of CEF calculations for $CeRhGe_2$, $CePtSi_2$, and $CeNiGe_2$, respectively, which well reproduce the

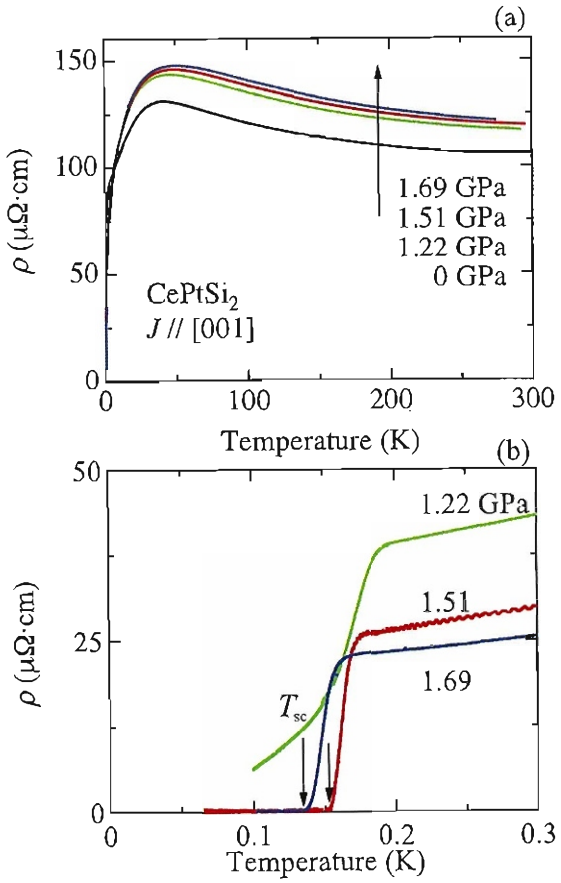

Fig. 5.15 Temperature dependence of the electrical resistivity under pressures in $CePtSi_2$.

experimental data. The CEF parameters of B_l^m, energy levels, and the corresponding wave functions for $CeTX_2$ are summarized in Tables 5.II, 5.III, and 5.IV, respectively. Here, we take the a-, b- and c-axes as the x-, y- and z-axes, respectively, for $CeRhSi_2$ and $CePtSi_2$. The CEF parameters for $CeNiGe_2$ are taken from the ref. 145.

The anisotropy of magnetic susceptibility and magnetization is approximately the same in these compounds. Overall, the CEF schemes are thus approximately the same. The splitting energies from the ground state doublet to the first and second excited doublets, Δ_1 and Δ_2, are $\Delta_1 = 83$ K and $\Delta_2 = 579$ K in $CeRhGe_2$, $\Delta_1 = 88$ K and $\Delta_2 = 826$ K in $CePtSi_2$, and $\Delta_1 = 93$ K and $\Delta_2 = 653$ K in $CeNiGe_2$. Previous CEF calculations for $CePtSi_2$ gave $\Delta_1 = 105$ K and $\Delta_2 = 433$ K.[123)]

Next we discuss the anisotropy of the electrical resistivity in $CeTX_2$ and the upper critical field H_{c2} in the superconductivity in $CePtSi_2$. The former anisotropy in $CeTX_2$, especially that in $CePtSi_2$ and $CeNiGe_2$, is simply understood on the basis of the nearly cylindrical Fermi surfaces along the b-axis, as noted above. The latter anisotropy, how-

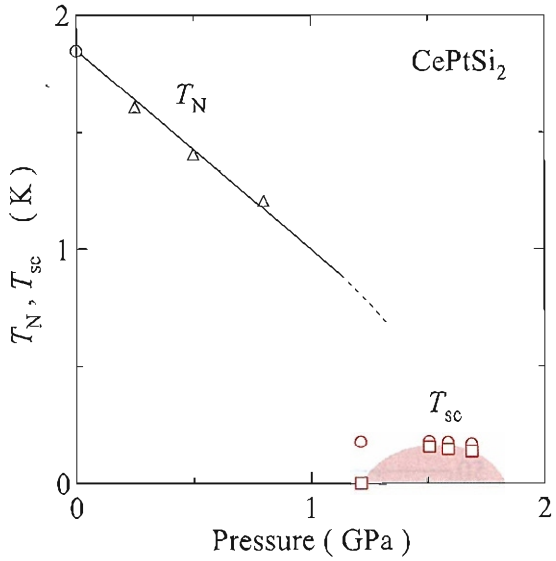

Fig. 5.16 Phase diagram of the Néel temperature T_N and superconducting transition temperature T_{sc} as a function of pressure in $CePtSi_2$, where onset and zero resistivity data for superconductivity are shown by circles and squares, respectively. The pressure dependence of T_N shown by triangles was cited from ref. 140.

ever, cannot be understood in terms of the nearly cylindrical Fermi surfaces. This is because the H_{c2} value for $H\|b$-axis should be small compared with those for $H\|a$- and c-axes if the effective mass model based on the nearly cylindrical Fermi surfaces is applicable to the upper critical field in $CePtSi_2$. The experimental result of H_{c2} is highly different from the present simple prediction, as shown in Fig. 5.18.

To understand the topology of the Fermi surfaces, energy band calculations were carried out for $CePtSi_2$ using a relativistic linearized-augmented plane wave method with a local density approximation.[150] The experimental values of the lattice parameter are used in the calculation. The band structure and the Fermi surface were calculated by the same calculational procedure as that used for $CeCoSi_2$.[151] The $4f$-itinerant Fermi surfaces are shown in Fig. 5.21, revealing semimetallic small closed Fermi surfaces. These Fermi surfaces are highly different from the nearly cylindrical Fermi surfaces in $CeCoGe_{1.2}Si_{0.8}$.[137]

Next, the Fermi energy is shifted downward by 3 mRy for the 28th hole Fermi surface of $CePtSi_2$, while the Fermi energy is shifted upward by 3 mRy for the 29th and 30th electron Fermi surfaces. Thus, obtained Fermi surfaces are cylindrical along the b-axis and also along the a-axis, as shown in Fig. 5.22. The Fermi surfaces are anisotropic, but open orbits are present for three principal field directions. The present anisotropy of H_{c2} cannot be simply explained by the anisotropic cyclotron mass based on the Fermi surfaces.

It is also noticed that the paramagnetic suppression of H_{c2} is realized in $CePtSi_2$. $H_{c2}(0)$ values were roughly estimated to be 33, 26, and 9.1 kOe for $H\|a$-, b-, and c-axes,

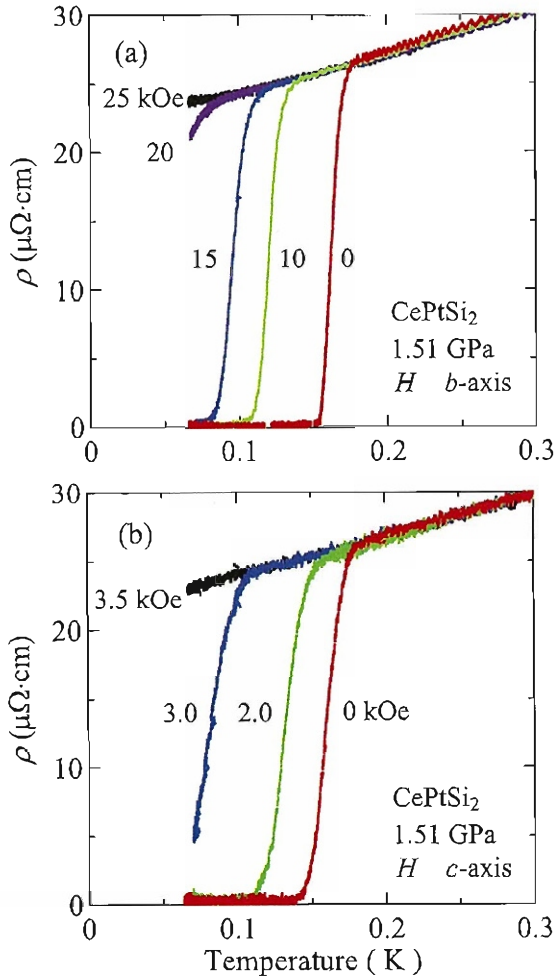

Fig. 5.17 Temperature dependence of the electrical resistivity in different magnetic fields for (a) $H \| b$- and (b) c-axes at 1.51 GPa in $CePtSi_2$.

respectively, using the Werthamer Helf and Hohenberg dirty-limit formula:[102]

$$H_{c2}(0) = 0.693 \left| \frac{dH_{c2}}{dT} \right|_{T_c} T_c. \tag{5.9}$$

These $H_{c2}(0)$ values are strongly reduced to the experimental values of $H_{c2}(0) = 11$, 22, and 3 kOe for $H \| a$-, b-, and c-axes, respectively. The amount of reduction depends on the field direction, and there is a possibility that the paramagnetic suppression is not uniform but anisotropic. From these discussions, it is not easy to explain the present anisotropy of H_{c2} in $CePtSi_2$, but the H_{c2} values are closely related to the anisotropic Fermi surfaces and paramagnetic suppression.

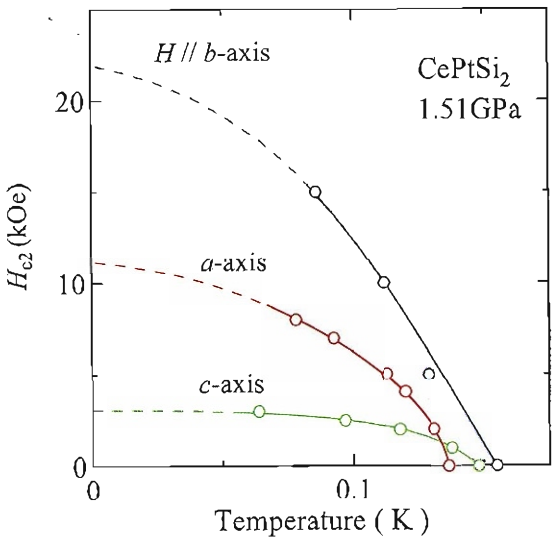

Fig. 5.18 Temperature dependence of the upper critical field for three principal directions in $CePtSi_2$. Solid and broken lines are guides to the eye.

Summary

We measured the electrical resistivity, magnetic susceptibility, magnetization, specific heat, and neutron scattering for antiferromagnets $CeRhGe_2$ and $CePtSi_2$, and we also performed electrical resistivity measurements under pressure. Experimental results are summarized as follows:

1) $CeRhGe_2$ was found to be a new compound with the orthorhombic $CeNiSi_2$-type structure. It orders antiferromagnetically below T_N = 7.6 K with an ordered moment of 1.3 μ_B/Ce. The antiferromagnetic easy-axis corresponds to the c-axis, while the a- and b-axes are hard axes in magnetization. The magnetic structure is, however, not simple. A remarkable superlattice peak at (0.475 0 0.330) was found below T_N in the neutron diffraction measurement, indicating an incommensurate antiferromagnetic structure. It was also found that the magnetic moments orient along the c-axis in the ordered state. The γ value was obtained to be 70 mJ/(K^2·mol).

2) The anisotropy of magnetic susceptibility and magnetization in $CeRhGe_2$ is approximately the same as that in $CePtSi_2$ and $CeNiGe_2$, reflecting the crystal structure. On the basis of these experimental results, we obtained the CEF schemes for these three compounds. The overall splitting energy is large, ranging from 600 to 800 K.

3) We confirmed the superconductivity of $CePtSi_2$ at around 1.5 GPa, revealing zero-resistivity at T_{sc} = 0.15 K. The upper critical field was roughly estimated to be $H_{c2}(0)$ = 11, 22, and 3 kOe for $H \| a$-, b-, and c-axes, respectively, which is closely related to the anisotropic Fermi surfaces and paramagnetic suppression. The similar pressure-induced

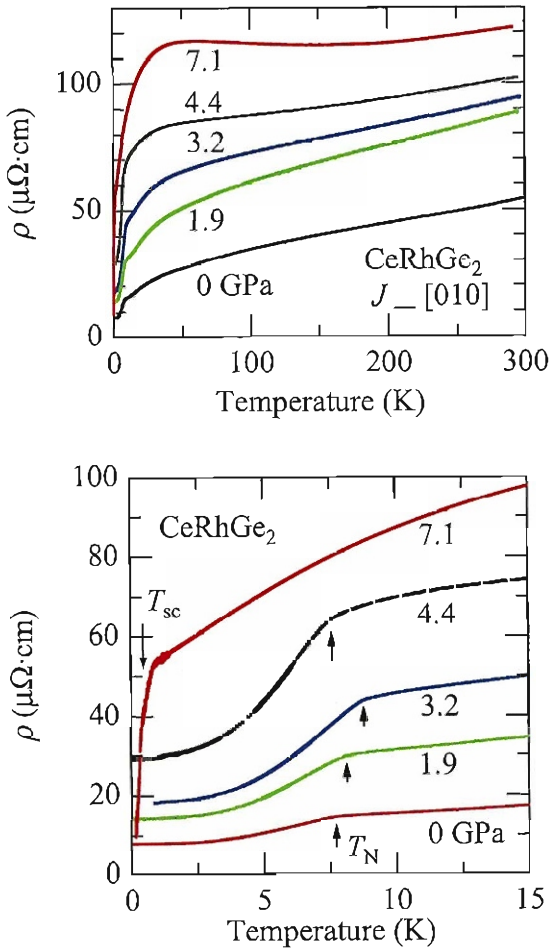

Fig. 5.19 Temperature dependence of the electrical resistivity in $CeRhGe_2$ under high pressure in (a) a wide temperature range and (b) at low temperatures.

superconductivity is most likely observed below 0.45 K under 7.1 GPa in $CeRhGe_2$.

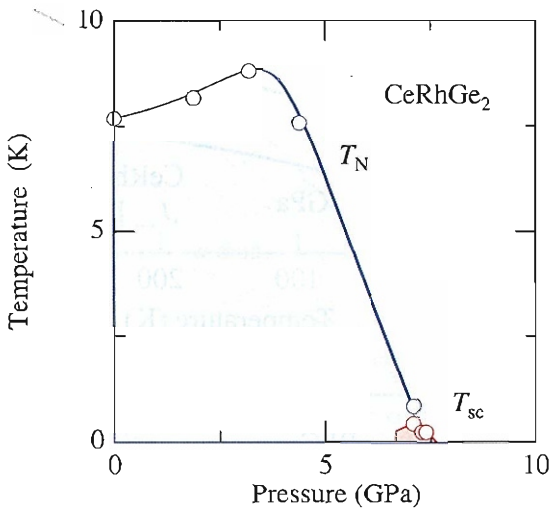

Fig. 5.20 Phase diagram of the Néel temperature T_N and superconducting transition temperature T_{sc} as a function of pressure in $CeRhGe_2$, where the onset of the superconducting transition is shown.

Table 5.II CEF parameters, energy level schemes, and the corresponding wave functions for $CeRhGe_2$.

CEF parameters						
B_2^0 (K)	B_2^2 (K)	B_4^0 (K)	B_4^2 (K)	B_4^4 (K)	χ_0^i (emu/mol)	
7.2	-2.9	0.48	7.0	-6.0	$\chi_0^{x,y,z} = -1.4 \times 10^{-4}$	
Energy levels and wave functions						
E (K)	$\|+5/2\rangle$	$\|+3/2\rangle$	$\|+1/2\rangle$	$\|-1/2\rangle$	$\|-3/2\rangle$	$\|-5/2\rangle$
579	0	-0.442	0	0.567	0	0.695
579	0.695	0	0.567	0	-0.442	0
83	0	0.287	0	-0.644	0	0.709
83	-0.709	0	0.644	0	-0.287	0
0	0	0.85	0	0.513	0	0.122
0	0.122	0	0.513	0	0.85	0

Table 5.III CEF parameters, energy level schemes, and the corresponding wave functions for $CePtSi_2$.

CEF parameters						
B_2^0 (K)	B_2^2 (K)	B_4^0 (K)	B_4^2 (K)	B_4^4 (K)	λ_i (mol/emu)	χ_0^i (emu/mol)
12.0	-7.5	-1	2.0	-15.0	$\lambda_x = -7$	$\chi_0^x = -2.0 \times 10^{-4}$
					$\lambda_z = -40$	$\chi_0^z = -2.5 \times 10^{-4}$

Energy levels and wave functions						
E (K)	$\|+5/2\rangle$	$\|+3/2\rangle$	$\|+1/2\rangle$	$\|-1/2\rangle$	$\|-3/2\rangle$	$\|-5/2\rangle$
826	0	0.746	0	-0.105	0	-0.658
826	-0.658	0	-0.105	0	0.746	0
88	0	-0.116	0	0.952	0	-0.283
88	-0.283	0	0.952	0	-0.116	0
0	0	0.656	0	0.288	0	0.698
0	0.698	0	0.288	0	0.656	0

Table 5.IV CEF parameters, energy level schemes, and the corresponding wave functions for $CeNiGe_2$ cited from ref. 145.

CEF parameters				
B_2^0 (K)	B_2^2 (K)	B_4^0 (K)	B_4^2 (K)	B_4^4 (K)
10.01	7.97	0.14	-7.54	-7.66

Energy levels and wave functions						
E (K)	$\|+5/2\rangle$	$\|+3/2\rangle$	$\|+1/2\rangle$	$\|-1/2\rangle$	$\|-3/2\rangle$	$\|-5/2\rangle$
653	0	-0.53	0	-0.5	0	0.69
653	-0.69	0	-0.5	0	-0.53	0
93	0	0.47	0	0.5	0	0.73
93	0.73	0	0.5	0	0.47	0
0	0	0.71	0	-0.71	0	0.032
0	0.032	0	-0.71	0	0.71	0

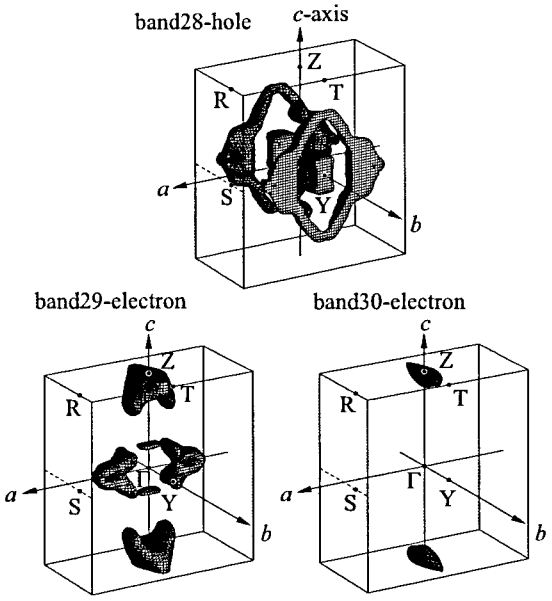

Fig. 5.21 Calculated $4f$-itinerant Fermi surfaces of $CePtSi_2$.

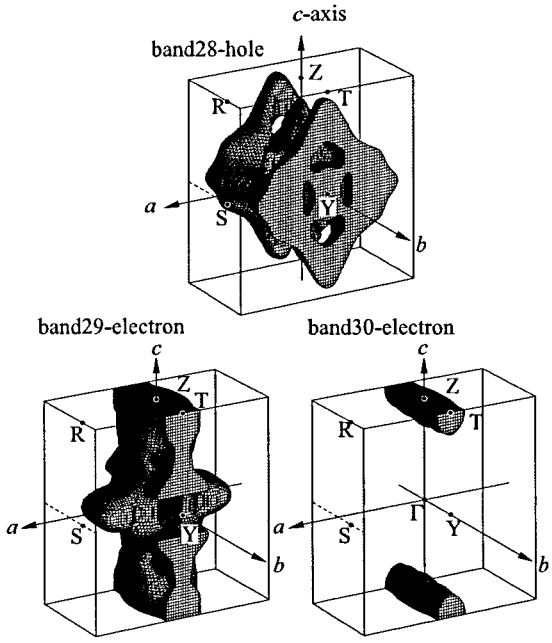

Fig. 5.22 Calculated $4f$-itinerant Fermi surfaces of $CePtSi_2$, where the Fermi energy was shifted by 3 mRy.

5.2 $CeIrGe_3$

Introduction

Recently, the interplay of magnetism and superconductivity has attracted great interest with the discovery of several compounds in which a superconducting phase appears at the border of a magnetic order.[1,152] These materials provide an important route to the understanding of superconductivity mediated by spin fluctuations associated with a magnetic quantum critical point. In most cases, these novel superconductors are based on either cerium or uranium. Of particular relevance is the influence of antiferromagnetism and superconductivity on each other in the cerium compounds that under pressure lose their antiferromagnetic ordering at a critical pressure around which emerges the superconducting state. This phenomenology has become one of the most interesting issues in strongly correlated electron systems.

$CeIrSi_3$,[10] $CeRhSi_3$[8] and $CeCoGe_3$[83,133,134] are among the Ce-compounds showing superconductivity near a magnetic quantum phase transition. They belong to the series $CeTX_3$ (T=transition metal, X=Si, Ge) that crystallizes in the tetragonal $BaNiSn_3$-type structure *without* inversion symmetry along [001] direction (c-axis) as shown in Fig. 5.23. Thus, they are also a part of the important class of novel superconductors that lack inversion symmetry. The absence of this symmetry causes the indistinguishability of the spin-singlet and spin-triplet states and the splitting of the parity-conserving spin degenerate energy bands. Due to this it is expected to see new phenomena in these superconductors. Some of the new behaviors indeed observed in $CeIrSi_3$, $CeRhSi_3$ and $CeCoGe_3$ are related to the upper-critical field $H_{c2}(T)$: extremely large $H_{c2}^{\parallel}(0)$ ($H \parallel [001]$) compared to the critical temperatures, large anisotropies $H_{c2}^{\parallel}(0)/H_{c2}^{\perp}(0)$, and anomalous upward curvatures in $H_{c2}^{\parallel}(T)$.

$CeNiGe_3$, another member of the $CeTX_3$ family but that crystallizes in the orthorhombic $SmNiGe_3$-type structure *with* inversion symmetry, has a quantum critical point and a superconducting phase appearing around this point.[153,154] Interestingly, however, $CeNiGe_3$ has neither a high $H_{c2}(0)$ nor a $H_{c2}(T)$ with positive curvature. Moreover, until now none unconventional behavior has been observed in this compound. Thus, the lack of inversion symmetry seems to play a crucial role for the appearance of the unusual superconducting properties of $CeIrSi_3$, $CeRhSi_3$, and $CeCoGe_3$. The search for new non-centrosymmetric superconductors with quantum criticality is then of high interest. Here we report on the discovery of superconductivity near a quantum critical point in the non-centrosymmetric compound $CeIrGe_3$.

Experimental procedure

To eliminate the possibility of having traces of Bi in the resulting crystals, as occurred in $CeCoGe_3$,[133] our single crystals of $CeIrGe_3$ were grown by the Sn-flux method as described in Chap.3. The crystals grown by the procedure display the same thermodynamic, transport, and magnetic properties as those grown by the Bi-flux technique. The inset

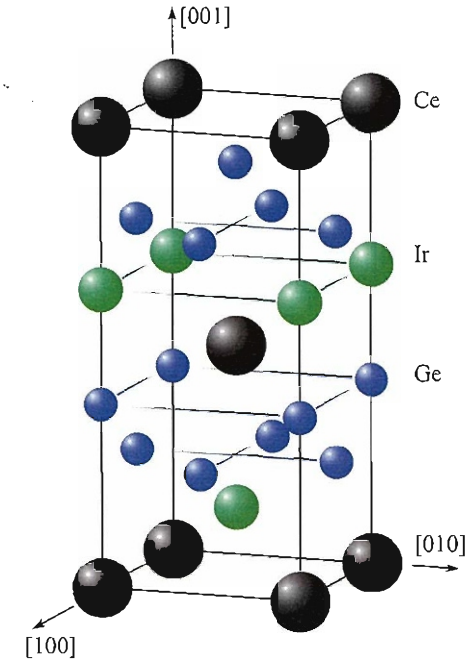

Fig. 5.23 Crystal structure of $CeIrGe_3$

to Fig. 5.24(a) shows a single crystal of $CeIrGe_3$ in which the flat plane is perpendicular to the c axis.

Four-probe electrical resistivity measurements were performed with an LR-700 AC resistance bridge operating at 16 Hz. Temperatures as low as 40 mK were obtained with a dilution refrigerator. Pressures up to 24 GPa were applied with a CuBe-made diamond anvil cell and were measured by the shift of the ruby R1 fluorescence line at room temperature. The pressure value was verified once at 40 K. NaCl powder was used as the pressure-transmitting medium. We were unable to carry out either AC susceptibility or specific heat measurements, because of the required high-pressure conditions.

Experimental results and discussion

Figures 5.24(a) and (c) show the temperature dependence of the electrical resistivity of $CeIrGe_3$ for the sensing current along the [100] direction and for different pressures in the range 0 - 24 GPa. At low pressures the resistivity decreases with temperature and shows the appearance of antiferromagnetic ordering at low temperatures, which is the usual behavior originated from localized $4f$ electrons. As pressure increases, the resistivity gradually develops a maximum around 100 K, from which it rapidly drops as temperature decreases, and ultimately shows a metallic response with no indication of antiferromagnetic ordering. This implies a smooth change from localized $4f$ electrons at high temperatures to itinerant $4f$ electrons with formation of heavy masses at low temperatures. Such a behavior provides a clear example of the crossover from localized

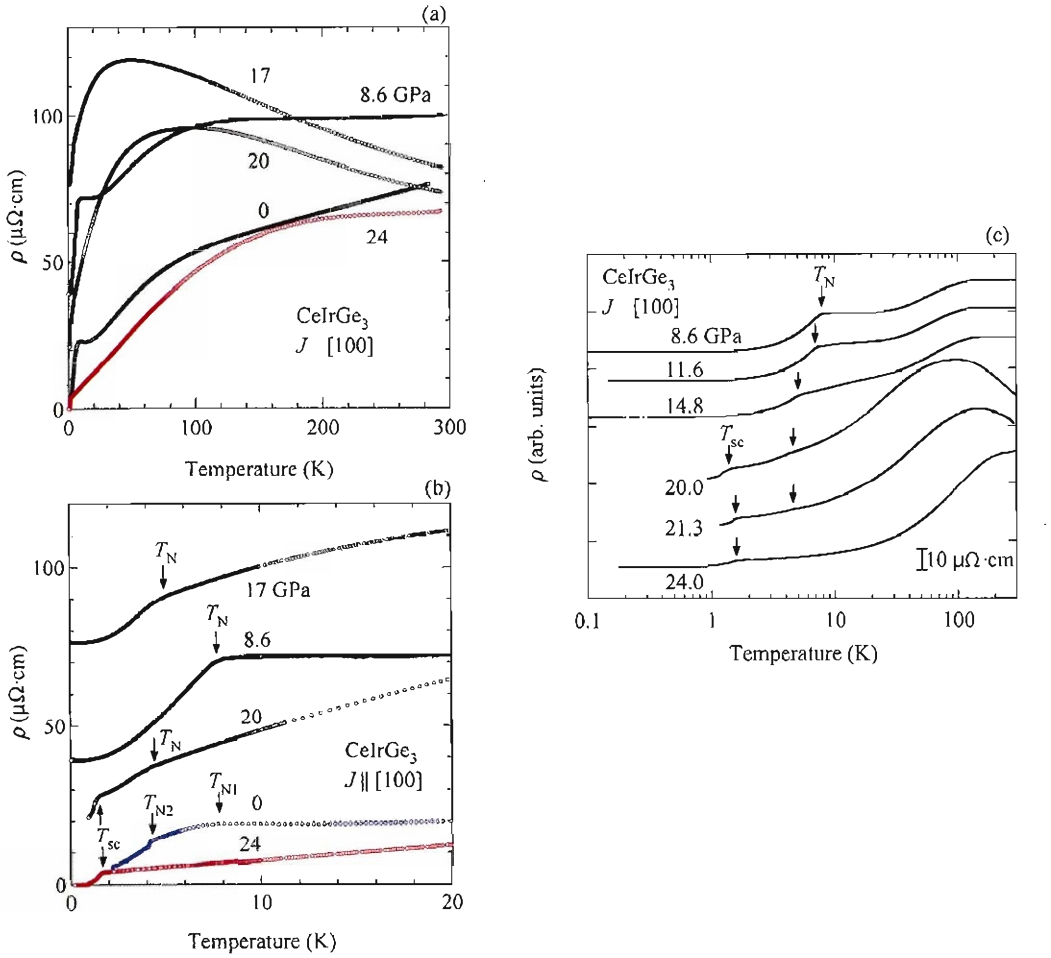

Fig. 5.24 Electrical resistivity of $CeIrGe_3$ as a function of temperature at several pressures in the range 0-24 GPa (a) below room temperature and (b) below 20 K. The inset to (a) shows a picture of a $CeIrGe_3$ single crystal. (c) Temperature dependence of the electrical resistivity of $CeIrGe_3$ under several pressures up to 24 GPa is shown by logarithmic scale.

to itinerant states caused by the Kondo-lattice phenomenon, as seen in $CeCu_2Si_2$[155] and $CeCu_2Ge_2$.[75] Notably, the temperature dependence of the resistivity of $CeIrGe_3$ below 300 K at different pressures differs from that of the sibling compounds $CeIrSi_3$, $CeRhSi_3$, and $CeCoGe_3$, though it looks qualitatively similar to the one of $CeNiGe_3$ with inversion symmetry.[153,154]

Figure 5.24(b) displays the resistivity in the low-temperature region. It is observed that superconductivity occurs at 20 GPa, whereas antiferromagnetic order fades away above 22 GPa. The resistivity above the superconducting transition at 24 GPa follows a T-linear response in the temperature range 1.7 - 70 K, indicating that the system becomes

a non-Fermi liquid. This behavior is found in the other four $CeTX_3$ superconductors as well. Although in the present experiment in $CeIrGe_3$ superconductivity initially appears at 20 GPa as a drop in the resistivity to a nonzero value at the lowest temperatures, superconductivity with zero resistivity is eventually observed at 24 GPa. Pressure-induced superconductivity with nonzero resistivity in the low-pressure region has been also found in other heavy fermions, like $CeNiGe_3$[153,154] and $CeCoGe_3$,[83] and interestingly in the oxypnictide LaFeAsO.[156] In all these materials superconductivity develops at relatively high pressures, which has led to the argument that the lack of zero resistivity could be due to defects or inhomogeneities created in the samples by the application of inherent nonuniform pressures. However, in $CeCoGe_3$ the resistivity sharply drops to zero only once the optimal pressure P_{opt}, at which the superconducting critical temperature has its maximum, has been applied.[83] Here a similar comportment of the resistivity is observed in $CeIrGe_3$.

In a previous report,[157] the pressure-temperature phase diagram of $CeIrGe_3$ was drawn up to 7 GPa with the solely existence of an antiferromagnetic phase. Here we present in Fig. 5.25 an almost complete phase diagram up to 24 GPa, in which the antiferromagnetic transition temperature T_N falls to zero in two steps, the first around 10 GPa and the second about 21 GPa, and superconductivity appears at 20 GPa below 1.5 K. The quantum critical point ($T_N \to 0$) is somewhere near 22 - 23 GPa, thus the superconducting state emerges at a pressure at which the antiferromagnetic phase still exists. The phase diagrams of $CeIrGe_3$ and the other four $CeTX_3$ superconductors are alike, all resembling Doniach's phase diagram[2] with the maximum T_N around ambient pressure and $|J_{cf}|D(E_F)$ replaced by pressure. Here, $|J_{cf}|$ is the magnitude of the magnetic exchange interaction and $D(E_F)$ is the density of states at the Fermi energy. This is in agreement with the discussion given above for the temperature dependence of the resistivity as a function of pressure, since Doniach model assumes a competition between the RKKY interaction, responsible for localization of Ce $4f$ electrons and magnetic ordering at low pressures, and the Kondo effect, that causes itinerancy in these electrons at high pressures. Doniach model, however, predicts a Fermi liquid phase above the quantum critical point pressure, whereas the $CeTX_3$ compounds show non-Fermi liquid behaviors.

The exchange interaction J_{cf} is also enhanced by the unit-cell volume contraction, and a plot of Néel temperature versus average interatomic distance $\sqrt[3]{a^2c}$ should be in close relation with Doniach's phase diagram. This is the case shown in Fig. 5.26 for the $CeTX_3$ materials, where the quantum critical point is located around a molar volume of 176 $Å^3$.[135] The figure indicates that whereas for example in $CeIrSi_3$ and $CeRhSi_3$ the quantum critical point appears at relatively low pressures, in $CeIrGe_3$ it should emerge at much higher pressure. This is confirmed by the present experiment.

We now discuss the low-temperature resistivity data of $CeIrGe_3$ under magnetic fields applied along the [001] direction at 24 GPa, shown in Fig. 5.27(a). The high level of noise was caused by the very low bias current used to avoid both heating the sample and destroying the superconducting state. Zero resistivity was observed only under these conditions. With increasing magnetic field the onset of the resistivity drop shifts to lower temperatures, providing further evidence that such a drop is due to superconductivity.

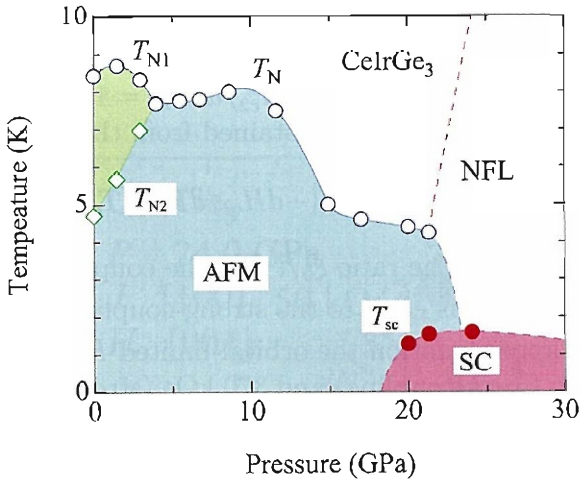

Fig. 5.25 Pressure-temperature phase diagram of $CeIrGe_3$. AFM and SC mean antiferromagnetic phase and superconductive phase, respectively.

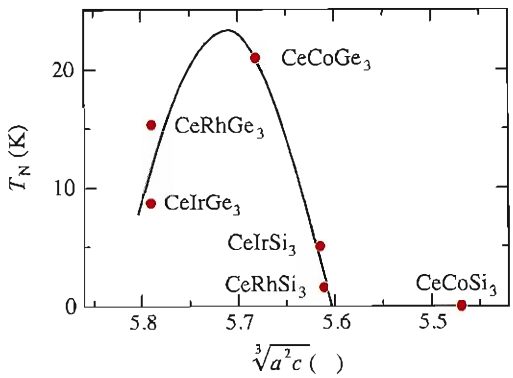

Fig. 5.26 Néel temperature with respect to the averaged interatomic distance, $\sqrt[3]{a^2c}$, in non-centrosymmetric $CeTX_3$ superconductors. This plot is related to Doniach's phase diagram (see text). Cited from Ref. 135.

Using this onset we deduce the $H_{c2}^{\parallel}$ plotted as a function of temperature in Fig. 5.27(b). It is unknown at this point whether or not the $H_{c2}^{\parallel}(T)$ of $CeIrGe_3$ will develop an upward curvature at lower temperatures and/or at higher pressures near the optimum, as occurs in $CeIrSi_3$, $CeRhSi_3$, and $CeCoGe_3$. Nevertheless, it is already clear from the data taken at 24 GPa (Fig. 5.27(b)) that $H_{c2}^{\parallel}(0) > 100$ kOe and that it is significantly larger than the weak-coupling paramagnetic limiting field $H_P \approx 30$ kOe.

$H_{c2}^{\parallel}(0) > H_P$ has been found in all non-centrosymmetric superconductors that emerge in the presence of an antiferromagnetic phase and have a large antisymmetric spin-orbit coupling; that is, in $CeIrSi_3$, $CeRhSi_3$, $CeCoGe_3$, $CePt_3Si$, and now $CeIrGe_3$. It is believed

that the absence of the spin paramagnetic limit is a common feature of these compounds, and thus that their superconductivity is limited by orbital effects. In $CeIrGe_3$ the initial slope of the $H_{c2}^{\parallel}$ vs T curve has the value $(-dH_{c2}^{\parallel}/dT)_{T_c} = 16$ T/K. The zero-temperature orbital upper-critical field $H_{c2}^{orb}(0)$ can be obtained from the formula[158)]

$$H_{c2}^{orb}(0) = h_0 \left[(-dH_{c2}/dT)_{T_c}\right] T_c \,. \tag{5.10}$$

The value h_0 depends on both the ratio ξ_0/l and the coupling parameter λ. In $CeIrSi_3$, $CeRhSi_3$, and $CeCoGe_3$ $H_{c2}^{\parallel}(0)$ is close to the strong-coupling limit of the orbital critical field H_{c2}^{orb}. In the clean approximation the orbital-limited $H_{c2}^{\parallel}(0)$ of $CeIrGe_3$ should have a value between 170 kOe (weak-coupling) and 370 kOe (strong-coupling). From this $11 < H_{c2}^{\parallel}(0)/T_c < 25$, a large ratio only seen in non-centrosymmetric $CeTX_3$ materials with an antiferromagnetic phase. We argue here that even though the present data already suggest a very high $H_{c2}^{\parallel}(0)$ in $CeIrGe_3$, in non-centrosymmetric $CeTX_3$ superconductors the highest $H_{c2}^{\parallel}(0)$ and a positive curvature of $H_{c2}^{\parallel}(T)$ are found at pressures very close to the optimum for superconductivity. It is possible that we did not reach the optimal pressure for $CeIrGe_3$.

Summary

In summary, we reported on the temperature dependence of the electrical resistivity of $CeIrGe_3$ under high pressures up to 24 GPa. Pressure-induced superconductivity was found at 20 GPa. A significantly large upper-critical field $H_{c2}(0) > 100$ kOe is observed, implying a large $H_{c2}^{\parallel}/T_c$ as in the other non-centrosymmetric $CeTX_3$ superconductors that emerge in an antiferromagnetic phase.

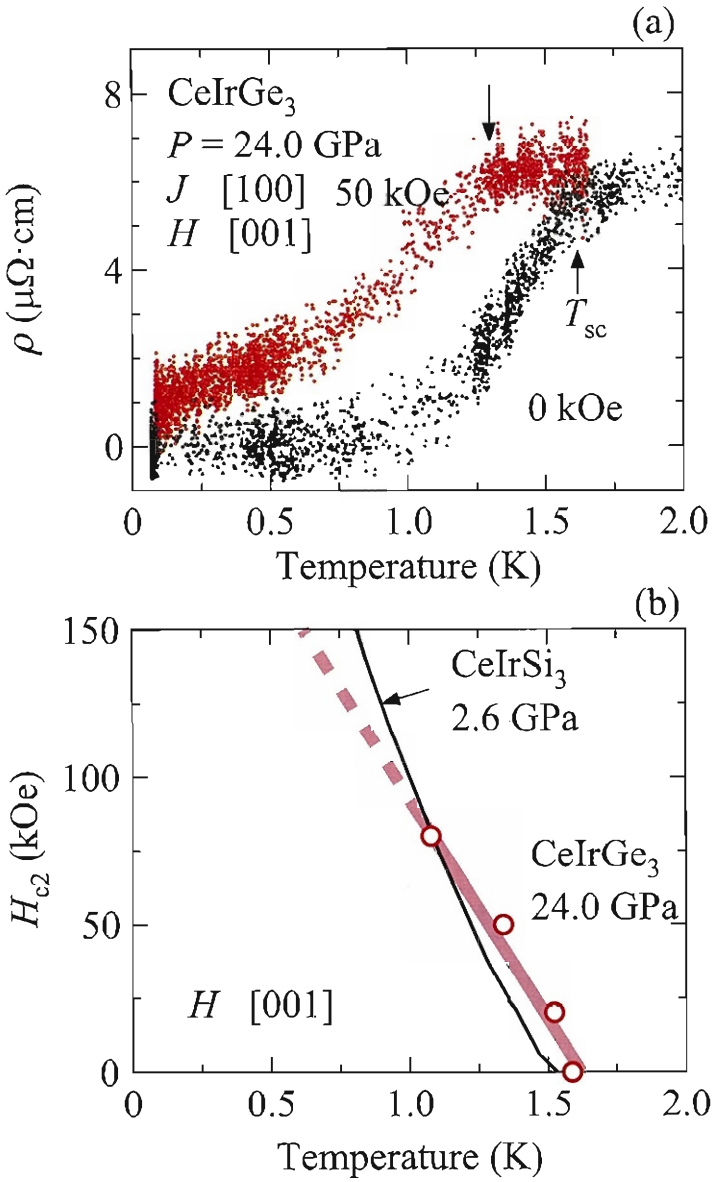

Fig. 5.27 Temperature dependence of (a) electrical resistivity of $CeIrGe_3$ under magnetic fields in 0 and 5 T at 24 GPa, and (b) the upper critical field of $CeIrGe_3$ with magnetic field along the [001] direction, together with the one of $CeIrSi_3$ at 2.6 GPa as shown in the solid line cited from ref. 87.

5.3 $LaNiC_2$

Introduction

Rare earth metal (R)-transition metal (T: Fe, Co, Ni)-carbides RTC_2 mainly crystallize in the $CeNiC_2$-type orthorhombic structure (space group Amm2)[159]. Carbon is not magnetic, and the magnetic contribution of nickel in $RNiC_2$ is also zero because $YNiC_2$ and $LaNiC_2$ do not show the presence of any magnetic moment[160]. Consequently, only the rare earth ions contribute to the magnetic exchange interaction based on the RKKY interaction[161].

The crystal structure of $RNiC_2$ is characteristic, as shown in Fig. 5.28. The space group is Amm2 with R in $2a$ (0 , 0 , 0), Ni in $2b$ (0.5 , 0 , z), and C in $4e$ (1/2 , y , z), for example a = 3.959 Å, b = 4.564 Å, and c = 6.204 Å in $LaNiC_2$[162]. We follow the space group of Amm2, but Cm2m is often used, showing the corresponding direction in the bracket of Fig. 5.28. The R plane, namely the La plane at $x = 0$ and NiC_2 plane at $x = 0.5$ are stacked sequentially along the a-axis. It is noted that the lattice constant a value is about 4.0 Å, and then a distance between the La plane and the NiC_2 plane is about 2.0 Å, revealing a very short distance. The Ni and C atoms form the hexagonal-like lattice, and two carbon atoms are strongly coupled and form a dimer-like coupling. Important is that the crystal structure lacks inversion symmetry along the c-axis, as shown in Figs. 5.28(c) and 5.28(d). The recent band calculation revealed spin-split Fermi surfaces based on the antisymmetric spin-orbit interaction[163].

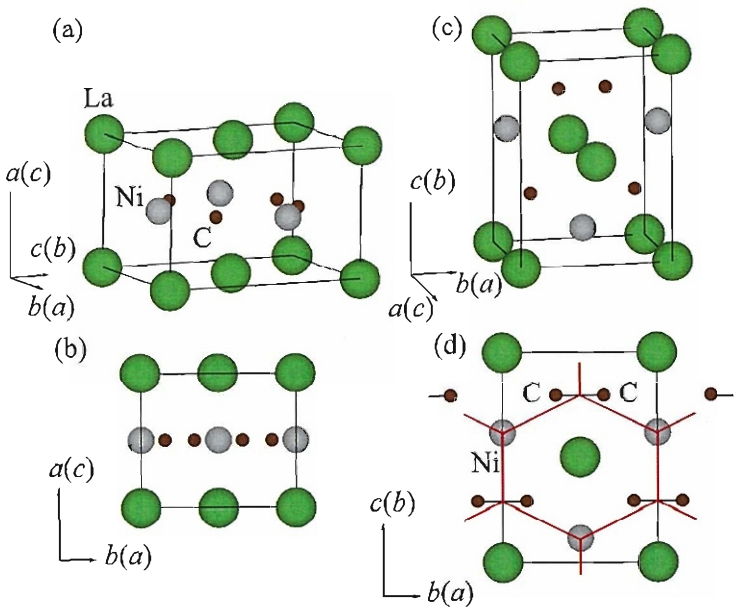

Fig. 5.28 Crystal structure with space group Amm2 (Cm2m) in $LaNiC_2$.

Very recently, $LaNiC_2$ attracts a special attention because the onset of superconductivity coincides with the appearance of spontaneous magnetic fields in the muon spin relaxation experiment, implying that time-reversal symmetry is broken in the superconducting state[164]. In the previous specific heat experiment, the specific heat C was also not exponential but followed a power-law form of T^3-dependence, claiming nodes in the superconducting energy gap[165]. The experimental results of magnetic penetration depth followed a T^2-dependence, suggesting the existence of nodes in the energy gap.[166] From these experiments, the triplet pairing state with the f-wave type is proposed for superconductivity of $LaNiC_2$ because the crystal structure lacks inversion symmetry, as in $CePt_3Si$[7], $CeTX_3$ (T : Co, Rh, Ir, X : Si, Ge)[135], and $Li_2(Pd_xPt_{1-x})_3B$ (x = 0 - 1)[167]. It is, however, noted that the nuclear spin relaxation rate $1/T_1$ in the ^{139}La-NQR signal was exponential, with an energy gap $2\Delta = 3.34k_BT_{sc}$, close to the BCS value of $3.52k_BT_{sc}$, suggesting that superconductivity of $LaNiC_2$ is of a conventional BCS-type[168].

All the previous experiments were carried out by using polycrystalline samples. It is needed to do the similar measurements by using a higher-quality single crystal sample. We therefore grew single crystals by the Czochralski method, and measured the electrical resistivity, de Haas-van Alphen (dHvA) effect and specific heat to clarify the Fermi surface and superconducting properties.

Experimental results and analyses

Single crystals were grown by the Czochralski method in a tetra-arc furnace. Starting materials were 99.9 % pure(3N-) La, 4N-Ni, and 4N-C, which were arc-melted, with a slightly off-stoichiometric composition of 1 : 1 : 2.04-2.08. We show in Fig. 5.29 as-grown ingots with 2-3 mm in diameter and 50 mm in length. The a-plane was easily identified from the X-ray Laue method.

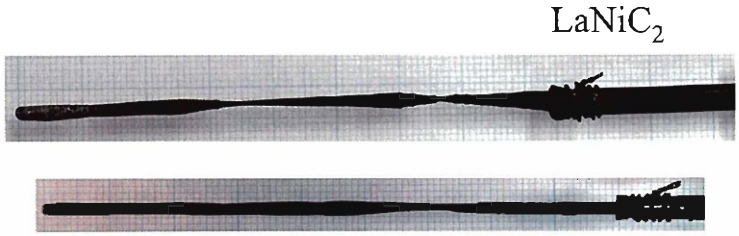

Fig. 5.29 Single crystal ingots of $LaNiC_2$ grown by the Czochralski method.

We show in Fig. 5.30 the temperature dependence of the electrical resistivity ρ for the current along three principal axes. The electrical resistivity decreases almost linearly with decreasing temperature, reaches a constant value below 10 K, and finally becomes zero at a superconducting transition temperature T_{sc} = 2.7 K. The residual resistivity ratio was 30 - 40 : the residual resistivity ρ_0 = 2.9 $\mu\Omega$·cm, and the resistivity at room temperature ρ_{RT} = 120 $\mu\Omega$·cm, and RRR = 41 for $J \parallel b$-axis, for example. It is noted that the T_{sc} value depends on the sample even in the same ingot and also the magnitude

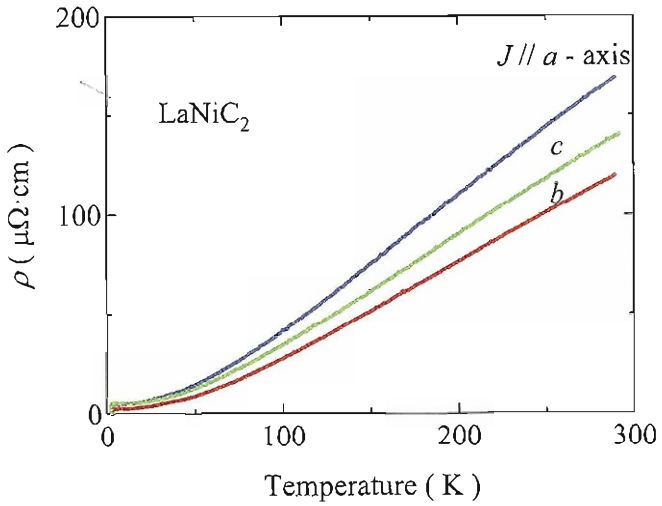

Fig. 5.30 Temperature dependence of the electrical resistivity in $LaNiC_2$.

of the current, ranging from 2.7 to 3.2 K, which is consistent with the previous report[165]. The anisotropy of the electrical resistivity is not large, suggesting that the Fermi surface is three dimensional, although the crystal structure is characteristic along the a-axis, as mentioned above.

Next we carried out the dHvA experiment by using the conventional field modulation method. Figure 5.31 shows the typical dHvA oscillations and the corresponding fast Fourier transformation spectrum (FFT) for the magnetic field along the a-axis. Two kinds of fundamental branches named α (α') and β (β') were observed, together with their harmonics. Each branch is split into two branches based on the antisymmetric spin-orbit interaction. Here, the dHvA frequency F ($= c\hbar S_F/2\pi e$) is proportional to the extremal (maximum or minimum) cross-sectional area of the Fermi surface S_F, which is expressed as a unit of magnetic field.

We rotated the sample against the field direction, and obtained the field dependence of the dHvA frequency, as shown in Fig. 5.32. Branch α (α') is due to an ellipsoidal Fermi surface. Solid lines represent ellipsoids of revolution with $k_a/k_{b,c} = 2.18$ for branch α and $k_a/k_{b,c} = 2.85$ for branch α', where k_a and $k_{b,c}$ are half of the caliper dimension of the Fermi surface, namely $\pi k_{b,c}^2 = S_F(H \parallel a)$. Branch β (β') is due to a small hyperboloidal pillar. Here, dotted lines represent the 1 / cosθ dependence, which corresponds to a cylindrical Fermi surface.

The present experimental results are approximately explained by the results of energy band calculations for $LaNiC_2$ done by Hase and Yanagisawa[163], although a hyperboloidal Fermi surface is not one but two in number, and the hyperboloidal Fermi surfaces are larger than the ellipsoidal Fermi surfaces in cross-section. In their paper, the Fermi surface of $YNiC_2$ was also calculated, which well explains the present experimental results. Figures 5.32(b) and 5.32(c) show the present theoretical angular dependence of dHvA

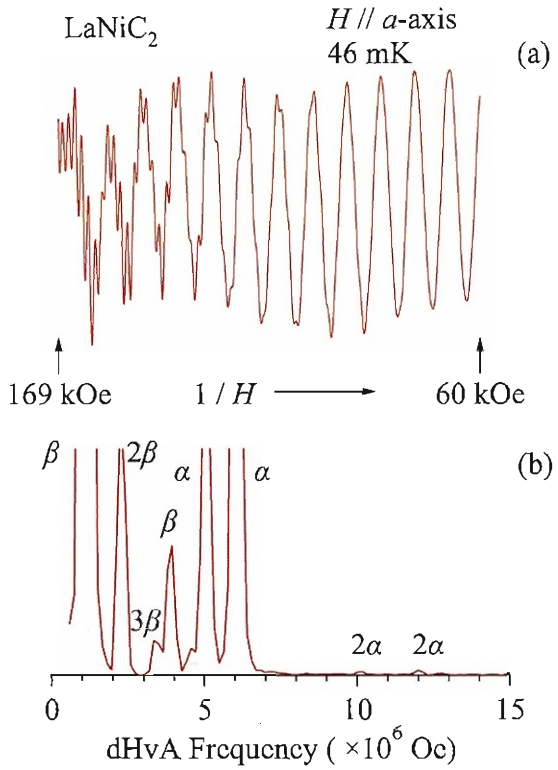

Fig. 5.31 (a) dHvA oscillations and (b) the corresponding FFT spectrum in $LaNiC_2$.

frequency for $YNiC_2$ and the corresponding Fermi surfaces, which were calculated as in the previous calculations[163], using the lattice parameters of $YNiC_2$ and the site position of $DyNiC_2$. Note that the cite position, especially the position along the y-axis for the C atom, is most likely different between $YNiC_2$ and $DyNiC_2$, together with for $LaNiC_2$. This might slightly change the Fermi surface. It is noted that the plate-like Fermi surfaces are connected by the hyperboloidal pillars. The cross-sectional area of the ellipsoidal Fermi surface is larger than that of the pillar Fermi surface. This is consistent with the experimental results, as shown in Figs. 5.32(a) and 5.32(b), and the splitting of the ellipsoidal Fermi surfaces is approximately the same between experiment and theory. On the other hand, the theoretical splitting of the pillar Fermi surfaces is negligibly small, inconsistent with the experimental result. One of the analyses is that branches β and β' belong to two different kinds of pillar Fermi surfaces and the splitting of branches β and β' is negligibly small, thus not observed. Namely one more small pillar Fermi surface exists along the a-axis (Y-T direction), as in the theoretical results for $LaNiC_2$ mentioned above.

We also measured the cyclotron effective mass m_c^* from the temperature dependence of the dHvA amplitude. The cyclotron effective mass is 0.58 m_0 (m_0 : rest mass of an electron) for branch α, for example. We calculated the magnitude of antisymmetric

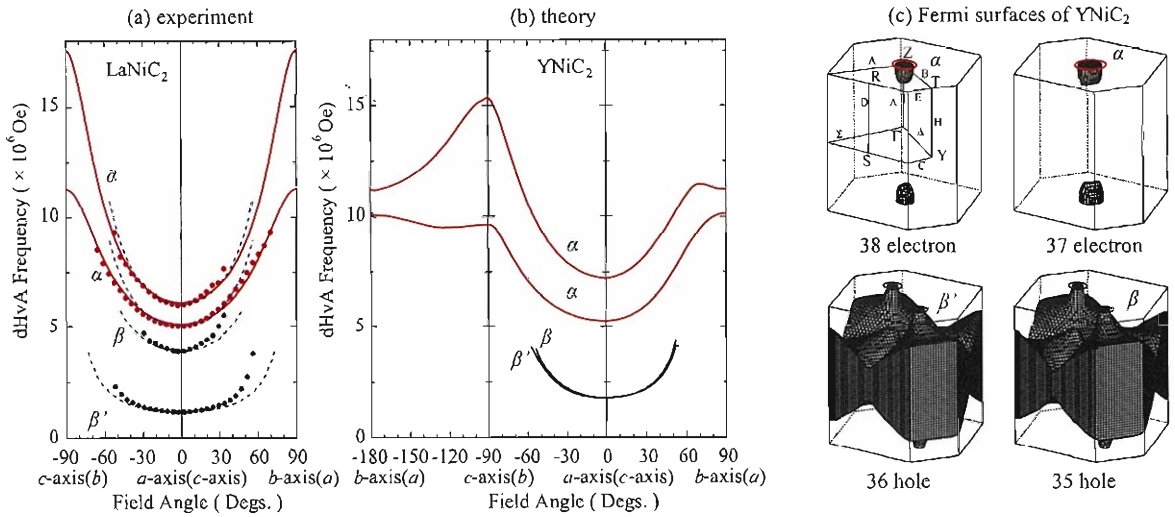

Fig. 5.32 (a) Angular dependence of the dHvA frequency in $LaNiC_2$. Solid and dotted lines correspond to ellipsoids of revolution and cylinders, respectively. (b) The corresponding theoretical one and (c) Fermi surfaces based on $YNiC_2$.

spin-orbit interaction $2|\alpha p_\perp|$, or a splitting energy by using the formula of $|F_+ - F_-| = \frac{2c}{\hbar e}|\alpha p_\perp| m_c^*$, which was done for $LaTGe_3$ and $LaTSi_3$ (T : Co, Rh, Ir).[169] The $2|\alpha p_\perp|$ value is 230 K for the ellipsoidal Fermi surface, for example. The dHvA frequency F, cyclotron mass m_c^* and splitting energy $2|\alpha p_\perp|$, together with the theoretical ones, are summarized in Table I.

Next, we studied the superconducting property. Figure 5.33 shows the temperature dependence of electrical resistivity at several low temperatures for $H \parallel c$-axis. We defined the superconducting transition temperature T_{sc} as the temperature showing zero resistivity. The temperature dependence of the upper critical field H_{c2} is shown in Fig. 5.34(a). The anisotropy of the upper critical field is not large. It is noted that a slope of H_{c2} possesses an upward curvature above 1 K.

Finally we measured the low-temperature specific heat C for two different samples. The specific heat consists of an electronic specific heat C_e and a phonon contribution C_{ph}. In the normal state, namely in the temperature range from 3 to 5.2 K, the specific heat C is expressed as $C = \gamma T + \beta T^3 (\gamma = 6.7$ mJ/(K^2·mol), $\beta = 0.15$ mJ/K^4·mol, and the Debye temperature $\theta_D = 370$ K). The present γ and θ_D values are close to $\gamma = 6.5$ mJ/(K^2·mol) and $\theta_D = 388$ K reported by Pechrasky *et al.*[170], and $\gamma = 7.83$ mJ/(K^2·mol) and $\theta_D = 496$ K reported by Lee *et al*[165]. The theoretical γ values based on the present band calculations is 3.6 mJ/(K^2·mol) for $YNiC_2$ and 5.2 mJ/(K^2·mol) for $LaNiC_2$.

We subtracted the phonon specific heat from the total specific heat. Figure 5.35(a) shows the T/T_{sc} dependence of the electronic specific heat C_e for two different samples. Note that the T_{sc} values are 2.70 K for the sample #1 and 2.75 K for the sample #2. The present C_e data below 2 K is well explained by the exponential function, with $2\Delta/k_B =$

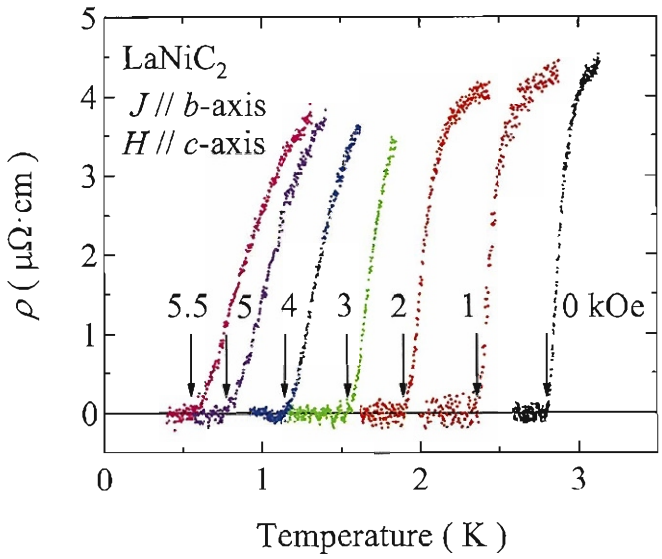

Fig. 5.33 Temperature dependence of the electrical resistivity at several magnetic fields for $H \parallel c$-axis in $LaNiC_2$.

7.8 K, or $2\Delta = 2.9k_BT_{sc}$ as shown by a thin solid line.

We also measured the specific heat under several magnetic fields, as shown in Fig. 5.35(b). The present superconductivity is destroyed by a magnetic field of about 2 kOe. We show in Fig. 5.34(b) the temperature dependence of upper critical field H_{c2}. The value of $H_{c2}(0)$ is estimated as about 2 kOe for $H \parallel b$-axis. A solid and a dotted lines are guide to eyes. The present H_{c2} value is smaller than the value of $H_{c2}(0) \simeq 6$ kOe obtained from the resistivity measurement. The similar discrepancy is obtained in $CeIrIn_5$[62]. The electrical resistivity is most likely sensitive to the surface as pointed out in the previous report.[7] The bulk H_{c2} value of $LaNiC_2$ is thus $H_{c2}(0) \simeq 2$ kOe.

Table 5.V dHvA frequency F, cyclotron effective mass m_c^*, and splitting energy $2|\alpha p_\perp|$ for $H \parallel a$-axis in $LaNiC_2$, together with the theoretical ones in $YNiC_2$.

	F ($\times 10^6$ Oe)	m_c^* (m_0)	$2\lvert\alpha p_\perp\rvert$ (K)	F_b ($\times 10^6$ Oe)	m_b (m_0)	$2\lvert\alpha p_\parallel\rvert$ (K)
α	6.04	0.58	230	7.26	0.488	590
α'	5.05	0.57		5.32	0.401	
β	3.91	0.58	0	1.78	0.172	3.9
				1.77	0.172	
β'	1.15	0.21	0			

Summary

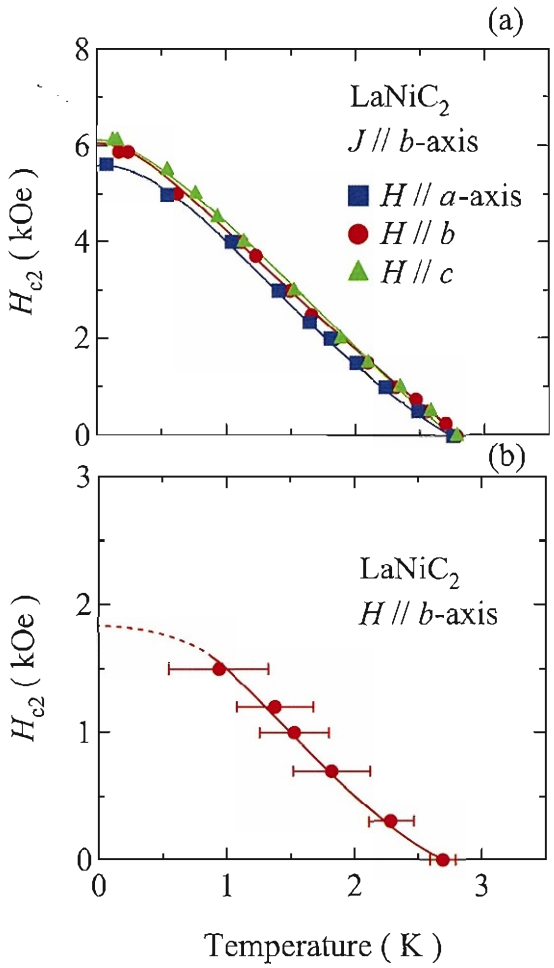

Fig. 5.34 Temperature dependence of the upper critical field H_{c2} obtained from (a) the resistivity and (b) specific heat measurements in $LaNiC_2$, where solid lines connecting the data are guide to eyes.

From these experimental results, we conclude that $LaNiC_2$ is of the BCS-type, with $2\Delta = 2.9k_BT_{sc}(T_{sc} = 2.70\text{-}2.75$ K). Reflecting the non-centrosymmetric crystal structure, the Fermi surface is split into two Fermi surfaces, with an splitting energy of 230 K in an ellipsoidal Fermi surface, for example.

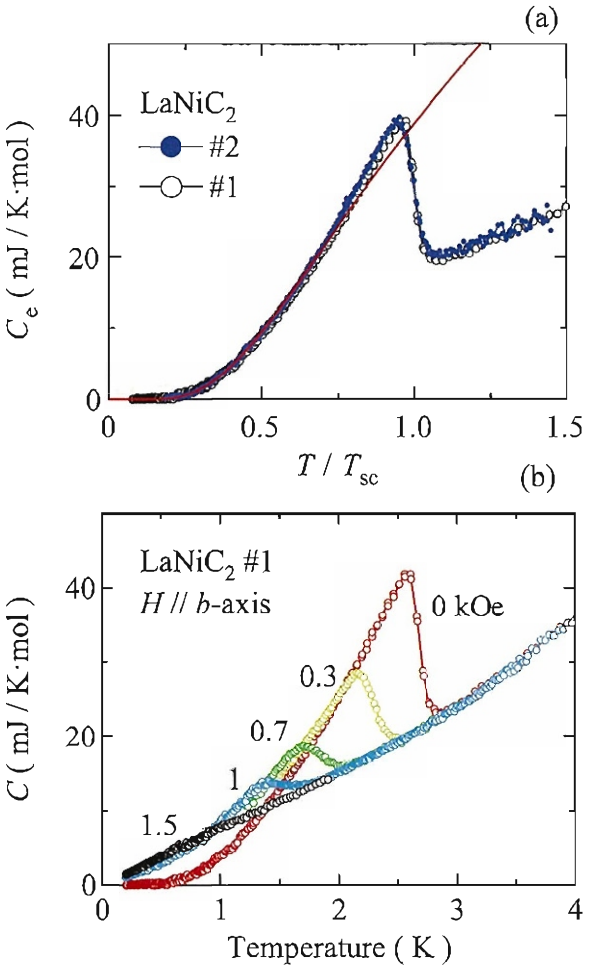

Fig. 5.35 (a) T/T_{sc} dependence of the electronic specific heat C_e, where a solid line indicates an exponential dependence of C_e, and (b) specific heat C under magnetic fields in $LaNiC_2$.

5.4 $CeCu_6$

Introduction

The metamagnetic behaviour or an abrupt nonlinear increase of magnetization is one of the characteristic properties in the Ce or U heavy fermion compounds. For example, the metamagnetic behaviour appears at H_m= 77 kOe and 200 kOe in $CeRu_2Si_2$ and UPt_3, respectively, as described in Chap.2 (see Fig. 2.14).[37,48] It is observed at temperatures lower than the characteristic temperature $T_{\chi max}$, where the magnetic susceptibility of these compounds deviates from the Curie-Weiss law and indicates a maximum. $T_{\chi max}$ approximately corresponds to the Kondo temperature T_K. Thus the f-electron nature is changed from localized to itinerant below $T_{\chi max}$.

We studied the metamagnetic behavior under pressure in a typical heavy fermion $CeCu_6$. $CeCu_6$ is a typical heavy fermion compound, which exhibits no long-range magnetic ordering.[171] We show in Fig. 5.36 the orthorhombic crystal structure.[172] The metamagnetic behavior is found below $T_{\chi max} = 1$ K and at $H_m \simeq 20$ kOe from the magnetization and magnetoresistance measurements.[36,173] This behavior was observed only when the magnetic field H is applied parallel to the magnetic easy axis (c-axis).

The effect of pressure on the electronic state in $CeCu_6$ was also studied.[174] With increasing pressure, the A value of the electrical resistivity ($\rho = \rho_0 + AT^2$) was found to decrease steeply as a function of pressure. At higher pressures, the heavy fermion state of $CeCu_6$ is changed into a so-called valence fluctuating electronic state[175]. Correspondingly, the A value is reduced as a function of pressure, as mentioned above. Theoretically it is, however, expected that the A value is enhanced in magnetic fields at around a characteristic pressure[176], namely in the pressure range from 2.0 to 3.4 GPa. In the present study, we measured the magnetoresistance to study the electronic state of $CeCu_6$

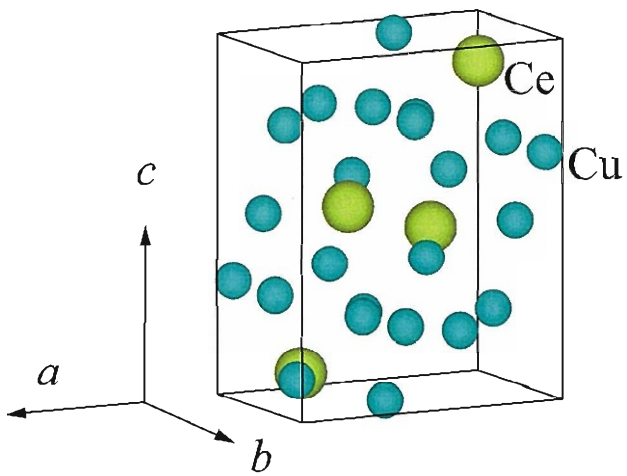

Fig. 5.36 Crystal structure of $CeCu_6$.

at higher pressures up to 5.1 GPa. We also carried out the dHvA experiment to directly obtain the cyclotron effective mass in magnetic fields.

Experimental procedure

Single crystals of $CeCu_6$ were prepared by the Czochralski pulling method, as described in Chap.3. The electrical resistivity measurement was carried out by using the ordinary four-probe DC or AC method. Pressure was generated in a piston cylinder cell up to 2 GPa and a Bridgman anvil cell up to 5.1 GPa, using a mixture of Daphne-7373 and Petroleum ether and Daphne-7373, respectively, as the pressure-transmitting medium. Pressure was calibrated via the superconducting transition of Sn and Pb, which were placed beside the sample in the pressure cell. The dHvA experiment was carried out by a standard field modulation method.

Experimental results and discussion

The temperature dependence of the electrical resistivity under various pressures is shown in Fig. 5.37. The temperature $T_{\rho\max}$, where the resistivity indicates a maximum, for example, 14 K at 0 GPa, are found to shift to higher temperatures with increasing pressure, as shown Figs. 5.37(a) and 5.37(b). Here, the resistivity peak is due to a combined phenomenon between the Kondo effect and a crystalline electric field (CEF) effect. The resistivity ρ follows the Fermi liquid relation of $\rho = \rho_0 + AT^2$ at low temperatures, as shown by thin solid lines in Fig. 5.37(c), where ρ_0 is the residual resistivity. Both the A and ρ_0 values decrease in magnitude with increasing pressure.

Here, the $\sqrt{A}$ value is proportional to the electronic specific heat coefficient γ, and then the $1/\sqrt{A}$ value is proportional to the Kondo temperature T_K from eq. (2.29) as mentioned in Sec 2.2. $T_{\rho\max}$, as mentioned above, is also closely related to T_K. The experimental result in Fig. 5.37(d) means a change of an electronic state from the heavy fermion state in the initial slope to the valence fluctuating state in the second slope as a function of $T_{\rho\max}$. These trends are approximately consistent with the previous data[175].

Figure 5.38 shows the transverse and longitudinal magnetoresistances at 100 mK for $H \parallel c$-axis. At $H_m = 20$ kOe, the longitudinal magnetoresistance indicates a shoulder-like structure, while the transverse one indicates a peak structure. A positive magnetoresistance in the transverse configuration is one of characteristic features in heavy fermion systems. Here we note that the magnetoresistance consists of two contributions. One is a positive magnetoresistance due to the cyclotron motion of conduction electrons, and the other is a negative magnetoresistance coming from a suppression of the Kondo effect expressed as $\Delta\rho/\rho(0) = -\sin^2(\pi M/2M_0) \sim -H^2$ in an impurity Kondo model.[177] At high temperatures, the negative magnetoresistance is dominant, but with decreasing temperature, almost localized $4f$-electrons become itinerant, forming a $4f$-derived heavy band. The latter effect is therefore diminished, and the former positive magnetoresistance becomes dominant, especially in the transverse magnetoresistance.

The transverse magnetoresistance $\Delta\rho/\rho(0) = \{\rho(H) - \rho(H = 0)\}/\rho(H = 0)$ was measured at various temperatures and pressures. The experimental results at 0.85 GPa

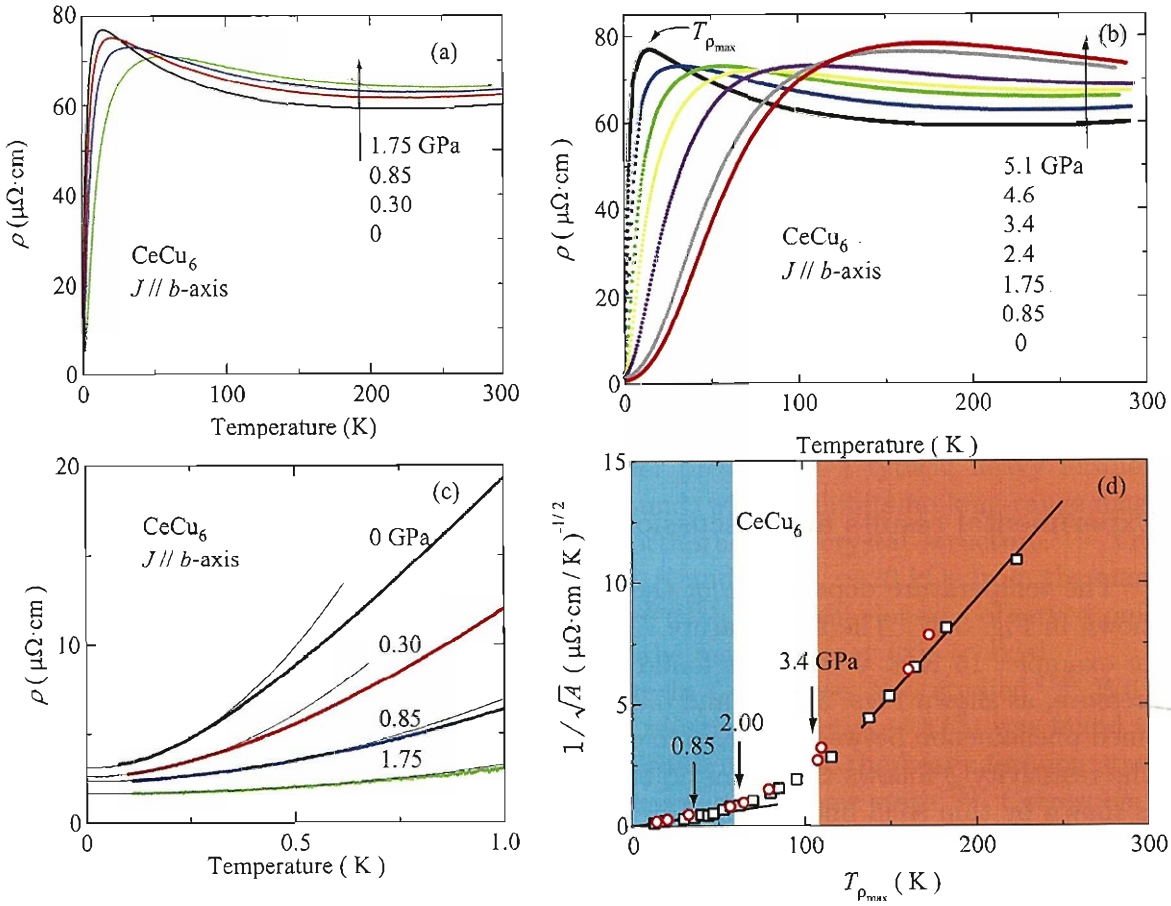

Fig. 5.37 (a) Temperature dependence of the resistivity under pressures up to 1.75 GPa and (b) up to 5.1 GPa, and (c) low-temperature resistivities under pressures up to 1.75 GPa in $CeCu_6$. Thin thin solid lines in (c) are the Fermi liquid relation of $\rho = \rho_0 + AT^2$. (d) The $T_{\rho\max}$ dependence of $1/\sqrt{A}$ (circles), together with the previous data (squares) cited from ref. 175.

are shown in Fig. 5.39. The metamagnetic behaviour is observed at $H_m = 50$ kOe under 100 mK. The magetoresistance decreases with increasing temperature, revealing a negative magnetoresistance based on the impurity Kondo effect mentioned above. This means that higher temperatures than 1 - 2 K destroy the heavy fermion state and suppress the positive magnetoresistance due to the cyclotron motion of the heavy quasiparticles. Up to 700 mK, the peak structure is observed at almost the same field, and disappears at 1.7 K. Thus H_m is defined as the magnetic field where the magnetoresistance indicates a peak and is almost independent of temperature.

Figure 5.40(a) shows the magnetoresistance $\rho(H)$ in the transverse configuration $J \perp H$ ($J \parallel b$-axis and $H \parallel c$-axis) at 0.1 K under several pressures. A peak in the

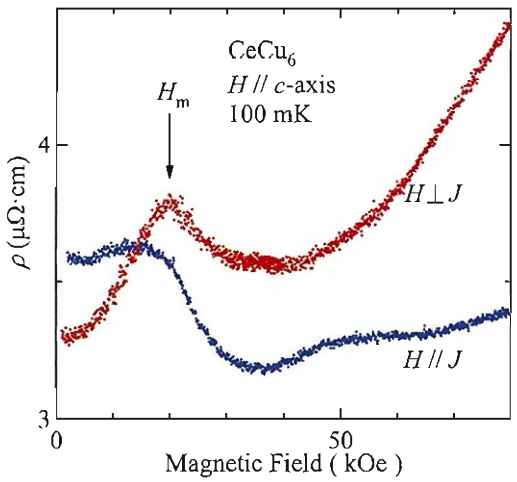

Fig. 5.38 Transverse and longitudinal magnetoresistances at 100 mK, applied magnetic field parallel to the c-axis in $CeCu_6$.

magnetoresistance corresponds to the metamagnetic behavior at H_m. H_m is found to increase monotonically as a function of pressure, as shown by arrows in Fig. 5.40(a) : $H_m \simeq 125$ kOe at 2.00 GPa, as shown by an arrow. On the other hand, the A value is changed from a shoulder-like structure at H_m to a peak structure above 1.75 GPa, shown in Fig. 5.40(b). The present change of the metamagnetic behavior becomes distinct when the ratio of the A value in the magnetic field H, $A(H)$, to the A value in $H = 0$, $A(0)$, namely $A(H)/A(0)$, is expressed as a function of H/H_m, as shown in Fig. 5.42. The metamagnetic behavior is enhanced with increasing pressure. The present enhancement most likely becomes maximum in the pressure range from 2.00 GPa to 3.4 GPa where the electronic state is changed from the heavy fermion state to the valence fluctuating state, as shown in Fig. 5.37(d), although a much higher magnetic field is needed to observe the metamagnetic behavior in this pressure region. This is because the metamagentic behavior does not occur in the valence fluctuating state, namely at pressures larger than 3.4 GPa. Here, the field dependence of ρ_0 shown in Fig. 5.40 (c) is the same as the magnetoresistance at 100 mK. The residual resistivity is also closely related to the heavy fermion state, as discussed theoretically.[178)]

Figure 5.41 shows the pressure dependence of H_m determined by the magnetoresistance and A value measurements. In addition to them, the data on $CeCu_{5.9}Au_{0.1}$ are also plotted : P = -0.21 GPa and $H_m = 0$. The pressure value of $CeCu_{5.9}Au_{0.1}$ is estimated from the bulk modulus of $CeCu_6$ and the difference of the volume between $CeCu_6$ and $CeCu_{5.9}Au_{0.1}$.[179,180)] $CeCu_{5.9}Au_{0.1}$ corresponds to the electronic state with $T_N = 0$ K, namely the quantum critical point.[180)] These experimental results indicate a linear relation between H_m and pressure.

Finally we carried out the dHvA experiment for $H \parallel c$-axis and determined the dHvA frequency F and the cyclotron effective mass m_c^*. Figure 5.43 shows the dHvA oscillation

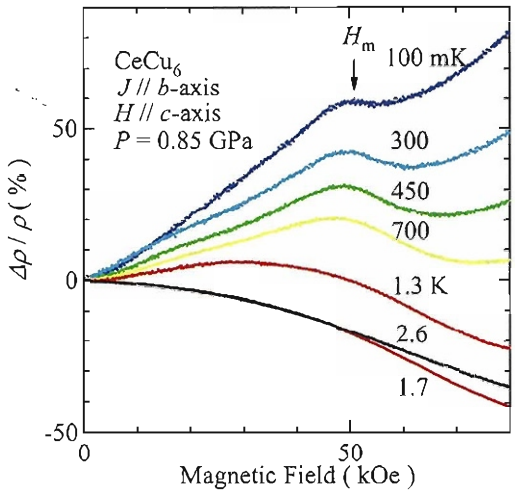

Fig. 5.39 Transverse magnetoresistance $\Delta\rho/\rho(0)$ at various temperatures under 0.85 GPa in $CeCu_6$.

and the corresponding FFT spectra. Six dHvA branches are observed. We also show in Fig. 5.44 the dHvA frequency for $H \parallel c$-axis (shown by red solid circles), together with the angular dependence of the previous data[181] shown by open circles. The present dHvA results are approximately consistent with the previous ones. Among the six detected dHvA branches, we show in Fig. 5.45(a) the field dependence of the cyclotron mass for three branches, revealing that the cyclotron mass decreases steeply with increasing magnetic fields. From the $\sqrt{A}$ value and the γ value in ref. 182, we estimated the cyclotron mass at $H = 0$, as shown in Figs. 5.45(b), 5.45(c), and 5.45(d). Here, the $\sqrt{A}$ value was determined for three different configuration ($J \parallel a$-axis and $H \parallel c$-axis, shown by circles, $J \parallel b$-axis and $H \parallel c$-axis, shown by triangles, and $J \parallel c$-axis and $H \parallel c$-axis, shown by squares). The cyclotron mass at $H = 0$ is thus estimated to be 23 m_0 for $F = 1.22\times10^6$ Oe (branch ζ), 160 m_0 for $F = 9.75\times10^6$ Oe (branch β), and 140 m_0 for $F = 1.24\times10^7$ Oe (branch α), revealing an extremely large cyclotron mass at $H = 0$.

Summary

The A value is steeply reduced with increasing pressure, revealing that the heavy fermion state below 1 GPa is changed into the so-called valence fluctuating state at pressures larger than 3.4 GPa. The magnetic field also strongly reduces the A value and the cyclotron mass. The A value, however, becomes distinct and is enhanced at the metamagnetic field in a characteristic pressure region where the electronic state deviates from the heavy fermion state, for example, at 2.00 GPa.

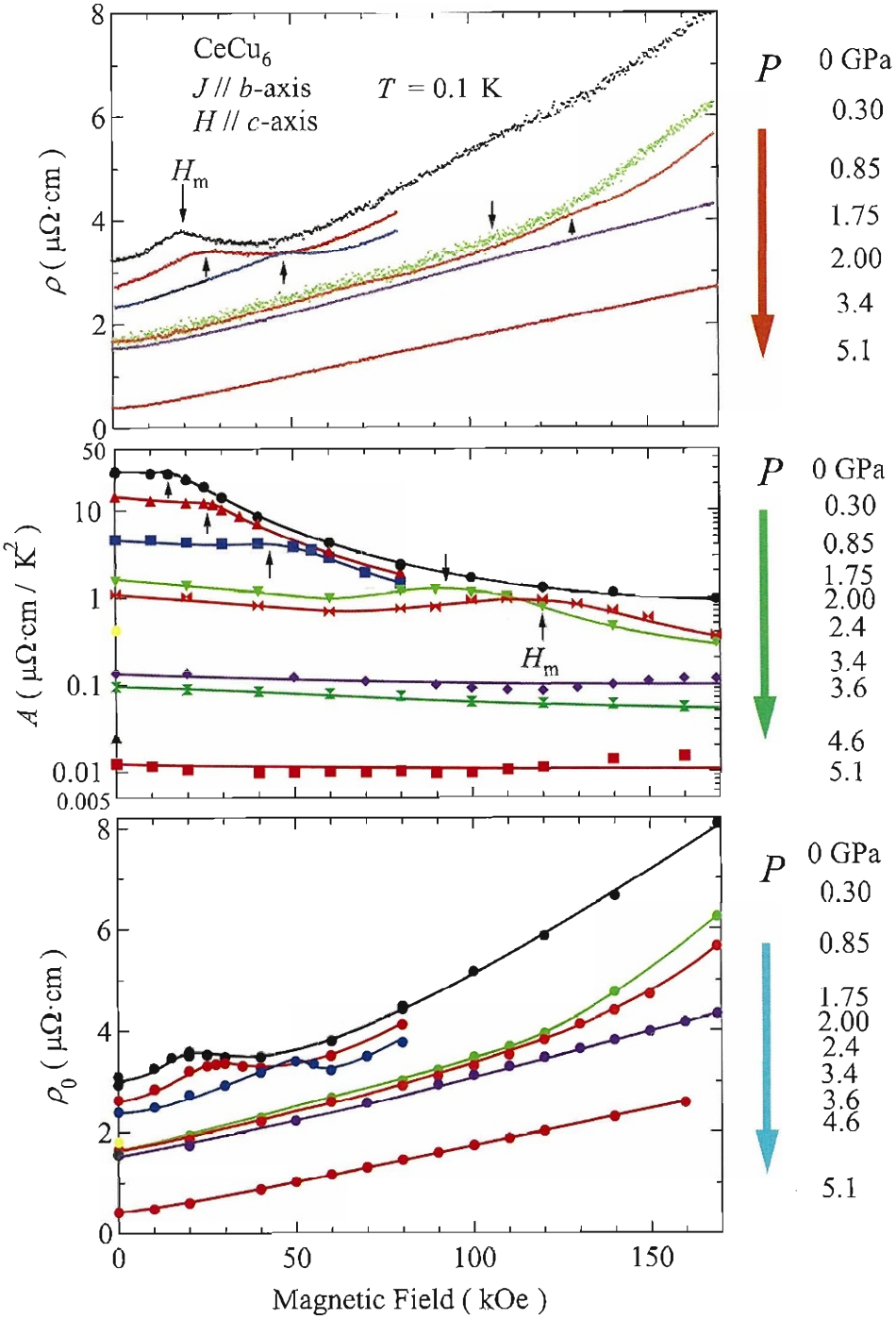

Fig. 5.40 (a) Magnetoresistance at 100 mK, field dependence of (b) A and (c) ρ_0 at various pressures up to 5.1 GPa in $CeCu_6$.

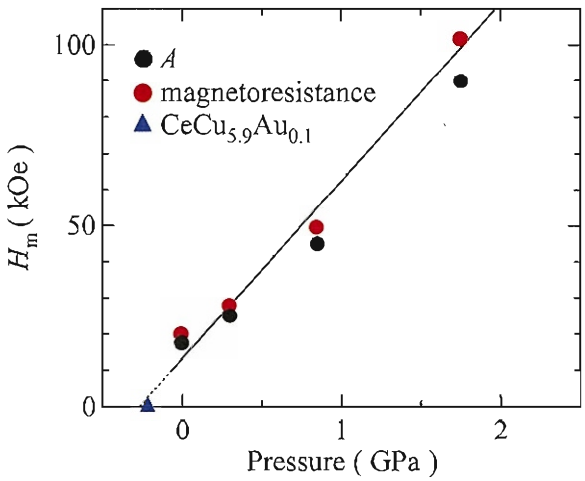

Fig. 5.41 Pressure dependence of H_m, which determined from the magnetoresistance and A values, together with the data on $CeCu_{5.9}Au_{0.1}$(triangle) cited from refs. 179 and 180.

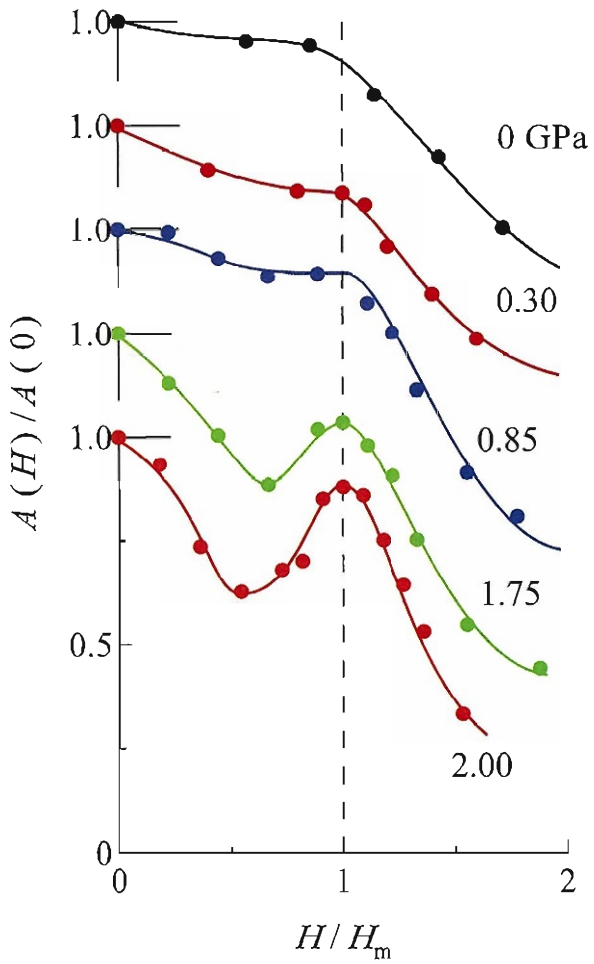

Fig. 5.42 H/H_{m}-dependence of $A(H)/A(0)$ under several pressures in $CeCu_6$.

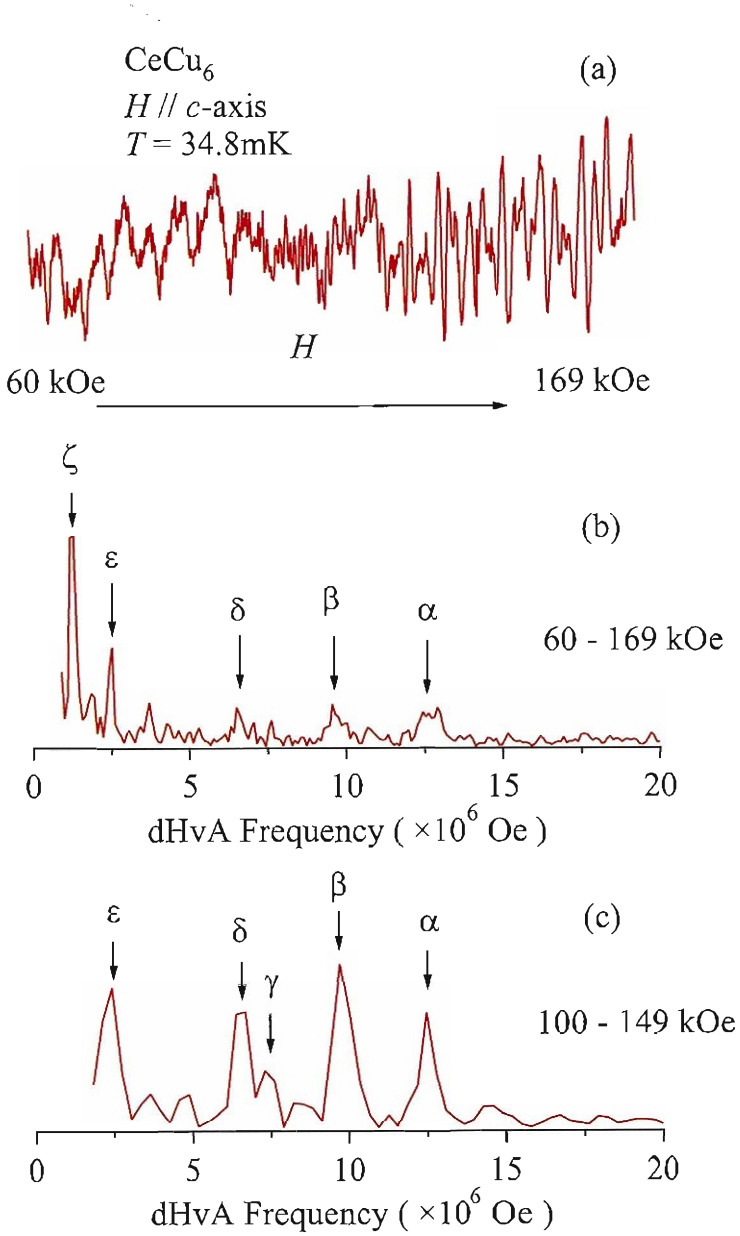

Fig. 5.43 (a) dHvA oscillation for $H \parallel c$-axis at 34.8 mK, and (b) and (c) the corresponding FFT spectra in different magnetic field ranges from 60 to 169 kOe and from 100 to 149 kOe, respectively.

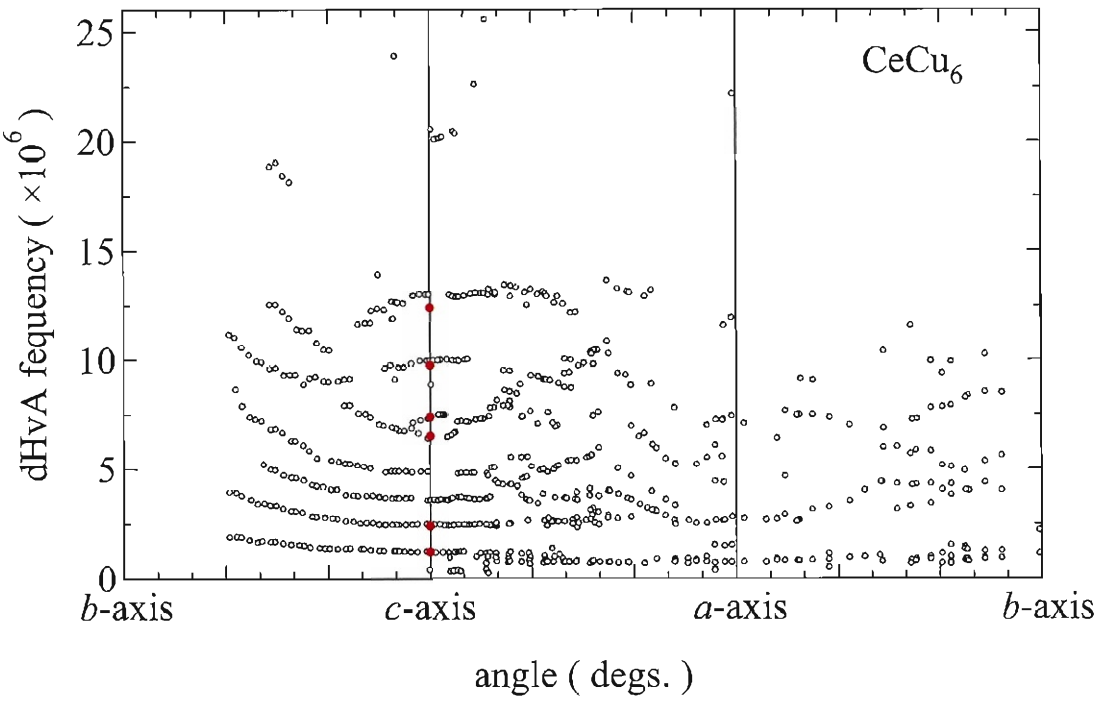

Fig. 5.44 Angular dependence of the dHvA frequency (red solid circles) in $CeCu_6$, together with the previous data (open circles) cited from ref. 181.

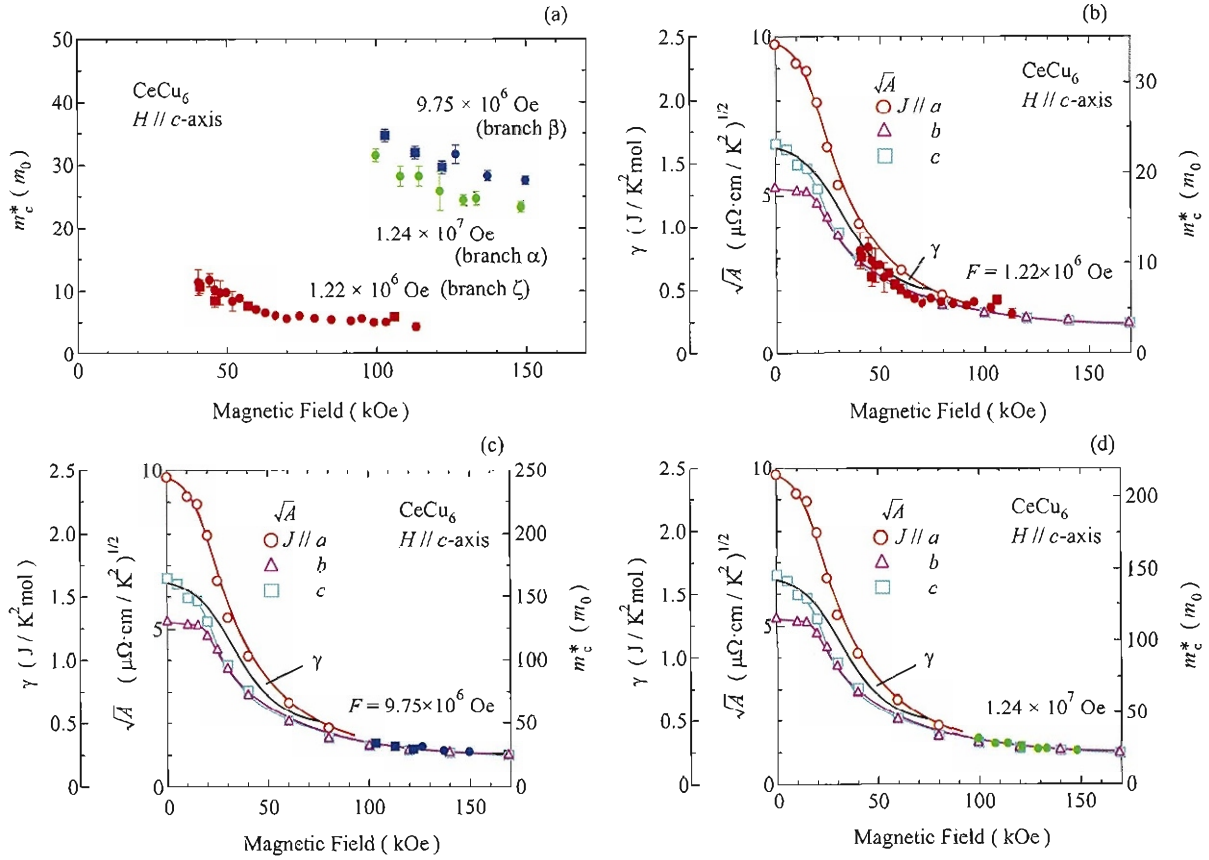

Fig. 5.45 (a) Magnetic field dependence of m_c^* for three different dHvA branches for the magnetic field along the c-axis : $F = 1.22 \times 10^6$ (branch ζ), 9.75×10^6 (branch β), and 1.24×10^7 Oe (branch α), (b), (c), and (d) field dependence of $\sqrt{A}$ ($\sqrt{A}$ data in $J \parallel a$, b, and c correspond to open circles, open triangles, and open squares, respectively), electronic specific coefficient γ (a solid line) cited from ref. 182, and m_c^* (solid circles), together with the previous data (solid squares) cited from ref. 181 for three dHvA frequencies in $CeCu_6$.

5.5 YbT_2Zn_{20}

Introduction

Most of Ce and U compounds order antiferromagnetically. Some compounds such as $CeCu_6$, $CeRu_2Si_2$ and UPt_3 exhibit no long-range magnetic ordering[1]. The magnetic susceptibility of these compounds shows a maximum at a characteristic temperature $T_{\chi max}$. Below $T_{\chi max}$, the susceptibility becomes almost temperature-independent, and an f-electron nature is changed into a new electronic state, called the heavy fermion state. Here, $T_{\chi max}$ approximately corresponds to the Kondo temperature T_K. One of the characteristic properties in the heavy fermion compounds is the metamagnetic behavior or an abrupt nonlinear increase of magnetization at the magnetic field H_m at temperatures lower than $T_{\chi max}$. The metamagnetic behavior appears at $H_m = 77$ kOe in $CeRu_2Si_2$ and $H_m = 200$ kOe in UPt_3, for example[37,48], as mentioned in Sec 2.3 (see Fig. 2.14), and furthermore we studied precisely the metamagnetic behavior in $CeCu_6$ in Sec. 5.4.

YbT_2Zn_{20} (T: Co, Rh, Ir) crystallizes in the cubic $CeCr_2Al_{20}$ ($Fd\bar{3}m$) crystal structure. It is remarkable that the lattice constant $a = 14.187$ Å in $YbIr_2Zn_{20}$ is very large, and thus the distance between Yb-Yb atoms is considerably large, 6.14 Å, compared with $a = 4.20$ Å in $YbAl_3$ with the $AuCu_3$-type cubic structure[]. Note that the Yb atom, which forms the diamond structure, is coordinated by 16 zinc atoms, and the Ir atom has an icosahedral zinc coordination, forming the caged structures, as shown in Fig. 5.46.

We studied the metamagnetic behavior of YbT_2Zn_{20} by measuring the magnetization, magnetic susceptibility, ac-susceptibility and magnetoresistance, and propose a relation between $T_{\chi max}$ and H_m in the heavy fermion compounds. Single crystals were grown by the Zn-self flux method, as described in Chap.4.

Experimental results and analyses

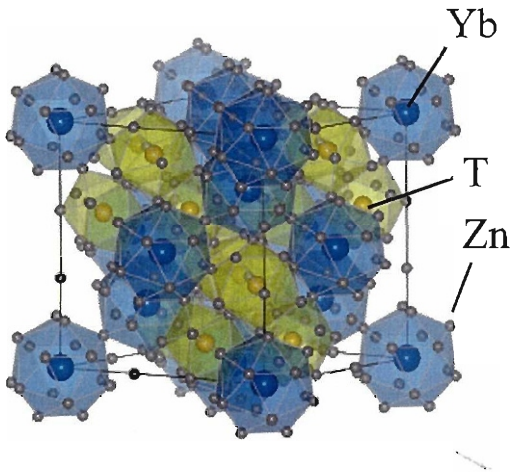

Fig. 5.46 Crystal structure of YbT_2Zn_{20}.

Figure 5.47(a) shows the temperature dependence of the magnetic susceptibility χ for $H \parallel \langle 100 \rangle$. The susceptibility follows the Curie-Weiss law of $\chi = C/(T + \theta_P) + \chi_0$: the Curie term with an effective magnetic moment $\mu_{eff} = 4.54\ \mu_B$/Yb, close to $\mu_{eff} = 4.57\ \mu_B$/Yb of Yb^{+3}, a paramagnetic Curie temperature θ_P = -27 K and χ_0 = -1.05×10^{-3} emu/mol. The susceptibility possesses a broad peak at $T_{\chi max} = 7.4$ K, which is characteristic in the heavy fermion compounds. The present result is the same as the previous one[183].

The high-field magnetization for $H \parallel \langle 100 \rangle$ is shown in Fig. 5.47(b), revealing a metamagnetic behavior at $H_m = 97$ kOe. The corresponding magnetoresistance is also shown in Fig. 5.47(c). A change of the magnetoresistance was observed at $H_m = 97$ kOe, as shown by an arrow, together with small changes at $H'_m = 60$ kOe and $H''_m = 120$ kOe. The metamgnetic transition field is slightly anisotropic : $H_m = 120$ kOe for $H \parallel \langle 110 \rangle$.

The similar measurements were carried out for $YbRh_2Zn_{20}$, as shown in Fig. 5.48. The magnetic susceptibility has a maximum at $T_{\chi max} = 5.3$ K, as shown in Fig. 5.48(a). The metamagnetic behvior was observed at $H_m = 64$ kOe in the magnetization, as shown in Fig. 5.48(b) and another anomaly was furthermore observed at $H'_m = 84$ kOe in the magnetoresistance, as shown in Fig. 5.48(c)

In $YbCo_2Zn_{20}$, the metamagnetic behavior was observed at a very small magnetic field $H_m = 6$ kOe at temperatures lower than 0.3 K. The susceptibility increases with decreasing temperature down to 1.8 K, following the Curie-Weiss law, as shown in Fig. 5.49(a). We therefore measured the ac-susceptibility below 1 K, and obtained a peak at $T_{\chi max} = 0.32$ K, as shown in inset of Fig. 5.49(a). The magnetization at 1.3 K didn't reveal the metamagnetic behavior, as shown in Fig. 5.49(b). The metamagnetic behavior at $H_m = 6$ kOe is reflected in the ac-susceptibility at 60 mK, as shown in inset of Fig. 5.49(b), and in the magnetoresistance at 100 mK, as shown in Fig. 5.49(c). $YbCo_2Zn_{20}$ is therefore located in the vicinity of the quantum critical point. In fact, the electronic specific heat coefficient γ is very large, 8000 mJ/K^2·mol[183].

From the present results of the metamagnetic behavior, together with the previous results of Ce and U compounds, we constructed the relation between $T_{\chi max}$ and H_m, as shown in Fig. 5.50. A solid line in Fig. 5.50 indicates a simple relation of H_m(kOe) = 15 $T_{\chi max}$(K), namely $\mu_B H_m = k_B T_{\chi max}$.

It is noted that the relation between A and γ is known as the Kadowaki-Woods plot[31], as described in Sec. 2.2. The A and γ values in YbT_2Zn_{20}(T : Co, Rh, Ir) are found to belong the generalized Kadowaki - Woods relation for $N = 4$[32,183,184], as shown Fig. 5.51. Shown later, the value of $A = 380\ \mu\Omega$·cm/K^2 at 0 kOe under 5.0 GPa in $YbIr_2Zn_{20}$ exceeds $\gamma = 10$ J/(K^2·mol) if we follow this relation. This is realized in YbT_2Zn_{20}, revealing $A = 160\ \mu\Omega$·cm/K^2 and $\gamma = 8000$mJ/(K^2·mol) in $YbCo_2Zn_{20}$.

Summary

A simple relation between the characteristic temperature $T_{\chi max}$ and the metamagnetic field H_m was obtained experimentally for heavy fermion compounds YbT_2Zn_{20} (T : Ir, Rh, and Co) : $H_m = 15\ T_{\chi max}$(K). In $YbCo_2Zn_{20}$, an electronic state with a very small Kondo temperature $T_{\chi max} = 0.32$ K is realized, which corresponds to a very large γ value

of 8000 mJ/K^2·mol. This might be mainly due to a long distance between Yb atoms, 6 Å, together with the cage structure.

Recent results in YbT_2Zn_{20}: an effect of pressure on the electronic state

The effect of pressure on the electronic state furthermore was studied in YbT_2Zn_{20}. This is because the quantum critical point and magnetic ordering are attained by applying pressure. The magnetoresistance at 0.1 K was measured under several pressures for $YbIr_2Zn_{20}$. With increasing pressure, the metamagnetic field $H_m = 97$ kOe at ambient pressure, shown by an arrow, shifts to lower magnetic fields and becomes zero at $P_c \simeq 5.2$ GPa[185], as shown in Fig. 5.52(a). It is remarkable that a shoulder-like feature of metamagnetic behavior at 0 and 1.2 GPa is changed into a sharp peak at higher pressures. The present peak, associated with the metamagnetic behavior, is a guiding parameter to reach the quantum critical point: $P \rightarrow P_c$ for $H_m \rightarrow 0$, as shown in Fig. 5.52(b). Here, the A value is extremely enhanced with increasing pressure and has a maximum at $P_c \simeq 5.2$ GPa, with $A = 380\,\mu\Omega$·cm/K^2 at 5.0 GPa, as shown in Fig. 5.52(c).

The experimental results are summarized in Fig. 5.52(b) as the pressure vs H_m and pressure vs T_N phase diagrams. At higher pressures than $P_c \simeq 5.2$ GPa, the electronic state is changed into an antiferromagnetic state because the magnetic field vs temperature phase diagram is closed for the present magnetic ordering.

The temperature dependence of the electrical resistivity below 0.8 K was furthermore measured under magnetic fields and pressures. The Fermi liquid relation of $\rho = \rho_0 + AT^2$ is satisfied in these experimental conditions, and the obtained A value is shown in Fig. 5.52(c) as a function of magnetic field. A broad peak at $H_m = 97$ kOe at ambient pressure in the A value is changed into a distinct peak at 2.2 and 3.4 GPa, together with an anomalous enhancement of A value at higher pressures: $A = 380\ \mu\Omega$·cm/K^2 at 0 kOe under 5.0 GPa, as mentioned above, which is strongly reduced with increasing magnetic field: $A = 1.45\,\mu\Omega$·cm/K^2 at 80 kOe under 5.0 GPa.

The similar phase diagrams are obtained for $YbRh_2Zn_{20}$ and $YbCo_2Zn_{20}$, as shown in Figs. 5.53 and 5.54, respectively. It is noted that T_{FL} in Fig. 5.53 means the temperature below which the Fermi liquid relation $\rho = \rho_0 + AT^2$ is satisfied. It is also noted that the quadrupolar ordering is realized in magnetic fields along the $\langle 111 \rangle$ direction for $YbCo_2Zn_{20}$, as shown in Figs. 5.54(b) and 5.54(c). The CEF level crossing creates the quadrupolar ordering. This is based on a small CEF level splitting energy : Γ_6(0 K) doublet - Γ_8(9.1 K) quartet - Γ_7(29 K) doublet.

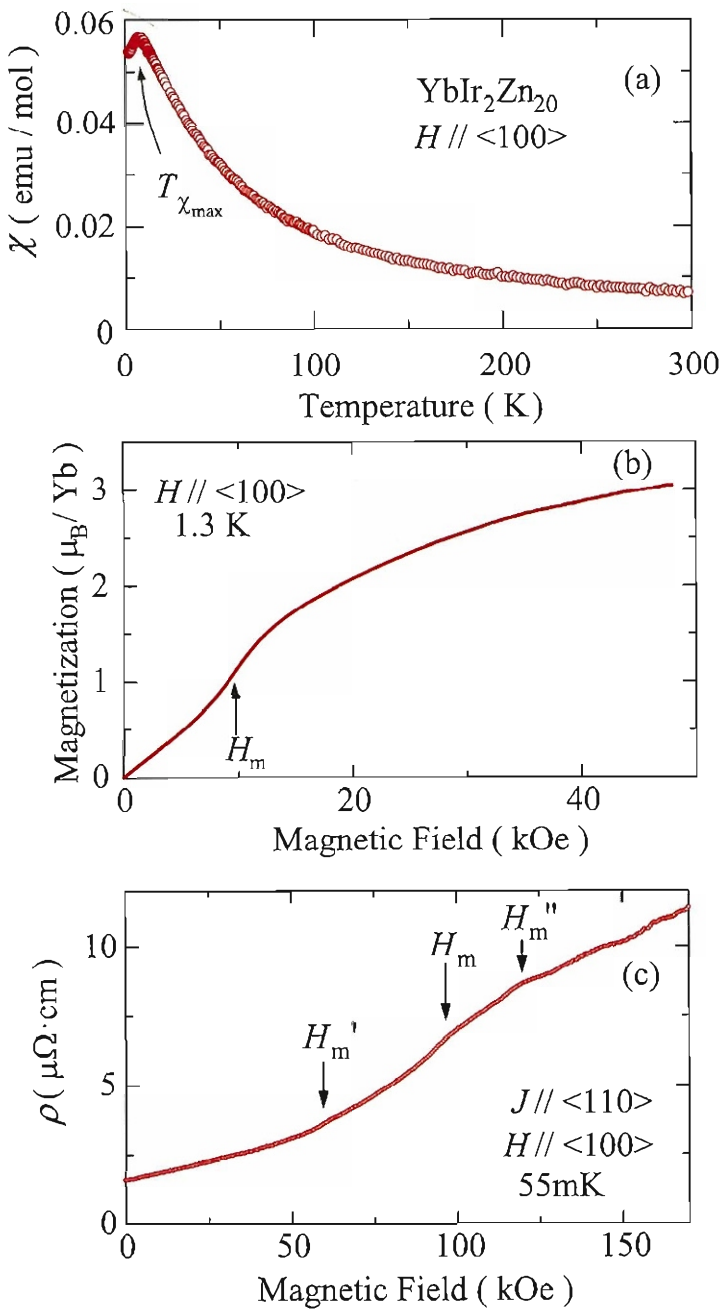

Fig. 5.47 (a) Temperature dependence of the magnetic susceptibility, (b) magnetization, and (c) transverse magnetoresistance in $YbIr_2Zn_{20}$.

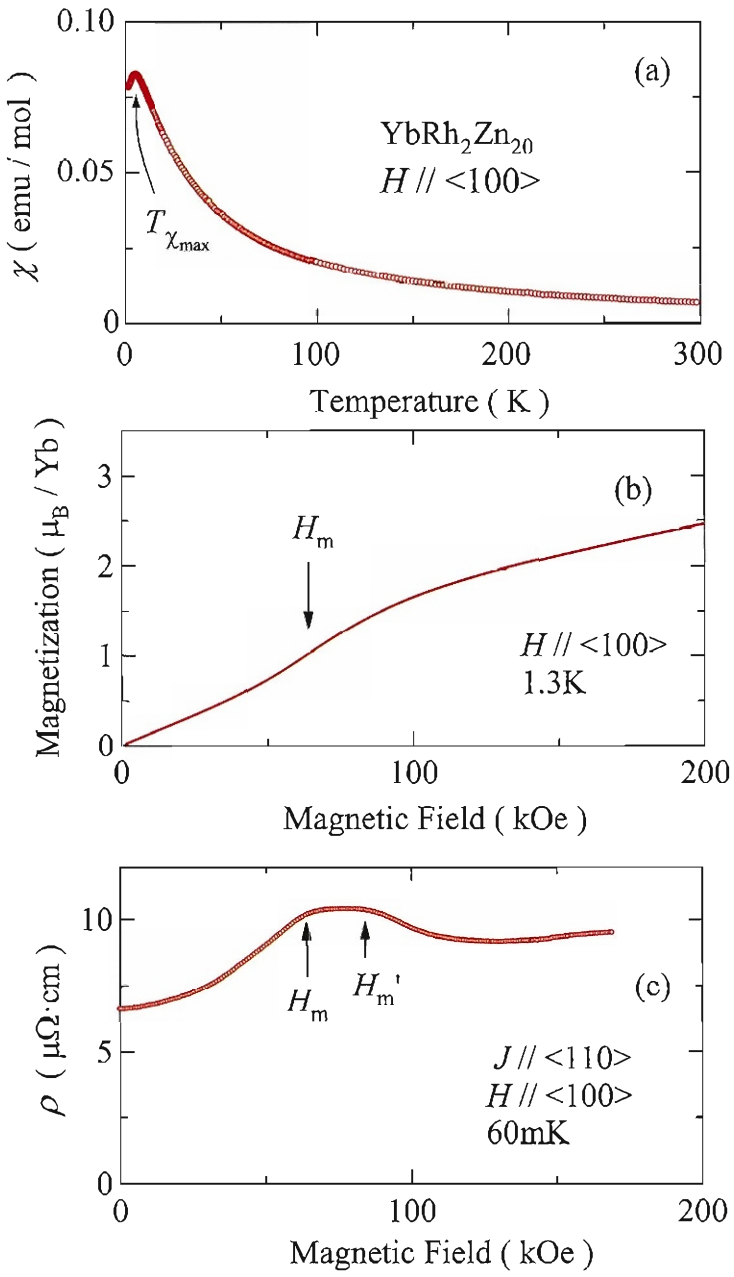

Fig. 5.48 (a) Temperature dependence of the magnetic susceptibility, (b) magnetization and (c) transverse magnetoresistance in $YbRh_2Zn_{20}$.

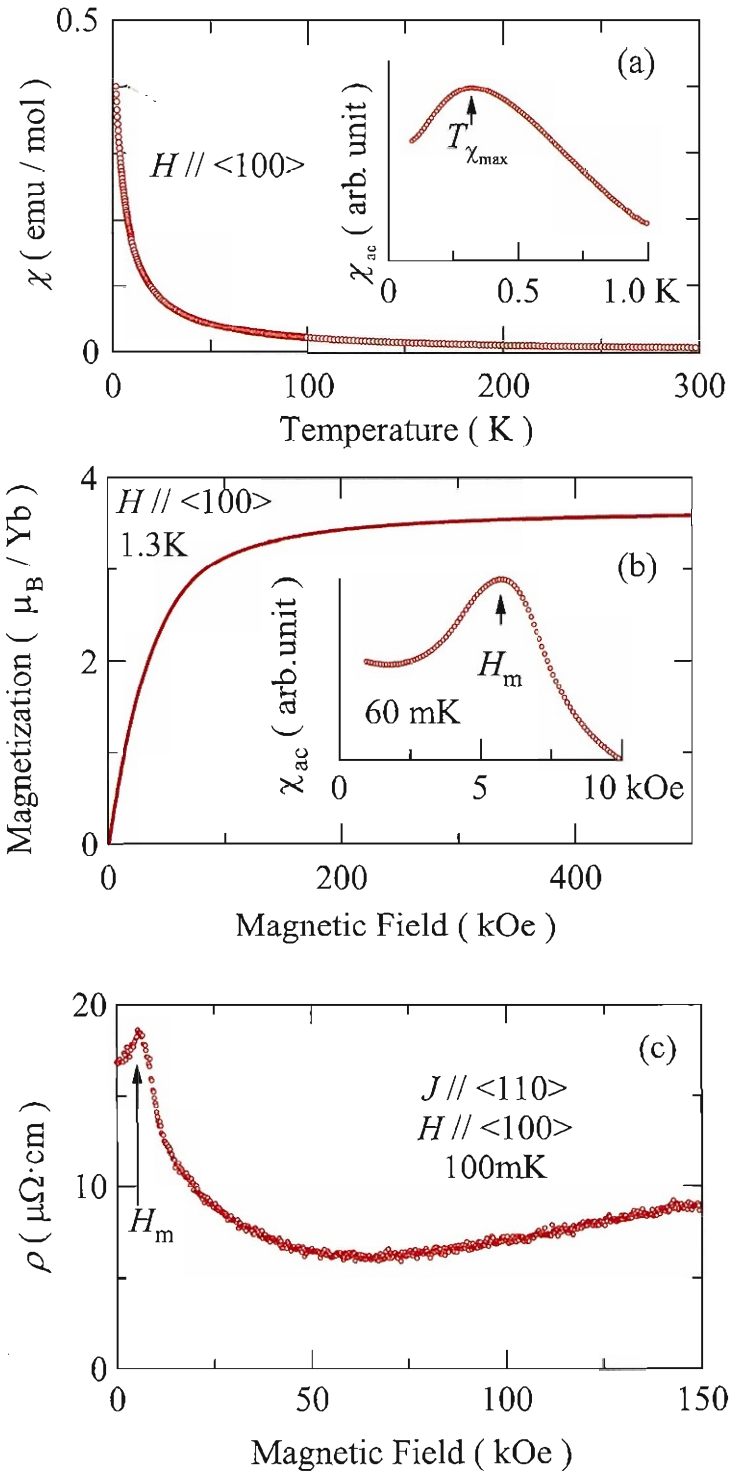

Fig. 5.49 (a) Temperature dependence of the magnetic susceptibility, (b) magnetization, and (c) transverse magnetoresistance in $YbCo_2Zn_{20}$.

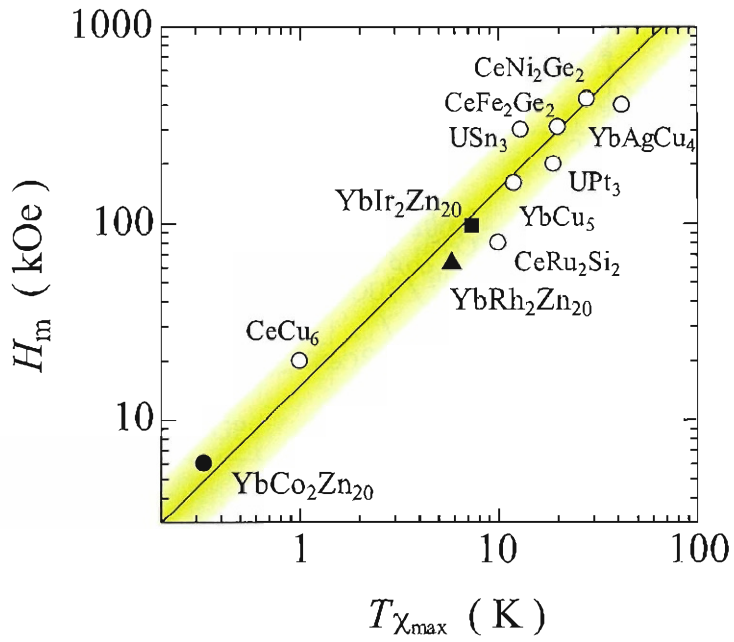

Fig. 5.50 Relation between H_m and $T_{\chi max}$ in heavy fermion compounds.

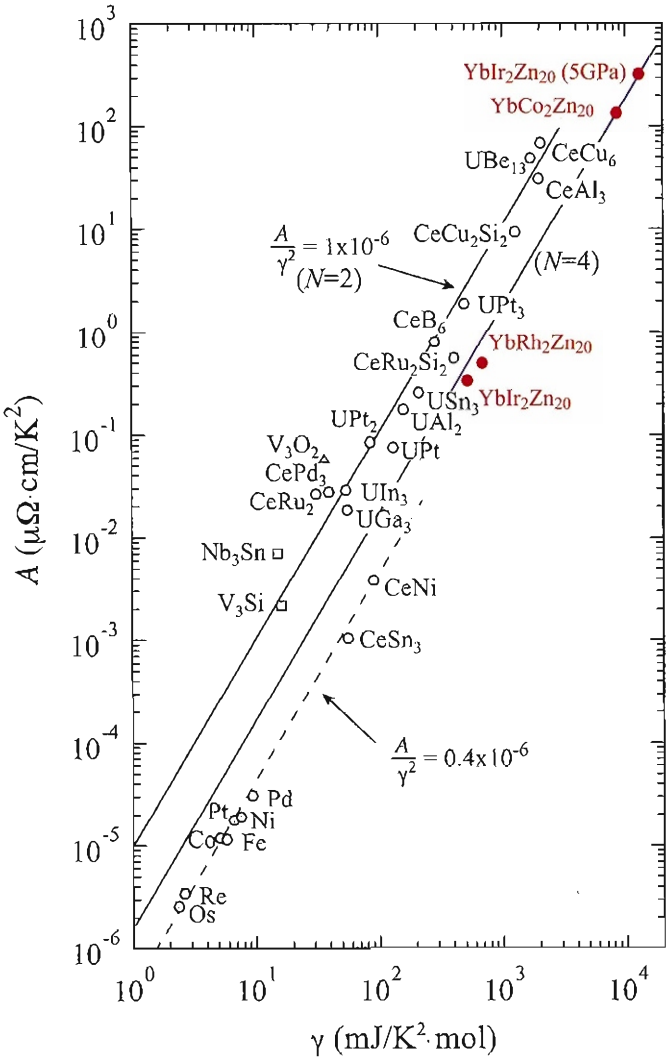

Fig. 5.51 Generalized Kadowaki - Woods plot in YbT_2Zn_{20}(T : Co, Rh, Ir).

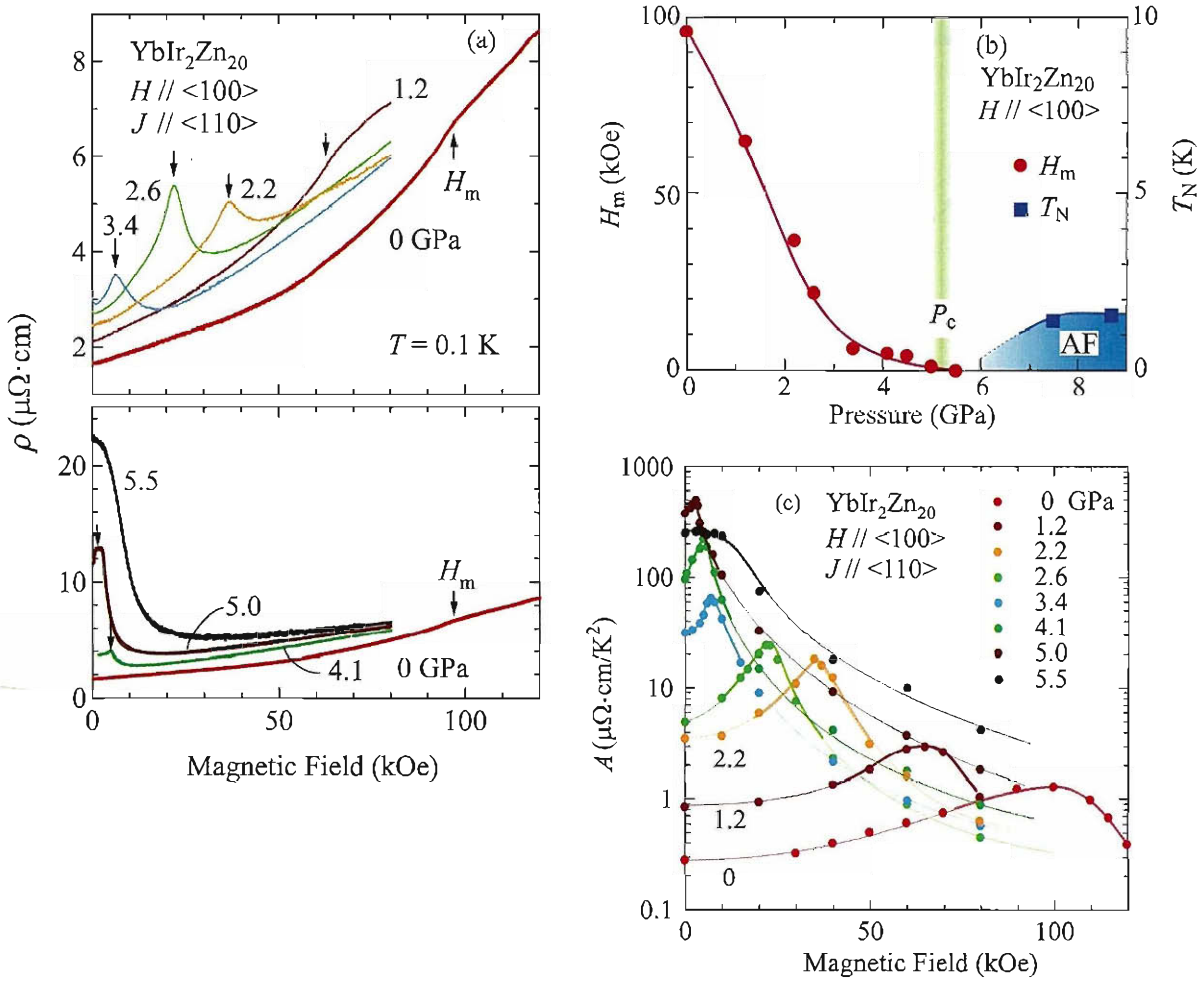

Fig. 5.52 (a) Transverse magnetoresistance in the pressure region from 0 to 5.5 GPa, (b) pressure dependence of the metamagnetic field H_m and the Néel temperature T_N, and (c) magnetic field dependence of the A value under several pressures in $YbIr_2Zn_{20}$, cited from ref. 185.

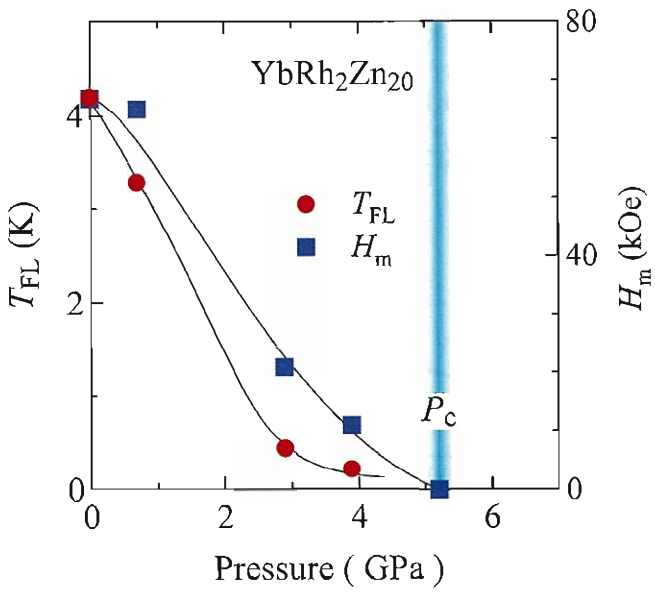

Fig. 5.53 Pressure effect of H_m and T_{FL}.

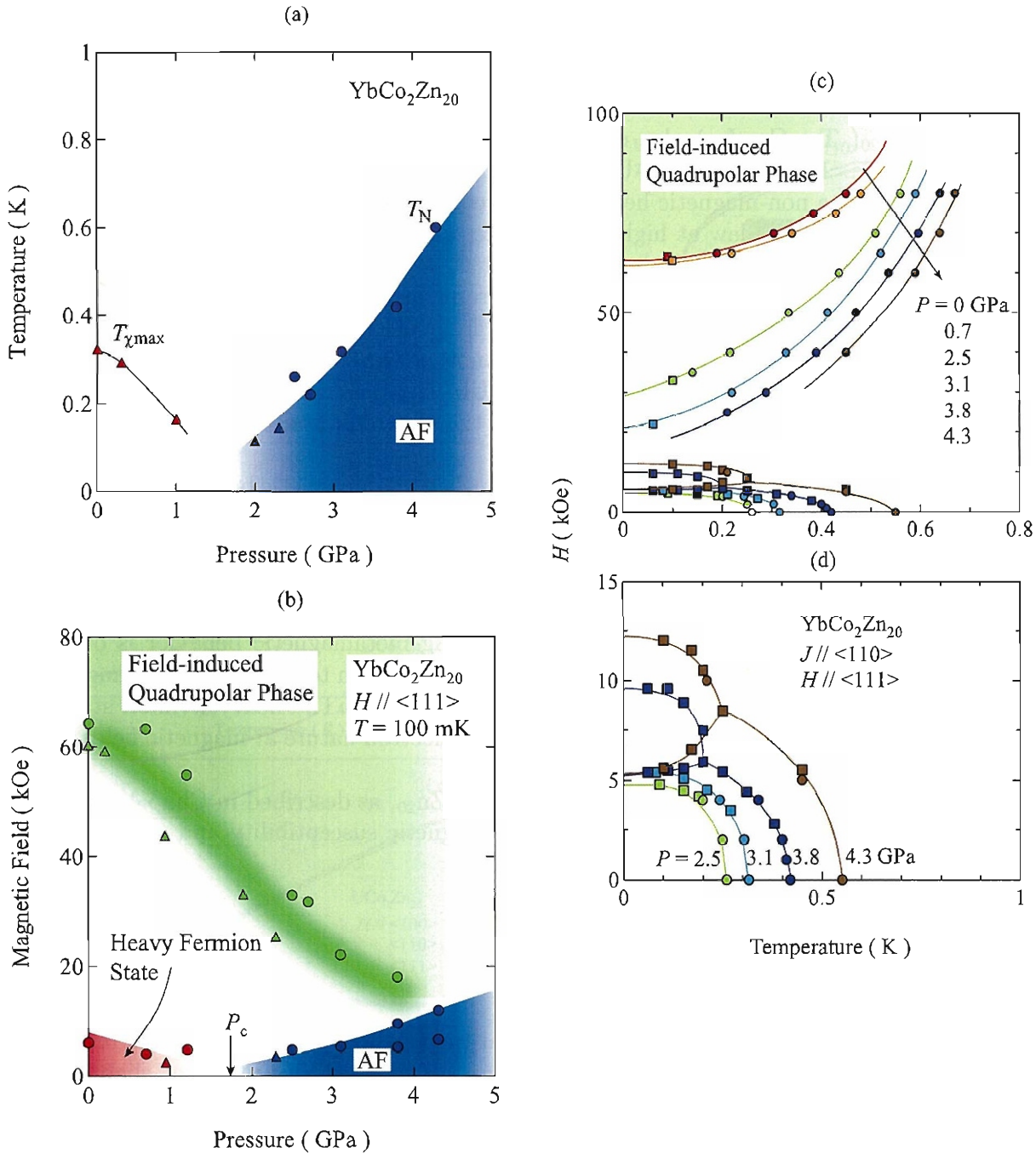

Fig. 5.54 (a) $T-P$ phase diagram, (b) $H-P$ phase diagram at 100 mK (triangles and circles are obtained from Bridgman anvil cell and piston cylinder cell, respectively), and (c) $H-T$ phase diagram at several pressures for $H \parallel \langle 111 \rangle$ in $YbCo_2Zn_{20}$ (circles and squares correspond to temperature dependence and field dependence measurements). (d) An extended figure in low magnetic field ranges in (c).

5.6 UT_2Zn_{20}

Introduction

UT_2Zn_{20}(T : Co, Ir) also crystallizes in the cubic structure with a large lattice constant $a \simeq 14$ Å and the U-U distance $d \simeq 6$ Å, as in YbT_2Zn_{20}. UCo_2Zn_{20} was reported to be a non-magnetic heavy fermion compound[186]. The magnetic susceptibility follows a Curie-Weiss law at high temperatures and possesses a maximum at $T_{\chi max} = 7$ K. The corresponding specific heat coefficient C/T also possesses a broad maximum at 5 K. On the other hand, UIr_2Zn_{20} was a ferromagnet with a Curie temperature $T_C = 2.1$ K[186]. Both compounds, however, possess large electronic specific heat coefficients $\gamma = 230$ and 450 mJ/(K^2·mol), respectively. Another experimental results were reported very recently, claiming that UCo_2Zn_{20} and UIr_2Zn_{20} are non-magnetic heavy fermion compounds with $T_{\chi max} = 8.2$ and 4.5 K, and the electronic specific heat coefficient $\gamma = 350$ and 400 mJ/(K^2·mol), respectively[187].

A non-linear increase of magnetization, namely a metamagnetic behavior was observed at the magnetic field H_m in the similar non-magnetic heavy fermion compounds YbT_2Zn_{20} (T : Co, Rh, and Ir)[188] as described in Sec 5.5. A simple relation between $T_{\chi max}$ and H_m in Ce-, U-, and Yb-based heavy fermion compounds including YbT_2Zn_{20} was obtained as $15T_{\chi max}(K) = H_m(kOe)$, namely $k_B T_{\chi max} = \mu_B H_m$. Here, $T_{\chi max}$ roughly corresponds to the Kondo temperature, and the corresponding metamagnetic behavior is observed below $T_{\chi max}$. The almost localized f-electron nature at high temperatures is changed into a heavy fermion state at temperatures lower than $T_{\chi max}$. The heavy fermion state can be, however, changed into the almost localized f-electron nature at magnetic fields larger than H_m.

We grew single crystals of UCo_2Zn_{20} and UIr_2Zn_{20}, as described in Chap.4, and measured the electrical resistivity, specific heat, magnetic susceptibility and magnetization to investigate the metamagnetic behavior.

Experimental results and analyses

UCo_2Zn_{20}

First, we show in Fig. 5.55(a) the temperature dependence of the electrical resistivity ρ in UCo_2Zn_{20}, together with that in UIr_2Zn_{20}. The resistivity increases slightly with decreasing temperature, has a broad maximum around 100 K, and decreases steeply at lower temperatures. The resistivity follows a Fermi liquid relation of $\rho = \rho_0 + AT^2$ below 3 K, as shown by a thin solid line in inset of Fig. 5.55(a). The A value is 0.49 $\mu\Omega$·cm/K^2, which corresponds to $\gamma \simeq 220$ mJ/(K^2·mol) from a Kadowaki-Woods relation $A/\gamma^2 = 1.0\times10^{-5}$ $\mu\Omega$·cmK^{-2}/(mJK^{-2}mol^{-1})$^{-2}$[31]. We note that $A = 1.3$ $\mu\Omega$·cm/K^2 and $\gamma = 360$ mJ/(K^2·mol) are obtained for UIr_2Zn_{20}.

The low-temperature specific heat coefficient C/T possesses a broad peak at 6 K, as shown Fig. 5.55(b), and the γ value is 300 mJ/(K^2·mol), which are approximately consistent with the previous results[186,187], together with $\gamma = 220$ mJ/(K^2·mol) estimated

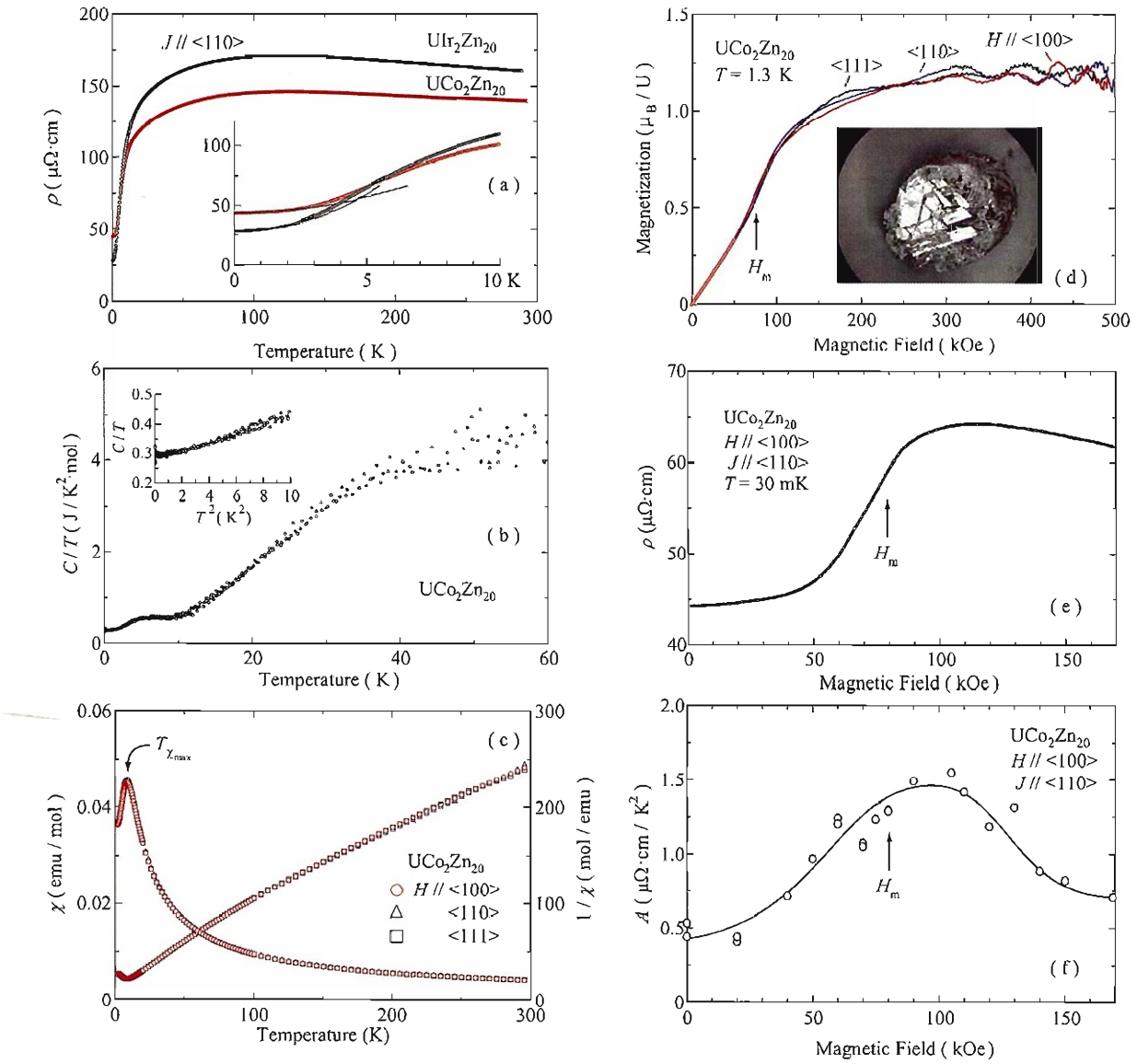

Fig. 5.55 (a) Electrical resistivity of UCo_2Zn_{20} and UIr_2Zn_{20}, (b) specific heat in the form of C/T(inset:C/T vs T^2), (c) magnetic susceptibility and the corresponding inverse susceptibility, (d) high-field magnetization and (inset:single crystal ingots), (d) transverse magnetoresistance, and (e) magnetic field dependence of the A value in UCo_2Zn_{20}.

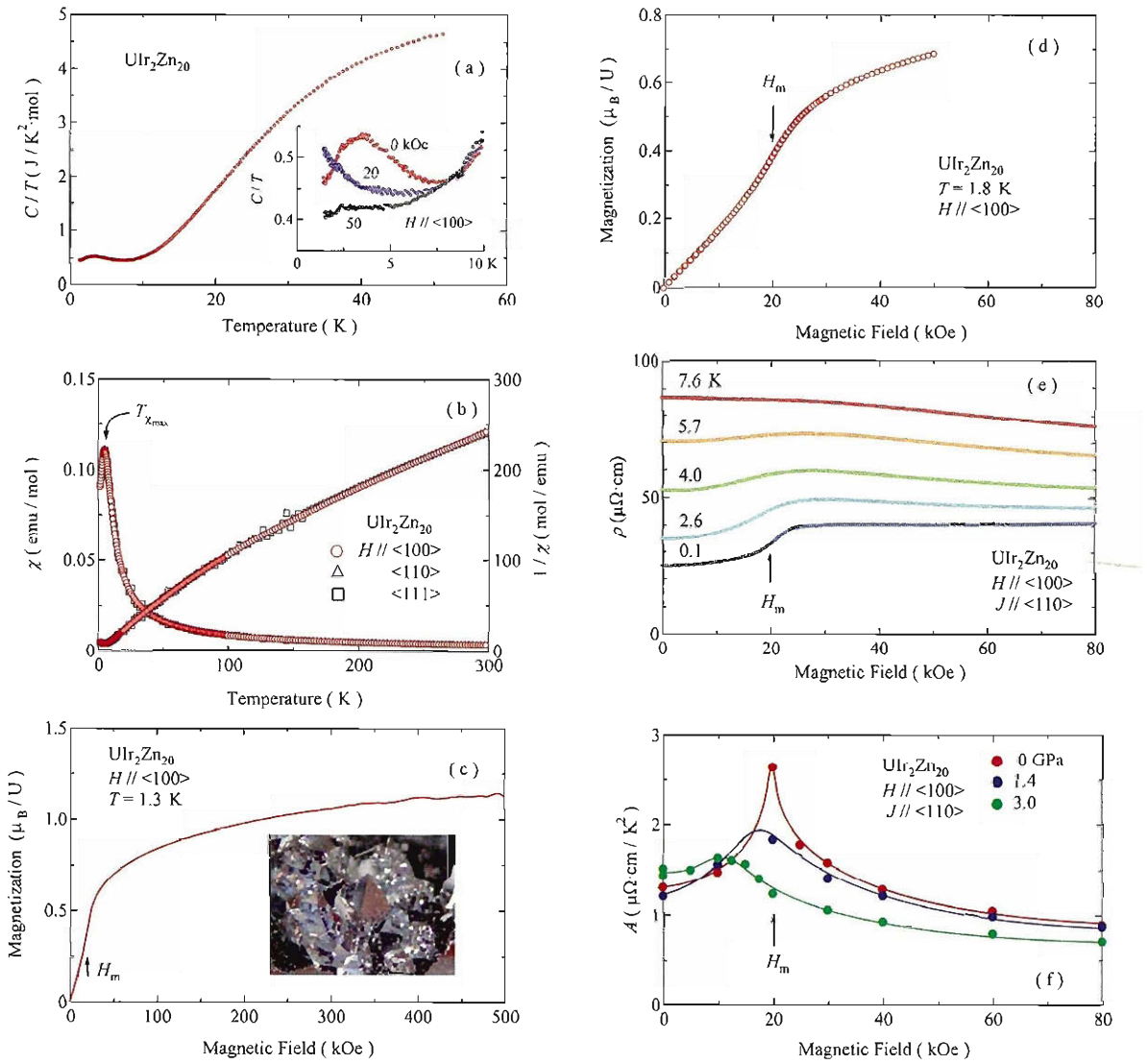

Fig. 5.56 (a) Specific heat in the form of C/T(inset:C/T under 0, 20, and 50 kOe), (b) magnetic susceptibility and the corresponding inverse susceptibility, (c) high-field magnetization (inset:single crystal ingots), (d) magnetization, (e) transverse magnetoresistance at several temperatures, and (e) field dependence of the A value under pressures in UIr_2Zn_{20}.

from the A value, mentioned above. The magnetic susceptibility χ increases with decreasing temperature, and possesses a peak at $T_{\chi max}$ = 8.5 K. No anisotropy is observed below and above $T_{\chi max}$ for $H \parallel \langle 100 \rangle, \langle 110 \rangle$, and $\langle 111 \rangle$. The present peak is therefore not due to a magnetic ordering, but is based on a characteristic heavy fermion behavior, as mentioned in Introduction. The effective magnetic moment and the paramagnetic Curie temperature are obtained as μ_{eff} = 3.44 μ_B/U and θ_P = -63 K, respectively. The present magnetic moment is close to 3.58 μ_B/U of $5f^2$ and 3.62 μ_B/U of $5f^3$ configuration.

A metamagnetic behavior, which is characteristic in heavy fermion compounds, is clearly observed at $H_m \simeq$ 80 kOe for $H \parallel \langle 100 \rangle, \langle 110 \rangle$, and $\langle 111 \rangle$, as shown in Fig. 5.55(d). The magnetic moment at 500 kOe is small, 1.1 μ_B/U. This means that the $5f$ electrons are not fully localized even at high magnetic fields and still contribute to the conduction electrons. The present metamagnetic behavior is also reflected in the transverse magnetoresistance, as shown in Fig. 5.55(e). We also obtained the A value from the temperature dependence of the resistivity under constant magnetic fields. The magnetic field dependence of the A value is shown in Fig. 5.55(f), revealing a broad maximum at around H_m.

UIr_2Zn_{20}

A broad maximum in C/T is observed at 3.5 K in UIr_2Zn_{20}, as shown in Fig. 5.56(a), and the γ value is roughly estimated as 450 mJ/(K^2·mol), which is also consistent with the previous results[187] and γ = 370 mJ/(K^2·mol) estimated from the A value. The present γ value is reduced to 400 mJ/(K^2·mol) at 50 kOe, as shown inset of Fig. 5.56(a). Note that C/T at 20 kOe, which is a metamagnetic field, shown below, increases with decreasing temperature. No anisotropy of the magnetic susceptibility is also observed for $H \parallel \langle 100 \rangle, \langle 110 \rangle$, and $\langle 111 \rangle$, as shown in Fig. 5.56(b). The μ_{eff} and θ_P are 3.55 μ_B/U and -85.8 K, respectively. $T_{\chi max}$ is obtained at 5.3 K.

The metamagnetic behavior is observed at H_m = 20 kOe, as shown in Figs. 5.56(c) and 5.56(d). An increase of transverse magnetoresistance below 4.0 K is suppressed above H_m, as shown in Fig. 5.56(e). It is noted that 4.0 K is below $T_{\chi max}$ = 5.2 K. The A value indicates a sharp peak at H_m = 20 kOe. This peak is, however, reduced with increasing pressure, and most likely diminishes at high pressures of 4 GPa. It is also noted that the A value at H = 0 kOe is approximately unchanged with respect to pressure. This behavior is in contract with that in $YbIr_2Zn_{20}$, where the peak structure is shifted to lower magnetic fields with increasing pressure, and finally H_m becomes zero at a critical pressure P_c = 5.2 GPa, reaching quantum critical point. The A value is increased from A = 0.29 $\mu\Omega$·cm/K^2 at ambient pressure to A = 380 $\mu\Omega$·cm/K^2 at P_c[185].

Summary

We observed a metamagnetic behavior at H_m = 80 kOe for $T_{\chi max}$ = 8.5 K in UCo_2Zn_{20} and at H_m = 20 kOe for $T_{\chi max}$ = 5.2 K in UIr_2Zn_{20}. The present metamagnetic behavior is typical in heavy fermion Ce, Yb, and U compounds, and a simple relation of 15 $T_{\chi max}$(K) = H_m(kOe) is roughly applied to UCo_2Zn_{20} and UIr_2Zn_{20}.

5.7 $YbPd_5Al_2$

Introduction

Superconductivity in the f-electron systems has been observed in Ce, Pr, Yb, U, and nowadays, even transuranium compounds. It was a surprise that heavy fermion superconductivity was discovered in $NpPd_5Al_2$[189]. This is because most of the Np compounds order magnetically. In fact, superconductivity of $NpPd_5Al_2$ is realized in the vicinity of antiferromagnetic ordering, or in the electronic state close to the so-called quantum critical point.

$CePd_5Al_2$, which is an analog of $NpPd_5Al_2$, is an antiferromagnet[190], but becomes superconductive under pressure[191]. Both $CePd_5Al_2$ and $NpPd_5Al_2$ compounds crystallize in the tetragonal $ZrNi_2Al_5$-type structure, where $CePd_3$ ($NpPd_3$) and Pd_2Al_2 layers are stacked along the [001] direction (c-axis) as shown in Fig. 5.57. They are layered compounds whose cleavage plane corresponds to the tetragonal (001) plane. Reflecting the layered structure, as shown in Fig. 5.57, the results of energy band calculations for $NpPd_5Al_2$ and RPd_5Al_2 (R: La, Ce) reveal that the electronic state is not three dimensional but quasi-two-dimensional. Namely, nearly cylindrical Fermi surfaces are observed in $CePd_5Al_2$ and $PrPd_5Al_2$[192].

We continued trying to grow a new RPd_5Al_2 compound, and succeeded in growing single crystals of $YbPd_5Al_2$. The electrical and magnetic properties are studied for a new compound $YbPd_5Al_2$.

Experimental procedure

We grew a single crystal of $YbPd_5Al_2$ by the Bridgman method, as described in Chap.3. The electrical resistivity was measured by the conventional four-probe DC and/or AC method. The magnetic susceptibility and magnetization measurements were carried out using a commercial SQUID magnetometer. The high-field magnetization was measured by the standard pick up coil method using a long-pulse magnet with a pulse duration of 50 ms. The specific heat was measured by the quasi-adiabatic heat pulse method. The electrical resistivity was also measured under pressure using a diamond anvil cell with glycerin as a pressure transmitting medium.

Experimental results and analyses

Figure 5.58(a) shows temperature dependences of the electrical resistivity for the current J along the [100] and [001] directions. Anisotropy of the resistivity is small compared with that of $CePd_5Al_2$[190,191], although the resistivity for $J \parallel [001]$ is larger than that for $J \parallel [100]$. The resistivity decreases almost lineally with decreasing temperature. This suggests that $YbPd_5Al_2$ is not a heavy fermion compound but either $4f$-localized or Yb^{2+}-Pauli-paramagnetic compound. As shown later, the $4f$ electrons are found to be magnetic and localized in nature.

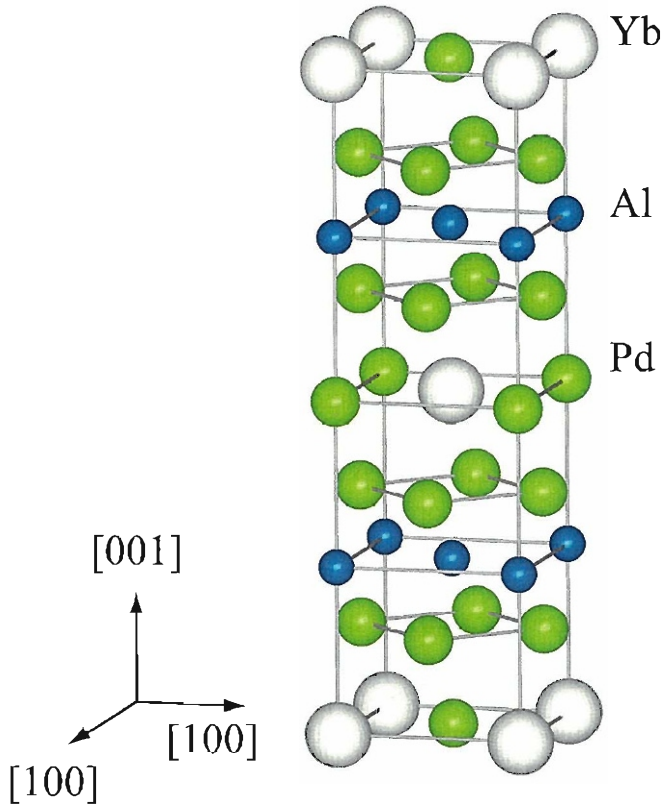

Fig. 5.57 Tetragonal crystal structure of $YbPd_5Al_2$. This crystal structure is the same with those in $CePd_5Al_2$ and $NpPd_5Al_2$.

We measured the electrical resistivity at low temperatures for $J \parallel [110]$ under magnetic fields for $H \parallel [110]$, as shown in Fig. 5.58(b). The resistivity at $H = 0$ kOe decreases almost lineally with decreasing temperature, but indicates a small drop of the resistivity below 0.3 - 0.4 K. This corresponds to an appearance of long-range ordering, presumably an antiferromagnetic ordering, as shown later in the specific heat. To know the A value of the Fermi liquid relation $\rho = \rho_0 + AT^2$, we measured the electrical resistivity under magnetic fields. The A value is obtained to be 0.001 - 0.002 $\mu\Omega$·cm for $H = 50$ and 80 kOe, as shown by solid lines in Fig. 5.58(b). These values approximately correspond to the electronic specific heat coefficient $\gamma \simeq 10$ mJ/(K^2·mol) from the Kadowaki-Woods relation, revealing a small γ value.

Figure 5.58(c) shows the temperature dependence of magnetic susceptibility χ and inverse susceptibility $1/\chi$. The susceptibility increases with decreasing temperature, approximately follows the Curie-Weiss law, but does not indicate a magnetic ordering down to the lowest measured temperature of 1.9 K. The effective magnetic moment $\mu_{\rm eff}$ and paramagnetic Curie temperature $\theta_{\rm P}$ are determined from fits of the Curie-Weiss law in the temperature range between 100 and 300 K to be $\mu_{\rm eff} = 4.68\ \mu_{\rm B}$/Yb and $\theta_{\rm P} = 7.2$

K for $H \parallel [100]$, and $\mu_{\rm eff}$ = 4.53 $\mu_{\rm B}$/Yb and $\theta_{\rm P}$ = -27 K for $H \parallel [001]$. The effective magnetic moment is close to 4.54 $\mu_{\rm B}$ for Yb^{3+}.

We measured the high-field magnetization at 1.3 K, as shown in Fig. 5.58(d). The measurement was thus done in the paramagnetic state. The magnetization reaches 3.6 $\mu_{\rm B}$/Yb at 500 kOe for $H \parallel [001]$, which is close to the saturated magnetic moment, 4 $\mu_{\rm B}$/Yb for Yb^{3+}. On the other hand, the magnetization for $H \parallel [100]$ increases rapidly below about 100 kOe and is almost saturated at higher magnetic fields, indicating 3.2$\mu_{\rm B}$ at 50 T. The present anisotropy of magnetization including the magnetic susceptibility is different from those in $CePd_5Al_2$ and $PrPd_5Al_2$, but is similar to that in $NpPd_5Al_2$[189–192]. The crystalline electric field is different between these compounds.

Figure 5.58(e) shows temperature dependences of specific heat of $YbPd_5Al_2$ and a reference compound $LuPd_5Al_2$. The specific heat of $YbPd_5Al_2$ shows a steep increase below 1 K, and indicates a λ-shaped sharp peak at 0.19 K, manifesting an appearance of long-range ordering below $T_{\rm N}$. This ordering corresponds presumably to an antiferromagnetic one because the paramagnetic Curie temperature is negative and this ordering was easily suppressed by an application of magnetic field of 5 kOe. We calculated the magnetic entropy $S_{\rm mag}$ by integrating $C_{\rm mag}/T$ over temperature, where $C_{\rm mag} = C(YbPd_5Al_2)$ - $C(LuPd_5Al_2)$. As shown in inset of Fig. 5.58(e), $S_{\rm mag}$ is about $0.5R$ln2 at $T_{\rm N}$ = 0.19 K and reaches Rln2 at 0.7 K. The large suppression of magnetic entropy at $T_{\rm N}$ and long tail above $T_{\rm N}$ up to about 1 K might simply suggest an existence of Kondo effect at low temperatures. However, the temperature dependence of electrical resistivity and the small value of the coefficient A indicate that $4f$-electrons are well localized. There is a possibility that a short-range antiferromagnetic ordering starts below 0.7 K. The reason of a small magnetic entropy is not clear at present, and is left as a future study.

In order to study the pressure effect of the long-range ordering at $T_{\rm N}$, we measured the electrical resistivity under pressures in the temperature range from 0.05 K to room temperature. Since the anomaly of the resistivity at $T_{\rm N}$ is very weak, the pressure dependence of $T_{\rm N}$ could not be determined in the present experiment. The resistivity at high temperatures is approximately unchanged up to 9.0 GPa, as shown in Fig. 5.58(f), although the residual resistivity is extremely enhanced with increasing pressure. It is thus concluded that the electronic state is almost unchanged by the application of pressure up to 9 GPa.

Summary

We succeeded in growing a single crystal of $YbPd_5Al_2$ by the Bridgman method. $YbPd_5Al_2$ is presumably an antiferromagnet with a very low ordering temperature $T_{\rm N}$ = 0.19 K. The A value is small, 0.001-0.002 $\mu\Omega$·cm, which roughly corresponds to 10 mJ/(K^2·mol). The temperature dependence of the electrical resistivity is not appreciably changed at high pressures up to 9.0 GPa.

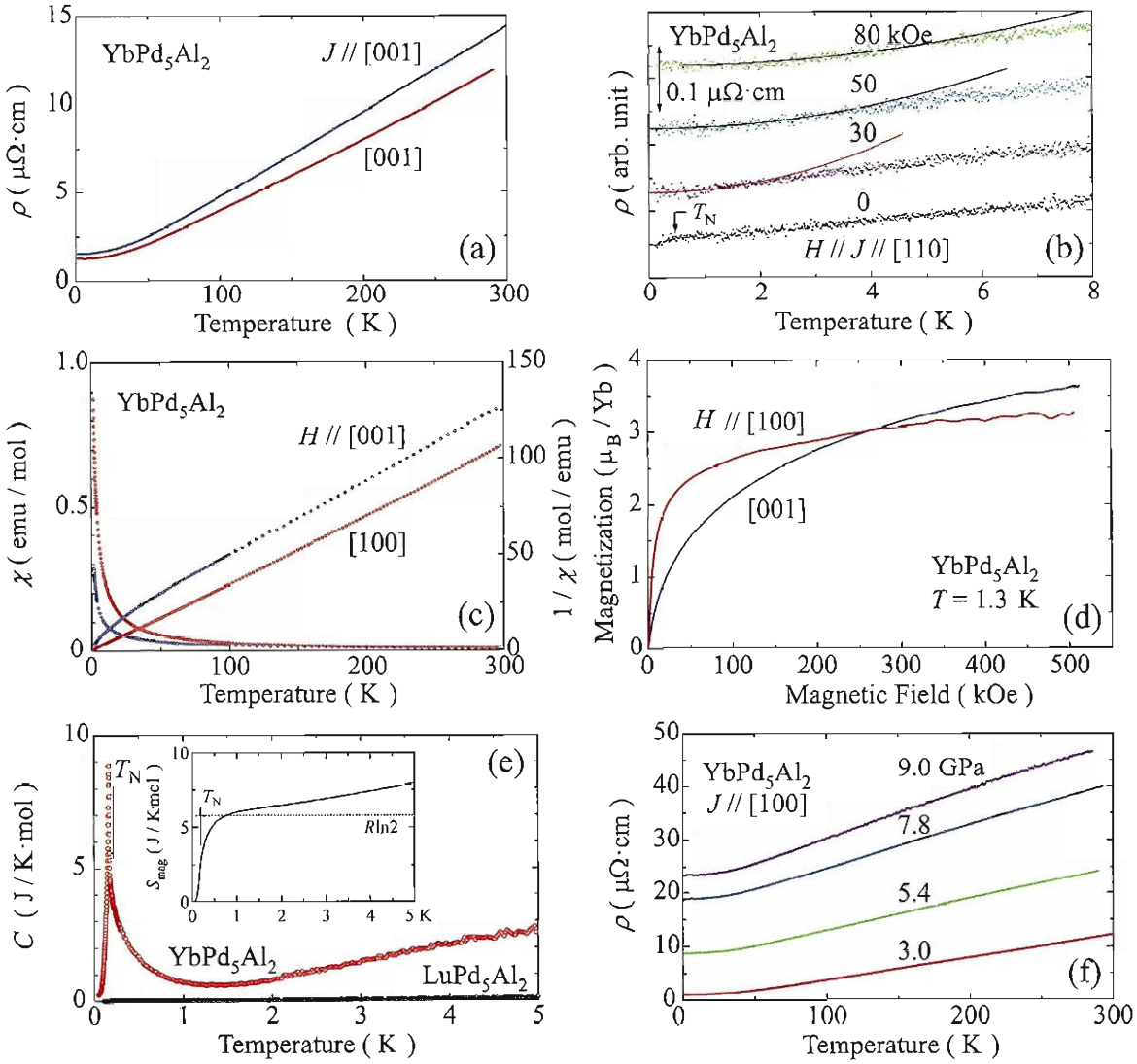

Fig. 5.58 (a) Temperature dependences of the electrical resistivity from room temperature to 1.3 K for $J \parallel [001]$ and [110], (b) low-temperature resistivities under magnetic fields for $J \parallel H \parallel [110]$, where thin solid lines represent the Fermi liquid relation of $\rho = \rho_0 + AT^2$, (c) magnetic susceptibility χ and inverse susceptibility $1/\chi$ in the temperature range from room temperature to 2 K for $H \parallel [001]$ and [100], (d) high-field magnetization curves at 1.3 K for $H \parallel [001]$ and [100] in $YbPd_5Al_2$, (e) low-temperature specific heats in $YbPd_5Al_2$ and $LuPd_5Al_2$(inset : magnetic entropy of $YbPd_5Al_2$), and (f) temperature dependences of the electrical resistivity for $J \parallel [100]$ at several pressures in $YbPd_5Al_2$.

5.8 $YbGa_4$

Introduction

There exist several Yb-Ga compounds such as Yb_2Ga, YbGa, $YbGa_2$, Yb_3Ga_8, $YbGa_{3-x}$, $YbGa_4$, $YbGa_5$, and $YbGa_6$.[122,193–195] Among them, $YbGa_2$ with the hexagonal structure is well known as a divalent compound.[196].

We studied the Ga-rich compounds and succeeded in growing single crystals of $YbGa_4$. The electrical and magnetic properties are clarified.

Experimental procedure

Single crystals were grown by the annealing method as described in Chap. 4. The X-ray diffraction measurements were done by using the single crystal sample. The measurements were performed on an imaging plate as a detector with graphite monochromated Mo K_α radiation. The lattice parameter were determined to be a = 6.123 Å, b = 6.110 Å, and c = 6.186 Å, which are in good agreement with the previous report[194]. The crystal data are summarized in Table 5.VI. It is noted that the crystal structure of $YbGa_4$ is the same structure as $CaGa_4$, a monoclinic distortion of $BaAl_4$ type, as shown Fig. 5.59.[197]

The electrical resistivity was measured by the conventional four probe DC and/or AC method. The magnetic susceptibility measurement was carried out by using a commercial SQUID magnetometer. The specific heat was measured by the quasi-adiabatic heat pulse method.

Experimental results and analyses

Figure 5.60 shows the temperature dependence of the electrical resistivity for the current along the c-plane based on the $BaAl_4$ type tetragonal structure. The resistivity is close to

Table 5.VI Lattice parameters, fractional coordinates and equivalent isotopic atomic displacement parameters in $YbGa_4$.

space group Amm2					
lattice parameters					
a [Å]	b [Å]	c [Å]	α	β	γ
6.123	6.110	6.186	90°	120.57°	90°
atom	x	y	z		
Yb	0	0	0		
Ga1	0.602	0	0.229		
Ga2	0	0.24	0.5		

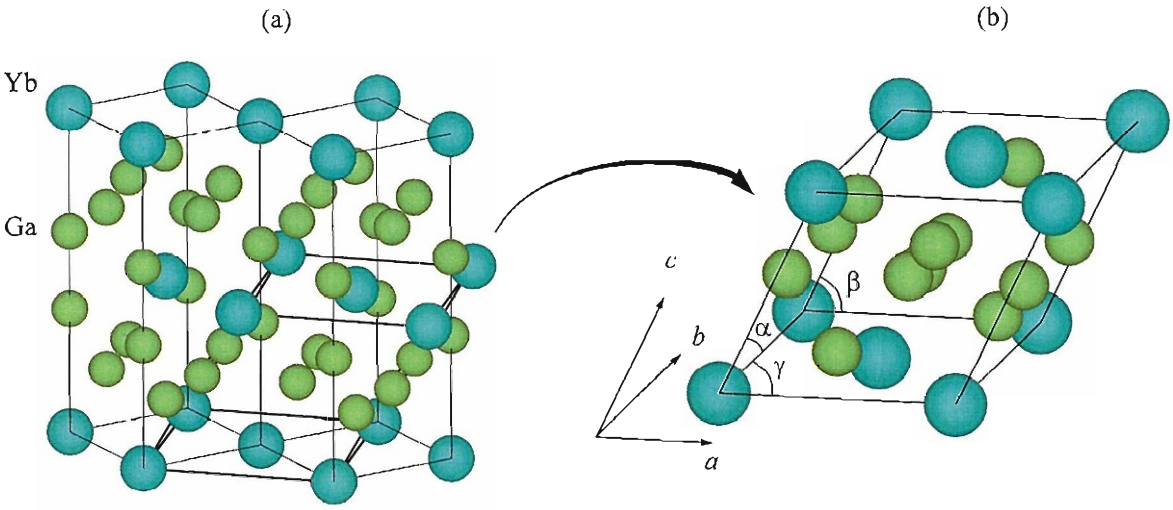

Fig. 5.59 (a) Geometrical relationship between the cells of the monoclinic $YbGa_4$ (thick lines), and the tetragonal $BaAl_4$ (thin lines) and (b) crystal structure of $YbGa_4$.

the divalent nature. In fact, the magnetic susceptibility is Pauli paramagnetic, as shown in Fig. 5.61. It is, however, noted that the sample contains some paramagnetic impurity, which amounts to about 0.2 % of Yb^{3+}.

Figures 5.62(a) shows the temperature dependence of the specific heat divided by temperature C/T. Below 1.8 K, an upward tail is observed in the temperature dependence of C/T, which might be due to the magnetic impurities. The entropy reaches only about $0.005R\ln 2$, as shown in Fig. 5.62(a), implying that an impurity amounts to 0.5 % at most, which is consistent with the magnetic susceptibility in magnitude. Neglecting this contribution, we estimated roughly the electronic specific heat coefficient and the Debye temperature as $\gamma = 1.9$ mJ/(K^2·mol) and $\Theta_D = 230$ K from a simple relation with higher order contribution of phonon $C = \gamma T + \beta T^3 + \eta T^5$, shown by a red solid line in Fig. 5.62(b). The Debye temperature of $YbGa_4$ is similar to that of $EuGa_4$ with 220 K and the tetragonal $BaAl_4$ type structure.[198]

Summary

We succeeded in growing the single crystals of $YbGa_4$, and determined the crystal data. $YbGa_4$ is found to be a divalent Pauli paramagnet with $\gamma = 1.9$ mJ/(K^2·mol).

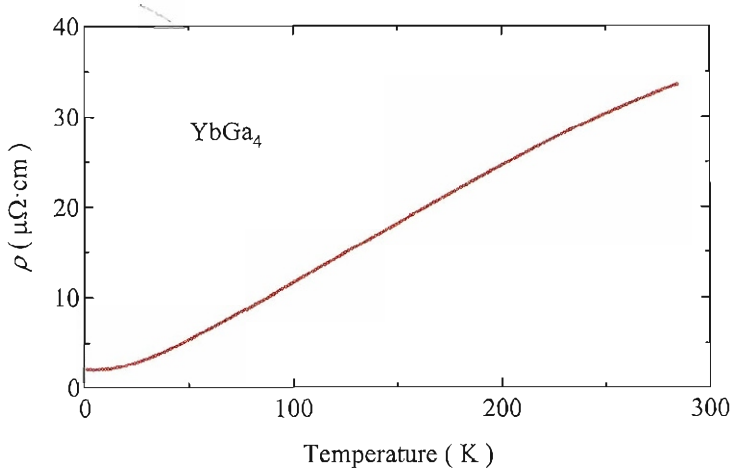

Fig. 5.60 (a) Temperature dependence of the resistivity of $YbGa_4$.

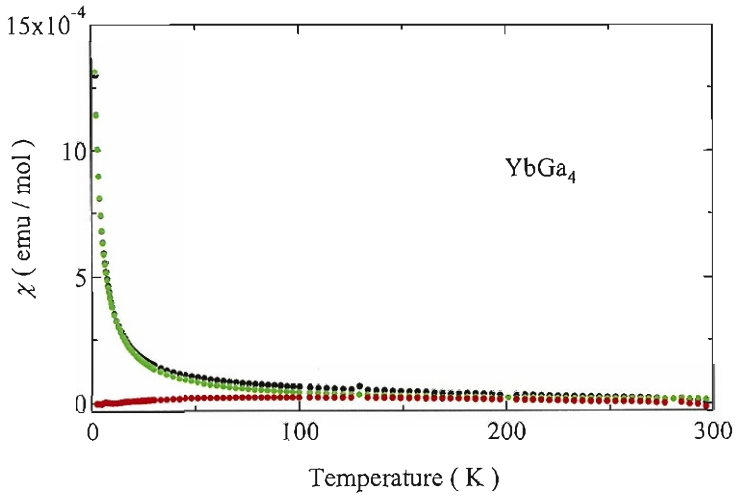

Fig. 5.61 Temperature dependence of the magnetic susceptibility of $YbGa_4$ (red circles), where the impurity contribution (green circles) was subtracted from the raw data (black circles).

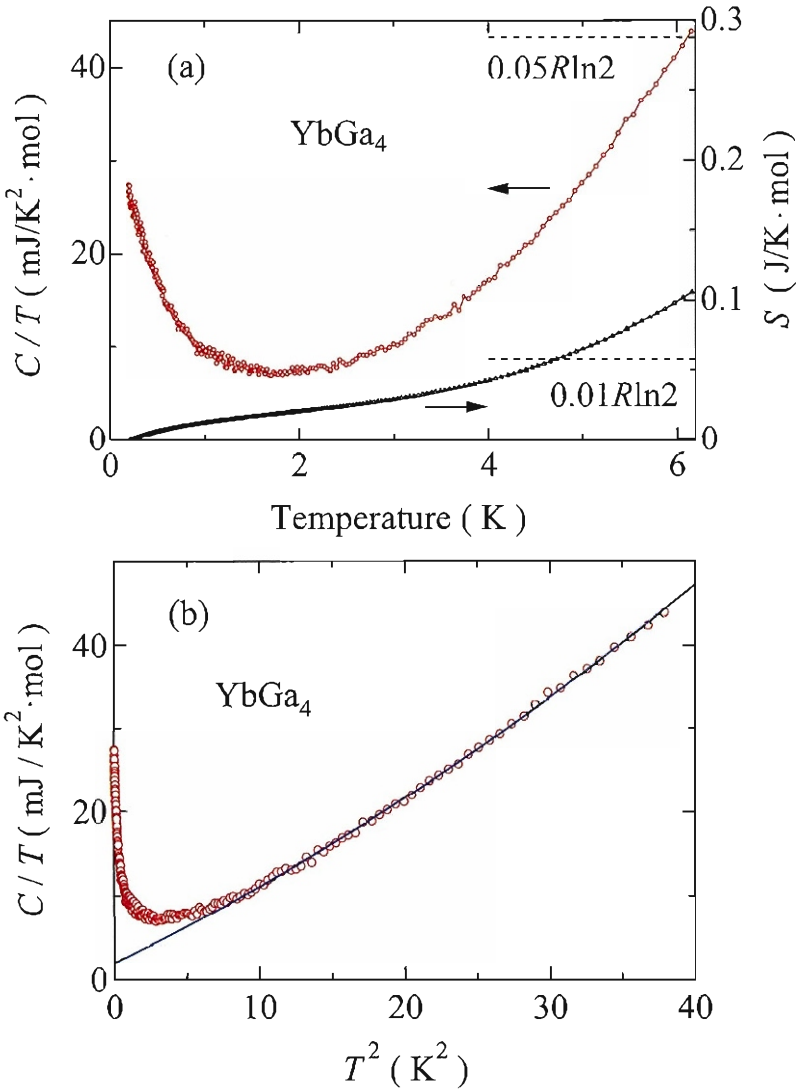

Fig. 5.62 (a) Temperature dependence of the specific heat devided by temperature C/T and its entropy, and (b) T^2 dependence of C/T of $YbGa_4$(a solid line is expressed by $C = \gamma T + \beta T^3 + \eta T^5$).

6 Conclusion

The present experimental studies of La, Ce, Yb, and U compounds are summarized as follows :

1) Pressure-induced superconductivity including superconductivity with the non-centrosymmetric crystal structure

$CePtSi_2$ and $CeRhGe_2$

We synthesized a new compound of $CeRhGe_2$ with the orthorhombic $CeNiSi_2$-type structure. By measuring the electrical resistivity, magnetic susceptibility, magnetization, specific heat, and neutron scattering for single crystals, $CeRhGe_2$ was found to order antiferromagnetically below T_N= 7.6 K with an ordered moment of 1.3 μ_B/Ce oriented along the magnetic easy-axis of the c-axis. Similar measurements were also carried out for $CePtSi_2$ single crystals. From the experimental results of anisotropic magnetic susceptibility and magnetization, the crystalline electric field (CEF) scheme was obtained for $CeRhGe_2$ and $CePtSi_2$, together with the similar compound $CeNiGe_2$. Furthermore, we carried out pressure experiments by measuring the electrical resistivity of $CePtSi_2$ and $CeRhGe_2$. In the quantum critical region where the Néel temperature becomes zero, we observed superconductivity in $CePtSi_2$ and most likely $CeRhGe_2$, at 1.5 and 7.1 GPa, respectively. The upper critical field of $CePtSi_2$ was found to be highly anisotropic with respect to the three principal field directions.

$CeIrGe_3$

We discovered superconductivity in an antiferromagnet $CeIrGe_3$ with the non-centrosymmetric tetragonal structure below 1.5 K at a pressure of 20 GPa. We performed electrical resistivity measurements in single crystals of $CeIrGe_3$ in the temperature range 0.04 - 300 K at pressures up to 24 GPa. From these measurements we deduced the $P-T$ phase diagram. The data implies a crossover from localized to itinerant $4f$ electrons of the type caused by a Kondo lattice phenomenon as pressure increases. The antiferromagnetic phase weakens with pressure and eventually vanishes above 22 GPa, indicative of the occurrence of a quantum critical point. Superconductivity appears inside the antiferromagnetic phase near this critical point. After the disappearance of the magnetic ordering a non-Fermi-liquid behavior is observed, and superconductivity becomes dominant. Resistivity measurements taken at 24 GPa in magnetic fields up to 80 kOe strongly suggest that $CeIrGe_3$ has a very large upper critical field for $H \parallel$ [001].

$LaNiC_2$

We succeeded in growing single crystals of $LaNiC_2$ with the non-centrosymmetric orthorhombic structure by the Czochralski method and measured the electrical re-

sistivity, de Haas-van Alphen effect (dHvA), and specific heat to clarify the Fermi surface and superconducting properties. This compound has been studied experimentally and theoretically from a viewpoint of the triplet superconducting pairing state based the non-centrosymmetric crystal structure. In the present experiment, we observed an ellipsoidal Fermi surface and a multiply-connected-pillar Fermi surface, although these Fermi surfaces are split into two Fermi surfaces, reflecting the antisymmetric spin-orbit interaction based on the non-centrosymmetric crystal structure. The two ellipsoidal Fermi surfaces are split by 230 K, for example. The anisotropy of electrical resistivity and upper critical field H_{c2} in superconductivity are not large for the three principal directions. From the low-temperature specific heat measurement, superconductivity in $LaNiC_2$ is of the BCS-type, with the superconducting energy gap $2\Delta = 2.85 k_B T_{sc} (T_{sc} = 2.7$ K), contrary to the above arguments. The upper critical field $H_{c2}(0)$, which was obtained from the specific heat under magnetic fields, is about 2 kOe.

2) Metamagnetic behavior and electronic instability

$CeCu_6$

The metamagnetic behavior, which corresponds to one of the characteristic properties in the heavy fermion compounds, was studied by measuring the electrical resistivity under pressure and magnetic field for a typical heavy fermion compound $CeCu_6$ with the orthorhombic structure. The transverse magnetoresistance at 100 mK indicated a peak structure at the metamagnetic field $H_m = 20$ kOe for the magnetic field $H \parallel c$-axis under ambient pressure. H_m is found to increase linearly as a function of pressure and indicates $H_m = 102$ kOe at 1.75 GPa, for example. The quantum critical point corresponds to a negative pressure of about 0.21 GPa from extrapolating H_m to zero. The ρ_0 and A values in the electrical resistivity $\rho = \rho_0 + AT^2$ decrease steeply in magnitude with increasing pressure and magnetic field, indicating that the heavy fermion state is destroyed by pressure and magnetic field. The A value, however, becomes distinct and/or is enhanced at the metamagnetic field, especially, in a characteristic pressure region where the electronic state deviates from the heavy fermion state to the valence fluctuating region, for example, at 2.00 GPa. It is also confirmed from the dHvA experiment that the cyclotron effective mass is reduced with increasing field. It other words, the cyclotron mass at zero field is extremely large, for example, 160 m_0 for $F = 9.75 \times 10^6$ Oe (branch β).

YbT_2Zn_{20}

We measured the magnetization in high magnetic fields up to 500 kOe, together with the magnetic susceptibility, ac-susceptibility and magnetoresistance for heavy fermion compounds YbT_2Zn_{20} (T : Co, Rh, Ir). The metamagnetic behavior or an abrupt nonlinear increase of magnetization was observed below the magnetic field

H_m at temperatures lower than a characteristic temperature $T_{\chi max}$ below which the magnetic susceptibility becomes almost constant : H_m = 97 kOe and $T_{\chi max}$ = 7.4 K in $YbIr_2Zn_{20}$, H_m= 64 kOe and $T_{\chi max}$ = 5.3 K in $YbRh_2Zn_{20}$, and H_m = 6 kOe and $T_{\chi max}$ = 0.32 K in $YbCo_2Zn_{20}$. From the present data and the previous data in several Ce and U heavy fermion compounds, a simple relation between H_m and $T_{\chi max}$ was obtained : $H_m(kOe) = 15T_{\chi max}(K)$, namely $\mu_B H_m = k_B T_{\chi max}$.

UT_2Zn_{20}

The metamagnetic behavior, which is typical in heavy fermion compounds, is also observed in UCo_2Zn_{20} and UIr_2Zn_{20} at H_m = 80 and 20 kOe, respectively. Reflecting the metamagnetic behavior, the magnetoresistance is suppressed in magnetic fields larger than H_m, and the corresponding A value of a Fermi liquid relation in the electrical resistivity $\rho = \rho_0 + AT^2$ indicates a peak at around H_m. Pressure suppresses this behavior in UIr_2Zn_{20}.

3) Searching for new Ce and Yb compounds

We searched for new Ce and Yb compounds, and succeeded in growing single crystals of $CeRhGe_2$ and $YbPd_5Al_2$. These compounds are new materials. The experimental results of $CeRhGe_2$ are described above. We also succeeded in growing single crystals of $YbGa_4$ of which the electrical and magnetic properties were previously unknown.

$YbPd_5Al_2$

We succeeded in growing a single crystal of $YbPd_5Al_2$ with the tetragonal structure. The temperature dependence of electrical resistivity and a small value of the coefficient A in the Fermi liquid relation $\rho = \rho_0 + AT^2$ suggest that the $4f$ electrons are well localized. An antiferromangeic ordering was found at T_N = 0.19 K in the specific heat measurement. On the other hand, the magnetic entropy exhibits only $0.5R\ln 2$ at T_N, and the magnetic specific heat shows a long tail above T_N.

$YbGa_4$

We succeeded in growing a single crystal of $YbGa_4$, and obtained the crystal structure data. $YbGa_4$ is found to be a divalent Pauli paramagnet with γ = 1.9 mJ/(K^2·mol).

It is noted that Ce-based antiferromagnets including $CePtSi_2$, $CeRhGe_2$, and $CeIrGe_3$ can be changed into heavy fermion superconductors in the quantum critical region, but it is difficult to observe superconductivity in the quantum critical region of Yb compounds including YbT_2Zn_{20}(T: Co, Rh, Ir).

Finally, we discuss the candidate for Yb based heavy fermion superconductor. In past, β-$YbAlB_4$ is only one compound that is reported as a Yb based heavy fermion

superconductor[112]. As mentioned above, the crystal structure of $CePtSi_2$ and $CeRhGe_2$ is quasi two dimension and the neutron experiment suggests quasi dimension q-vector. Two dimensional character is one of important factors for superconductivity. The effect of dimensionality is consistent with theoretical suggestion[199]. Second point, generally, a large effective mass suppresses a superconductive transition temperature. Because a heavy mass implies narrow band width, corresponding to small Debye temperature in terms of electron-phonon interaction. Actually, γ value in β-$YbAlB_4$ is estimated about 150 mJ/(K^2·mol), much smaller than YbT_2Zn_{20}. Although we did not observe the superconductive state of YbT_2Zn_{20} down to 100 mK, we are interested also in what happens at extremely lower temperatures. Third point, $4f$ electrons of trivalent Yb ion is more localized than that of trivalent Ce ion, leading a small exchange interaction between Yb atoms. It is generally said that Yb compounds indicate small magnetic transition temperature rather than Ce one due to the small exchange interaction. To overcome these difficulties, we propose a following crystal structure, quasi two dimensional and the short distance between Yb atoms for enhancing a magnetic interaction, for example, Yb 1-1-2 system with the same structure $CePtSi_2$ and $CeRhGe_2$.

Acknowledgments

My doctoral research was supported by a lot of people. I wish to express my sincere acknowledgments to them. First of all, I would like to express my appreciation to Prof. Yoshichika Ōnuki for valuable advices and an encouragement throughout this work. Prof. Ōnuki recently became Emeritus Professor. I really appreciated Prof. Setsuko Tajima's contribution to all the procedures for my thesis work. I would also like to express thanks to Profs. Rikio Settai, Kiyohiro Sugiyama, Fuminori Honda, Dr. Takeshi Takeuchi, Dr. Ismaldo Bonalde, Prof. Kazumasa Miyake, and Prof. Yoshio Kitaoka for helpful supports, advices, and discussions.

The present research was performed by various experimental methods. I would like to express special thanks to Dr. Yoshinori Haga, Dr. Etsuji Yamamoto, Dr. Tatsuma D. Matsuda, and Dr. Naoyuki Tateiwa in Japan Atomic Energy Agency (JAEA) for experimental suppo-
rts on the single crystal growth of uranium compounds and crystal structure analyses, together with fruitful discussions. The measurement of the high-field magnetization was performed at Center for Quantum Science and Technology under Extremely Conditions, Osaka University. I am grateful to Prof. Masayuki Hagiwara and Prof. Koichi Kindo for providing a chance to carry out the experiment. I am also grateful to Dr. Naoto Matsuura and late Prof. Kazuma Hirota for their supports of neutron scattering experiments. In order to perform the resistivity measurement under high pressure, I used the cubic anvil cell in Institution for Solid State Physics, University of Tokyo (ISSP). Prof. Yoshiya Uwatoko and Dr. Kazuya Matsubayashi supported my experiment. I am grateful to them. I wish to express acknowledgments to Mr. Ryoichi Koki for his supports with technical skills. At the same time, these people had very kindly supported me during the whole term of my research.

I also express special thanks to Ms. Toshiko Yura, Ms. Mariko Miyamoto, Ms. Chiaki Nakaki-
hara, and Ms. Shoko Kitagawa for arrangements of academic conferences and laboratory events and so on.

I also express my thanks to Mr. Shingo Yoshiuchi, Mr. Naoto Nishimura, Mr. Masahiro Ohya, Mr. Junya Sakaguchi, Mr. Yuki Taga, Mr. Akinobu Mori, Mr. Yasunao Miura, and Mr. Toshihiko Kishino and other members in Ōnuki group in Graduate School of Science, Osaka University for their helpful supports and a delightful University life.

The researching activity was supported by Global COE program "Core Research and Engineering of Advanced Materials - Interdisciplinary Education Center for Materials Science"(No G10) and Grant-in-Aid for JSPS Fellows.

Finally, I would like to thank my parents and family for their supports and encouragements.

References

1) Y. Ōnuki, R. Settai, K. Sugiyama, T. Takeuchi, T. C. Kobayashi, Y. Haga, and E. Yamamoto: J. Phys. Soc. Jpn. **73** (2004) 769.

2) S. Doniach: in *Valence Instabilities and Related Narrow Band Phenomena*, ed. R. D. Parks (Plenum, New York, 1977), p. 169.

3) N. D. Dung, T. D. Matsuda, Y. Haga, S. Ikeda, E. Yamamoto, T. Ishikura, T. Endo, S. Tatsuoka, Y. Aoki, H. Sato, T. Takeuchi, R. Settai, H. Harima, and Y. Ōnuki: J. Phys. Soc. Jpn. **78** (2009) 084711.

4) F. Steglich, J. Aarts, C. D. Bredl, W. Lieke, D. Meschede, W. Franz, and H. Schafer: Phys. Rev. Lett. **43** (1979) 1892.

5) G. R. Stewart, Z. Fisk, J. O. Willis, and J. L. Smith: Phys. Rev. Lett. **52** (1984) 679 .

6) C. Geibel, C. Schank, S. Thies, H. Kitazawa, C. D. Bredl, A. Bohm, M. Rau, A. Grauel, R. Caspary, R. Helfrich, U. Ahlheim, G. Weber, and F. Steglich: Z. Phys. B **84** (1991) 1.

7) E. Bauer, G. Hilscher, H. Michor, C. Paul, E. W. Scheidt, A. Gribanov, Y. Seropegin, H. Noel, M. Sigrist, and P. Rogl: Phys. Rev. Lett. **92** (2004) 027003.

8) N. Kimura, K. Ito, K. Saitoh, Y. Umeda, H. Aoki, and T. Terashima: Phys. Rev. Lett. **95** (2005) 247004.

9) N. Kimura, K. Ito, H. Aoki, S. Uji, and T. Terashima: Phys. Rev. Lett. **98** (2007) 197001.

10) I. Sugitani, Y. Okuda, H. Shishido, T. Yamada, A. Thamizhavel, E. Yamamoto, T. D. Matsuda, Y. Haga, T. Takeuchi, R. Settai, and Y. Ōnuki: J. Phys. Soc. Jpn. **75** (2006) 043703.

11) Y. Okuda, Y. Miyauchi, Y. Ida, Y. Takeda, C. T., Y. Oduchi, T. Yamada, N. D. Dung, T. D. Matsuda, Y. Haga, T. Takeuchi, M. Hagiwara, K. Kindo, H. Harima, K. Sugiyama, R. Settai, and Y. Ōnuki: J. Phys. Soc. Jpn. **76** (2007) 044708.

12) R. Settai, T. Takeuchi, and Y. Ōnuki: J. Phys. Soc. Jpn. **76** (2007) 051003.

13) Y. Ōnuki and A. Hasegawa: in*the Physics and Chemistry of Rare Earths*, ed. J. K. A. Gschneidner and L. Eyring (North-Holland, Amsterdam, 1995), Vol. 20, p. 1.

14) K. Ueda and Y. Ōnuki: *Physics of Heavy Fermions* (Shokabo, 1988).

15) K. W. H. Stevens: Proceedings of the Physical Society. Section A **65** (1952) 209.

16) M. T. Hutchings: in*Solid State Physics, Advances in Research and Applications*, ed. F. Seitz and B. Turnbull (Academic, New York, 1965), Vol. 16, p. 227.

17) A. Galatanu, Y. Haga, T. D. Matsuda, S. Ikeda, E. Yamamoto, D. Aoki, T. Takeuchi, and Y. Ōnuki: J. Phys. Soc. Jpn. **74** (2005) 1582.

18) M. A. Ruderman and C. Kittel: Phys. Rev. **96** (1954) 99.

19) T. Kasuya: Prog. Theor. Phys. **16** (1956) 45.

20) K. Yosida: Phys. Rev. **106** (1957) 893.

21) J. Kondo: Prog. Theor. Phys. **32** (1964) 37.

22) K. H. J. Buschow, H. J. van Daal, F. E. Maranzana, and P. B. van Aken: Phys. Rev. B **3** (1971) 1662.

23) A. Sumiyama, Y. Oda, H. Nagano, Y. Ōnuki, K. S., and T. Komatsubara: J. Phys. Soc. Jpn. **55** (1986) 1294.

24) K. Yamada and K. Yosida: Prog. Theor. Phys. **76** (1986) 621.

25) K. Satoh, T. Fujita, Y. Maeno, Y. Ōnuki, and T. Komatsubara: J. Phys. Soc. Jpn. **58** (1989) 1012.

26) H. Aoki, S. Uji, A. K. Albessard, and Y. Ōnuki: J. Phys. Soc. Jpn. **61** (1992) 3457.

27) H. Aoki, S. Uji, A. K. Albessard, and Y. Ōnuki: Phys. Rev. Lett. **71** (1993) 2110 .

28) C. Bredl: J. Magn. Magn. Mater. **63-64** (1987) 355 .

29) J. Etourneau, J.-P. Mercurio, R. Naslain, and P. Hagenmuller: J. Solid State Chem. **2** (1970) 332 .

30) G. R. Stewart: Rev. Mod. Phys. **56** (1984) 755.

31) K. Kadowaki and S. Woods: Solid State Commun. **58** (1986) 507 .

32) K. Miyake, T. Matsuura, and C. Varma: Solid State Commun. **71** (1989) 1149 .

33) P. A. Lee, T. M. Rice, J. W. Serene, L. J. Sham, and J. W. Wilkins: Condens. Matter Phys. **12** (1986) 99.

34) N. B. Brandt and V. V. Moshchalkov: Adv. Phys. **33** (1984) 373.

35) J. Rossat-Mignod, L. Regnault, J. Jacoud, C. Vettier, P. Lejay, J. Flouquet, E. Walker, D. Jaccard, and A. Amato: J. Magn. Magn. Mater. **76-77** (1988) 376 .

36) A. Schroder, H. Schlager, and H. Lohneysen: J. Magn. Magn. Mater. **108** (1992) 47 .

37) P. Haen, J. Flouquet, F. Lapierre, P. Lejay, and G. Remenyi: J. Low Temp. Phys. **67** (1987) 391.

38) G. Lonzarich: J. Magn. Magn. Mater. **76 - 77** (1988) 1 .

39) Y. Ōnuki, I. Umehara, A. K. Albessard, T. Ebihara, and K. Satoh: J. Phys. Soc. Jpn. **61** (1992) 960.

40) H. Yamagami and A. Hasegawa: J. Phys. Soc. Jpn. **62** (1993) 592.

41) I. Umehara, Y. Kurosawa, N. Nagai, M. Kikuchi, K. Satoh, and Y. Ōnuki: J. Phys. Soc. Jpn. **59** (1990) 2848.

42) A. Hasegawa, H. Yamagami, and H. Johbettoh: J. Phys. Soc. Jpn. **59** (1990) 2457.

43) D. Jaccard, P. Link, E. Vargoz, and K. Alami-Yadri: Physica B: Cond. Matt. **230 - 232** (1997) 297 .

44) H. H. Hill: in *Plutonium and Other Actinides*, ed. W. N. Miner (AIME, New York, 1970), p. 2.

45) Y. Muro, D. Eom, N. Takeda, and M. Ishikawa: J. Phys. Soc. Jpn. **67** (1998) 3601.

46) A. Thamizhavel, T. Takeuchi, T. D. Matsuda, Y. Haga, K. Sugiyama, R. Settai, and Y. Ōnuki: J. Phys. Soc. Jpn. **74** (2005) 1858.

47) N. Kimura, Y. Muro, and H. Aoki: J. Phys. Soc. Jpn. **76** (2007) 051010.

48) K. Sugiyama, M. Nakashima, D. Aoki, K. Kindo, N. Kimura, H. Aoki, T. Komatsubara, S. Uji, Y. Haga, E. Yamamoto, H. Harima, and Y. Ōnuki: Phys. Rev. B **60** (1999) 9248 .

49) L. Puech, J. M. Mignot, P. Lejay, P. Haen, J. Flouquet, and J. Voiron: J. Low Temp. Phys. **70** (1988) 237.

50) H. P. van der Meulen, A. de Visser, J. J. M. Franse, T. T. J. M. Berendschot, J. A. A. J. Perenboom, H. van Kempen, A. Lacerda, P. Lejay, and J. Flouquet: Phys. Rev. B **44** (1991) 814 .

51) S. Holtmeier, P. Haen, A. Lacerda, P. Lejay, J. Tholence, J. Voiron, and J. Flouquet: Physica B: Cond. Matt. **204** (1995) 250 .

52) Y. Aoki, T. Matsuda, H. Sugawara, H. Sato, H. Ohkuni, R. Settai, Y. Ōnuki, E. Yamamoto, Y. Haga, A. Andreev, V. Sechovsky, L. Havela, H. Ikeda, and K. Miyake: J. Magn. Magn. Mater. **177 - 181** (1998) 271 .

53) T. Sakakibara, T. Tayama, K. Matsuhira, H. Mitamura, H. Amitsuka, K. Maezawa, and Y. Ōnuki: Phys. Rev. B **51** (1995) 12030 .

54) R. Daou, C. Bergemann, and S. R. Julian: Phys. Rev. Lett. **96** (2006) 026401.

55) H. Satoh and F. J. Ohkawa: Phys. Rev. B **57** (1998) 5891 .

56) K. Hanzawa, K. Ohara, and K. Yosida: J. Phys. Soc. Jpn. **66** (1997) 3001.

57) Y. Ōno: J. Phys. Soc. Jpn. **67** (1998) 2197.

58) K. Miyake and H. Ikeda: J. Phys. Soc. Jpn. **75** (2006) 033704.

59) S. M. M. Evans: Europhys. Lett. **17** (1992) 469.

60) F. Bagehorn and K. Becker: Physica B: Cond. Matt. **259 - 261** (1999) 75 .

61) H. Shishido, R. Settai, H. Harima, and Y. Ōnuki: J. Phys. Soc. Jpn. **74** (2005) 1103.

62) H. Shishido, R. Settai, D. Aoki, S. Ikeda, H. Nakawaki, N. Nakamura, T. Iizuka, Y. Inada, K. Sugiyama, T. Takeuchi, K. Kindo, T. C. Kobayashi, Y. Haga, H. Harima, Y. Aoki, T. Namiki, H. Sato, and Y. Ōnuki: J. Phys. Soc. Jpn. **71** (2002) 162.

63) R. Settai, H. Shishido, S. Ikeda, Y. Murakawa, M. Nakashima, D. Aoki, Y. Haga, H. Harima, and Y. Ōnuki: J. Phys.: Condens. Matter **13** (2001) L627.

64) Y. Ida, R. Settai, Y. Ota, F. Honda, and Y. Ōnuki: J. Phys. Soc. Jpn. **77** (2008) 084708.

65) M. Yashima, S. Kawasaki, Y. Kitaoka, H. Shishido, R. Settai, and Y. Ōuki: Physica B: Cond. Matt. **378 - 380** (2006) 94 .

66) G. Knebel, D. Aoki, D. Braithwaite, B. Salce, and J. Flouquet: Phys. Rev. B **74** (2006) 020501.

67) T. Park, F. Ronning, H. Q. Yuan, M. B. Salamon, R. Movshovich, J. L. Sarrao, and J. D. Thompson: Nature (London) **440** (2006) 65 .

68) S. Araki, R. Settai, T. C. Kobayashi, H. Harima, and Y. Ōnuki: Phys. Rev. B **64** (2001) 224417.

69) S. Araki, M. Nakashima, R. Settai, T. C. Kobayashi, and Y. Ōnuki: J. Phys.: Condens. Matter **14** (2002) L377.

70) R. Settai, T. Kubo, T. Shiromoto, D. Honda, H. Shishido, K. Sugiyama, Y. Haga, T. D. Matsuda, K. Betsuyaku, H. Harima, T. C. Kobayashi, and Y. Ōnuki: J. Phys. Soc. Jpn. **74** (2005) 3016.

71) J. Bardeen, L. N. Cooper, and J. R. Schrieffer: Phys. Rev. **108** (1957) 1175 .

72) M. Kyogaku, Y. Kitaoka, K. Asayama, C. Geibel, C. Schank, and F. Steglich: J. Phys. Soc. Jpn. **62** (1993) 4016.

73) H. Tou, Y. Kitaoka, K. Ishida, K. Asayama, N. Kimura, Y. Ōnuki, E. Yamamoto, Y. Haga, and K. Maezawa: Phys. Rev. Lett. **80** (1998) 3129.

74) N. D. Mathur, F. M. Grosche, S. R. Julian, I. R. Walker, D. M. Freye, R. K. W. Haselwimmer, and G. G. Lonzarich: Nature (London) **394** (1998) 39 .

75) D. Jaccard, K. Behnia, and J. Sierro: Phys. Lett. A **163** (1992) 475 .

76) R. Movshovich, T. Graf, D. Mandrus, M. Hundley, J. Thompson, R. Fisher, N. Phillips, and J. Smith: Physica B: Cond. Matt. **223 - 224** (1996) 126 .

77) R. Movshovich, T. Graf, D. Mandrus, J. D. Thompson, J. L. Smith, and Z. Fisk: Phys. Rev. B **53** (1996) 8241 .

78) A. T. Holmes, D. Jaccard, and K. Miyake: Phys. Rev. B **69** (2004) 024508.

79) B. Bellarbi, A. Benoit, D. Jaccard, J. M. Mignot, and H. F. Braun: Phys. Rev. B **30** (1984) 1182 .

80) M. Yogi, Y. Kitaoka, S. Hashimoto, T. Yasuda, R. Settai, T. D. Matsuda, Y. Haga, Y. Ōnuki, P. Rogl, and E. Bauer: Phys. Rev. Lett. **93** (2004) 027003.

81) T. Akazawa, H. Hidaka, T. Fujiwara, T. C. Kobayashi, E. Yamamoto, Y. Haga, R. Settai, and Y. Ōnuki: J. Phys.: Condens. Matter **16** (2004) L29.

82) T. Akazawa, H. Hidaka, H. Kotegawa, T. C. Kobayashi, T. Fujiwara, E. Yamamoto, Y. Haga, R. Settai, and Y. Ōnuki: J. Phys. Soc. Jpn. **73** (2004) 3129.

83) R. Settai, Y. Okuda, I. Sugitani, Y. Ōnuki, T. D. Matsuda, Y. Haga, and H. Harima: Int. J. Mod. Phys. B **21** (2007) 3238.

84) S. K. Yip: Phys. Rev. B **65** (2002) 144508.

85) E. I. Rashba: Sov. Phys. Solid State. **2** (1960) 1109.

86) S. Fujimoto: Phys. Rev. B **72** (2005) 024515.

87) R. Settai, Y. Miyauchi, T. Takeuchi, F. Lévy, I. Sheikin, and Y. Ōnuki: J. Phys. Soc. Jpn. **77** (2008) 073705.

88) V. M. Edelstein: Sov. Phys. JETP **68** (1989) 1244.

89) L. P. Gor'kov and E. I. Rashba: Phys. Rev. Lett. **87** (2001) 037004.

90) I. A. Sergienko and S. H. Curnoe: Phys. Rev. B **70** (2004) 214510.

91) V. M. Edelstein: Phys. Rev. Lett. **75** (1995) 2004.

92) S. K. Yip: J. Low Temp. Phys. **140** (2005) 67.

93) K. V. Samokhin: Phys. Rev. B **70** (2004) 104521.

94) R. P. Kaur, D. F. Agterberg, and M. Sigrist: Phys. Rev. Lett. **94** (2005) 137002.

95) N. Hayashi, K. Wakabayashi, P. A. Frigeri, and M. Sigrist: Phys. Rev. B **73** (2006) 092508.

96) N. Hayashi, K. Wakabayashi, P. A. Frigeri, and M. Sigrist: Phys. Rev. B **73** (2006) 024504.

97) T. Yokoyama, Y. Tanaka, and J. Inoue: Phys. Rev. B **72** (2005) 220504(R).

98) M. Oka, M. Ichioka, and K. Machida: Phys. Rev. B **73** (2006) 214509.

99) P. A. Frigeri, D. F. Agterberg, A. Koga, and M. Sigrist: Phys. Rev. Lett. **92** (2004) 097001.

100) P. A. Frigeri, D. F. Agterberg, A. Koga, and M. Sigrist: Phys. Rev. Lett. **93** (2004) 099903.

101) T. Takeuchi, T. Yasuda, M. Tsujino, H. Shishido, R. Settai, H. Harima, and Y. Ōnuki: J. Phys. Soc. Jpn. **76** (2007) 014702.

102) N. R. Werthamer, E. Helfand, and P. C. Hohenberg: Phys. Rev. **147** (1966) 295 .

103) A. M. Clogston: Phys. Rev. Lett. **9** (1962) 266 .

104) B. S. Chandrasekhar: Appl. Phys. Lett. **1** (1962) 7.

105) K. Scharnberg and R. A. Klemm: Phys. Rev. B **22** (1980) 5233 .

106) P. A. Frigeri, D. F. Agterberg, and M. Sigrist: New J. Phys. **6** (2004) 115.

107) N. Tateiwa, Y. Haga, T. D. Matsuda, S. Ikeda, E. Yamamoto, Y. Okuda, Y. Miyauchi, R. Settai, and Y. Ōnuki: J. Phys. Soc. Jpn. **76** (2007) 083706.

108) H. Mukuda, T. Fujii, T. Ohara, A. Harada, M. Yashima, Y. Kitaoka, Y. Okuda, R. Settai, and Y. Ōnuki: Phys. Rev. Lett. **100** (2008) 107003.

109) R. Settai, K. Katayama, D. Aoki, I. Sheikin, G. Knebel, J. Flouquet, and Y. Ōnuki: J. Phys. Soc. Jpn. **80** (2011) 094703.

110) G. Knopp, A. Loidl, K. Knorr, L. Pawlak, M. Duczmal, R. Caspary, U. Gottwick, H. Spille, F. Steglich, and A. P. Murani: Z. Phys. B **77** (1989) 95.

111) T. Takeuchi, S. Yasui, M. Toda, M. Matsushita, S. Yoshiuchi, M. Ohya, K. Katayama, Y. Hirose, N. Yoshitani, F. Honda, K. Sugiyama, M. Hagiwara, K. Kindo, E. Yamamoto, Y. Haga, T. Tanaka, Y. Kubo, R. Settai, and Y. Ōnuki: J. Phys. Soc. Jpn. **79** (2010) 064609.

112) S. Nakatsuji, K. Kuga, Y. Machida, T. Tayama, T. Sakakibara, Y. Karaki, H. Ishimoto, S. Yonezawa, Y. Maeno, E. Pearson, G. G. Lonzarich, L. Balicas, H. Lee, and Z. Fisk: Nature Phys. **4** (2008) 603 .

113) E. K. Okudzeto, K. Kuga, S. Nakatsuji, and J. Y. Chan: Crystal Growth & Design **9** (2009) 1956.

114) Y. Isikawa, D. Kato, A. Mitsuda, T. Mizushima, and T. Kuwai: J. Magn. Magn. Mater. **272 - 276** (2004) 635 .

115) N. V. Hieu, T. Takeuchi, H. Shishido, C. Tonohiro, T. Yamada, H. Nakashima, K. Sugiyama, R. Settai, T. D. Matsuda, Y. Haga, M. Hagiwara, K. Kindo, S. Araki, Y. Nozue, and Y. Ōnuki: J. Phys. Soc. Jpn. **76** (2007) 064702.

116) J. Thompson, M. Nicklas, A. Bianchi, R. Movshovich, A. Llobet, W. Bao, A. Malinowski, M. Hundley, N. Moreno, P. Pagliuso, J. Sarrao, S. Nakatsuji, Z. Fisk, R. Borth, E. Lengyel, N. Oeschler, G. Sparn, and F. Steglich: Physica B: Cond. Matt. **329 - 333** (2003) 446 .

117) J. L. Sarrao, L. A. Morales, J. D. Thompson, B. L. Scott, G. R. Stewart, F. Wastin, J. Rebizant, P. Boulet, E. Colineau, and G. H. Lander: Nature (London) **420** (2002) 297 .

118) F. Wastin, P. Boulet, J. Rebizant, E. Colineau, and G. H. Lander: J. Phys.: Condens. Matter **15** (2003) S2279.

119) Z. Fisk and J. P. Remeika: in *Handbook on the Physics ans Chemistry of Rare Earths*, ed. K. A. G. Jr. and L. Eyring (North-Holland, Amsterdam, 1995), Vol. 12, Chap. 81.

120) Z. Kletowski, N. Iliev, Z. Henkie, and B. Staliński: J. Less-Common Met. **110** (1985) 235 .

121) T. Massalski: in *Binary Alloy Phase Diagrams, II Ed*, ed. T. Massalski and H. Okamoto (ASM International, 1990), Vol. 2.

122) R. Giedigkeit, R. Niewa, W. Schnelle, Y. Grin, and R. Kniep: Z. Anorg. Allg. Chem. **628** (2002) 1692 .

123) M. Kasaya, M. Ito, A. Ono, and O. Sakai: Physica B: Cond. Matt. **223 - 224** (1996) 336 .

124) T. G. Y. Ōnuki and T. Kasuya: in*Materials Science and Technology*, ed. K. H. J. Buschow (VCM, Weinheim, 1991), Vol. 3A, Chap. 7, p. 545.

125) D. Shoenberg: *Magnetic Oscillations in Metals* (Cambridge University Press, Cambridge, 1984).

126) I. R. Walker: Rev. Sci. Instrum. **70** (1999) 3402.

127) T. Smith, C. Chu, and M. Maple: Cryogenics **9** (1969) 53 .

128) T. Osakabe and K. Kakurai: Jpn. J. Appl. Phys. **47** (2008) 6544.

129) G. J. Piermarini and S. Block: Rev. Sci. Instrum. **46** (1975) 973.

130) H. K. Mao and P. M. Bell: Science **200** (1978) 1145.

131) F. Steglich: Physica B: Cond. Matt. **359-361** (2005) 326 .

132) N. D. Dung, Y. Ota, K. Sugiyama, T. D. Matsuda, Y. Haga, K. Kindo, M. Hagiwara, T. Takeuchi, R. Settai, and Y. Ōnuki: J. Phys. Soc. Jpn. **78** (2009) 024712.

133) G. Knebel, D. Aoki, G. Lapertot, B. Salce, J. Flouquet, T. Kawai, H. Muranaka, R. Settai, and Y. Ōnuki: J. Phys. Soc. Jpn. **78** (2009) 074714.

134) M.-. Méasson, H. Muranaka, T. Kawai, Y. Ota, K. Sugiyama, M. Hagiwara, K. Kindo, T. Takeuchi, K. Shimizu, F. Honda, R. Settai, and Y. Ōnuki: J. Phys. Soc. Jpn. **78** (2009) 124713.

135) T. Kawai, H. Muranaka, M.-A. Measson, T. Shimoda, Y. Doi, T. D. Matsuda, Y. Haga, G. Knebel, G. Lapertot, D. Aoki, J. Flouquet, T. Takeuchi, R. Settai, and Y. Ōnuki: J. Phys. Soc. Jpn. **77** (2008) 064716.

136) F. Honda, I. Bonalde, K. Shimizu, S. Yoshiuchi, Y. Hirose, T. Nakamura, R. Settai, and Y. Ōnuki: Phys. Rev. B **81** (2010) 140507.

137) H. J. Im, T. Ito, H.-D. Kim, S. Kimura, K. E. Lee, J. B. Hong, Y. S. Kwon, A. Yasui, and H. Yamagami: Phys. Rev. Lett. **100** (2008) 176402.

138) O. I. Bodak and E. I. Gladyshevskii: Sov. Phys. Crystallogr. **14** (1970) 859.

139) A. Gribanov, A. Grytsiv, P. Rogl, Y. Seropegin, and G. Giester: J. Solid State Chem. **183** (2010) 1278 .

140) T. Nakano, M. Ohashi, G. Oomi, K. Matsubayashi, and Y. Uwatoko: Phys. Rev. B **79** (2009) 172507.

141) A. Morozkin, Y. Seropegin, A. Gribanov, I. Sviridov, J. Kurenbaeva, and A. Kurenbaev: J. Alloys Compd. **264** (1998) 190 .

142) V. K. Pecharsky, K. A. Gschneidner, and L. L. Miller: Phys. Rev. B **43** (1991) 10906.

143) C. R. Rotundu and B. Andraka: Phys. Rev. B **74** (2006) 224423.

144) P. S. Salamakha, O. L. Sologub, and O. I. Bodak: in *Handbook on the Physics and Chemistry of Rare Earth*, ed. J. K. A. Gschneidner and L. Eyring (Elsevier, Amsterdam, 1999), Vol. 27, p. 1.

145) Y. Okada, Y. Inada, A. Galatanu, E. Yamamoto, R. Settai, and Y. Ōnuki: J. Phys. Soc. Jpn. **72** (2003) 2692.

146) A. Gil, B. Penc, L. Gondek, A. Szytula, and J. Hernandez-Velasco: J. Alloys Compd. **346** (2002) 43 .

147) E. F. Bertaut: Acta Cryst. Sec. A **24** (1968) 217.

148) A. Holmes, T. Muramatsu, A. Miyake, D. Kaczorowski, Z. Bukowski, T. Kagayama, and K. Shimizu: J. Magn. Magn. Mater. **310** (2007) 343 .

149) M. Ohashi, G. Oomi, and I. Satoh: J. Phys. Soc. Jpn. **76** (2007) 114712.

150) H. Yamagami: J. Phys. Soc. Jpn. **67** (1998) 3176.

151) A. Yasui, H. Yamagami, and H. Im: J. Phys. Soc. Jpn. **78** (2009) 104705.

152) C. Pfleiderer: Rev. Mod. Phys. **81** (2009) 1551 .

153) M. Nakashima, K. Tabata, A. Thamizhavel, T. C. Kobayashi, M. Hedo, Y. Uwatoko, K. Shimizu, R. Settai, and Y. Ōnuki: J. Phys.: Condens. Matter **16** (2004) L255.

154) H. Kotegawa, K. Takeda, T. Miyoshi, S. Fukushima, H. Hidaka, T. C. Kobayashi, T. Akazawa, Y. Ohishi, M. Nakashima, A. Thamizhavel, R. Settai, and Y. Ōnuki: J. Phys. Soc. Jpn. **75** (2006) 044713.

155) D. Jaccard, J. Mignot, B. Bellarbi, A. Benoit, H. Braun, and J. Sierro: J. Magn. Magn. Mater. **47 - 48** (1985) 23 .

156) H. Okada, K. Igawa, H. Takahashi, Y. Kamihara, M. Hirano, H. Hosono, K. Matsubayashi, and Y. Uwatoko: J. Phys. Soc. Jpn. **77** (2008) 113712.

157) Y. Okuda, I. Sugitani, H. Shishido, T. Yamada, A. Thamizhavel, E. Yamamoto, T. Matsuda, Y. Haga, T. Takeuchi, R. Settai, and Y. Ōuki: J. Magn. Magn. Mater. **310** (2007) 563 .

158) E. Helfand and N. R. Werthamer: Phys. Rev. **147** (1966) 288 .

159) W. Jeitschko and M. Gerss: J. Less-Common Met. **116** (1986) 147 .

160) P. Kotsanidis, J. Yakinthos, and E. Gamari-Seale: J. Less-Common Met. **152** (1989) 287 .

161) W. Schafer, G. Will, J. Yakinthos, and P. Kotsanidis: J. Alloys Compd. **180** (1992) 251 .

162) K. N. Semenenko, A. A. Putyatin, I. V. Nikol'fskaya, , and V. V. Burnasheva: Russ. J. Inorg. Chem. **28** (1983) 943.

163) I. Hase and T. Yanagisawa: J. Phys. Soc. Jpn. **78** (2009) 084724.

164) A. D. Hillier, J. Quintanilla, and R. Cywinski: Phys. Rev. Lett. **102** (2009) 117007.

165) W. Lee, H. Zeng, Y. Yao, and Y. Chen: Physica C: Superconductivity **266** (1996) 138 .

166) I. Bonalde, R. L. Ribeiro, K. J. Syu, H. H. Sung, and W. H. Lee: New J. Phys. **13** (2011) 123022.

167) P. Badica, T. Kondo, and K. Togano: J. Phys. Soc. Jpn. **74** (2005) 1014.

168) Y. Iwamoto, Y. Iwasaki, K. Ueda, and T. Kohara: Phys. Lett. A **250** (1998) 439 .

169) T. Kawai, H. Muranaka, T. Endo, N. D. Dung, Y. Doi, S. Ikeda, T. D. Matsuda, Y. Haga, H. Harima, R. Settai, and Y. Ōnuki: J. Phys. Soc. Jpn. **77** (2008) 064717.

170) V. K. Pecharsky, L. L. Miller, and K. A. Gschneidner: Phys. Rev. B **58** (1998) 497 .

171) Y. Ōnuki, Y. Shimizu, and T. Komatsubara: J. Phys. Soc. Jpn. **53** (1984) 1210.

172) D. T. Cromer, A. C. Larson, and R. B. R. Jnr: Acta Cryst. **13** (1960) 913.

173) A. Sumiyama, Y. Oda, H. Nagano, Y. Ōnuki, and T. Komatsubara: J. Phys. Soc. Jpn. **54** (1985) 4470.

174) J. D. Thompson and Z. Fisk: Phys. Rev. B **31** (1985) 389.

175) S. Raymond and D. Jaccard: J. Low Temp. Phys. **120** (2000) 107.

176) K. Miyake: J. Phys.: Condens. Matter **19** (2007) 125201.

177) K. Satoh, A. Fukada, I. Umehara, Y. Ōnuki, H. Sato, and S. Takayanagi: J. Phys. Soc. Jpn. **61** (1992) 3267.

178) K. Miyake and H. Maebashi: J. Phys. Soc. Jpn. **71** (2002) 1007.

179) G. Oomi, T. Kagayama, H. Takahashi, N. Mōri, Y. Ōnuki, and T. Komatsubara: J. Alloys Compd. **192** (1993) 236 .

180) H. v. Lohneysen, T. Pietrus, G. Portisch, H. G. Schlager, A. Schroder, M. Sieck, and T. Trappmann: Phys. Rev. Lett. **72** (1994) 3262 .

181) S. Chapman, M. Hunt, P. Meeson, P. H. P. Reinders, M. Springford, and M. Norman: J. Phys.: Condens. Matter **2** (1990) 8123.

182) A. Amato, D. Jaccard, J. Flouquet, F. Lapierre, J. L. Tholence, R. A. Fisher, S. E. Lacy, J. A. Olsen, and N. E. Phillips: J. Low Temp. Phys. **68** (1987) 371.

183) M. S. Torikachvili, S. Jia, E. D. Mun, S. T. Hannahs, R. C. Black, W. K. Neils, D. Martien, S. L. Bud'ko, and P. C. Canfield: Proc. Natl. Acad. Sci. USA **104** (2007) 9960.

184) N. Tsujii, H. Kontani, and K. Yoshimura: Phys. Rev. Lett. **94** (2005) 057201.

185) F. Honda, S. Yasui, S. Yoshiuchi, T. Takeuchi, R. Settai, and Y. Ōnuki: J. Phys. Soc. Jpn. **79** (2010) 083709.

186) E. Bauer, J. Thompson, J. Sarrao, and M. Hundley: J. Magn. Magn. Mater. **310** (2007) 449 .

187) P. Swatek and D. Kaczorowski: J. Phys. Soc. Jpn. **80** (2011) SA106.

188) Y. Hirose, M. Toda, S. Yoshiuchi, S. Yasui, K. Sugiyama, F. Honda, M. Hagiwara, K. Kindo, R. Settai, and Y. Ōnuki: J. Phys.: Condens. Matter **273** (2011) 012003.

189) D. Aoki, Y. Haga, T. D. Matsuda, N. Tateiwa, S. Ikeda, Y. Homma, H. Sakai, Y. Shiokawa, E. Yamamoto, A. Nakamura, R. Settai, and Y. Ōnuki: J. Phys. Soc. Jpn. **76** (2007) 063701.

190) T. Onimaru, Y. F. Inoue, K. Shigetoh, K. Umeo, H. Kubo, R. A. Ribeiro, A. Ishida, M. A. Avila, K. Ohoyama, M. Sera, and T. Takabatake: J. Phys. Soc. Jpn. **77** (2008) 074708.

191) F. Honda, M.-A. Measson, Y. Nakano, N. Yoshitani, E. Yamamoto, Y. Haga, T. Takeuchi, H. Yamagami, K. Shimizu, R. Settai, and Y. Ōnuki: J. Phys. Soc. Jpn. **77** (2008) 043701.

192) Y. Nakano, F. Honda, T. Takeuchi, K. Sugiyama, M. Hagiwara, K. Kindo, E. Yamamoto, Y. Haga, R. Settai, H. Yamagami, and Y. Ōnuki: J. Phys. Soc. Jpn. **79** (2010) 024702.

193) A. Palenzona and S. Cirafici: J. Less-Common Met. **63** (1979) 105 .

194) S. Cirafici and M. Fornasini: J. Less-Common Met. **163** (1990) 331 .

195) M. Tillard and C. Belin: Inorg. Chem. **48** (2009) 9250.

196) H. Sugawara, K. Motoki, T. Yamazaki, T. Ebihara, N. Kimura, M. Takashita, J. Itoh, H. Toshima, R. Settai, and Y. Ōnuki: J. Phys. Soc. Jpn. **64** (1995) 3360.

197) G. Bruzzone, M. Fornasini, and F. Merlo: J. Less-Common Met. **154** (1989) 67 .

198) S. Bobev, E. D. Bauer, J. Thompson, and J. L. Sarrao: J. Magn. Magn. Mater. **277** (2004) 236 .

199) P. Monthoux and G. G. Lonzarich: Phys. Rev. B **63** (2001) 054529.

Publication List

1) S. Yoshiuchi, M. Toda, M. Matsushita, S. Yasui, **Y. Hirose**, M. Ohya, K. Katayama, F. Honda, K. Sugiyama, M. Hagiwara, K. Kindo, T. Takeuchi, E. Yamoto, Y. Haga, R. Settai, T. Tanaka, Y. Kubo, and Y. Ōnuki,
Heavy Fermion State in $YbIr_2Zn_{20}$,
J. Phys. Soc. Jpn. **78**, 123711 (2009).

2) F. Honda, I. Bonalde, K. Shimizu, S. Yoshiuchi, **Y. Hirose**, R. Settai, T. Nakamura, and Y. Ōnuki,
Pressure-induced superconductivity and large upper critical field in the noncentrosymmetric antiferromagnet $CeIrGe_3$,
Phys. Rev. B **81**, 140507 (2010).

3) F. Honda, I. Bonalde, S. Yoshiuchi, **Y. Hirose**, T. Nakamura, K. Shimizu, R. Settai, and Y. Ōnuki,
Pressure-induced superconductivity in non-centrosymmetric compound $CeIrGe_3$,
Physica C **470** S543, (2010).

4) F. Honda, S. Yoshiuchi, **Y. Hirose**, T. Nakamura, E. Yamamoto, N. Tateiwa, Y. Haga, T. Takeuchi, R. Settai, and Y. Ōnuki,
Pressure-induced superconductivity in $CePd_5Al_2$ and $CeRhGe_2$, new family of heavy fermion superconductors
Phys. Status Solidi (b) **247** 617, (2010).

5) T. Takeuchi, S. Yasui, M. Toda, M. Matsushita, S. Yoshiuchi, M. Ohya, K. Katayama, **Y. Hirose**, N. Yoshitani, F. Honda, K. Sugiyama, M. Hagiwara, K. Kindo, E. Yamamoto, Y. Haga, T. Tanaka, Y. Kubo, R. Settai, and Y. Ōnuki,
Metamagnetic Behavior in Heavy-Fermion Compound $YbIr_2Zn_{20}$,
J. Phys. Soc. Jpn. **79**, 064609 (2010).

6) **Y. Hirose**, N. Nishimura, F. Honda, K. Sugiyama, M. Hagiwara, K. Kindo, T. Takeuchi, E. Yamamoto, Y. Haga, M. Matsuura, K. Hirota, A. Yasui, H. Yamagami, R. Settai, and Y. Ōnuki,
Magnetic and Superconducting Properties of $CeRhGe_2$ and $CePtSi_2$
J. Phys. Soc. Jpn. **80** 024711, (2011).

7) **Y. Hirose**, F. Honda, R. Settai, and Y. Ōnuki,
Metamagnetic Behaviour in $CeCu_6$,
J. Phys. Soc. Jpn. **80** *Suppl. A*, 065 (2011).

8) **Y. Hirose**, M. Toda, S. Yoshiuchi, S. Yasui, K. Sugiyama, F. Honda, M. Hagiwara, K. Kindo, R. Settai, and Y. Ōnuki,
Metamagnetic Transition in Heavy Fermion Compounds YbT_2Zn_{20} (T : Co, Rh, Ir),
J. Phys : Conf. Ser. **273**, 012003 (2011).

9) M. Matsushita, J. Sakaguchi, Y. Taga, M. Ohya, S. Yoshiuchi, H. Ota, **Y. Hirose**, K. Enoki, F. Honda, K. Sugiyama, M. Hagiwara, K. Kindo, T. Tanaka, Y. Kubo, T. Takeuchi, R. Settai, and Y. Ōnuki.
Fermi surface property and characteristic crystalline electric field effect in $PrIr_2Zn_{20}$.
J. Phys. Soc. Jpn. **80**, 074605 (2011).

10) M. Nakashima, T. Kawata, Y. Amako, S. Yoshiuchi, **Y. Hirose**, K. Matsubayashi, Y. Uwatoko, A. Thamizhavel, F. Honda, R. Settai, and Y. Ōnuki.
Electrical resistivity of $Ce_2Ir_3Ge_5$ under high pressure.
J. Phys. Soc. Jpn. **80** *Suppl. A*, 066 (2011).

11) Y. Ōnuki, S. Yasui, M. Matsushita, S. Yoshiuchi, M. Ohya, **Y. Hirose**, N. D. Dung, F. Honda, T. Takeuchi, R. Settai, K. Sugiyama, E. Yamamoto, T. D. Matsuda, Y. Haga, T. Tanaka, Y. Kubo, and H. Harima.
Characteristic heavy fermion properties in $YbCu_2Si_2$ and YbT_2Zn_{20} (T: Co, Rh, Ir).
J. Phys. Soc. Jpn. **80** *Suppl. A*, 003 (2011).

12) Y. Ōnuki, S. Yasui, S. Yoshiuchi, M. Ohya, M. Matsushita, **Y. Hirose**, T. Takeuchi, F. Hond, R. Settai, K. Sugiyama, E. Yamamoto, and Y. Haga,
Relation between Metamagnetic Transition and Quantum Critical Point in Heavy Fermion Compound $YbIr_2Zn_{20}$,
J. Phys : Conf. Ser. **273**, 012013 (2011).

13) K. Sugiyama, **Y. Hirose**, K. Enoki, S. Ikeda, E. Yamamoto, N. Tateiwa, Y. Haga, T. Kida, M. Hagiwara, K. Kindo, F. Honda, R. Settai, and Y. Ōnuki,
Magnetic-Field-Induced Metallic State in β-US_2,
J. Phys. Soc. Jpn. **80** *Suppl. A* 104 (2011).

14) T. Takeuchi, S. Yoshiuchi, M. Ohya, Y. Taga, **Y. Hirose**, K. Sugiyama, F. Honda, M. Hagiwara, K. Kindo, R. Settai, and Y. Ōnuki,
Field-Induced Quadrupolar Ordered Phase for $H \parallel \langle 111 \rangle$ in Heavy-Fermion Compound $YbCo_2Zn_{20}$,
J. Phys. Soc. Jpn. **80**, 114703 (2011).

15) A. Mori, H. Ota, S. Yoshiuchi, K. Iwakawa, Y. Taga, **Y. Hirose**, T. Takeuchi, E. Yamamoto, Y. Haga, F. Honda, R. Settai, and Y. Ōnuki,
Electrical and Magnetic Properties of Quasicrystal Approximants RCd_6 (R: Rare Earth),
J. Phys. Soc. Jpn. **81**, 024720 (2012).

16) **Y. Hirose**, K. Enoki, S. Yoshiuchi, T. Takeuchi, F. Honda, K. Sugiyama, E. Yamamoto, Y. Haga, M. Hagiwara, K. Kindo, R. Settai, and Y. Ōnuki,
Metamagnetic Behavior in Heavy Fermion Compounds UCo_2Zn_{20} and UIr_2Zn_{20},
printed in J. Phys : Conf. Ser. (2012).

17) **Y. Hirose**, N. Nishimura, K. Enoki, F. Honda, T. Takeuchi, K. Sugiyama, M. Hagiwara, K. Kindo, R. Settai, and Y. Ōnuki,
Electrical and Magnetic Properties of Antiferromagnet $YbPd_5Al_2$,
printed in J. Phys. Soc. Jpn. **81** *Suppl. A*, (2012).

18) **Y. Hirose**, J. Sakaguchi, M. Ohya, M. Matsushita, F. Honda, R. Settai, and Y. Ōnuki,
Collapse and Enhancement of the Heavy Fermion State in $CeCu_6$ under Magnetic,
printed in J. Phys. Soc. Jpn. **81** *Suppl. A*, (2012).

19) K. Enoki, **Y. Hirose**, S. Yoshiuchi, K. Sugiyama, F. Honda, T. Takeuchi, M. Hagiwara, K. Kindo, E. Yamamoto, Y. Haga, R. Settai, and Y. Ōnuki,
Moderate Heavy Fermion State in Ferromagnet YbPdGe,
printed in J. Phys. Soc. Jpn. **81** *Suppl. A*, (2012).

20) F. Honda, Y. Taga, S. Yasui, S. Yoshiuchi, **Y. Hirose**, T. Takeuchi, R. Settai, and Y. Ōnuki,
Pressure-induced super heavy fermion state and antiferromagnetism in $YbIr_2Zn_{20}$,
printed in J. Phys. Soc. Jpn. **81** *Suppl. A*, (2012).

21) K. Ishida, Y. Taga, **Y. Hirose**, K. Iwakawa, A. Mori, F. Honda, T. Takeuchi, R. Settai, and Y. Ōnuki,
Antiferromagnetic Heavy Fermion State in $CeAl_3$,
printed in J. Phys. Soc. Jpn. **81** *Suppl. A*, (2012).

22) K. Iwakawa, **Y. Hirose**, K. Enoki, K. Sugiyama, T. Takeuchi, F. Honda, M. Hagiwara, K. Kindo, T. Nakano, Y. Nozue, R. Settai, and Y. Ōnuki,
Multiple Metamagnetic Transitions in Antiferromagnet Yb_2Pt_2Pb with the Shastry-Sutherland Lattice,
printed in J. Phys. Soc. Jpn. **81** *Suppl. A*, (2012).

23) A. Mori, H. Ota, S. Yoshiuchi, K. Iwakawa andY. Taga, **Y. Hirose**, T. Takeuchi, E. Yamamoto, Y. Haga, F. Honda, R. Settai, and Y. Ōnuki,
Characteristic Electronic State in Quasicrystal Approximants RCd_6 (R:Rare Earth),
printed in J. Phys. Soc. Jpn. **81** *Suppl. A*, (2012).

24) J. Sakaguchi, H. Tsutsumi, **Y. Hirose**, Y. Miura, F. Honda, H. Harima, R. Settai, and Y. Ōnuki,
de Haas-van Alphen Effect and Fermi Surface Properties in $YbTIn_5$ (T : Co, Rh, Ir) and $YbCoGa_5$,
printed in J. Phys. Soc. Jpn. **81** *Suppl. A*, (2012).

25) Y. Taga, K. Sugiyama, K. Enoki, **Y. Hirose**, K. Iwakawa, A. Mori, K Ishida, T. Takeuchi, M. Hagiwara, K. Kindo, R. Settai, and Y. Ōnuki,
Magnetic Properties of RIr_2Zn_{20} (R:Rare Earth) with the Caged Structure,
printed in J. Phys. Soc. Jpn. **81** *Suppl. A*, (2012).

26) Y. Taga, S. Yoshiuchi, M. Ohya, J. Sakaguchi, **Y. Hirose**, F. Honda, T. Takeuchi, R. Settai, and Y. Ōnuki,
Quantum Criticality and Heavy Fermion State in $YbCo_2Zn_{20}$ under Pressure and Magnetic Field
printed in J. Phys. Soc. Jpn. **81** *Suppl. A*, (2012).

27) Y. Taga, S. Yoshiuchi, M. Ohya, J. Sakaguchi, **Y. Hirose**, F. Honda, T. Takeuchi, R. Settai, and Y. Ōnuki,
Quantum Criticality and Heavy Fermion State in $YbCo_2Zn_{20}$ under Pressure and Magnetic Field
printed in J. Phys. Soc. Jpn. **81** *Suppl. A*, (2012).

28) E. Yamamoto, **Y. Hirose**, K. Enoki, K. Mitamura, K. Sugiyama, T. Takeuchi, M. Hagiwara, K. Kindo, Y. Haga, R. Settai, and Y. Ōnuki,
Heavy Fermion State in Antiferromagnet UCd_{11}
printed in J. Phys. Soc. Jpn. **81** *Suppl. A*, (2012).

29) **Y. Hirose**, T. Kishino, J. Sakaguchi, Y. Miura, F. Honda, T. Takeuchi, E. Yamamoto, Y. Haga, H. Harima, R. Settai, and Y. Ōnuki,
Fermi Surface and Superconducting Properties of Non-centrosysmetric $LaNiC_2$
to be published in J. Phys. Soc. Jpn. (2012)